Yukon
Exploration & Geology
2022

Yukon

Yukon Geological Survey staff

Left to right: Rosie Cobbett, Scott Casselman, Brett Elliot, Yury Klyukin, David Moynihan, Sarah Ellis, Warwick Bullen, Tyler Ambrose, Jeff Bond, Bailey Staffen, Maurice Colpron, Derek Cronmiller, Chad Cote, Diane Skipton, Justin Emberley, Karen MacFarlane, Panya Lipovsky, Sydney van Loon, Carolyn Relf, Moya Painter and Julie Minor.

Missing from photo: Leyla Weston, Patrick Sack and Sarah Sternbergh.

Yukon

Yukon
Exploration & Geology
2022

Edited by
K.E. MacFarlane

Yukon Geological Survey
Energy, Mines and Resources
Government of Yukon

Published under the authority of the Department of Energy, Mines and Resources, Government of Yukon, https://yukon.ca.

Printed in Whitehorse, Yukon, 2023.

Publié avec l'autorisation du Ministères de l'Énergie, des Mines et des Ressources du gouvernement du Yukon, https://yukon.ca.

Imprimé à Whitehorse (Yukon) en 2023.

ISSN 1718-8326 (online version)

Yukon Geological Survey publications can be obtained from:
Yukon Geological Survey
102-300 Main Street
Box 2703 (K-102)
Whitehorse, Yukon, Canada Y1A 2C6

email geology@yukon.ca

Yukon Geological Survey website https://yukon.ca/en/science-and-natural-resources/geology.

In referring to this publication, please use the following citation:
Yukon Geological Survey, 2023. Yukon Exploration and Geology 2022, K.E. MacFarlane (ed.), Yukon Geological Survey, 126 p.

Front cover photograph: Boudinaged vein containing large tourmaline crystals, hosted in metatonalite of the Simpson Range suite.

Back cover photograph: Field notes from the Teslin area.

Preface

Yukon Exploration and Geology (YEG) papers and the Yukon Exploration and Geology Overview are two of the main publications of the Yukon Geological Survey (Energy, Mines and Resources, Government of Yukon). Individual YEG papers, with colour images, are available in digital format and can be downloaded from our website. The YEG Overview is available in digital format and in a limited colour print run.

YEG 2022 contains up-to-date information on mining and mineral exploration activity, studies by industry, and results of recent geological field studies. Information in this volume comes from prospectors, exploration and government geologists, mining companies, and students, all of whom are willing to contribute to public geoscience for the benefit of the scientific community, general public and mineral industries of Yukon. Their work is appreciated.

As another calendar year comes to an end, I wonder, where did it go? Luckily, I get an early crack at reading the papers submitted to our YEG volumes and, at least in terms of work, get a recap to remind me of what went on. Once again, I thank my colleagues at the Yukon Geological Survey for their continued efforts in providing geoscience information and support to clients, and then writing about it for YEG. You know you have as much fun with it as I do...

Input or suggestions that you may have to improve future YEG publications are welcomed. Please contact us at (867) 667-8519, or by email at geology@yukon.ca.

Karen

Karen MacFarlane

Yukon Exploration and Geology 2022

Table of Contents

Preliminary double-difference relocation earthquake catalogue for southwestern Yukon centred along the Denali fault zone

Katherine Biegel*, Jeremy Gosselin and Jan Dettmer
Department of Geoscience, University of Calgary, Calgary, Alberta, Canada

Biegel, K., Gosselin, J. and Dettmer, J., 2023. Preliminary double-difference relocation earthquake catalogue for southwestern Yukon centred along the Denali fault zone. *In:* Yukon Exploration and Geology 2022, K.E. MacFarlane (ed.), Yukon Geological Survey, p. 1–18, plus digital appendices.

Abstract

Southwestern Yukon is a seismically active zone of crustal deformation including multiple large, dextral strike-slip fault systems with overlapping activity. In this study, we perform double-difference relocation to the USGS earthquake catalogue for this region to produce a relocated catalogue of 5536 seismic events above magnitude 1.5 from 2010–2021. The relocated catalogue demonstrates better spatial resolution of linear features and the removal of grid location artifacts in depth. The relocated catalogue has smaller travel time residuals and smaller residual standard deviations showing that the new catalogue has improved absolute locations. From bootstrapping, we estimate the location uncertainties for the relocated events to be on the order of 1.2–2.4 km in the horizontal direction and 1.5–2.1 km in the vertical direction. From the relocated events, we interpret new faults including a fault connecting the Totschunda and Denali faults, a connector fault between the Totschunda-Duke River fault system and the Fairweather fault, and multiple smaller faults connecting the Fairweather and Denali faults. The significantly reduced uncertainty in depth also permits constraining the seismicity predominantly to the uppermost 10 km of the crust.

* katherine.biegel@ucalgary.ca

Introduction

Regional tectonic setting

Southwestern Yukon is a zone of active tectonic deformation. The Yakutat block, a tectonic microplate, is obliquely colliding with the North American Plate. The microplate bridges the transition zone from the Aleutian Trench, where the Pacific Plate is subducting under the North American Plate, to the Fairweather/ Queen Charlotte fault, the dextral transform zone that delineates the boundary between the Pacific and North American plates. Current subduction of the Yakutat block is occurring at a rate of 2 mm/yr (Lundgren et *al.*, 1995) with crustal deformation focused in the St. Elias Mountain Range. The Pacific Plate is moving at a rate of 5.7 cm/yr to the northwest (Fig. 1) relative to the North American Plate (DeMets et *al.*, 1990).

Southwestern Yukon has several major dextral crustal strike-slip fault systems including the Chugach-St. Elias fault, Fairweather fault, Denali fault and the Teslin fault farther to the east (Fig. 1). Most regional deformation occurs in the St. Elias region along the Chugach–St. Elias fault or the Fairweather fault. While this region in the St. Elias Mountains is dominated by thrust faulting,

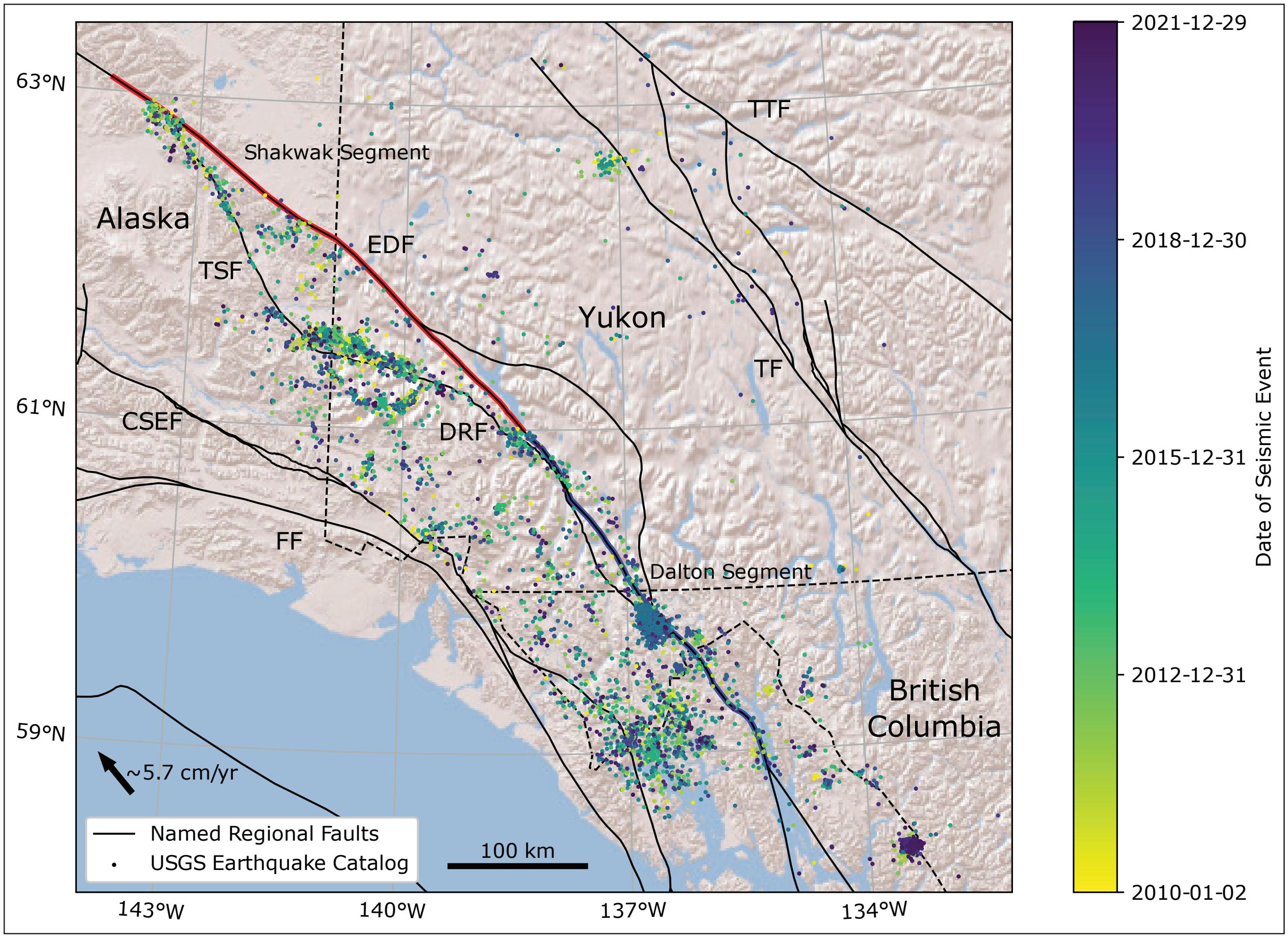

Figure 1. *Seismic events of interest. Epicentral locations (dots) of intraplate seismic events over magnitude 1.5 occurring between Jan. 2010 and Dec. 2021 (colour scale) as defined by the USGS earthquake catalogue. Mapped major regional faults (black lines; after Yukon Geological Survey, 2020) are indicated with major faults of interest labeled including the Tintina fault (TTF), Teslin fault (TF), Eastern Denali fault (EDF), Totschunda fault (TSF), Duke River fault (DRF), Chugach-St. Elias fault (CSEF), and Fairweather fault (FF). Coloured lines indicate subdivisions of the Eastern Denali fault including the Shakwak segment (red line; Grantz, 1966) and the Dalton Segment (blue line; Lanphere, 1977). Political boundaries are denoted by a dashed line.*

the Fairweather fault is a predominately dextral strike-slip fault with slip estimated between 36.6 and 58 mm/yr (Plafker et *al.*, 1978; Fletcher and Freymueller, 2003; Elliott et *al.*, 2010). The St. Elias Mountains are an accretionary mountain range consisting of multiple terranes that were juxtaposed during Yakutat block subduction. The St. Elias Mountains are bound on the eastern side by the Denali fault. Most current crustal seismicity in the region occurs in the zone of deformation between the Fairweather and Denali faults.

The Denali fault is a major dextral, strike-slip fault zone that stretches from central Alaska to British Columbia through southwestern Yukon. Historically there is approximately 400 to 480 km of accumulated slip along the Denali fault (Lowey, 1998; Waldien et *al.*, 2021). Grantz (1966) subdivided the Denali fault into three segments: the Western Denali fault in west-central Alaska, the Central Denali fault in eastern Alaska, and the Eastern Denali fault in southwestern Yukon (Fig. 2). The fault was most active during the Holocene, particularly along the McKinley segment of its central portion and along the Totschunda fault to the south (Lanphere, 1977). The last major earthquake in this area was the 2002 magnitude (M) 7.9 Denali earthquake, a slip-partitioned event, rupturing portions of the Central Denali fault before rupturing the Totschunda fault (Eberhart-Phillips et *al.*, 2003). Slip estimates along the Central Denali fault are ~12.1 mm/yr (Matmon et *al.*, 2006).

The Eastern Denali fault in Yukon is further divided into the Shakwak and Dalton sections (Grantz, 1966; Lanphere, 1977). The Shakwak section of the Denali fault extends from the junction with the Totschunda fault to the Duke River fault (Fig. 1). The Shakwak section is less active than the Central Denali fault in Alaska. Previous studies place movement on the Shakwak section in the range of 5 to 8.4 mm/yr (Matmon et *al.*, 2006; Seitz et *al.*, 2008; Kalbas et *al.*, 2008). The Dalton section of the Denali fault extends from the Duke River fault to the Chatham Strait (Fig. 1) and

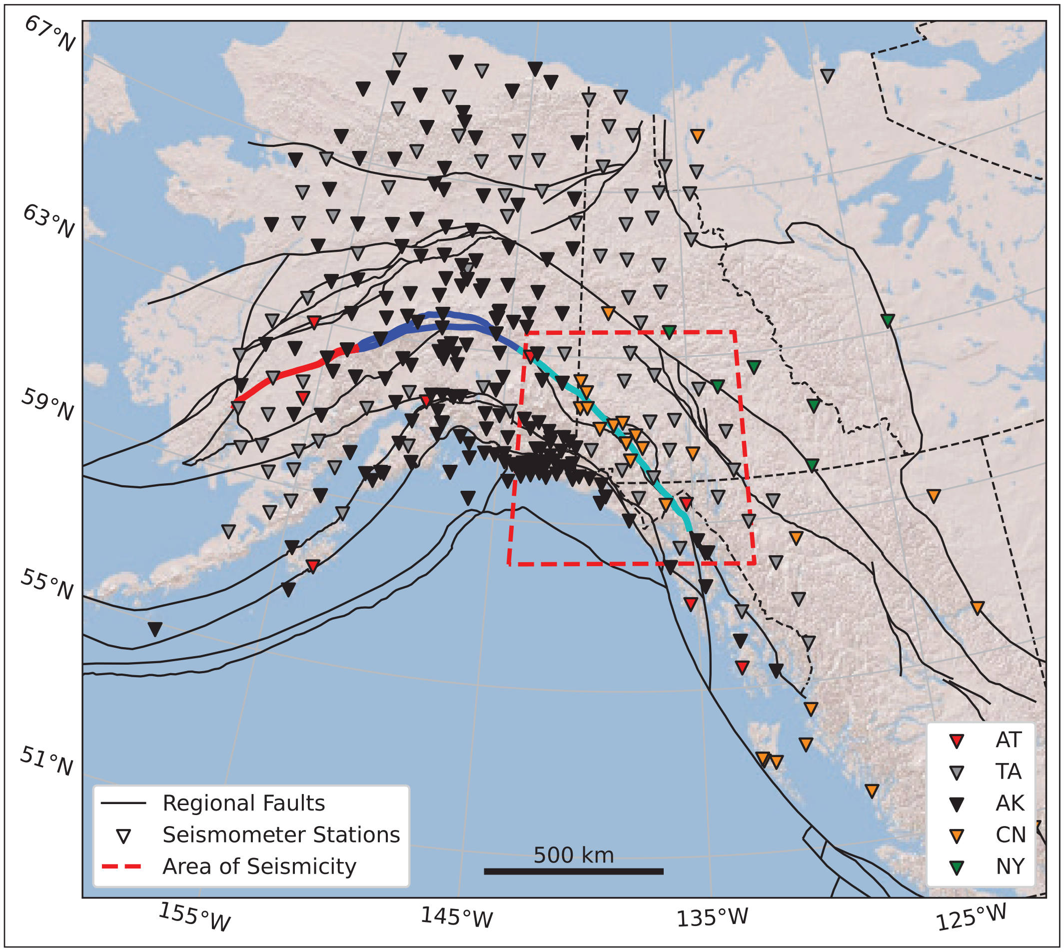

***Figure 2.** Locations of seismic stations (triangles) in Alaska and Canada with at least 1 pick arrival for seismicity (Fig. 1) occurring within the study area of seismicity (red dashed box). Seismic networks are denoted by the colour and include the Alaska Tsunami Network (AT; red), the Transportable Array (TA; gray), the Alaska Regional Network (AK; black), the Canadian National Network (CN; orange), and the Yukon-Northwest Network (NY; green). Major regional faults (black lines) are also shown (after Yukon Geological Survey, 2020). The major subdivisions of the Denali fault (Grantz, 1966) are denoted by the coloured line sections: the Western Denali fault (red), the Central Denali fault (blue) and the Eastern Denali fault (cyan).*

has the smallest slip rate of 1.0–2.5 mm/yr as well as approximately 1.5 mm/yr of contraction (Plafker et *al.*, 1994; Kalbas et *al.*, 2008; Leonard et *al.*, 2008; Elliott et *al.*, 2010). Prior studies suggest that the Eastern Denali fault serves as a regional stress boundary while active deformation occurs on other fault systems such as the Duke River fault (Choi et *al.*, 2021).

Relative seismic event location and relocation

Double-difference (DD) relocation is a relative earthquake location methodology that focuses on relative precision of clusters of earthquakes, rather than the absolute location of individual events. Relative location methods can generally be categorized by how events are paired or related to one another. Parent event approaches (Ito, 1985; Scherbaum and Wendler, 1986; VanDecar and Crosson, 1990) define larger, well-located events as the "parent" events and locate surrounding seismicity ("child" events) in relation to these. Joint hypocentre methods rely on the concept of the earthquake doublet (Fréchet, 1985), for events of similar source location and mechanism. For these methods (Douglas, 1967; Dodge et *al.*, 1995; Waldhauser and Ellsworth, 2000), the location of the doublet is defined by the centroid or joint hypocentre for the pair. Many relative location methods can be used to define an initial seismic event catalogue or as a relocation method to further refine catalogue precision for an existing seismic event catalogue.

As a widely applied joint-hypocentre (doublet) relocation method, DD relocation is a method of defining a relocation catalogue from differential travel time pairs. Pairs of differential travel times come from either an event-pair (a pair of events measured at a common station) or a station-pair (a common event measured at a pair of stations). The most widely applied DD method is event-pair DD relocation (Waldhauser and Ellsworth, 2000) which can be applied across seismic event scales from microseismic studies (Castellanos and Van der Baan, 2013) to regional tectonic studies (Schaff et al., 2002; Waldhauser et *al.*, 2004; Waldhauser and Schaff, 2008). This method can be used to recover absolute event locations (Menke and Schaff, 2004) and reduces the effect of velocity model errors on the relocation. However, the method does not completely remove reliance on the choice of velocity model and a poorly chosen velocity model can lead to bias in the final solution (Wolfe, 2002; Michelini and Lomax, 2004). The reciprocal solution, station-pair DD relocation, has been applied to non-volcanic tremors as an absolute location method (Zhang et *al.*, 2010). Finally, the double-pair DD method, combining both event and station-pair information, has also been shown to improve both relative and absolute event locations (Guo and Zhang, 2016). The double-pair method has been applied at regional tectonic scales (Guo et *al.*, 2017; Li et *al.*, 2018; Ogwari et *al.*, 2018; Share et *al.*, 2021).

Study motivation

This study is part of a larger, multi-year investigation of the geothermal energy potential and natural hazards of major fault zones in southern Yukon. Previous studies have suggested that southern Yukon may have geothermal resources indicated by shallow Curie point depths (Li et *al.*, 2017), large regional fault systems, and the surface manifestations of warm water circulation such as hot springs (Langevin et *al.*, 2020).

In this study, we present a relocated earthquake catalogue for seismicity in southwestern Yukon (Fig. 1) using the event-pair DD relocation method. Our results further refine event locations and improve cluster location precision to help highlight existing fault structures. The relocated catalogue is provided as a geophysical dataset as part of this report (Appendix A). This result will allow for a refined regional tectonic interpretation of active seismicity leading to further studies of source mechanisms and regional stress (Gosselin et *al.*, 2023).

Methods

Double-difference relocation

The DD relocation begins with the linearization of the travel time, t, equation (Geiger, 1910) for earthquake i at station k,

$$r_k^i = \frac{\partial t_k^i}{\partial \boldsymbol{m}} \Delta \boldsymbol{m}^i + \Delta\tau_i + s_k \tag{1}$$

where r_k^i is the travel time residual (t^{obs}-t^{cal}), $\Delta\mathbf{m}^i$ are model parameter perturbations (Δx^i, Δy^i, Δz^i), $\Delta\tau_i$ is the origin time correction, and s_k is the station correction.

For a catalogue of events observed with a seismic network, differential residuals can be taken for pairs of travel time residuals. This differential residual is known as a *double-difference*.

The event-pair DD (Waldhauser and Ellsworth, 2000) is defined for an event pair, events i and j, at a common station, k,

$$dr_k^{ij} = \left(\frac{\partial t_k^i}{\partial \boldsymbol{m}} \Delta \boldsymbol{m}^i + \Delta\tau_i\right) - \left(\frac{\partial t_k^j}{\partial \boldsymbol{m}} \Delta \boldsymbol{m}^j + \Delta\tau_j\right) \qquad (2)$$

where dr_k^{ij} is the differential residual, $(t_k^i - t_k^j)^{obs} - (t_k^i - t_k^j)^{cal}$, and model perturbations, $\Delta\boldsymbol{m}^i$ and $\Delta\boldsymbol{m}^j$, are defined for the two events. The station correction term cancels.

Inversion methods and data weighting

Over an entire catalogue of pairs, Eq. (2) can be characterized by the linear form

$$\boldsymbol{WGm} = \boldsymbol{Wd} \qquad (3)$$

where vector $\boldsymbol{d}$ are the data (DD residuals), vector $\boldsymbol{m}$ contains model parameters (4 perturbations per seismic event), $\boldsymbol{G}$ is a matrix of partial time derivatives with respect to the model parameters, and $\boldsymbol{W}$ is a diagonal matrix containing data weights.

For the relocation problem considered here, the most appropriate method for solving for $\boldsymbol{m}$ is by iterative linear least-squares (Paige and Saunders, 1982). The iterative least-squares method requires a regularization or damping parameter, λ, to minimize DD residuals over the system

$$\begin{bmatrix} \boldsymbol{WG} \\ \lambda I \end{bmatrix} \boldsymbol{m} = \begin{bmatrix} \boldsymbol{Wd} \\ 0 \end{bmatrix} \qquad (4)$$

We employ damping parameter selection by an automated L-curve criterion test (Aster et *al*., 2018).

A priori data weights are based on catalogue pick quality and cross-correlation coefficients. Data weights are recalculated for each iteration of the inversion until the solution reaches stability. Due to the Gaussian error assumption in the linear least-square method, large residuals are down-weighted using bi-weighting (Mosteller and Tukey, 1977).

Using a method similar to Waldhauser and Ellsworth (2000), we assess relative location error estimates using a statistical resampling bootstrap approach (Billings, 1994; Shearer, 1997). For error estimation, we resample the differential-time data by drawing random samples with replacement from the observed residual distribution of the relocation catalogue. We relocate the catalogue using these resampled data as the starting catalogue, incorporating noise into the relocations. Resampling and relocation are repeated 250 times with the cumulative results allowing for estimation of the relocation catalogue uncertainty.

Data set

Earthquake catalogue

For this study, we have identified 6010 crustal seismic events from the USGS catalogue (Fig. 1). This catalogue includes all seismicity of magnitude >1.5 and occurring between 2010 and 2021 in the study area. Our catalogue is limited by the installation date of broadband seismic stations in Yukon which occurred in 2010 and effectively reduced the magnitude of completeness from ~3 to ~1 in some regions of Yukon (Meighan et *al*., 2013). Our catalogue is also limited by the number of phase arrival observations for each event. As we solve for eight model parameters per event pair, event pairs require a minimum of eight shared observations per pair to become an evenly-determined problem. We have therefore limited the minimum magnitude of 1.5 based on the number of phase arrivals per event. Due to our interest in intraplate crustal seismicity, events occurring in proximity of the plate boundary or at depths greater than 30 km were removed from the initial catalogue.

The events of the starting catalogue were observed at 359 seismic stations (Fig. 2) in Alaska and Canada. These stations are part of the International Federation of Digital Seismograph Networks (FDSN) and include parts of the Alaska Tsunami (AT) Seismic Network, the USArray Transportable Array (TA), the Alaska Regional Network (AK), the Canadian National (CN)

Seismograph Network, and the Yukon–Northwest (NY) Seismic Network. Not all stations are temporally available for the entirety of this dataset. The AT, AK, CN, and NY are permanent networks. Most stations within these networks were operating throughout the entirety of the catalogue duration. The TA was a dense temporary station deployment that began in Alaska and parts of Yukon in 2014 and ended in 2021 (Busby and Aderhold, 2020). While not permanent as part of the TA, some of the temporary stations used in the TA deployment were transitioned to permanent stations as part of the AT, AK, and CN networks. Most of the TA stations in Yukon were removed during the 2020/2021 field seasons.

For this catalogue, the USGS identifies 140 186 phase arrivals including 100 265 P arrivals and 39 321 S arrivals. These catalogue arrivals are used as the starting measurements for calculating differential time catalogues.

Event pairing

Event-pairs are required for the calculation of differential time measurements. In this case, we limit event-pairs by the inter-event separation of 12.5 km and to a minimum of 8 common stations for shared measurements. Figure 3 shows the event-pairs included in the differential time catalogues. There were 30 542 event-pairs defined for the 6010 events. The average inter-event distance between event pairs is 4.094 km.

Differential time catalogues

For DD relocation, we develop two differential time (DT) catalogues: one from pick arrivals and one from waveform cross-correlations for each method of relocation. The DT catalogues from pick arrivals are calculated from travel time differences for event-pairs while the cross-correlation catalogues are calculated from up-sampled waveform cross-correlations centred on pick arrivals. This cross-correlation further refines

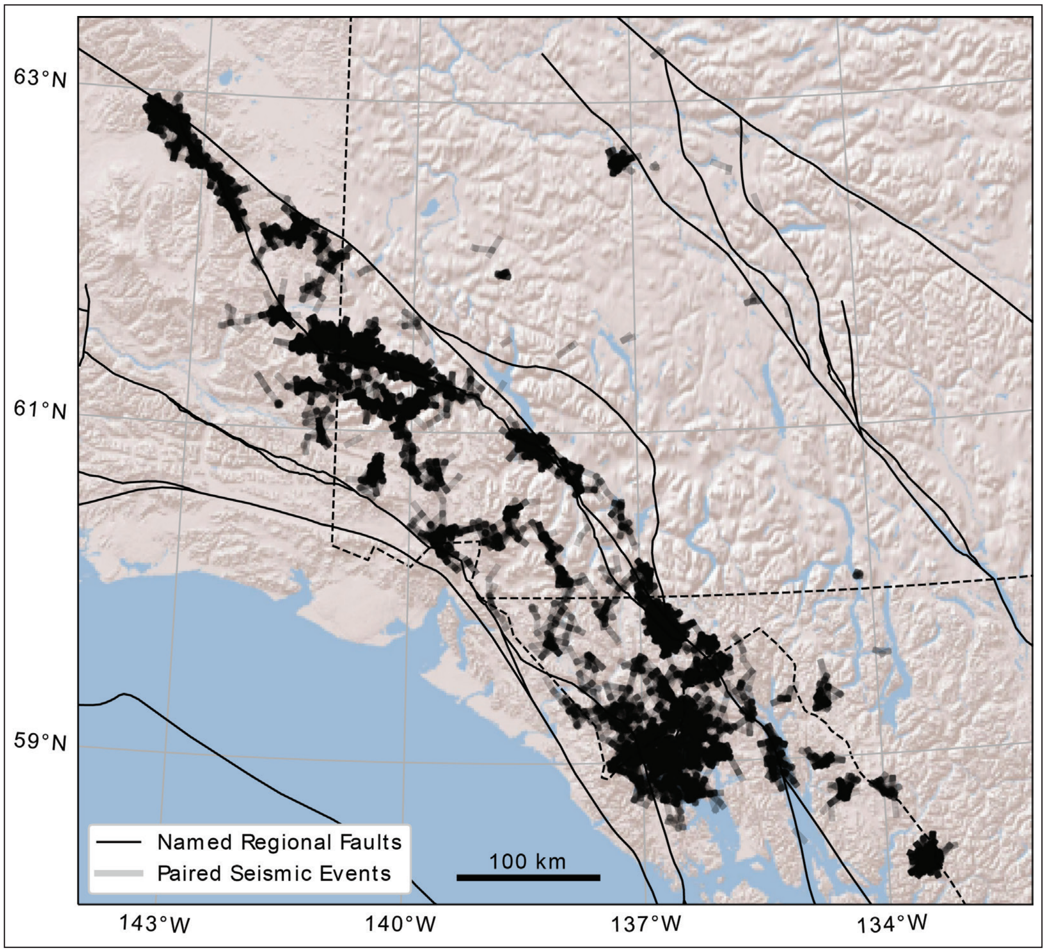

Figure 3. *Density of event-pairs over the study area. Event-pairs are plotted as transparent lines between paired events – darker areas indicate denser spatial coverage of event-pairing.*

the precision of catalogue picks to the onset of waveform similarities and leads to a more precise DT. Cross-correlations must have a correlation coefficient of 0.8 to be included in the cross-correlation DT catalogue.

For the event-pair DD relocations, the DT phase arrival catalogues include 320 028 P wave DTs and 120 600 S wave DTs. The event-pair DD cross-correlation DT catalogue includes 235 724 P wave DTs and 377 504 S wave DTs.

Results and preliminary interpretation

Event-pair relocation catalogue

Using the event-pair DD method, we relocated 5536 events (92% of the USGS catalogue). The full relocation catalogue is shown in Figure 4. where six areas of interest, labeled AA' to FF', are identified. From this relocation catalogue, we find improved spatial linearization of seismicity as well as the removal of grid artifacts from catalogue locations, particularly in depth.

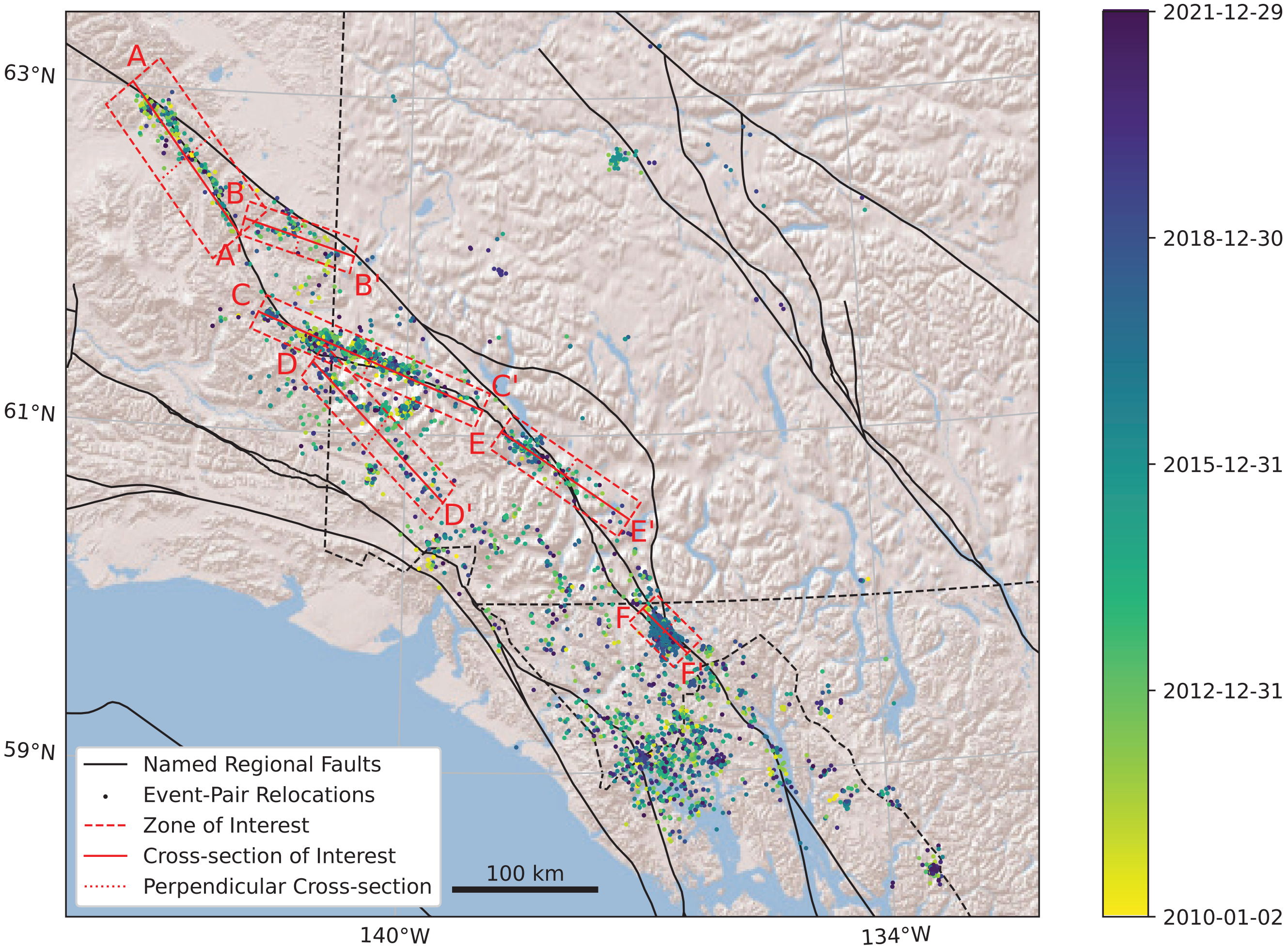

Figure 4. *Event-pair relocations (dots) coloured by date with 6 zones of interest (shown in red). The zones of interest are AA' (Totschunda fault seismicity), BB' (seismicity between the Totschunda and Denali faults), CC' (Duke River fault seismicity), DD' (Connector fault Seismicity), EE' (seismicity south of Kluane Lake crosscutting the Denali fault), and FF' (2017 St. Elias sequence aftershock events). Each zone of interest includes the cross section of interest (solid line), the perpendicular cross section (dotted line), and the included seismicity (dashed box).*

The cross section AA' contains 239 events occurring on the Totschunda fault (Fig. 5). The majority of the seismicity here occurs along the segment of the Totschunda fault that ruptured during the 2002 M 7.9 Denali earthquake. Depth cross sections AA' and aa' (Fig. 5) show that event depths are predominantly <15 km. Along the main cross section (AA'), we see two NW–SE trends of decreasing depths from 0 to 75 km and 100 to 150 km.

Zone BB' (Fig. 6), containing only 76 events, is the smallest highlighted feature. It is a feature running parallel to the Duke River fault to the south and connecting the Totschunda and Denali faults. From the depth cross sections for both BB' and bb' (Fig. 6), the relocated event depths in this zone are 5 to 12 km. We interpret this feature as an active fault that connects the Totschunda and Denali faults. This fault could release stress due to rotation of the inter-fault region bounded by the Totschunda, Duke River and Denali faults.

Figure 7 shows 968 events in Zone CC', including events in proximity to the Duke River fault. Most events in this zone occur north of the mapped Duke River fault surface trace and the perpendicular cross section, cc', does not indicate this seismicity is occurring on a dipping fault surface. There are several areas along CC' that indicate linear features running perpendicular

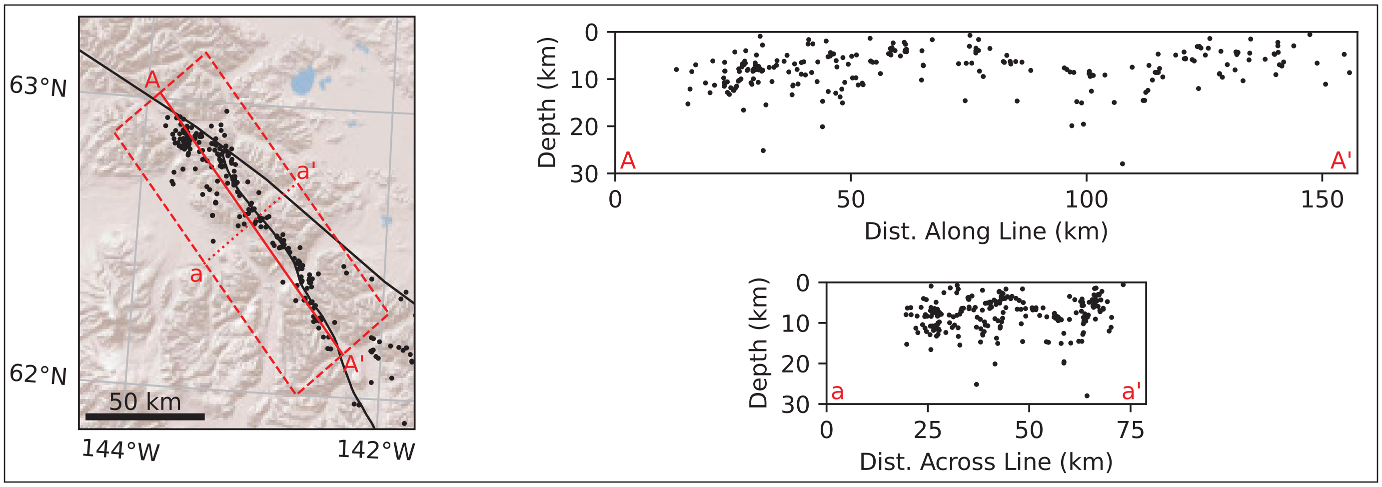

Figure 5. *Event-pair relocations for Zone AA' (in red) including map view (left), depth cross section AA' (solid line; top right), and the perpendicular cross section aa' (dotted line; bottom right). The seismicity considered along the Totschunda fault includes 239 events (dashed box).*

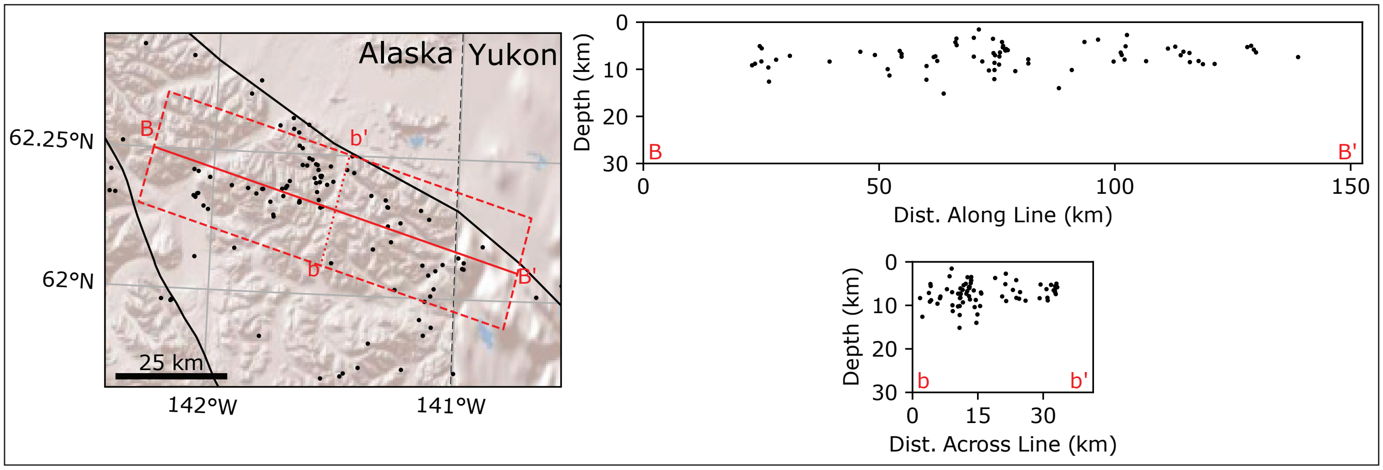

Figure 6. *Event-pair relocations for Zone BB' (in red) including map view (left), depth cross section BB' (solid line; top right) and the perpendicular cross section bb' (dotted line; bottom right). The seismicity includes 76 events (dashed box) that occur in the area between the Totschunda and Eastern Denali faults.*

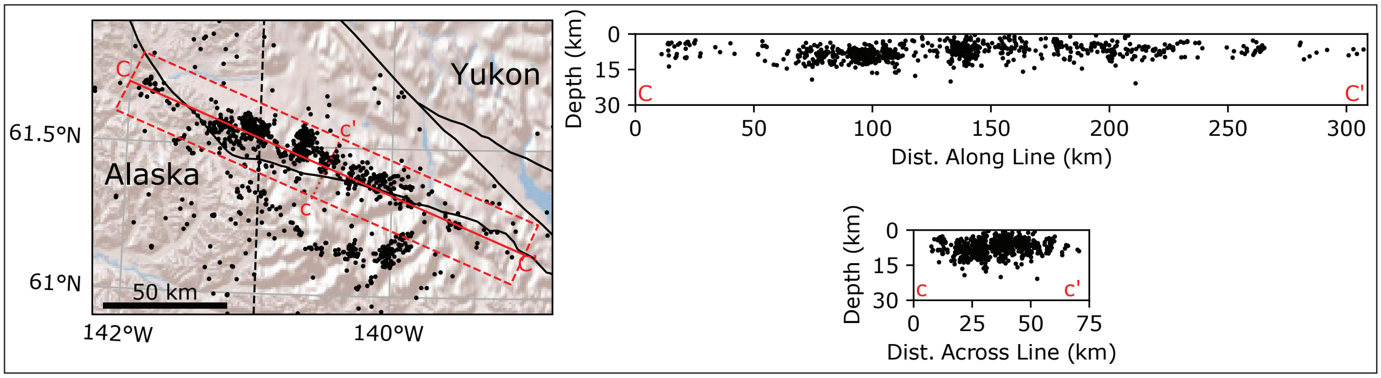

Figure 7. *Event-pair relocations for Zone CC' (in red) including map view (left), depth cross section CC' (solid line; top right) and the perpendicular cross section cc' (dotted line; bottom right). The seismicity includes 968 events (dashed box) that occur along the Duke River fault.*

to the Duke River fault system (occurring at ~90 km, ~140 km and ~160 km). For both cross sections CC' and cc', the majority of events are <15 km in depth. There are no trends in depth along either cross section. It is possible that the mapped surface feature is simply inconsistent with current seismicity or that the seismic data insufficiently constrain the absolute location of the events. The latter can be due to limitations in the velocity model employed for this location, or insufficient network coverage. Recently deployed stations by our group near Burwash Landing aim to improve resolution for similar events.

The Connector fault (Richter and Matson Jr, 1971; Lahr and Plafker, 1980) is a proposed fault connecting the Totschunda fault with the Fairweather fault system located under the St. Elias ice fields. Due to the significant ice coverage in the area, this fault has not been mapped at the surface. Slip is suggested to be up to 10 mm/yr to compensate for low slip on the Eastern Denali fault (Kalbas et *al.*, 2008). Further studies (*e.g.*, Doser, 2014) suggest that the Connector fault is seismically active. Rupture mechanisms along this fault are mostly dextral strike-slip with some oblique components (Doser, 2014). In this study, we relocate 159 events in the geographic area of the Connector fault. These relocations indicate a clear linear feature between the Totschunda-Duke River fault system in the north and the Fairweather fault system in the south (Fig. 8). Event depths generally decrease from northwest to southeast along cross section DD'. Depths are <10 km making this the shallowest feature identified in this study.

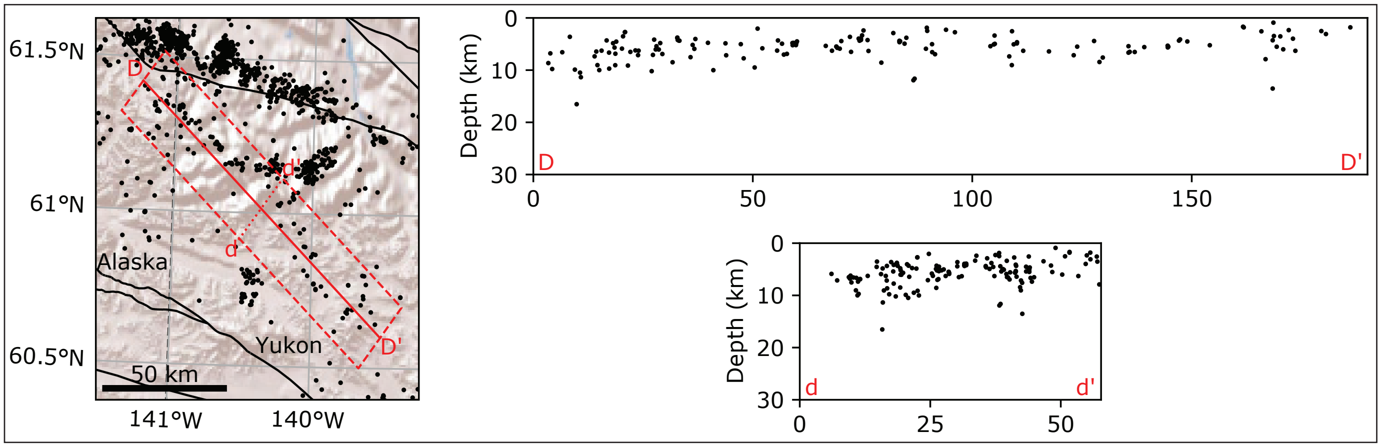

Figure 8. *Event-pair relocations for Zone DD' (in red) including map view (left), depth cross section DD' (solid line; top right) and the perpendicular cross section dd' (dotted line; bottom right). The seismicity includes 159 events (dashed box) that occur in the area of the Connector fault between the Totschunda-Duke River and Fairweather faults.*

Zone EE' (Fig. 9) is located at the southern end of Kluane Lake, and includes 135 events that start on the Duke River fault to the west and cross the surface trace of the Denali fault to the east. The seismicity does not follow the surface trace of the Denali fault, curving instead to the east along topographic lows. Event depths for this zone are interesting in both the EE' and ee' cross sections. For both EE' and ee', seismicity near the Denali fault (at ~75 km on EE' and at ~30 km on ee') is shallowest along the cross section (<8 km). Depths increase for events farther away from where the cross section crosses the Denali fault.

Zone FF' (Fig.10) includes the aftershocks of the 2017 St. Elias earthquakes (He et *al.*, 2018) with 1585 relocated events. Previous studies of this area (Choi et *al.*, 2021) have included DD relocations for portions of this aftershock sequence (1314 events) and resolved two aftershock clusters (one cluster for each of the two M 6 earthquakes). Both clusters are interpreted to be located west of the Eastern Denali fault and not directly related to it. Our relocations of the 1585 events are consistent with previous studies showing two distinct clusters: one quasi-parallel to the Eastern Denali fault and one at an angle to the Eastern Denali fault. However, there is no apparent fault dip observed on either cross sections (FF' or ff'), rather, events are densely clustered.

Travel time residuals

Figure 11 and Table 1 summarize RMS of the travel time residuals, which is modestly reduced by relocation for the overall catalogue from 1.568 to 1.501 s. The RMS of the residuals improves for Zones BB', DD', EE', and FF'. A smaller RMS means the overall residual distribution more closely matches observed data, and that we have improved absolute locations for the overall catalogue along with the events in Zones BB' (Totschunda to Denali inter-fault seismicity), DD' (Connector fault), EE' (Kluane Lake seismicity), and FF' (St. Elias sequence aftershocks). For Zones AA' and CC', the relocation RMS residuals are larger than the USGS catalogue. Therefore, we do not recover improved absolute locations for events along the Totschunda fault or along the Duke River fault. However, we do significantly improve relative cluster location precision, as event-pair residuals are reduced from 637 to 431 ms (31.8% reduction) for catalogue DTs and from 820 to 88 ms (89.6% reduction) for cross-correlation DTs.

Review of the travel time residuals both for the entire catalogue, and for each cluster, show that the widths of the residual distributions improve after relocation. Table 1 shows that for the full catalogue and for all clusters the residual standard deviation decreases after relocation.

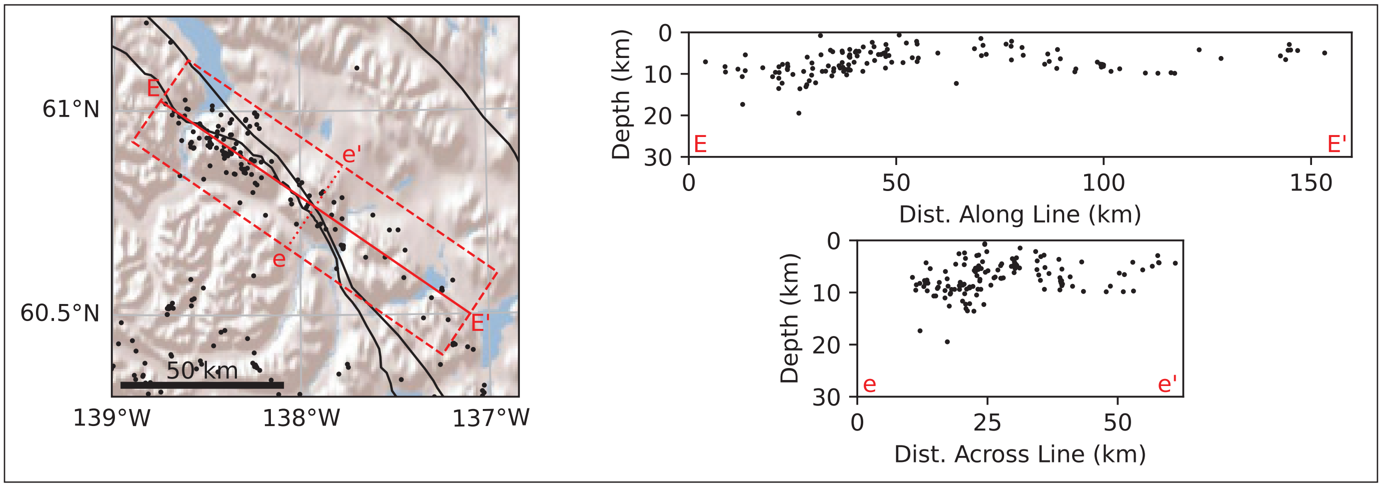

Figure 9. *Event-pair relocations for Zone EE' (in red) including map view (left), depth cross section EE' (solid line; top right) and the perpendicular cross section ee' (dotted line; bottom right). The seismicity includes 135 events (dashed box) that occur at the south end of Kluane Lake in proximity to the Duke River and Denali faults.*

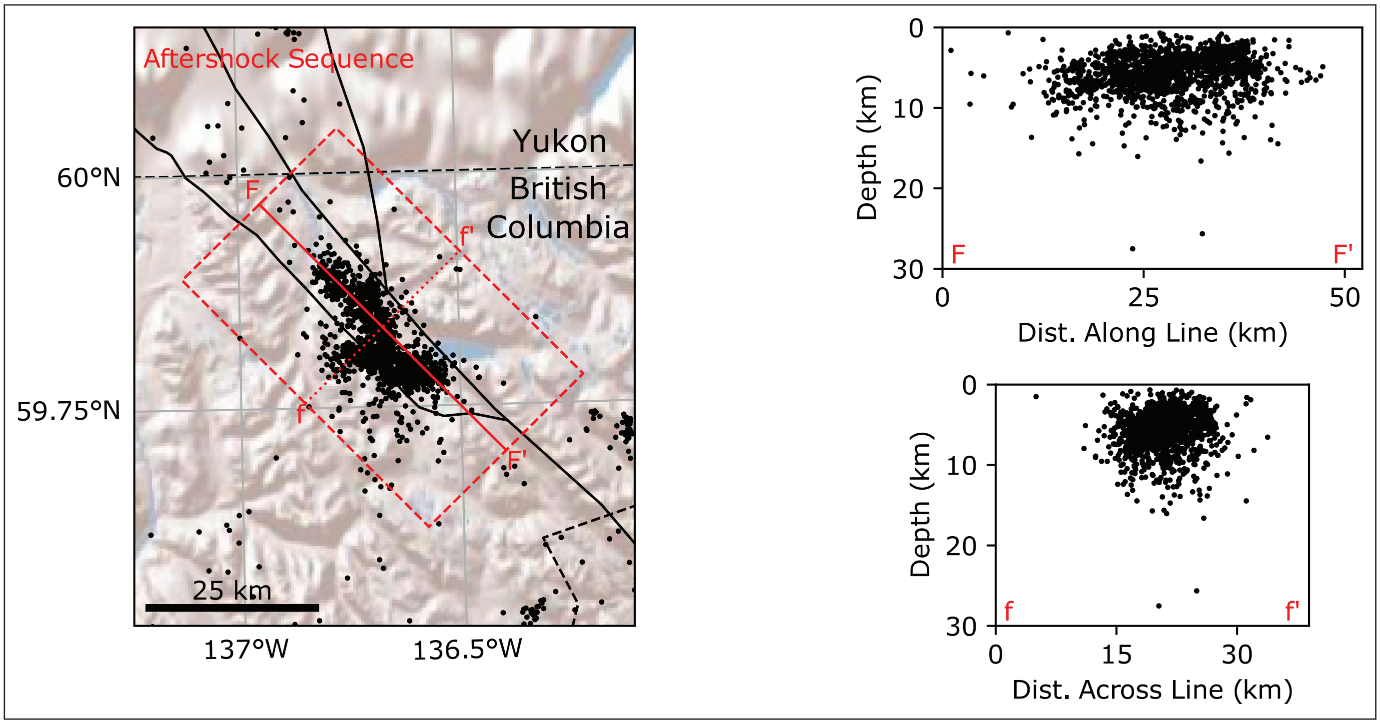

Figure 10. *Event-pair relocations for Zone FF' (in red) including map view (left), depth cross section FF' (solid line; top right) and the perpendicular cross section ff' (dotted line; bottom right). The seismicity includes 1585 events (dashed box) that are part of the aftershock sequence for the 2017 St. Elias sequence.*

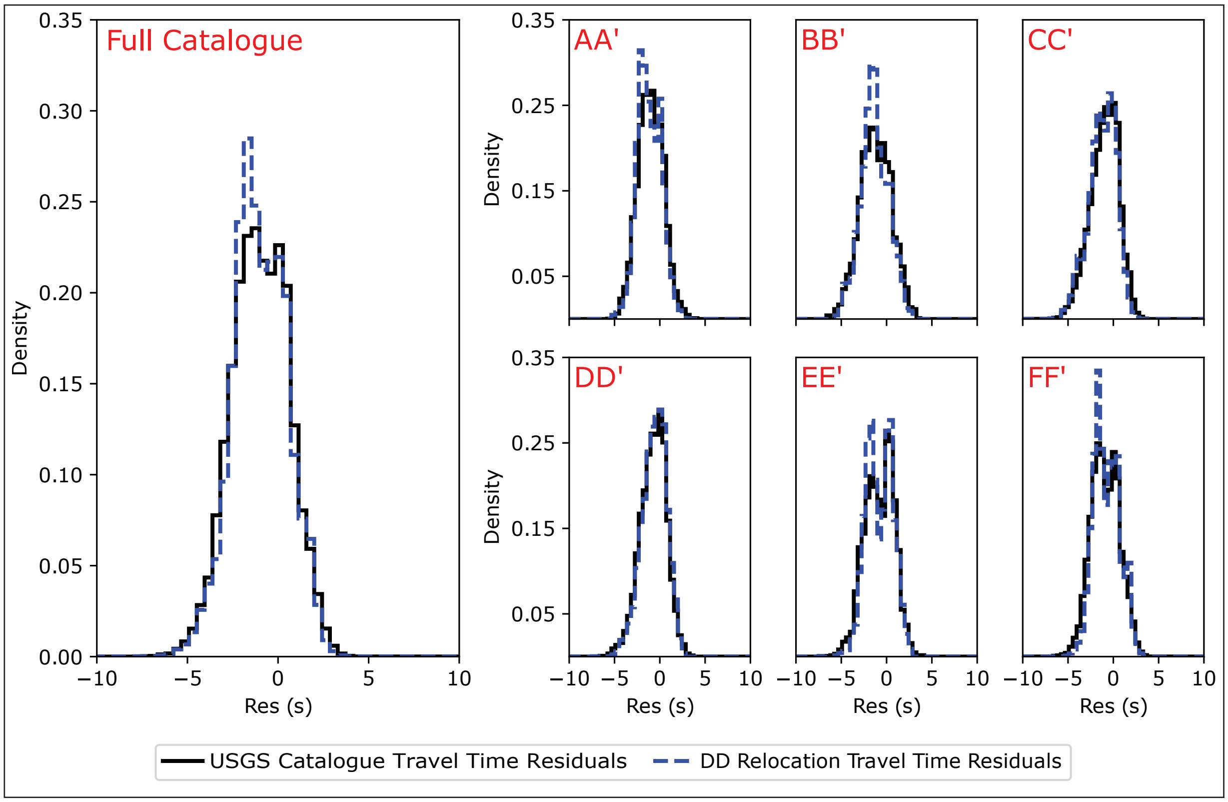

Figure 11. *Travel time residuals for starting USGS catalogue (black line) compared to travel time residuals for relocated catalogue (blue dashed line) for the full catalogue of seismic events (left) and for zones of interest AA' to FF'.*

***Table 1.** Travel time residual statistics (s) for both the USGS event catalogue and the DD relocation catalogue including RMS and standard deviations for the full catalogues as well as zones of interest AA' through FF'.*

	USGS Catalogue		**DD Relocation Catalogue**	
	RMS Residual (s)	**Residual St. Dev. (s)**	**RMS Residual (s)**	**Residual St. Dev. (s)**
Full Catalogue	1.847	1.568	1.796	1.501
Zone AA'	1.726	1.392	1.745	1.302
Zone BB'	2.096	1.714	2.030	1.540
Zone CC'	1.845	1.566	1.956	1.535
Zone DD'	1.617	1.444	1.481	1.353
Zone EE'	1.789	1.599	1.660	1.462
Zone FF'	1.797	1.552	1.604	1.407

The travel time residuals carry a negative bias, likely due to the misfit between the velocity model (Ma and Audet, 2017) used in forward modelling and the true velocity structure. Because of the large study area, a velocity model applicable to a large region is used. Such models ignore local variations in velocity structure, which can be particularly significant in complicated tectonic settings such as the complex fault zones and mountainous regions considered here. Previous tomographic studies of the region indicate large velocity contrasts in fault zones as well as strong directional anisotropy in areas of southwestern Yukon (Schaeffer and Lebedev, 2014; Estève *et al.*, 2021). Improving the forward modelling by including such effects is a plausible but non-trivial future research objective.

Relocation uncertainty estimates

To estimate location uncertainties, we carried out 250 bootstrap iterations for several of the areas of interest. For bootstrap iterations, noisy data are resampled for relocations. Table 2 shows the median, mean and RMS location uncertainty for all spatial parameters for the relocated areas of interest. From Table 2, we see consistent uncertainties in the 1–3 km range for events in these clusters. For many events in the USGS catalogue, we have no initial uncertainty estimate for the location parameters.

Southwestern Yukon is a region of complex dextral strike-slip and oblique thrust systems. From the relocation catalogue, we propose new faults connecting the existing Totschunda-Duke River fault, Denali fault, and Fairweather fault systems and interpret the region as one regional shear zone (Fig. 12). The interpreted faults in Figure 12 include a fault in the region of Zone BB' that connects the southern end of seismicity on the Totschunda fault to the Denali fault. In addition, our results clearly show the Connector fault (Richter and Matson Jr, 1971; Lahr and Plafker, 1980) between the Totschunda-Duke River fault system and the Fairweather fault. Finally, we interpret a series of faults between the Fairweather fault and the Denali fault south of the Connector fault.

Table 2. *Median, mean and RMS uncertainties (km) for X, Y and Z location parameters for events in Zones AA', BB', DD' and EE'*

	Location Uncertainty (km)								
	Median			Mean			RMS		
	X	Y	Z	X	Y	Z	X	Y	Z
Zone AA'	1.40	1.50	1.66	2.00	2.17	2.08	2.83	3.07	2.79
Zone BB'	0.89	0.87	1.44	1.22	1.26	1.45	1.64	1.68	1.77
Zone DD'	1.39	1.31	1.11	2.04	2.02	1.61	2.87	2.93	2.19
Zone EE'	1.47	1.97	1.36	1.93	2.40	1.85	2.66	3.11	2.50

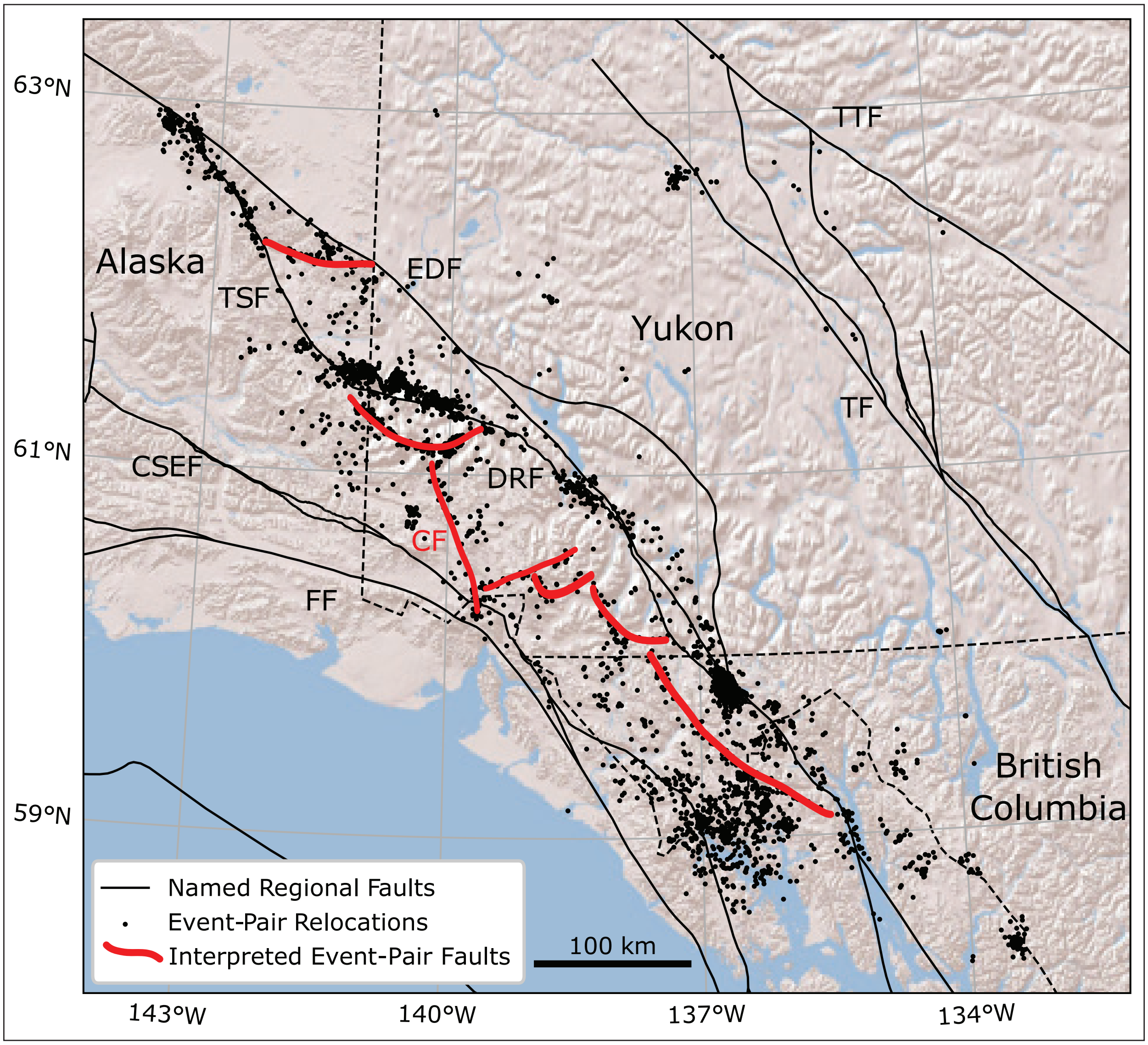

Figure 12. *Interpreted faults (red lines) identified from the event-pair relocation catalogues (black dots) plotted alongside existing named regional faults (black lines). The Connector fault (CF) is labeled in red.*

Conclusions

The DD relocation method allows for clearer images of seismicity and better precision in cluster location. In this study, we present a DD relocation catalogue of 5536 seismic events occurring between 2010 and 2021 in southwestern Yukon. We observe more precise locations of seismicity occurring in the complex dextral strike-slip systems consisting of the Totschunda, Duke River, Denali and Fairweather faults. In this location, the USGS earthquake catalogue contains significant location grid artifacts, particularly in depth, which have been removed in the DD relocation catalogue. Our relocation not only improves cluster location precision, but also improves the overall travel time residuals for the DD catalogue indicating that absolute event locations are also improved. From the relocated catalogue, we have been able to identify several new regional faults. We have identified a fault connecting the Totschunda and Denali faults at the southern end of Totschunda fault seismicity following the M 7.9 Denali earthquake. We have identified and mapped the Connector fault between the Totschunda-Duke River fault and the Fairweather fault system. We have also identified other seismically active fault features including a fault south of the Duke River fault and various faults connecting the Fairweather fault and the Denali fault to the south of the Totschunda-Duke River fault.

Acknowledgments

Funding for this research comes from the Canadian Natural Science and Engineering Research Council (NSERC), Alberta Innovates, the Society of Exploration Geophysicists (SEG), and the Yukon Geological Survey through funding from NRCan's Emerging Renewal Power Program and the Yukon government's *Our Clean Future* initiative. All seismic data are freely available through the Federation of Digital Seismograph Networks (FDSN) web services of the Incorporated Research Institutions for Seismology (IRIS; https://service.iris.edu/). The authors would like to thank the Kluane First Nation for their support of this research, Maurice Colpron for constructive feedback on this report, and David Eaton for his critical review of this work.

References

Aster, R.C., Borchers, B. and Thurber, C.H., 2018. Parameter estimation and inverse problems, Third Edition. Elsevier, https://doi.org/10.1016/C2015-0-02458-3.

Billings, S.D., 1994. Simulated annealing for earthquake location. Geophysical Journal International, vol. 118, p. 680–692, https://doi.org/10.1111/j.1365-246X.1994.tb03993.x.

Busby, R.W. and Aderhold, K., 2020. The Alaska Transportable Array: As Built. Seismological Research Letters, vol. 91, p. 3017–3027, https://doi.org/10.1785/0220200154.

Castellanos, F. and van der Baan, M., 2013. Microseismic event locations using the double-difference algorithm. CSEG Recorder, vol. 38, p. 26–37.

Choi, M., Eaton, D.W. and Enkelmann, E., 2021. Is the Eastern Denali fault still active? Geology, vol. 49, p. 662–666, https://doi.org/10.1130/G48461.1.

DeMets, C., Gordon, R.G., Argus, D.F. and Stein, S., 1990. Current plate motions. Geophysical Journal International, vol. 101, p. 425–478, https://doi.org/10.1111/j.1365-246X.1990.tb06579.x.

Dodge, D.A., Beroza, G.C. and Ellsworth, W.L., 1995. Foreshock sequence of the 1992 Landers, California, earthquake and its implications for earthquake nucleation. Journal of Geophysical Research: Solid Earth, vol. 100, p. 9865–9880, https://doi.org/10.1029/95JB00871.

Doser, D.I., 2014. Seismicity of Southwestern Yukon, Canada, and its relation to slip transfer between the Fairweather and Denali fault systems. Tectonophysics, vol. 611, p. 121–129, https://doi.org/10.1016/j.tecto.2013.11.018.

Douglas, A., 1967. Joint epicentre determination. Nature, vol. 215, p. 47–48, https://doi.org/10.1038/215047a0.

Eberhart-Phillips, D., Haeussler, P.J., Freymueller, J.T., Frankel, A.D., Rubin, C.M., Craw, P., Ratchkovski, N.A., Anderson, G., Carver, G.A., Crone, A.J., Dawson, T.E., Fletcher, H., Hansen, R., Harp, E.L., Harris, R.A., Hill, D.P., Hreinsdóttir, S., Jibson, R.W., Jones, L.M., Kayen, R., Keefer, D.K., Larsen, C.F., Moran, S.C., Personius, S.F., Plafker, G., Sherrod, B., Sieh, K., Sitar, N. and Wallace, W.K., 2003. The 2002 Denali Fault Earthquake, Alaska: A Large Magnitude, Slip-Partitioned Event. Science, vol. 300, p. 1113–1118, https://www.science.org/doi/10.1126/science.1082703.

Elliott, J.L., Larsen, C.F., Freymueller, J.T. and Motyka, R.J., 2010. Tectonic block motion and glacial isostatic adjustment in southeast Alaska and adjacent Canada constrained by GPS measurements. Journal of Geophysical Research: Solid Earth, vol. 115, https://doi.org/10.1029/2009JB007139.

Estève, C., Gosselin, J.M., Audet, P., Schaeffer, A.J., Schutt, D.L. and Aster, R.C., 2021. Surface-Wave Tomography of the Northern Canadian Cordillera Using Earthquake Rayleigh Wave Group Velocities. Journal of Geophysical Research: Solid Earth, vol. 126, https://doi.org/10.1029/2021JB021960.

Fletcher, H.J. and Freymueller, J.T., 2003. New constraints on the motion of the Fairweather fault, Alaska, from GPS observations. Geophysical Research Letters, vol. 30, https://doi.org/10.1029/2002GL016476.

Fréchet, J., 1985. Sismogenése et doublets sismiques. PhD thesis, Université Scientifique et Médicale de Grenoble, 149 p.

Geiger, L., 1910. Herdbestimmung bei Erdbeben aus den Ankunftszeiten. Nachrichten von der Gesellschaft der Wissenschaften zu Göttingen, Mathematisch-Physikalische Klasse, vol. 4, p. 331–351.

Gosselin, J., Biegel, K., Hamidbeygi, M. and Dettmer, J., 2023. Improvements in the regional earthquake focal mechanism catalogue for southwestern Yukon. In: Yukon Exploration and Geology 2022, K.E. MacFarlane (ed.), Yukon Geological Survey.

Grantz, A., 1966. Strike-slip faults in Alaska. USGS Open File Report 66-53, 82 p.

Guo, H. and Zhang, H., 2016. Development of double-pair double difference earthquake location algorithm for improving earthquake locations. Geophysical Journal International, vol. 208, p. 333–348, https://doi.org/10.1093/gji/ggw397.

Guo, H., Zhang, H., Nadeau, R.M. and Peng, Z., 2017. High-resolution deep tectonic tremor locations beneath the San Andreas Fault near Cholame, California, using the double-pair double-difference location method. Journal of Geophysical Research: Solid Earth, vol. 122, p. 3062–3075, https://doi.org/10.1002/2016JB013919.

He, X., Ni, S., Zhang, P. and Freymueller, J., 2018. The 1 May 2017 British Columbia - Alaska earthquake doublet and implication for complexity near sourthern end of Denali fault system. Geophysical Research Letters, vol. 45, p. 5937–5947, https://doi.org/10.1029/2018GL078014.

Ito, A., 1985. High resolution relative hypocenters of similar earthquakes by cross-spectral analysis method. Journal of Physics of the Earth, vol. 33, p. 279–294, https://doi.org/10.4294/jpe1952.33.279.

Kalbas, J.L., Freed, A.M. and Ridgway, K.D., 2008. Contemporary fault mechanics in southern Alaska. In: Active Tectonics and Seismic Potential of Alaska, J.T. Freymueller, P.J. Haeussler, R.L. Wesson and G. Ekström (eds.), AGU Geophysical Monograph Series 179, p. 321–336.

Lahr, J.C. and Plafker, G., 1980. Holocene Pacific–North American plate interaction in southern Alaska: Implications for the Yakataga seismic gap. Geology, vol. 8, p. 483–486, https://doi.org/10.1130/0091-7613(1980)8<483:HPAPII>2.0.CO;2.

Langevin, H., Raymond, J. and Fraser, T., 2020. Assessment of thermo-hydraulic properties of rock samples near Takhini Hot Springs, Yukon. In: Yukon Exploration and Geology 2019, K.E. MacFarlane (ed.), Yukon Geological Survey, p. 57–73.

Lanphere, M.A., 1977. Displacement history of the Denali fault system, Alaska and Canada. Canadian Journal of Earth Sciences, vol. 15, p. 817–822, https://doi.org/10.1139/e78-086.

Leonard, L.J., Mazzotti, S. and Hyndman, R.D., 2008. Deformation rates estimated from earthquakes in the northern Cordillera of Canada and eastern Alaska. Journal of Geophysical Research: Solid Earth, vol. 113, https://doi.org/10.1029/2007JB005456.

Li, C.F., Lu, Y. and Wang, J., 2017. A global reference model of Curie-point depths based on EMAG2. Scientific Reports, vol. 7.

Li, C., Peng, Z., Yao, D., Guo, H., Zhan, Z., and Zhang, H., 2018. Abundant aftershock sequence of the 2015 M w7. 5 Hindu Kush intermediate-depth earthquake. Geophysical Journal International, vol. 213, p. 1121–1134, https://doi.org/10.1093/gji/ggy016.

Lowey, G., 1998. A new estimate of the amount of displacement on the Denali fault system based on the occurrence of carbonate megaboulders in the Dezadeash Formation (Jura-Cretaceous), Yukon, and the Nutzotin Mountains sequence (Jura-Cretaceous), Alaska. Bulletin of Canadian Petroleum Geology, vol. 46, p. 379–386, https://doi.org/10.35767/gscpgbull.46.3.379.

Lundgren, P., Saucier, F., Palmer, R. and Langon, M., 1995. Alaska crustal deformation: Finite element modeling constrained by geologic and very long baseline interferometry. Journal of Geophysical Research: Solid Earth, vol. 100, p. 22033–22046, https://doi.org/10.1029/95JB00237.

Ma, S. and Audet, P., 2017. Seismic velocity model of the crust in the northern Canadian Cordillera from Rayleigh wave dispersion data. Canadian Journal of Earth Sciences, vol. 54, p. 163–172, https://doi.org/10.1139/cjes-2016-0115.

Matmon, A., Schwartz, D.P., Haeussler, P.J., Finkel, R., Lienkaemper, J.J., Stenner, H.D. and Dawson, T.E., 2006. Denali fault slip rates and Holocene–late Pleistocene kinematics of central Alaska. Geology, vol. 34, p. 645–648, https://doi.org/10.1130/G22361.1.

Meighan, L.N., Cassidy, J.F., Mazzotti, S., and Pavlis, G.L., 2013. Microseismicity and tectonics of southwest Yukon Territory, Canada, using a local dense seismic array. Bulletin of the Seismological Society of America, vol. 103, p. 3341–3346, https://doi.org/10.1785/0120130068.

Menke, W. and Schaff, D., 2004. Absolute earthquake locations with differential data. Bulletin of the Seismological Society of America, vol. 94, p. 2254–2264, https://doi.org/10.1785/0120040033.

Michelini, A. and Lomax, A., 2004. The effect of velocity structure errors on double-difference earthquake location. Geophysical Research Letters, vol. 31, https://doi.org/10.1029/2004GL019682.

Mosteller, F. and Tukey, J.W., 1977. Data analysis and linear regression. Addison-Wesley, Reading, Massachusetts.

Ogwari, P.O., DeShon, H.R. and Hornbach, M.J., 2018. The Dallas-Fort Worth airport earthquake sequence: Seismicity beyond injection period. Journal of Geophysical Research: Solid Earth, vol. 123, p. 553–563, https://doi.org/10.1002/2017JB015003.

Paige, C.C. and Saunders, M.A., 1982. LSQR: An algorithm for sparse linear equations and sparse least squares. ACM Transactions on Mathematical Software, vol. 8, p. 43–71.

Plafker, G., Hudson, T., Bruns, T. and Rubin, M., 1978. Late Quaternary offsets along the Fairweather fault and crustal plate interactions in southern Alaska. Canadian Journal of Earth Sciences, vol. 15, p. 805–816, https://doi.org/10.1139/e78-085.

Plafker, G., Moore, J.C. and Winkler, G.R., 1994. Geology of the southern Alaska margin. In: The Geology of Alaska, G. Plafker and H.C. Berg (eds.), Geological Society of America, p. 389–448.

Richter, D.H. and Matson Jr., N.A., 1971. Quaternary faulting in the eastern Alaska Range. GSA Bulletin, vol. 82, p. 1529–1540, https://doi.org/10.1130/0016-7606(1971)82[1529:QFITEA]2.0.CO;2.

Schaeffer, A.J. and Lebedev, S., 2014. Imaging the North American continent using waveform inversion of global and USArray data. Earth and Planetary Science Letters, vol. 402, p. 26–41, https://doi.org/10.1016/j.epsl.2014.05.014.

Schaff, D.P., Bokelmann, G.H.R., Beroza, G.C., Waldhauser, F. and Ellsworth, W.L., 2002. High-resolution image of Calaveras fault seismicity. Journal of Geophysical Research: Solid Earth, vol. 107, https://doi.org/10.1029/2001JB000633.

Scherbaum, F. and Wendler, J., 1986. Cross spectral analysis of Swabian Jura (SW Germany) three-component microearthquake recordings. Journal of Geophysics, vol. 60, p. 157–166.

Seitz, G.J., Haeussler, P.J., Crone, A.J., Lipovsky, P. and Schwartz, D.P., 2008. Eastern Denali fault slip rate and paleoseismic history, Kluane Lake area, Yukon Territory, Canada. In: AGU Fall Meeting 2008, San Francisco, California, abstract i.d. T53B-1947.

Share, P.-E., Castro, R.R., Vidal-Villegas, J.A., Mendoza, L. and Ben-Zion, Y., 2021. High-resolution seismic imaging of the plate boundary in northern Baja California and southern California using double-pair double-difference tomography. Earth and Planetary Science Letters, vol. 568, https://doi.org/10.1016/j.epsl.2021.117004.

Shearer, P.M., 1997. Improving local earthquake locations using the L1 norm and waveform cross correlation: Application to the Whittier Narrows, California, aftershock sequence. Journal of Geophysical Research: Solid Earth, vol. 102, p. 8269–8283, https://doi.org/10.1029/96JB03228.

VanDecar, J.C. and Crosson, R.S., 1990. Determination of teleseismic relative phase arrival times using multi-channel cross-correlation and least squares. Bulletin of the Seismological Society of America, vol. 80, p. 150–169, https://doi.org/10.1785/BSSA0800010150.

Waldhauser, F. and Ellsworth, W.L., 2000. A double-difference earthquake location algorithm: Method and application to the northern Hayward fault, California. Bulletin of the Seismological Society of America, vol. 90, p. 1353–1368, https://doi.org/10.1785/0120000006.

Waldhauser, F., Ellsworth, W.L., Schaff, D.P. and Cole, A., 2004. Streaks, multiplets, and holes: High-resolution spatio-temporal behavior of Parkfield seismicity. Geophysical Research Letters, vol. 31, https://doi.org/10.1029/2004GL020649.

Waldhauser, F. and Schaff, D.P., 2008. Large-scale relocation of two decades of Northern California seismicity using cross-correlation and double-difference methods. Journal of Geophysical Research: Solid Earth, vol. 113, https://doi.org/10.1029/2007JB005479.

Waldien, T.S., Roeske, S.M. and Benowitz, J.A., 2021. Tectonic underplating and dismemberment of the Maclaren-Kluane Schist records Late Cretaceous terrane accretion polarity and ~480 km of post-52 Ma dextral displacement on the Denali fault. Tectonics, vol. 40, https://doi.org/10.1029/2020TC006677.

Wolfe, C.J., 2002. On the mathematics of using difference operators to relocate earthquakes. Bulletin of the Seismological Society of America, vol. 92, p. 2879–2892, https://doi.org/10.1785/0120010189.

Yukon Geological Survey, 2020. A digital atlas of terranes for the northern Cordillera. Yukon Geological Survey, http://data.geology.gov.yk.ca/Compilation/2, [accessed November 2022].

Zhang, H., Nadeau, R.M. and Toksoz, M.N., 2010. Locating nonvolcanic tremors beneath the San Andreas fault using a station-pair double-difference location method. Geophysical Research Letters, vol. 37, https://doi.org/10.1029/2010GL043577.

Appendix A. Relocation catalogue

As part of this report, we have attached the DD relocation earthquake catalogue as a CSV file (Biegel_yukon_relocation.csv). The attached CSV file includes one header line with the following designations:

- EVENT ID – Event ID is the USGS origin time in the format YRMODYHRMNSEC where YR is the 4-digit integer year; MO, DY, HR, and MN are 2-digit integer codes; and SEC is the 4-digit decimal second as an integer.
- LATITUDE, LONGITUDE – These columns are the relocation latitude and longitude in decimal degree format.
- DEPTH (KM) – Depth is the relocation depth in km.
- YEAR, MONTH, DAY – The event date should be the same as the USGS event date.
- HOUR, MINUTE, SECOND – DD relocation can change the event origin time so the time columns may include a relocation time difference which leads to an updated event origin time.
- MAGNITUDE – The USGS catalogue magnitude remains unchanged during relocation.
- MEAN X UNCERTAINTY (KM), MEAN Y UNCERTAINTY (KM), MEAN DEPTH UNCERTAINTY (KM) – From the bootstrap uncertainty analysis, we have location uncertainties in km for events within Zones AA’, BB’, DD’, and EE’. A null value in the location uncertainty means that the event belongs to one of Zones AA’, BB’, DD’, or EE’, but bootstrap did not include the event likely due to poor event pairing.
- RMS TRAVELTIME RESIDUAL (S) – For each event, we present the RMS travel time residual which is the RMS of the residual between the relocation travel times and the measured travel times from phase arrivals in the USGS catalogue. A null value for the travel time residual means that there were no phase arrivals at the stations in shown in Figure 2. These events were therefore relocated using cross-correlation differential times.

The Sunnydale landslide, current understanding and research, Dawson (NTS 116B/3)

Jackson Bodtker* and Dan Shugar
Water, Sediment, Hazards, and Earth-surface Dynamics (waterSHED) Lab, Department of Geoscience,
University of Calgary

Derek C. Cronmiller and Jeffrey D. Bond
Yukon Geological Survey

Bodtker, J., Cronmiller, D.C, Bond, J.D. and Shugar, D., 2023. The Sunnydale landslide, current understanding and research, Dawson (NTS 116B/3). *In:* Yukon Exploration and Geology 2022, K.E. MacFarlane (ed.), Yukon Geological Survey, p. 19–33.

Abstract

The Sunnydale landslide is a slow-moving rock-slope deformation on the western bank of the Yukon River directly across from Dawson, Yukon. While recent data suggest acceleration of the slide, which could pose a potential hazard to Dawson if the acceleration continues to the point of rapid failure, limited data precludes certainty on probability and timing of this occurrence. Field mapping allowed for documentation of road subsidence, expanding tension cracks, recent and ongoing rockfall and production of detailed geomorphological and surficial geology maps of the slide. Differencing from 2014, 2018, 2019, 2020 and 2022 aerial lidar data, and data from physical monitoring stations indicate current movement rates of up to 11 cm/yr across the slide area. Ongoing work including terrestrial lidar change analysis and installation of a near-real-time monitoring system in early 2023 will increase our understanding of current movement trends. Additionally, in-progress geologic dating of deformation features will further our understanding of the history and context of this feature on a geologic timescale.

---

* Jackson.Bodtker@ucalgary.ca

Introduction

The Sunnydale landslide is an approximately 100 000 m^2 progressively developing rock slope deformation within an approximately 180 000 m^2 larger deep-seated gravitational slope deformation (DSGSD) located on the western bank of the Yukon River, directly across from Dawson, Yukon (Fig. 1). Rock slope instabilities of this nature are characterized by slow deformation on hundred-to-thousand-year timescales (Pánek and Klimeš, 2016; Hungr et *al*., 2014). While many of these features pose little hazard and may never accelerate to the point of rapid failure, some do evolve into large destructive rock avalanche events (Pánek and Klimeš, 2016; Hungr et *al*., 2014).

Forcing mechanisms that cause DSGSDs to progress into rapid rock avalanches can range from seismic activity to anomalously heavy rainfall or snowmelt that change porewater pressure in the slope (Pánek and Klimeš, 2016). Hilger et *al*. (2021) provide evidence for permafrost degradation as a trigger for reactivation and acceleration of DSGSDs while Chigira et *al*., (2013) show that location above incising rivers can be a precursory influence. While these factors may both apply to the Sunnydale slide, no evidence of permafrost was found during fieldwork and ongoing influence of the river is likely small due to the location of the suspected failure plane approximately 30 m above water levels.

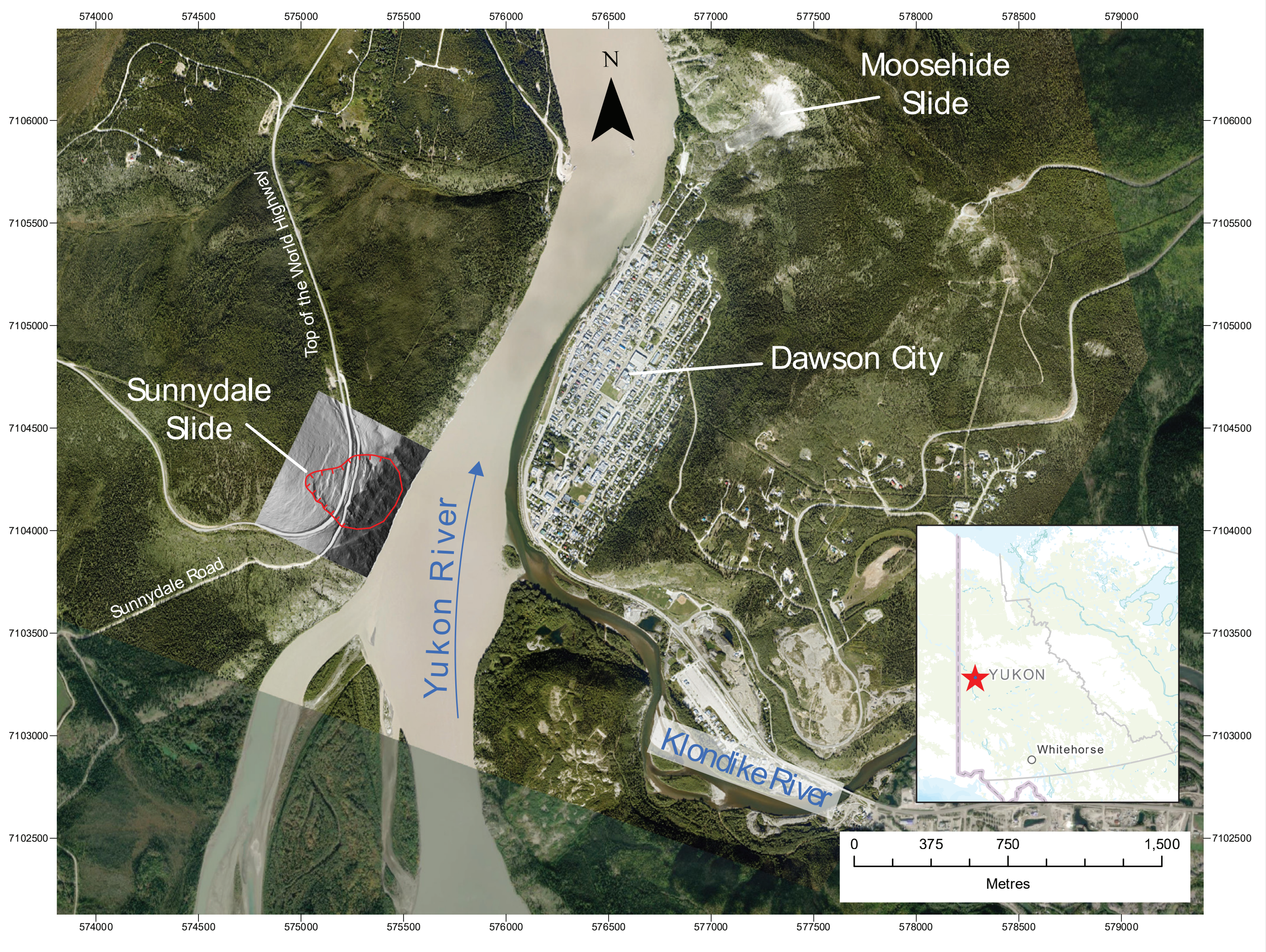

***Figure 1.** Overview map showing the location of the Sunnydale slide relative to Dawson and the Klondike Valley. Satellite imagery from 2017 and 2020 (Esri, 2022) paired with lidar hillshade from 2022.*

The timing of the initial displacement is currently unknown; however, weathering on the upper portion of the headscarp suggests exposure for several thousand if not tens-of-thousands of years. Ages this old or older are possibly due to the slide location within Beringia, an area of Yukon that was not glaciated in the Quaternary (Duk-Rodkin, 1996; Froese et *al*., 2000).

The landslide was first brought to the attention of the Yukon Geological Survey in 2020 by Dawson local Greg Hakonson; he made a connection between deformation along the Top of the World Highway and shallow landslide activity on the steeper front above the Yukon River (Pers. Comm.). Peter Nagano, road foreperson for the Dawson region, stated that the deformation of the Top of the World Highway road surface has been noticeable for approximately 30 years but has gotten worse in the last six years (Pers. Comm.). Further investigation by the Yukon Geological Survey confirmed the presence of the landslide and concerns were such that engineering firm BGC was hired to perform a preliminary investigation (BGC 2020a). This report included an initial map of the area, initial lidar-based change detection, and a recommendation for further study. A second report from BGC estimated the annual failure probability to be between 0.0005 and 0.009 or an approximately 15% chance in the next 50 years (BGC, 2020b).

Regional setting

Bedrock in the slide area is mapped as the Dawson–Clinton Creek unit, a part of the Yukon-Tanana terrane. The unit consists of metavolcanic and metasedimentary rocks including greenstone, phyllite and metachert of Permian age. While no faults are mapped across the slide itself, the local area is cut by several thrust faults (Mortensen, 1988).

The Yukon River has played an extensive role in shaping the Dawson region throughout the Quaternary. Until the latest Pliocene, the Yukon River flowed to the south with headwaters north of Dawson. Following the formation of Glacial Lake Yukon, and contemporaneous with its drainage, the river reversed drainage at about 2.64 Ma (Tempelman-Kluit 1980; Froese et *al*., 2000; Hidy et *al*., 2012). This reversal greatly expanded the drainage area of the river and began down-cutting, which formed the slope on which the Sunnydale slide is located. Loess sedimentation has occurred during glacial periods throughout the Quaternary (Fraser and Burn, 1997).

The Dawson area contains numerous other rockslides. The Moosehide slide, for example, has been a key landmark of the region since time immemorial and several other prehistoric rockslide deposits have been mapped throughout the region (McKenna and Lipovsky, 2014). The Moosehide slide has been studied in detail (Brideau et *al*., 2007, 2012; BGC, 2020b, 2021a,b) and recently instrumented with a near-real-time monitoring system consisting of GNSS-Rovers, extensometers, tiltmeters and a weather station (BGC, 2021c).

Climate records dating to 1901 show an average annual air temperature of -4.58°C and average annual precipitation of 323.37 mm (Environment Canada, 2022). Dawson and the Sunnydale landslide are located within the zone of extensive discontinuous permafrost (Heginbottom et *al*., 1995). While a detailed regional model suggests a 0.7 to 0.8 probability of permafrost on the slope (Bonnaventure et *al*., 2012), no evidence of permafrost was observed during field investigations or desktop analysis.

The Dawson region experiences only minor seismic activity. Small, infrequent, local earthquakes under magnitude four have been observed in the Dawson area over the last century. Larger events occur more regularly to the north and south of the region but at distances from the Sunnydale landslide that make them unlikely to act as a landslide trigger (cf., Keefer, 1984).

Geomorphological mapping and geologic history

A combination of airborne lidar, aerial photos and field mapping was used to identify and characterize geomorphic features and variations in surficial and bedrock geology (Figs. 2 and 3). The landslide consists of two main geomorphic areas. The lower half of the slide (roughly 50 000 m^2) is a steep, sparsely vegetated face consisting of bedrock, boulder fields, and mixed loess and bedrock colluvium. The upper half (roughly 50 000 m^2) is characterized by gentler slopes, spruce forests and a covering of loess and mixed loess and weathered bedrock colluvium. The headscarp is approximately 6 m in height and 150 m long, and displays three distinct degrees of weathering and vegetation cover that increase with height (Fig. 4). Competent bedrock is best exposed at the southern margin of the slide at TCMS station 3 (Fig. 2). The headscarp here has a strike and dip of 300/75 and slickenlines covering the bottom ~1 m at a plunge and trend of 67/070 (Fig. 4). The bedrock forming the headscarp becomes increasingly, but non-linearly, weathered and vegetated first with lichen and then moss and grasses towards the top. These differences may indicate episodic movement on a timescale of thousands to tens of thousands of years. Rock samples taken from the headscarp are being analyzed for cosmogenic-nuclide measurement to determine the timing of surface exposure and to further elucidate a chronology of prehistoric movement.

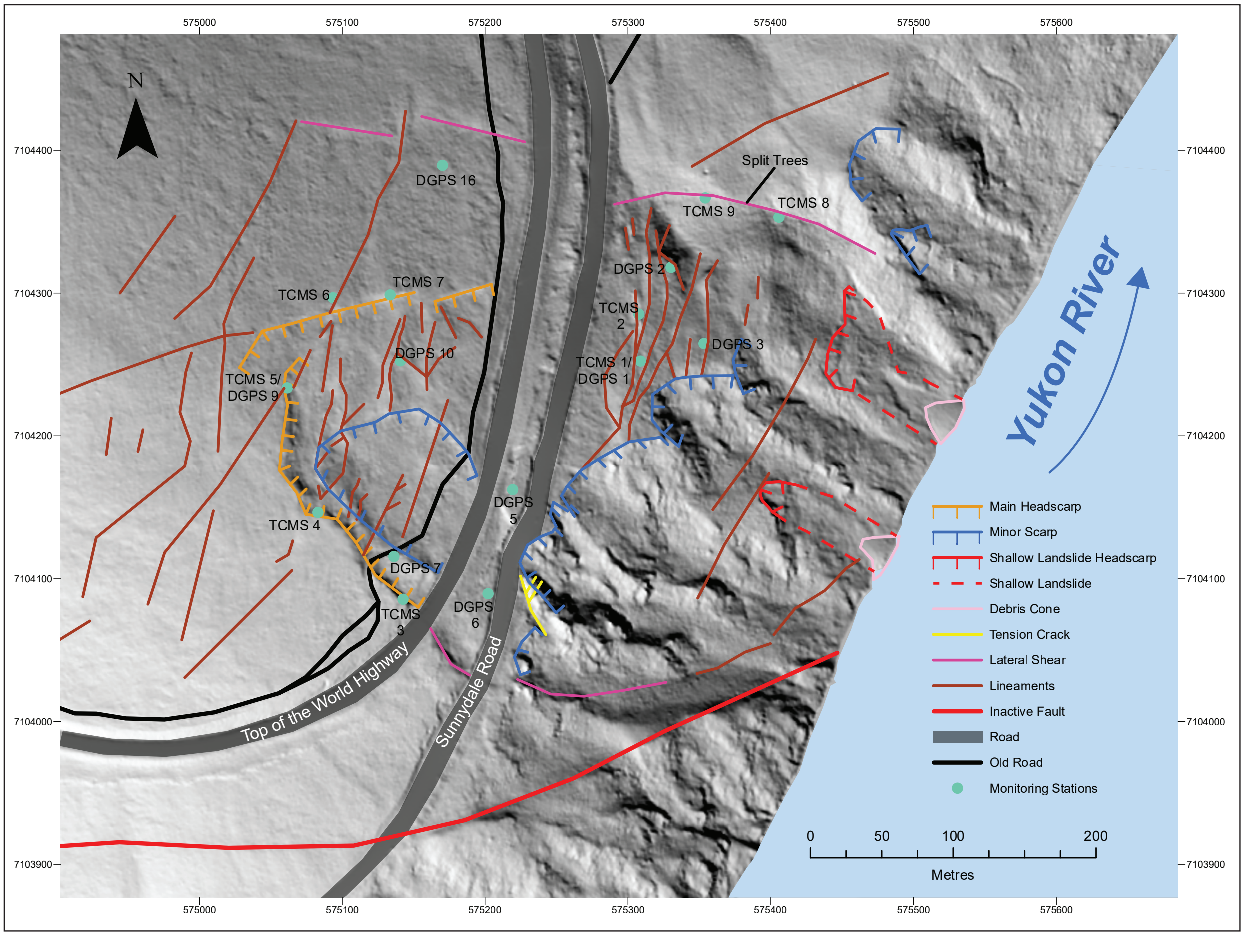

Figure 2. *Geomorphological map of the Sunnydale slide including locations of DGPS and TCMS physical monitoring stations.*

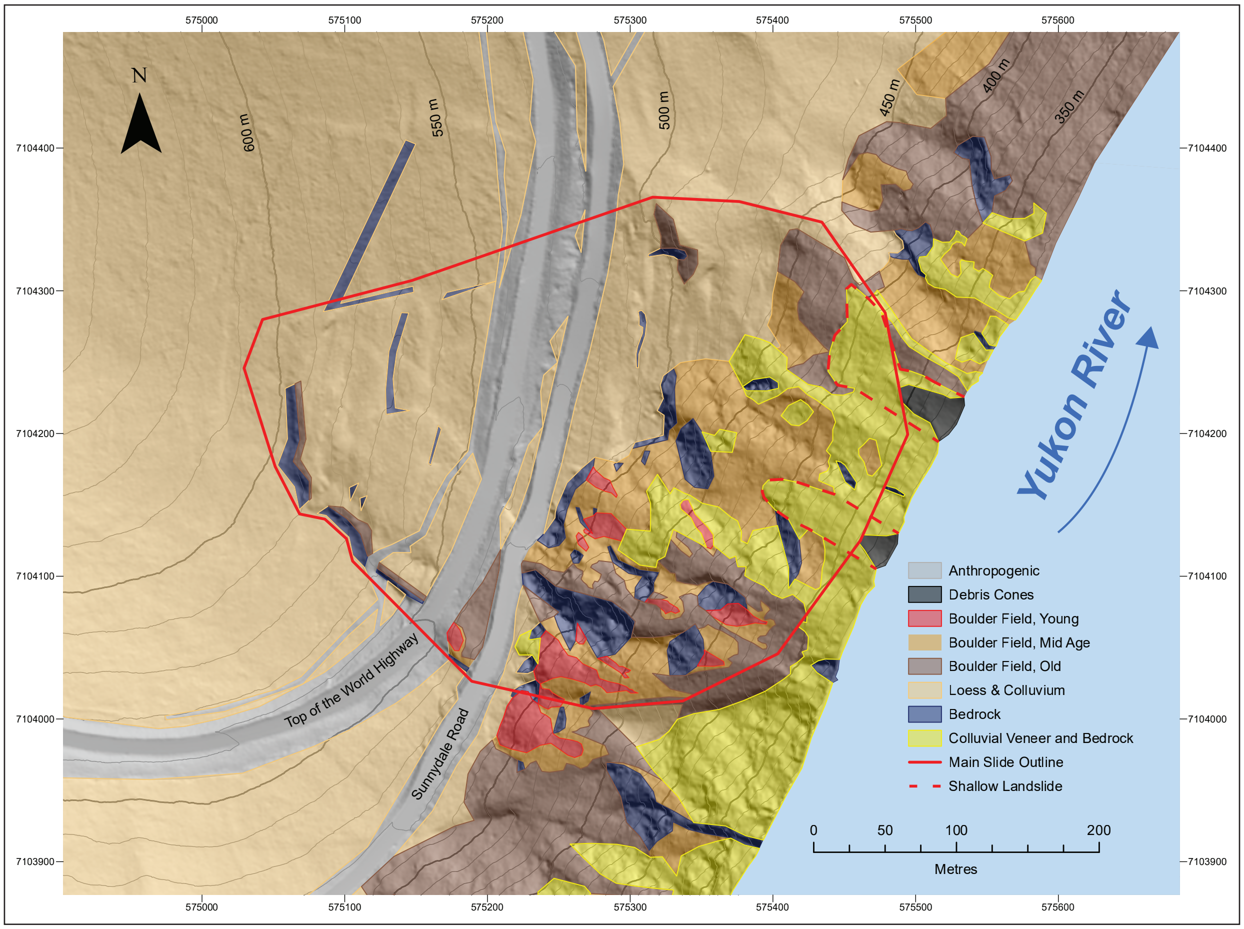

Figure 3. *Surficial geology map of the Sunnydale slide.*

Figure 4. (a) *The headscarp of the slide near TCMS station 3. Note the distinct change in vegetation at approximately waist height.* ***(b)*** *Slickenlines on the headscarp.*

Many of the lineaments mapped on the upper half of the slide consist of sediment-filled grabens or tension cracks. Several of these features were investigated using soil trenches to document the stratigraphy of the sediments that have filled them (Fig. 5). Tephra from the northern lobe of the White River ash volcanic event found within these features date them to approximately 1625 years old (Reuther et *al.*, 2020) providing a current minimum age of displacement; however this minimum age is expected to be a significant underestimate. Results from additional ongoing dating work will further constrain minimum age of opening of these features.

Two shallow landslides are present at the toe of the main slide; each is 1–3 m deep and has an approximate volume of 1000–3000 m^3. The northern landslide

***Figure 5. (a)** Tension crack near TCMS station 2. Recent movement is shown by the gap between the rock and moss growth. **(b)** TCMS station 6. **(c)** Split tree near TCMS 8 with nail monitoring installed. This crack opened 2.2 cm and 3.3 cm between June and September 2022 at the upper and lower nail sets respectively. **(d)** Terrestrial lidar scanner with the Sunnydale slide in the background across the Yukon river, note the shallow landslide directly left of the scanner.*

initially failed in 2018, while the southern slide occurred in 2019. While both slides continue to grow, the northern slide has experienced significant enlargement as recently as September 2022. These slides are likely related to over-steepening at the toe of the larger Sunnydale rock mass as it pushes out towards the river (Fig. 6).

Extensive bedrock exposure across many areas of the slide allowed for analysis through use of joint and fabric mapping as well as Geological Strength Index (GSI) characterization. Prior work used these techniques for preliminary slope stability analysis and the new data will be added to enhance any future modeling work (BGC, 2021a). GSI results span a wide range of values from 5–75 with a mean of 43. These results indicate blocky, disturbed and disintegrated rock across the slide area (Hoek and Brown, 1997).

Current measurable motion is constrained to an area of approximately 100 000 m^2 but evidence of past deformation exists across much of the adjacent hillslope, encompassing an area of approximately 180 000 m^2. While the depth of the failure plane is uncertain, lidar differencing and geomorphic evidence have allowed for an approximate delineation of a daylighting surface on the face of the slide (Fig. 6).

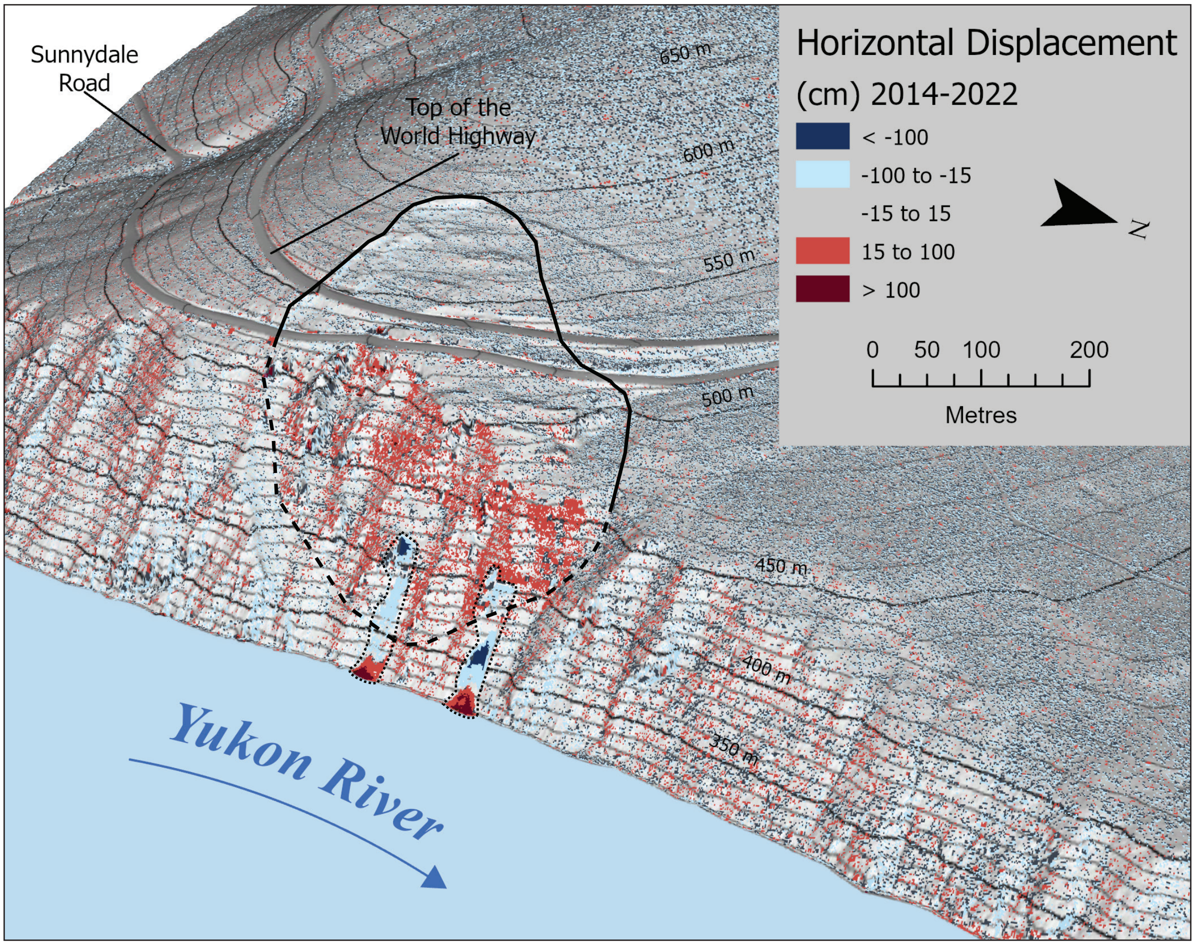

Figure 6. *Horizontal lidar differencing between 2014 and 2022 aerial lidar data. Dashed line indicates the inferred failure plane where it daylights on the steep river cut slope. Solid line shows the approximate upper extent of the slide. Two small shallow landslides are visible and indicated by dotted lines.*

Physical displacement monitoring

Three types of physical monitoring stations are currently in use on the landslide; GPS pin stations (DGPS; Table 1), tension crack monitoring stations (TCMS; Table 2), and nails in split trees (NT; Fig. 5; Table 2). The DGPS consist of a single rebar pin, these stations were installed on July 2 and 3, 2021 by Jeffrey Bond and Peter von Gaza. The TCMS consist of two rebar pins spanning a tension crack or scarp feature to assess rates of opening. TCMS 1 to 5 were established by Jeffrey Bond and Peter von Gaza coincidentally with the DGPS stations while TCMS 6 to 9 were established by Jackson Bodtker and Holly Basiuk on June 24 and 30, 2022. The NT stations consist of trees that have been split due to differential ground motion below them (Fig. 5), and were installed by Jackson Bodtker and Holly Basiuk on June 30, 2022.

Results from comparing repeat DGPS measurements show significant and potentially accelerating movement of 6 to 11 cm/year across the slide since installation (Figs. 7, 8 and 9; Table 1). TCMS measurements also indicate motion on the slide (Fig. 10).

Table 1. *Differential GPS station locations and change analysis.*

Station	Number	UTM Position (m)								
		2–3 July 2021			22 June 2022			7 October 2022		
		Easting	Northing	Height	Easting	Northing	Height	Easting	Northing	Height
DGPS	1	575308.319	7104267.632	510.257	575308.441	7104267.603	510.194	575308.485	7104267.612	510.181
	2	575330.931	7104315.234	499.335	575331.117	7104315.225	499.267	575331.164	7104315.224	499.215
	3	575355.352	7104283.389	485.159	575355.498	7104283.386	485.102	575355.536	7104283.376	485.05
	4	575283.442	7104361.339	514.886	Destroyed					
	5	575222.011	7104164.164	539.44	575222.102	7104164.145	539.404	575222.115	7104164.141	539.389
	6	575199.443	7104077.596	532.936	575199.524	7104077.601	532.868	575199.545	7104077.588	532.839
	7	575139.777	7104111.815	562.111	575139.835	7104111.805	562.053	575139.865	7104111.795	562.047
	9	575064.509	7104235.78	594.638	575064.558	7104235.774	594.641	No Measurement		
	10	575145.015	7104250.971	567.998	575145.094	7104250.971	567.929	575145.126	7104250.964	567.895
	16	Measurement Error			575162.638	7104385.318	555.95	575162.639	7104385.313	555.932

Station	Number	Change (cm)								
		July 2021 – June 2022			June 2022 – Oct. 2022			July 2021 – Oct. 2022		
		Easting	Northing	Height	Easting	Northing	Height	Easting	Northing	Height
DGPS	1	-12.2	2.9	-6.3	-4.4	-0.9	-1.3	-16.6	2.0	-7.6
	2	-18.6	0.9	-6.8	-4.7	0.1	-5.2	-23.3	1.0	-12.0
	3	-14.6	0.3	-5.7	-3.8	1.0	-5.2	-18.4	1.3	-10.9
	4	Destroyed								
	5	-9.1	1.9	-3.6	-1.3	0.4	-1.5	-10.4	2.3	-5.1
	6	-8.1	-0.5	-6.8	-2.1	1.3	-2.9	-10.2	0.8	-9.7
	7	-5.8	1.0	-5.8	-3.0	1.0	-0.6	-8.8	2.0	-6.4
	9	-4.9	0.6	+0.3	N/A			N/A		
	10	-7.9	0.0	-6.9	-3.2	0.7	-3.4	-11.1	0.7	-10.3
	16	N/A			-0.1	0.5	-1.8	N/A		

Table 2. *Tension crack and split tree monitoring station locations and change analysis.*

Station Type	Number	Measurements (cm)				Change (cm)		Error (cm)	Latitude	Longitude
		2–3 July 2021	23 May 2022	23–30 June 2022	22 Sept. 2022	July 2021 – Sept. 2022	June – Sept. 2022			
TCMS	1	660.5	661.0	661.3	661.0	0.5	-0.3	1.0	64.05691	-139.45706
	2	788.7	790.0	790.0	789.8	+1.0	-0.2		64.05714	-139.45718
	3 U	92.6	94.4	94.5	94.8	+2.2	+0.3		64.05531	-139.46050
	3 L	56.0	57.0	57.3	57.6	+1.6	+0.3			
	4	695.9	N/A	699.0	698.5	+2.6	-0.5		64.05583	-139.46160
	5	405.0		409.0	409.5	+4.5	+0.5		64.05667	-139.46220
	6	N/A		721.5	720.7	N/A	-0.8		64.05716	-139.46148
	7			713.0	713.3		+0.3		64.05725	-139.46049
	8			790.7	797.2		+6.5		64.05766	-139.45545
	9			708.5	709.5		+1.0		64.05782	-139.45608
Split Trees	1 Upper	N/A	N/A	13.2	12.8	N/A	-0.4	0.2	64.05782	-139.45662
	1 Lower			23.4	22.8		-0.6			
	1.5			7.2	7.0		-0.2			
	2 Upper			11.9	12.4		+0.5		64.05785	-139.45631
	2 Lower			23.5	24.3		+0.8			
	3 Upper			14.6	14.7		+0.1		64.05774	-139.45577
	3 Middle			33.2	33.4		+0.2			
	3 Lower			41.9	42.4		+0.5			
	4 Upper			23.5	25.7		+2.2		64.05766	-139.45545
	4 Lower			43.7	47.0		+3.3			

Displacements across TCMS 1 and 2 of less than 1 cm/year compared to 16.6 to 23.3 cm of eastward change seen at adjacent DPGS 1, 2 and 3 indicate that these tension cracks are not currently opening, and this area of the slide is likely moving as a larger semi-coherent block. TCMS 3, 4 and 5 are located along the margins of the slide and show 1 to 3 cm/year movement relative to areas with less or no current motion. TCMS 6 to 9 only have measurements across ~3 months from June to September 2022, yet TCMS 8 shows an alarming 6.5 cm of motion on the northern margin of the slide during this time. We assume up to 1 cm of error in these measurements due to approximately 0.5 cm of flex at each rebar pin.

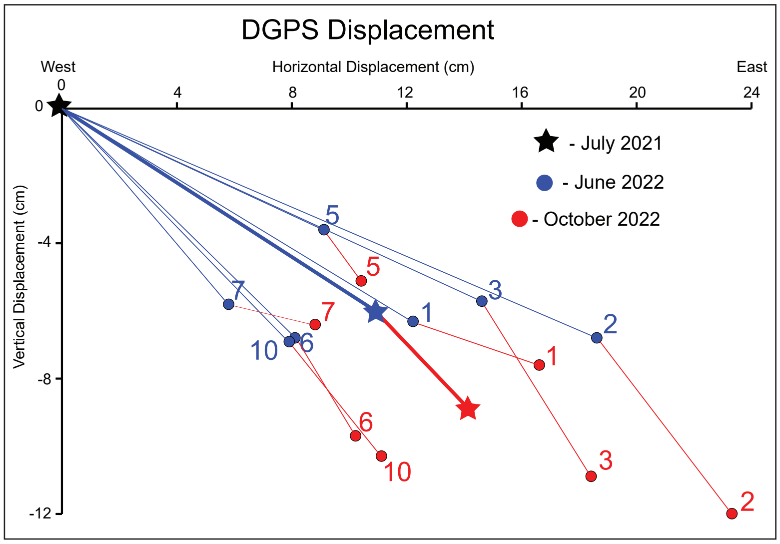

Figure 7. *Vertical and horizontal displacement observed at DGPS stations. Positions from the original July 2021 measurements have been normalized to the origin. Stars indicate average values given time intervals.*

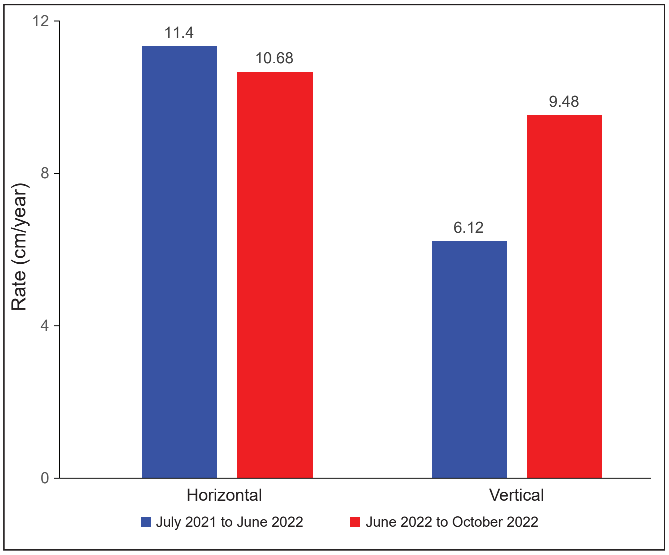

Figure 8. *Average rate of change in the vertical and horizontal directions observed at DGPS stations from July 2021 to June 2022 and June 2022 to October 2022.*

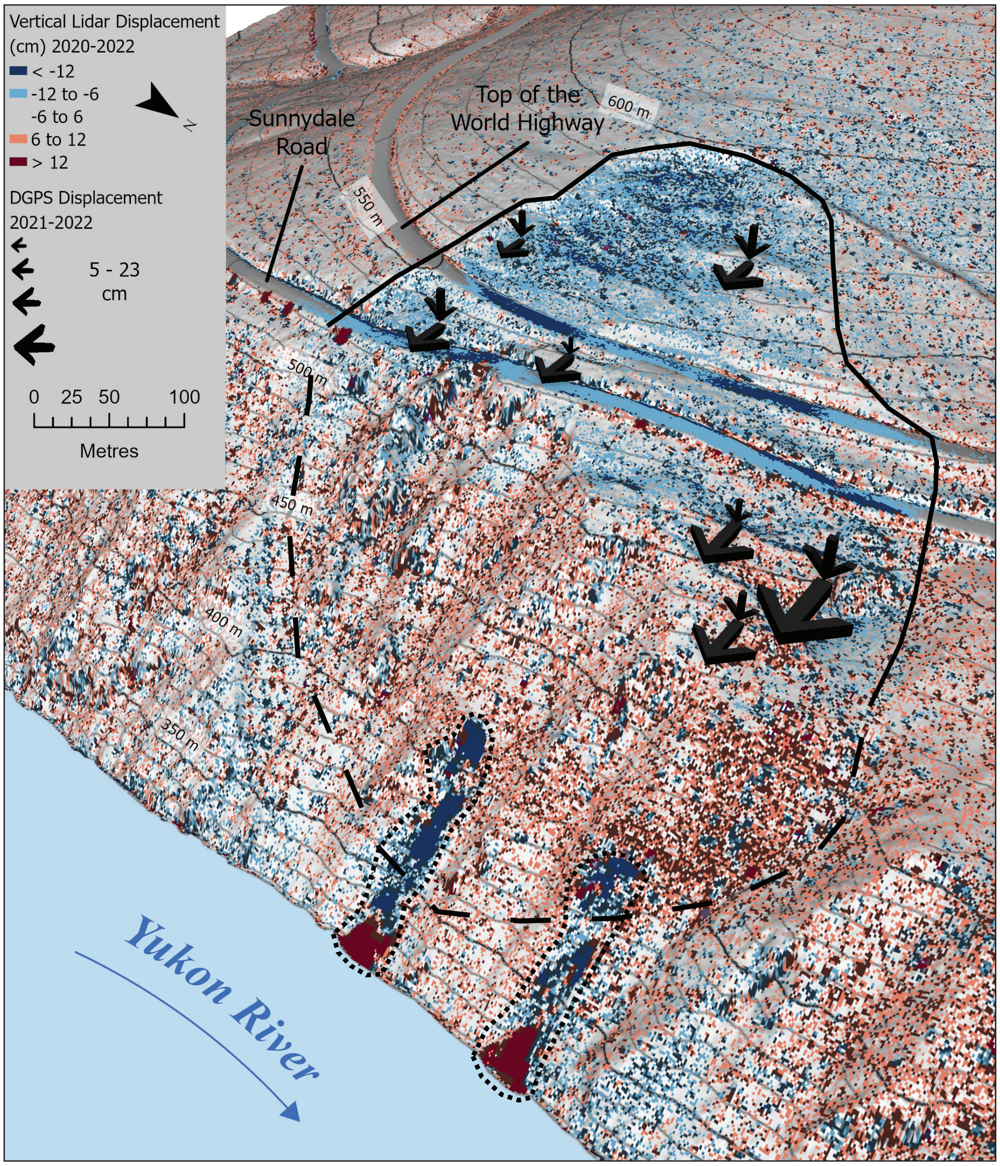

Figure 9. *Vertical lidar displacement from 2020 to 2022 overlain by arrows showing measured vertical and horizontal displacement at DGPS stations from 2021 to 2022 (see Fig. 7).*

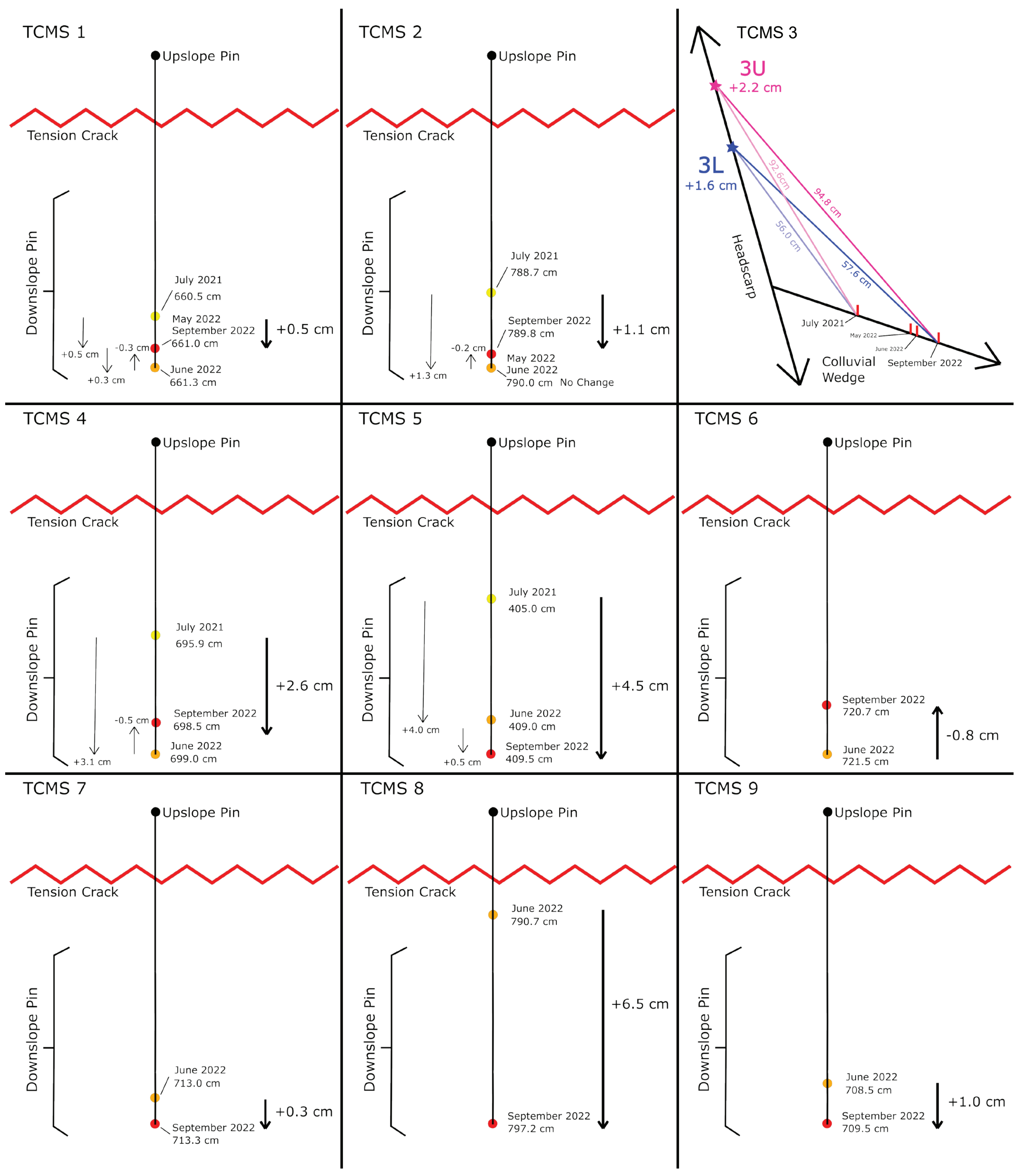

Figure 10. *Periodic measurement of displacement across tension cracks and scarps. See figure 2 for station locations.*

Lidar change analysis

Aerial lidar data from 2014, 2018, 2019, 2020 and 2022 were analyzed to characterize changes to the ground surface (Table 3). Point clouds were registered and analyzed using cloud to cloud distance differencing in CloudCompare (CloudCompare, 2022). Differencing was completed for 2014 to 2018, 2018 to 2019, 2019 to 2020, 2020 to 2022, 2014 to 2022, and 2018 to 2022. Deviations in positions of points between years were split into x, y and z components with the z-axis oriented vertically and the x-axis oriented at 110°, perpendicular to the Yukon River, and approximately parallel to the direction of horizontal ground motion observed from DGPS data. Rasters with a one-metre cell size were created from the final differenced point clouds (Figs. 6, 9 and 11)) and the surface of the Top of the World Highway was subsampled down to 500 randomly distributed points to compare change along the z-axis. The road surface was chosen due to the lack of noise associated with lidar pulse returns on vegetated surfaces and the relatively flat surface minimizing vertical error arising from small differences in nearest-point locations between collection years. Results from these data show continuing vertical drop (3–5 cm/year) throughout the period of available data (Fig. 12). Ongoing work will further analyze airborne lidar data and incorporate repeat terrestrial lidar scans completed during June and September of 2022.

Conclusions

Current rates of motion on the Sunnydale slide paired with its volume and location adjacent to the community of Dawson make this one of the highest priority geohazards in the Yukon. Work in progress to further understand this landslide includes implementation of a near-real-time GNSS monitoring system on the slide,

Table 3. *Lidar metadata and subsample change analysis.*

Station	Range	Change (cm)					Mean Rate (cm/year)
		Minimum	Maximum	Mean	Median	Standard Deviation	
Lidar Subsample	2014–2018	-32	13	-15	-15	4	3.64
	2018–2019	-8	12	-3	-3	2	2.96
	2019–2020	-12	10	-3	-3	3	3.34
	2020–2022	-16	13	-9	-9	3	4.93
Lidar Data	**Date**	**Vertical Accuracy (m)**	**Point Density (ppm)**	**Source**	**Horizontal Datum**	**Vertical Datum**	**Projection**
	Sept. 8 and 15, **2014**	0.119	7.5	Government of Yukon Lidar Repository (Contractor: McElhanney)	NAD83(CSRS)	CGVD28	UTM Zone 7N
	Sept. 19, 21 and 29, **2018**	0.14	10.7				
	June 7, 11 and 13, **2019**	0.02	18.4				
	Aug. 19, **2020**	0.05	18.1				
	June 17, **2022**	0.021	11.7				

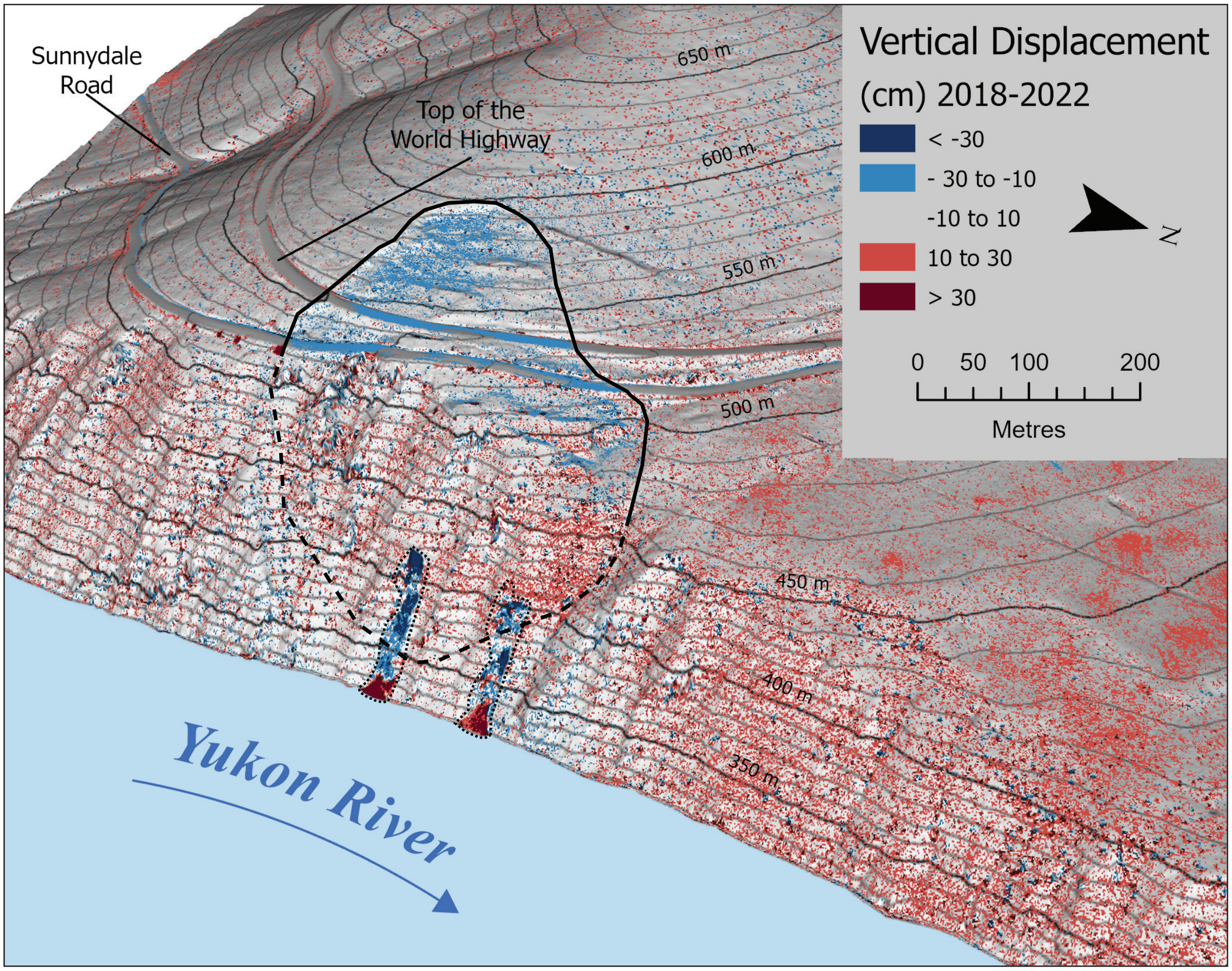

Figure 11. *Vertical displacement from aerial lidar differencing from 2018 to 2022. Anomalous areas of elevation gain north of the slide area are likely due to discrepancies in last return picking across different years.*

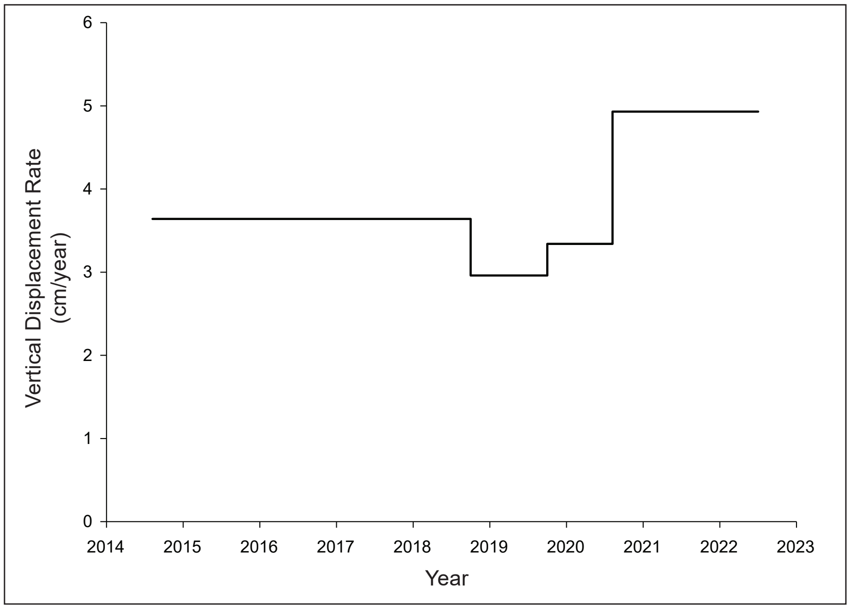

Figure 12. *Vertical displacement along the Top of the World highway from aerial lidar data. Values are the mean of 500 randomly-distributed points along the roadway within the boundaries of the main slide.*

repeat lidar surveys and a variety of dating analyses to further our understanding of the timing and rate of prehistoric movement. Additional complimentary work is being undertaken by several consultants to further constraint the current rates of movement and model theoretical rapid failure scenarios. This ongoing work will help us evaluate the risk posed to the community by the Sunnydale slide and set a standard for landslide assessment monitoring in the territory.

Acknowledgements

The authors would like to thank field assistant Holly Basiuk, as well as Dawson locals Peter Nagano and Greg Hakonson for sharing their knowledge of the slide. Funding from the Yukon Geological Survey, the Northern Scientific Training Program, the Geological Society of America and the Natural Sciences and Engineering Research Council of Canada (grant #DG-2020-04207) was invaluable to completion of this work. Dr. Gioachino Roberti is sincerely thanked for his helpful review. Finally, we would like to thank the Tr'ondëk Hwëch'in First Nation for granting us access to their lands and traditional territory.

References

BGC, 2020a. Initial Site Visit at Sunnydale Slide. Unpublished Report, 39 p.

BGC, 2020b. Initial Site Visit at the Moosehide Landslide. Unpublished Report, 23 p.

BGC, 2021a. Sunnydale Slide Deformation Mechanism and Preliminary Failure Probability. Unpublished Report, 23 p.

BGC, 2021b. Moosehide Landslide Hazard Characterization. Unpublished Report, 32 p.

BGC, 2021c. Moosehide Landslide – Dawson City, Yk, Quantitative Risk Assessment. Unpublished Report, 58 p.

Bonnaventure, P.P., Lewkowicz, A.G., Kremer, M. and Sawada, M., 2012. A regional permafrost probability model for the southern Yukon and northern British Columbia, Canada. Permafrost and Periglacial Processes, vol. 23, p. 52–68, https://doi.org/10.1002/ppp.1733.

Brideau, M.-A., Stead, D., Roots, C. and Lipovsky, P.S., 2012. Ongoing displacement monitoring at the Dawson City landslide (Dawson map area NTS 116B/3). In: Yukon Exploration and Geology 2011, K.E. MacFarlane and P.J. Sack, (eds.), Yukon Geological Survey, p. 17–26.

Brideau, M.-A., Stead, D., Stevens, V., Roots, C., Lipovsky, P. and Von Gaza, P., 2007. The Dawson City landslide (Dawson map area, NTS 116B/3), central Yukon. *In:* Yukon Exploration and Geology 2006, D.S. Emond, L.L. Lewis and L.H. Weston (eds.), Yukon Geological Survey, p. 123–137.

Chigira, M., Tsou, C.-Y., Matsushi, Y., Hiraishi, N. and Matsuzawa, M., 2013. Topographic precursors and geological structures of deep-seated catastrophic landslides caused by Typhoon Talas. Geomorphology, vol. 201, p. 479–493, https://doi.org/10.1016/j.geomorph.2013.07.020.

CloudCompare (version 2.12.4), 2022. GPL software. Retrieved from http://www.cloudcompare.org/.

Duk-Rodkin, A., 1996. Surficial geology, Dawson, Yukon Territory. Geological Survey of Canada, Open File 3288, scale 1:250 000, https://doi.org/10.4095/207910.

Environment Canada, 2022. National Climate Data and Information Archive, https://climate.weather.gc.ca/historical_data/search_historic_data_e.html, [accessed November 7, 2022].

Esri, 2022. World Imagery, https://www.arcgis.com/home/item.html?id=10df2279f9684e4a9f6a7f08febac2a9, [accessed December 6, 2022].

Fraser, T.A. and Burn, C.R., 1997. On the nature and origin of “muck” deposits in the Klondike area, Yukon Territory. Canadian Journal of Earth Sciences, vol. 34. p. 1333–1344, https://doi.org/10.1139/e17-106.

Froese, D.G., Barendregt, R.W., Enkin, R.J. and Baker, J., 2000. Paleomagnetic evidence for multiple Late Pliocene - Early Pleistocene glaciations in the Klondike area, Yukon Territory. Canadian Journal of Earth Sciences, vol. 37, p. 863–877.

Heginbottom, J.A., Dubreuil, M.A. and Harker, P.A., 1995. Canada – Permafrost. In: The National Atlas of Canada, 5th edition, Natural Resources Canada, MCR Series no. 4177, Plate 2.1: MCR4177.

Hidy, A.J., Gosse, J.C., Sanborn, P. and Froese, D.G., 2012. Age-erosion constraints on an Early Pleistocene paleosol in Yukon, Canada, with profiles of 10Be and 26Al: Evidence for a significant loess cover effect on cosmogenic nuclide production rates, Quaternary Science Reviews, vol. 165, p. 260–271.

Hilger, P., Hermanns, R.L., Czekirda, J., Myhra, K.S., Gosse, J.C. and Etzelmüller, B., 2021. Permafrost as a first order control on long-term rock-slope deformation in (Sub-)Arctic Norway. Quaternary Science Reviews, vol. 251, https://doi.org/10.1016/j.quascirev.2020.106718.

Hoek, E. and Brown, E.T., 1997. Practical estimates of rock mass strength. International Journal of Rock Mechanics and Mining Sciences, vol. 34, p. 1165–1186, https://doi.org/10.1016/S1365-1609(97)80069-X.

Hungr, O., Leroueil, S. and Picarelli, L., 2014. The Varnes Classification of Landslide Types, an Update. Landslides, vol. 11, p. 167–194.

Keefer, D.K., 1984. Landslides caused by earthquakes. Geological Society of America Bulletin, vol. 95, p. 406–421.

McKenna, K.M. and Lipovsky, P.S., 2014. Surficial geology, Dawson region, Yukon, parts of NTS 115O/14 & 15 and 116B/1, 2, 3, & 4. Yukon Geological Survey, Open File 2014-12, 1:25 000 scale.

Mortensen, J.K., 1988. Geology, southwestern Dawson map area, Yukon. Geological Survey of Canada, Open File 1927, 1:250 000 scale, https://doi.org/10.4095/130455.

Pánek, T. and Klimeš, J., 2016. Temporal behavior of deep-seated gravitational slope deformations: A review. Earth Science Reviews, vol. 156, p. 14–38, https://doi.org/10.1016/j.earscirev.2016.02.007.

Reuther, J., Potter, B., Coffman, S., Smith, H. and Bigelow, N., 2020. Revisiting the timing of the northern lobe of the White River Ash volcanic event in eastern Alaska and western Yukon. Radiocarbon, vol. 62, p. 169–188.

Tempelman-Kluit, D.J., 1980. Evolution of physiography and drainage in southern Yukon. Canadian Journal of Earth Sciences, vol. 17, p. 1189–1203, https://doi.org/10.1139/e80-125.

Fracture network analysis in the Duke River area, southwestern Yukon

F.M. Chapman*, M. Miranda, R. Soucy La Roche and J. Raymond
Institut national de la recherche scientifique (Centre Eau Terre Environment, Québec, QC)

Chapman, F.M., Miranda, M., Soucy La Roche, R. and Raymond, J., 2023. Fracture network analysis in the Duke River area, southwestern Yukon. *In:* Yukon Exploration and Geology 2022, K.E. MacFarlane (ed.), Yukon Geological Survey, p. 35–62.

Abstract

Deep geothermal reservoir potential depends on the local temperature gradient and host rock permeability. In areas with low primary porosity, such as the Duke River area, large-scale permeability is primarily associated with fracture networks. Fractures in the Duke River area are described based on 36 scanlines collected across 9 rock types from 0.8 to 22 km from the Denali fault. The majority of fractures are steeply dipping but have no preferential strike. The linear fracture intensity is high, and most fractures range from open to moderately wide. These attributes vary slightly by lithology but can be grouped into distinct hydrostratigraphic units. The distance from the Denali fault has a non-linear influence on fracture intensity and aperture and a negligible effect on fracture spacing and length. The fracture analysis presented will be used to develop a discrete fracture network to evaluate permeability in the Duke River area.

* fiona.chapman@inrs.ca

Introduction

This research is part of an on-going project to evaluate the deep geothermal potential in the Duke River area, southwestern Yukon. The Duke River area was selected as a study site due to a promising temperature gradient measured in a shallow well, elevated Curie point depth and potential for elevated permeability due to extensive fracturing of the bedrock associated with the Denali fault (*e.g.*, Witter, 2020). Extensional fractures can be important conduits for geothermal fluids in hard rock areas where the primary porosity is low, such as in the Duke River area (Singhal and Gupta, 2010).

Fractures is an all-encompassing term to denote a planar surface, with at some scale, an opening (Fossen, 2010). Fractures occur as a result of external (*e.g.*, tectonic) or internal (*e.g.*, thermal) stress (Fossen, 2010). They include shear fractures (or faults) and extensional fractures (joints, fissures, veins and dikes; Fossen, 2010). The strike of fractures and their apertures will depend on the principal stresses. Here, we are interested in the impact of fractures on subsurface permeability. Fracture-derived permeability depends on geometric fracture attributes, such as fracture density, spacing, length, aperture and connectivity (Singhal and Gupta, 2010). Therefore, it is essential to describe regional fracture networks prior to estimating permeability and defining reservoir potential. The permeability is an important hydrogeological characteristic which contributes to potential reservoir productivity, be it for drinking water or open-loop geothermal systems (Singhal and Gupta, 2010).

In southwestern Yukon, the shallow (385 m) temperature gradient in Quaternary sediments that overlay the Denali fault is characteristic of conductive heat transfer (F. Chapman, unpublished data). However, elevated topography such as around the Denali fault provides an ideal geological context for forced convection to occur (*e.g.*, Morgan et al., 1981; Štulc, 1998; Saar, 2010; Townend et *al*., 2017). The differences in surface pressures and hydraulic head on either side of the Denali fault is expected to force meteoric water into deep circulation where it can be heated before rising toward Kluane Lake at lower elevation. The spatial distribution of permeability in the Duke River area influences regional groundwater flow and convection potential.

Fractures in the Duke River area are thought to be associated, at least in part, with stresses that caused the Denali fault. The objective of this research is to evaluate the influence of lithology and fault proximity on regional scale fracture networks around the Denali fault to better understand the spatial distribution of permeability. We are interested in large scale permeability to understand the potential for convective heat transfer that can affect the extent of geothermal resources. We therefore evaluated fracture networks on a regional scale (*e.g.*, Camanni et *al*., 2021): up to 24 km from the Denali fault and across nine different rock types. We hypothesize that geometric fracture attributes (linear fracture intensity, fracture length and fracture aperture) will decrease with distance from the fault. The results of this regional scale analysis will inform future research wherein the spatial distribution of permeability will be integrated into a coupled heat-flow model to quantify geothermal potential based on conductive and advective heat transfer.

Geological setting

Canadian Cordillera

The Canadian Cordillera is an orogenic belt composed of a collage of allochthonous terranes (Colpron et *al*., 2007) that were accreted to autochthonous and parautochthonous units of the western margin of Laurentia. The terranes that make up the Canadian Cordillera are primarily sedimentary basins and platforms, magmatic arcs, and microcontinents, which can be grouped into four categories: Intermontane terranes, Insular and Northern Alaska terranes, Oceanic and accretionary complex terranes, and Mesozoic and younger arc and accretionary terranes (Fig. 1; Colpron et *al*., 2007; Nelson and Colpron, 2007). Accretion of the Canadian Cordillera was ongoing during the Late Triassic to earliest Jurassic (Colpron et *al*., 2015, 2022; George et *al*., 2021), and possibly started as early as late Permian (Beranek and Mortensen, 2011) and continues today with the Yakutat microplate collision along the southern Alaskan coast (Elliott et *al*., 2010).

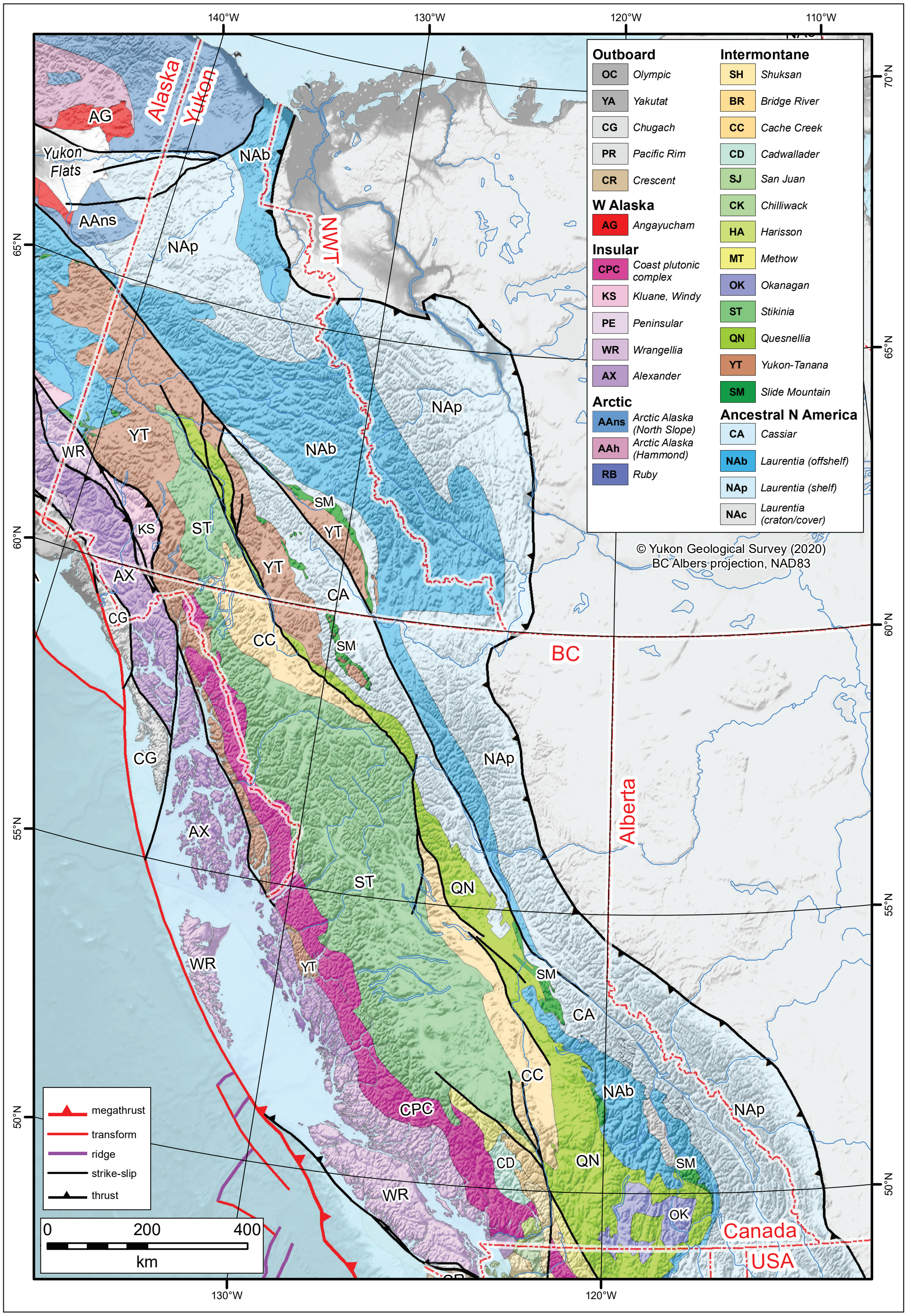

Figure 1. *Distribution of terranes of the Canadian Cordillera (Yukon Geological Survey, 2020).*

Denali fault

The Denali fault is a major right-lateral strike-slip fault in the Canadian Cordillera which extends over 2000 km across central Alaska, through southwestern Yukon, and into northern British Columbia (Fig. 1; Nelson and Colpron, 2007; Choi et *al*., 2021). In southwestern Yukon, the eastern Denali fault separates the Alexander and Wrangellia terranes on the southwest from metamorphic rocks of the Kluane schist and the Yukon-Tanana terrane on the northeast (Fig. 1). Since the Early Cretaceous, the Denali fault has accommodated a dextral displacement of ~400–480 km (Lowey, 1998; Waldien et *al*., 2021). Today, the eastern Denali fault experiences less activity than the Alaska portion of the Denali fault (Bender and Haeussler, 2017; Blais-Stevens et *al*., 2020). This is reflected in the present-day average slip rate of ~5 to 12 mm per year along the east-west striking Alaskan portion of the Denali fault, compared to ~2 to 5 mm per year along the southeast–northwest striking eastern Denali fault which passes through Yukon and British Columbia (Leonard et *al*., 2008; Haeussler et *al*., 2017; Blais-Stevens et *al*., 2020). Though strike-slip displacement along the eastern Denali fault is dominant, vertical displacement of 0.2 to 0.9 mm per year has been reported (Marechal et *al*., 2018; McDermott et *al*., 2019).

Study site

Increased permeability due to brittle fracturing is expected along the Denali fault relative to other areas in Yukon due to the recent activity, including seismic shaking in the past 6000 years (Blais-Stevens et *al*., 2020). A transtensional pull-apart was identified along the Denali fault near the community of Burwash Landing in southwestern Yukon where the main fault is mapped as three fault strands, though only a single strand has had a visible effect on the overlying sediments (Witter, 2020; Finley et *al*., 2022; Tschirhart et *al*., 2022). This releasing bend is expected to generate an area of increased local permeability. Faulds and Hinz (2015) associated transtensional pull-aparts along strike-slip faults with increased local permeability, such as in the Great Basin Region, USA, where this tectonic setting houses 3% of mapped geothermal fields.

The Duke River area, southwest of the Denali fault between Duke River and Congdon Creek, was previously mapped by Israel et *al.* (2006; Fig. 2). The area is underlain by rocks of Wrangellia and the Alexander terrane to the south. The Ruby Range batholith and Kluane schist occur northeast of the Denali fault. Late Paleozoic to mid-Cretaceous plutons are distributed throughout the Wrangellia and Alexander terranes (Colpron et *al*., 2016).

The study area is bound to the southwest by flow divides and to the northeast by the Kluane Lake (Fig. 2), which form no flow or constant hydraulic head boundaries that will facilitate the integration of fracture analysis results into a hydrothermal model to quantify geothermal resources. Figure 3 is a conceptual model which will be the basis for a quantitative groundwater flow model in future research. Fracture measurements were taken along several transects to ensure that fracture measurements for all pertinent rock types were collected on representative outcrops.

Lithological units

All the lithological units defined by Israel et *al.* (2006) in Wrangellia (WR), overlap assemblages (OA), intrusive rocks (IR) and Alexander terrane (AX), as well as the Kluane schist crop out in the study area (Figs. 2 and 4). Descriptions of lithological units are based on Israel et *al.* (2006) and were complemented by our field observations. The dominant units exposed on the south side of the fault are the Station Creek and Hasen Creek formations of the Skolai Group, and the Nikolai formation (all units of WR). The Station Creek Formation is a Pennsylvanian to Permian volcanic unit including breccia, crystallithic tuffs, tuffaceous siltstone, and augite-phyric basalt flows. The thickness is poorly constrained but is at least several hundred metres. The lower Permian Hasen Creek Formation overlies the Station Creek Formation and is dominated by fossiliferous siltstone, turbidites and mudstones in the Duke River area. The Upper Triassic Nikolai formation consists of basalt flows around 1000 m thick in the Kluane Ranges.

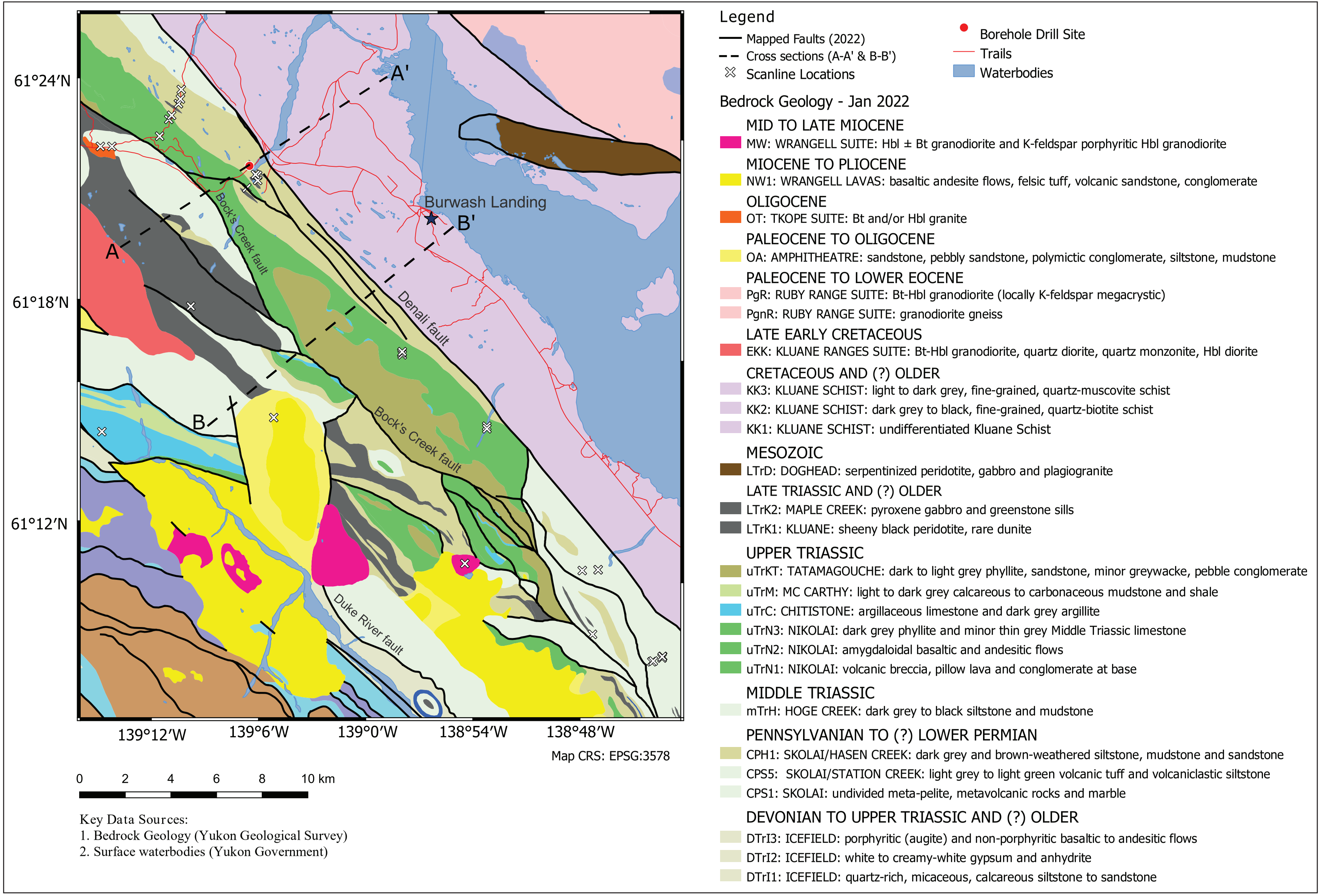

Figure 2. *Geological map of the Duke River and surrounding area (Yukon Geological Survey, 2022).*

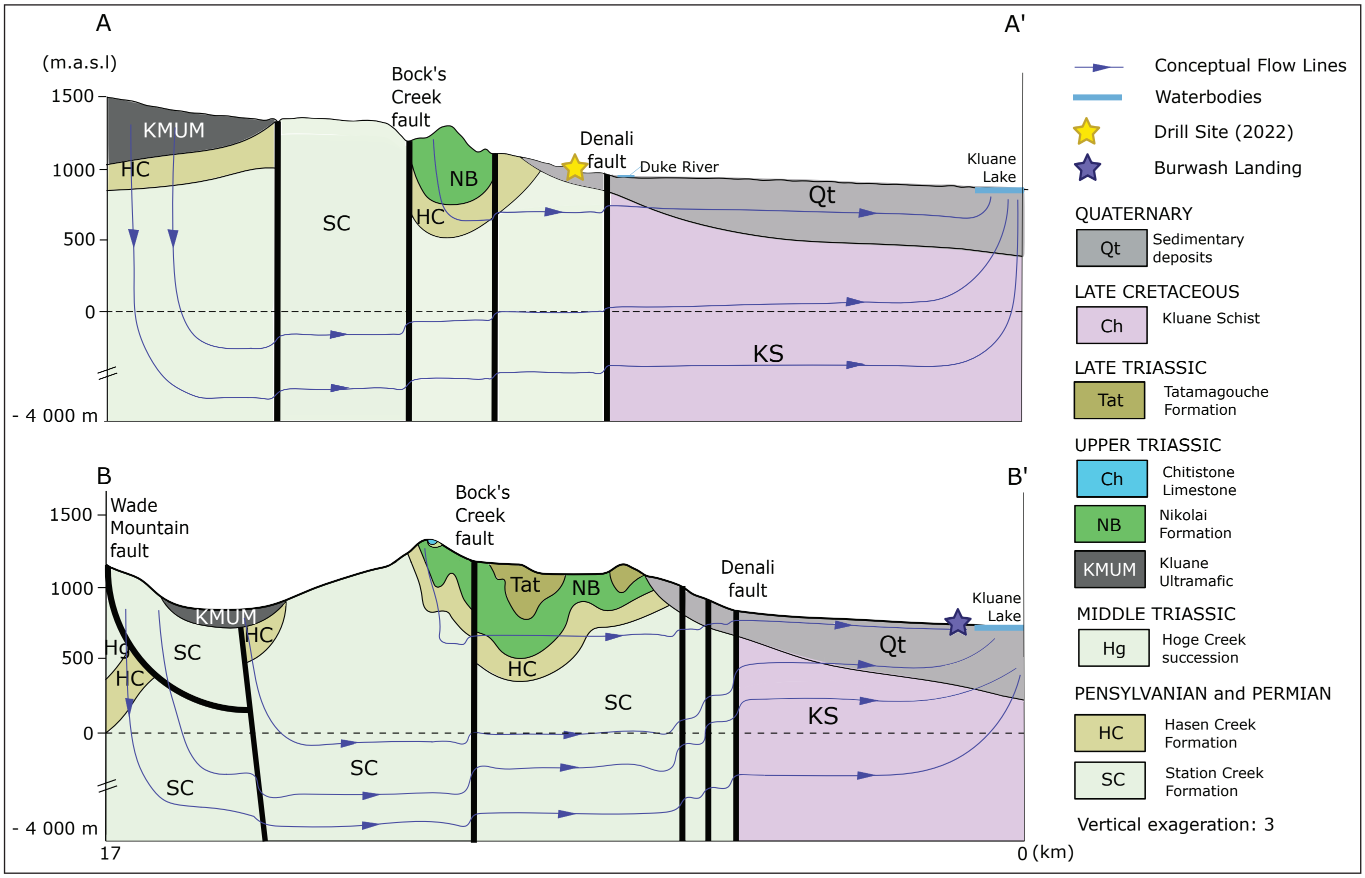

Figure 3. *Conceptual groundwater flow model for two cross sections of interest in the Duke River area. The location of cross section A-A' and B-B' are indicated in Figure 2. The geological cross sections are based on geological bedrock mapping, field observations, and cross sections presented in Israel et al. (2006). The geological units were extended below sea level with uncertainty as the thickness of the Station Creek Formation and Kluane schist are unknown. Flow lines present potential flow pathways. The mapped fault dips are also poorly to not defined in the area and are extended with uncertainty.*

Less volumetrically important units that are also exposed on the southwest side of the Denali fault include:

1. the Middle Triassic Hoge Creek succession (WR), a thin and discontinuous sedimentary layer;
2. the Upper Triassic Chitistone Limestone (WR) of variable thickness (hundreds of metres to discontinuous lenses);
3. the Upper Triassic McCarthy Formation (WR), a highly folded sedimentary layer primarily found in Hoge Creek syncline;
4. the Upper Triassic to Lower Cretaceous Tatamagouche succession composed of marine clastic sedimentary rocks (OA); and
5. the Eocene to Oligocene terrestrial sedimentary rocks of the Amphitheatre Formation and Wrangell Lavas (OA).

Intrusive rocks include the Late Triassic Maple Creek gabbro and Kluane mafic-ultramafic complex, the Early Cretaceous Kluane Ranges suite, the Oligocene Tkope suite, and the Miocene Wrangell suite. The Kluane mafic-ultramafic complex is the most extensive intrusive unit in the Duke River area. The thickness of the Kluane mafic-ultramafic complex is poorly defined but it is inferred to underlie the Burwash Uplands.

Figure 4. *Outcrop examples of each accessible unit in the study area.*

The Late Cretaceous Kluane schist is a highly deformed metasedimentary unit on the northeastern side of the Denali fault (Mezger et *al*., 2001a; Stanley, 2012). The Kluane schist exposed northeast of Kluane Lake extends beneath at least 380 m of Quaternary sediments near the Denali fault southwest of the lake. The metamorphic grade of the Kluane schist decreases southwestward from amphibolite facies near the Paleocene Ruby Range batholith to greenschist facies closest to the Denali fault (Mezger et *al*., 2001b; Stanley, 2012).

Methods

Sampling locations

The study area is mountainous, with creeks that carve through the mountains. These creeks are inlets to Kluane Lake. Throughout the field campaign, most outcrops used for fracture measurements were reached on foot along the creeks. A total of 35 outcrops were accessed southwest of the Denali fault, either along creeks: Congdon Creek, Nines Creek, Bock's Creek, Lewis Creek, Copper Joe Creek, Duke River, Burwash Creek, or by helicopter on August 13, 2022. General areas were identified prior to the field campaign using the Yukon Geological Survey bedrock geology map (2022) to ensure that measurements were taken to be representative of each lithology. Potential outcrops were identified remotely prior to fieldwork but the outcrop exposure and accessibility were uncertain due to the quality of available satellite images. The final outcrops were identified on site.

There are no Kluane schist outcrops in the study area. One Kluane schist outcrop was accessed on the northeast side of Kluane Lake and the study area. Future sites have been identified based on Stanley (2012) to describe the Kluane schist but require a helicopter assist. These sites are expected to be representative of the Kluane schist below the Quaternary sediments southwest of Kluane Lake northeast of the Denali fault.

Field data acquisition

Fracture data were collected by manual fracture measurements. Manual observations were selected over digital methods, such as lidar or other GIS methods, due to interest in the variation of fracture networks between units and at varying distances from the Denali fault. Manual observations allow for recording micro and macro-fractures on outcrops which is required to study the influence of lithology on fracture attributes (Formenti et *al*., 2022).

Fracture measurements

In this study, we use the linear scanline method. The linear scanline method is commonly used to evaluate fractures on outcrops, in borehole imagery, and on core samples (Zeeb et *al*., 2013). The linear scanline method involves measuring fracture attributes (strike, dip, spacing, length and mechanical aperture) of all the fractures which cross the scanline (Watkins et *al*., 2015). Measurements were taken by the same observer for each scanline to minimize observational bias (Andrews et *al*., 2019; Formenti et *al*., 2022). A tagline was set up along the outcrop to delineate the scanline with a length that was determined based on the size of the outcrop and the fracture density. When not limited by the size of the outcrop, at least 20 fracture measurements were taken per scanline, which ranged from 0.47 m to 2.86 m.

The fracture strike and dip were measured using the FieldMove Clino App by Midland Valley. FieldMove Clino is a digital compass-clinometer designed for smartphones (Vaughn et *al*., 2014). This accelerates the rate at which planar and linear field measurements can be taken and georeferenced directly onto a basemap (Vaughn et *al*., 2014).

Fracture spacing was determined based on the position of the fracture along the tagline. The length of fractures was measured below the scanline unless the fracture only projected above the scanline. These fracture measurements provide a relative length, but not absolute length of exposed fracture. The majority of fractures continue above the scanline and may extend beyond the visible outcrop. This results in truncation bias (Zeeb et *al*., 2013). Fracture aperture was recorded using a digital caliper. For fractures with consistent aperture, the aperture was measured at the scanline. For fractures with variable aperture, an aperture measurement was taken above and below the scanline and a range was assigned. Closed fractures were assigned an aperture of zero. The aperture of filled fractures was measured but fractures were noted as being filled or partially filled. Where possible, the mineral filling the fractures was described. The fracture data are presented based on the percent of fractures filled per scanline.

Scanline data collected

Overall, fracture data were collected on the following units (number of scanlines, *s*; number of fracture measurements, *f*): Station Creek Formation (s = 10; f = 270); Hasen Creek Formation (s = 8; 138), Nikolai formation (s = 9; f = 203); Kluane mafic-ultramafic complex (s = 2; f = 62); McCarthy Formation (s = 3; f = 31); Chitistone Limestone (s = 1; f = 9); Wrangell Lavas (s = 1; f = 17); Wrangell plutonic suite (s = 1; f = 31); Kluane schist (s = 1; f = 4).

Fracture data analysis

Fracture orientation

Stereonet version 11.4.5 (Allmendinger, 2022) is used to visualize orientation of fracture data. Rose diagrams of strike are used to visualize the distribution of fracture strike for each fracture category (all fractures, open fractures, filled and partially filled fractures, and closed fractures).

A Mixture of von Mises (MvM) distribution was used to identify fracture families based on strike following the approach outlined in Chabani et *al.* (2020). Fracture families are represented in the distribution as components (H). The optimal number of components for each fracture category are unknown. Therefore, multiple models are fit to each fracture family to determine the most representative number of components based on a combination of the negative log-likelihood of each distribution and geological feasibility. Statistically, minimizing the negative log-likelihood provides the best fit of the distribution. However, understanding the fracture data is essential to determine the true number of fracture families (or components; H) in the data. The MvM distributions for varying components were determined using the fit_vmmix function from the R package "BAMBI" which encompasses the log-likelihood (logLik; Chakraborty and Wong, 2021). A description of the MvM distribution is provided in Appendix A.

Fracture data are projected to poles and contoured in Stereonet version 11.4.5. (Allmendinger, 2022). Kamb contours with a contour interval of a standard deviation is used with a significance level of 3 × standard deviation used to contour the poles (Allmendinger, 2022). Kamb contours are based on the binomial probability distribution of the data and are used to describe the dominant dip of each facture category (Haneberg, 2004).

Geometrical fracture attributes

The fracture data were analyzed first with respect to the geometrical fracture attributes: length, aperture, spacing and intensity. Prior to the analysis, the required corrections were applied to the scanline data. There are no corrections required for the fracture length or aperture measured in the field. However, not all fracture data were collected on fractures perpendicular to the scanline. Therefore, the Terzaghi correction must be applied to correct the spacing between fractures (Equation 1; Tang et *al.*, 2016).

$$S = S_{apparent} \times |cos\,(a - a')| \quad (1)$$

where S is the corrected spacing, $S_{apparent}$ is the recorded spacing, a (°) is the strike of the fracture and a' (°) is the strike of the scanline.

The scanline length is adjusted such that the start and end of the scanline are delimited by the first and last fracture (Sanderson and Peacock, 2019). The position of each fracture along the scanline must be adjusted by:

$$P = P - P_i \quad (2)$$

where P (m) is the position of the fracture measurement within a scanline, and P_i (m) is the initial position of the first fracture along the scanline. The length of the scanline can then be calculated by:

$$L = P_f - P_i \quad (3)$$

where L is the scanline length (m), P_f (m) is the position of the last measured fracture along a scanline and P_i (m) is the position of the first fracture in the scanline.

The linear fracture intensity (I; m^{-1}) can then be calculated by:

$$I = \frac{N}{L} \quad (4)$$

where N is the number of fractures which cross the scanline and L is the scanline length.

The coefficient of variation (CV) of fracture spacing describes fracture distribution and is calculated by:

$$CV = \frac{\sigma_S}{\mu_S} \quad (5)$$

where σ_S is the standard deviation and μ_S is the mean fracture spacing (Glaas et *al.*, 2021).

Lithology and Distance from the Denali fault

Geometric fracture parameters are evaluated for each set of fracture measurements based on lithology and distance from the Denali fault. The distance from the Denali fault to the scanline is measured in QGIS perpendicular to the surface map trace (Bender and Haeussler, 2017). An ANCOVA test is used to evaluate the influence of lithology on geometric fracture attributes independent of distance from the fault. The ANCOVA test is limited to data within the first 4 km from the fault where data are abundant. A pairwise t-test is used to compare rock types across the whole study area.

Results

Fracture orientation

The best-fit number of fracture families was determined based on a combination of the lowest log-likelihood and geological feasibility. The number of fracture families is equivalent to the number of components (H) in the MvM distribution for each fracture category. The constraints imposed by Chabani et *al.* (2020) were used to evaluate the geological feasibility of the statistically optimal number of fracture families. Fracture families with dispersion parameter (k) less than 8 are considered not geologically feasible, as the range of values that would fall within the group is not representative of a fracture family. Fracture families with dispersion parameter greater than 32 were also discarded as these are uninformative (equivalent to a standard deviation of less than 10°). Finally, models with weightings of less than 10% were also discarded. As a result, the number of components chosen were not consistently those with the lowest log-likelihood (Fig. 5).

Based on the best-fit number of fracture families and geological feasibility of suggested fracture families, there is no preferential strike considering all fracture data (H = 4) or for open fractures (H = 4). For both categories, the four fracture families are near-equally distributed and the difference in weight between fracture families is not significant. The filled fractures can be represented by six fracture families (H = 6). The difference in weight between fracture families is also not significant; however the mean strike of fracture families ranges from NE–SW to SE–NW, with no N–S oriented fracture families. The closed fractures are also represented by six fracture families (H = 6), which range in strike from WSW–ENE to NW–SE. The dominant fracture family (F2) is oriented around a mean strike of 86.5° (E–W).

Fracture dip

There is a tendency towards steeply dipping fractures for open and filled fractures with median dips of 64.6° and 62.2°, respectively. All fracture data and the open fracture data show a left-skewed distribution (Fig. 6). The median dip of filled fractures is 62.8°. The median dip of closed fractures is 51.8° but have a bimodal distribution with the greatest number of dips ranging between 35° and 45°, and 75° and 85°.

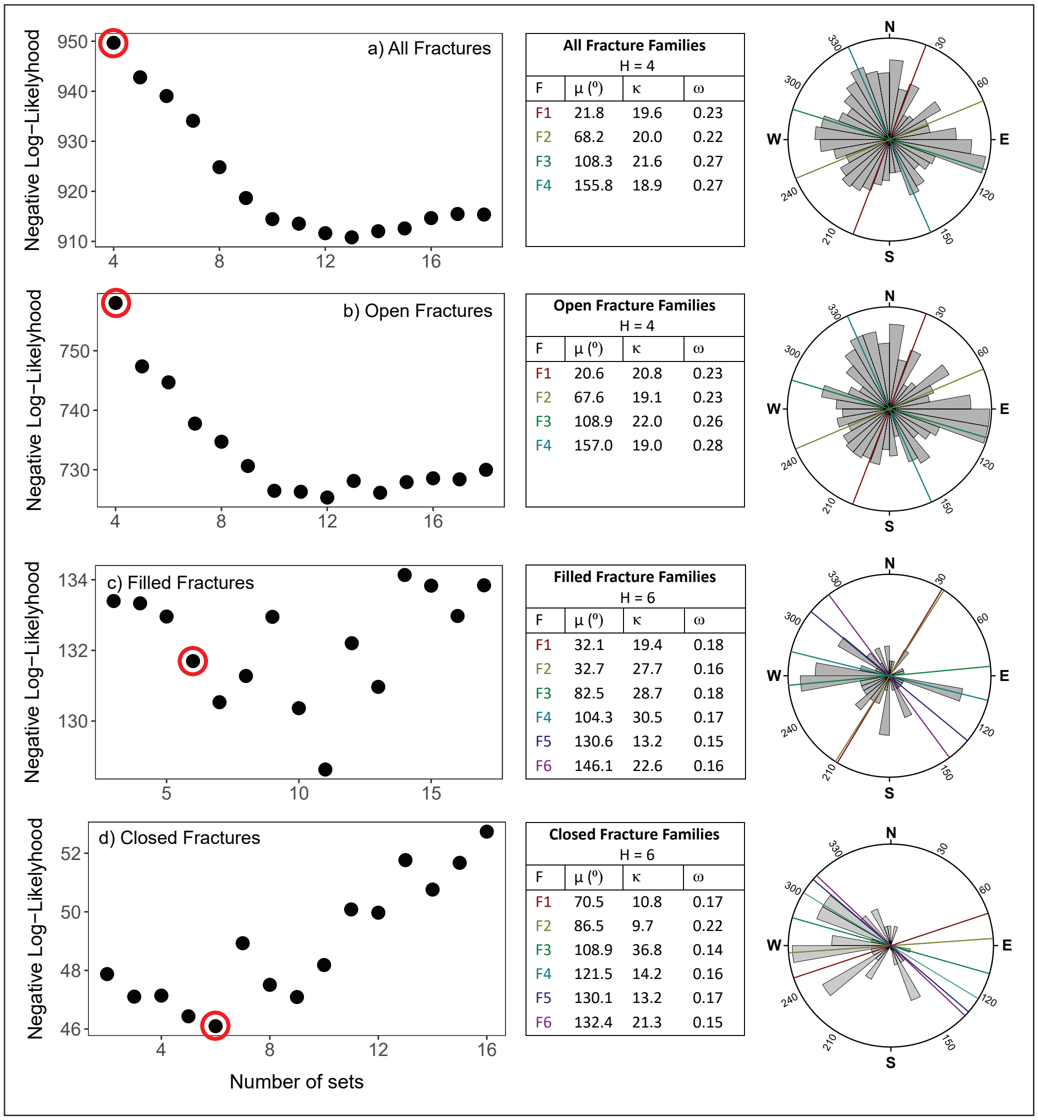

All Fracture Families
H = 4

F	μ (º)	κ	ω
F1	21.8	19.6	0.23
F2	68.2	20.0	0.22
F3	108.3	21.6	0.27
F4	155.8	18.9	0.27

Open Fracture Families
H = 4

F	μ (º)	κ	ω
F1	20.6	20.8	0.23
F2	67.6	19.1	0.23
F3	108.9	22.0	0.26
F4	157.0	19.0	0.28

Filled Fracture Families
H = 6

F	μ (º)	κ	ω
F1	32.1	19.4	0.18
F2	32.7	27.7	0.16
F3	82.5	28.7	0.18
F4	104.3	30.5	0.17
F5	130.6	13.2	0.15
F6	146.1	22.6	0.16

Closed Fracture Families
H = 6

F	μ (º)	κ	ω
F1	70.5	10.8	0.17
F2	86.5	9.7	0.22
F3	108.9	36.8	0.14
F4	121.5	14.2	0.16
F5	130.1	13.2	0.17
F6	132.4	21.3	0.15

Figure 5. *The fracture families determined based on the negative log-likelihood and geological feasibility of statistically defined fracture families. The number of fracture families identified based on these conditions is circled in red to highlight the respective log-likelihood.*

Average geometric fracture attributes

The geometric fracture attributes measured are the fracture linear intensity, spacing, length and aperture. These are summarized for each fracture family (Table 1). The median linear fracture intensity is 13.7 fractures per metre whereas the mean spacing of all fractures is 0.04 m. However, the spacing is highly variable. The mean length of open fractures is longer than both the filled and closed fractures. The fracture apertures are highly variable, but the majority are considered open to moderately wide on the ISRM (1978) fracture aperture scale (Table 2). The fracture apertures show a scale dependence based on fracture length (Fig. 7a) but no correlation with fracture strike (Fig. 7b).

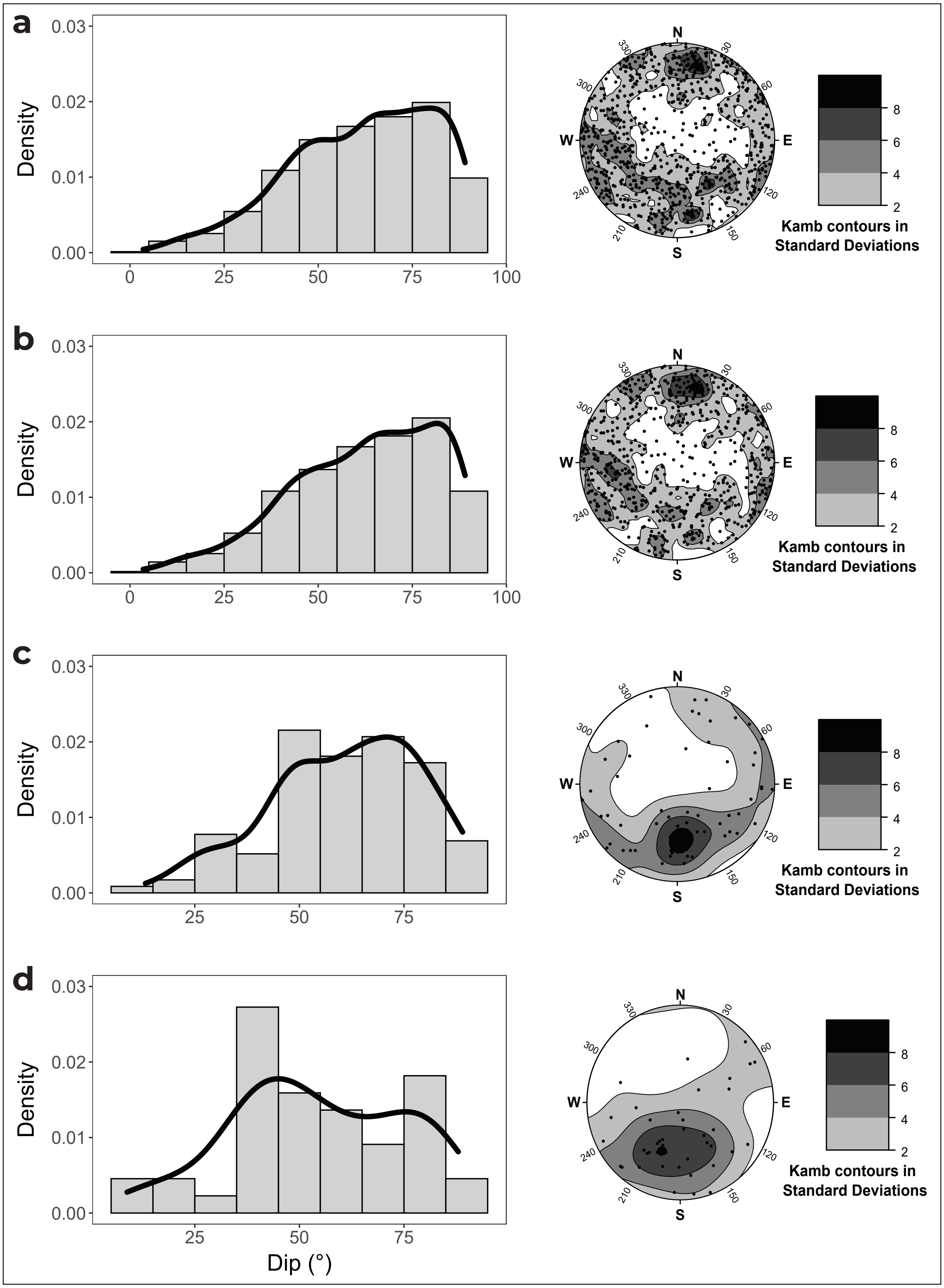

Figure 6. Kamb-contoured projected poles of scanline data by fracture category: ***(a)*** all fractures, ***(b)*** open fractures, ***(c)*** filled fractures, and ***(d)*** closed fractures.

Table 1. *Average values of the geometric attributes measured during, or calculated based on, the scanline surveys. CV: coefficient of variation; S.D.: standard variation.*

	Linear Intensity (m^{-1})		**Spacing**	**Length (m)**		**Aperture (mm)**	
	Median	Range	CV	Mean	S.D.	Mean	S.D.
All	13.7	3.8 – 55.6	1.6	0.8	5.9	2.0	3.4
Open	11.3	2.1 – 42.6	1.6	0.9	6.7	2.2	3.7
Filled	3.3	1.1 – 19.4	1.5	0.4	0.4	1.5	1.3
Closed	1.9	0.3 – 9.7	1.6	0.1	0.1	0	0

Table 2. *Qualitative classification of fracture apertures based on ISRM (1978) fracture aperture classification.*

Aperture (mm)	**Classification**	**Measured Fracture Apertures (%)**
0	Closed	8
< 0.1	Very tight	1
0.1 – 0.25	Tight	1
0.25 – 0.50	Partly open	9
0.50 – 2.50	Open	20
2.50 – 10	Moderately wide	60
> 10	Wide	1

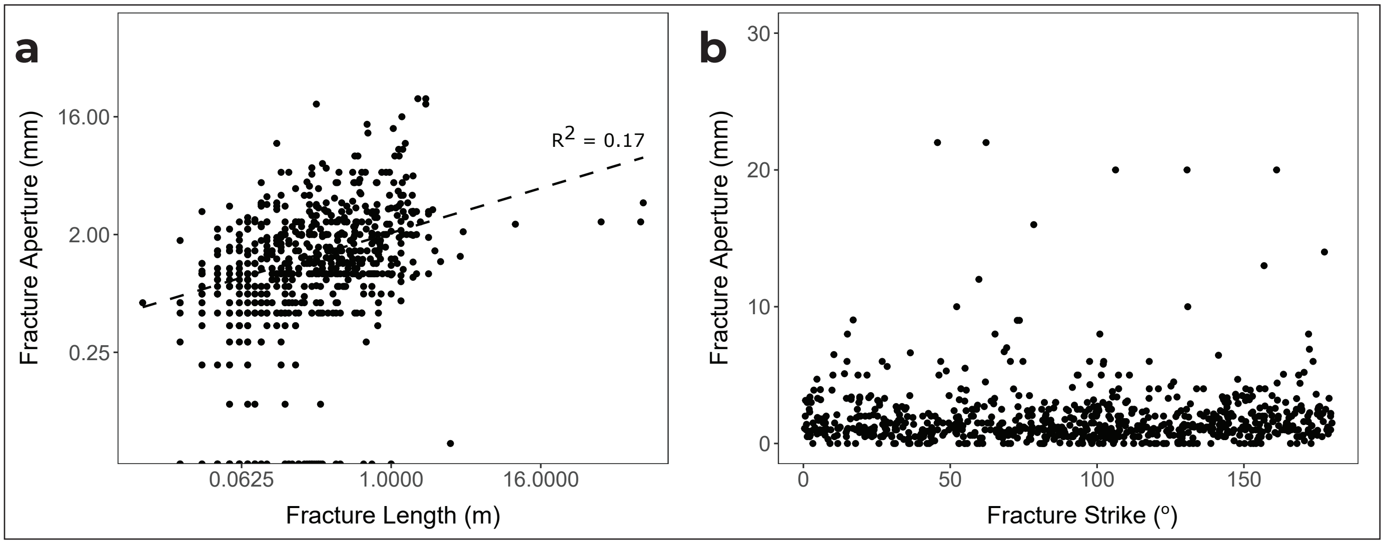

Figure 7. *Fracture aperture scale and strike dependence relative to* ***(a)*** *fracture length (fitted with a power-law distribution), and* ***(b)*** *fracture strike.*

Geometric fracture attribute variation by lithology and distance from Denali fault

Lithology

The influence of lithology (Appendix B) and distance from the Denali fault on geometric fracture attributes is illustrated in Figure 8. Each geometric attribute was tested to confirm if they met the required assumptions for an analysis of covariance (ANCOVA; Fig. 9; Table 3). The ANCOVA test was only applied on the three dominant rock types and within the first 4 km where sufficient data allowed statistical relevance.

The correlation of all geometric attributes by distance is poor, with certain exceptions. There are moderate positive and negative correlations of linear fracture intensity with increasing distance from the Denali fault for the Station Creek and Hasen Creek formations, respectively. The Nikolai formation has a weak to moderate correlation and also shows a decrease in linear fracture intensity with increasing distance from the Denali fault. Spacing is intrinsically related to the linear fracture intensity but the coefficient of variation (CV) describes the heterogeneity of fracture distribution (Glaas *et al*., 2021). The heterogeneity of fracture spacing increases in both the Hasen Creek and Nikolai formations but decreases in the Station Creek Formation with respect to the distance from the fault. There is no correlation between fracture mineralization and distance from the fault for any units. The Hasen Creek Formation has a weak to moderate positive correlation with fracture length, and a weak to moderate negative correlation with fracture aperture. The Nikolai formation shows a weak positive correlation such that aperture may increase farther from the fault.

Linearity is an important assumption for an ANCOVA test. The other assumptions are presented in Table 3. Testing for homogeneity of regression slopes confirms a significant interaction between distance and unit for linear fracture intensity. Therefore, the influence of units cannot be evaluated independently of the distance. There is no significant interaction between distance and unit with respect to the coefficient of variation of fracture spacing, mineralization, fracture length, or fracture aperture. However, neither mineralization nor fracture length residuals are normally distributed therefore an ANCOVA test cannot be applied. A complete ANCOVA test may only be applied to the fracture spacing (CV) and fracture aperture as the data distribution respects all of the assumptions.

After controlling for distance, there was not a significant difference in the coefficient of variation of fracture spacing between the major units ($F(2,20) = 1.90$, $p = 0.18$). There was a significant difference in the fracture aperture of the Station Creek, Nikolai and Hasen Creek formations ($F(2,20) = 5.04$, $p < 0.10$). Based on a post-hoc test, there is no significant difference in fracture aperture between the Nikolai formation and the Skolai Group (Station Creek and Hasen Creek formations), but there is a significant difference within the Skolai Group between Station Creek and Hasen Creek formations at a 90% confidence interval.

The mean of geometric fracture attributes, without considering distance are presented in Appendix B. The following analysis describes the influence of lithology on geometric attributes over the complete study area. This analysis was not controlled for distance. However, based on a 90% confidence interval, there is a significant difference in linear fracture intensity between Station Creek Formation and both the Hasen Creek and Nikolai formations. There are no significant differences in coefficients of variance for fracture spacing (CV), fracture length, or fracture aperture between the units (Table 4).

Distance

The influence of distance from the Denali fault is non-linear and summarized by distance interval (Table 4). Eight distance categories were created to represent available data. Based on Figure 8 and Table 5, there is a general decrease in linear fracture intensity with distance from the fault, however the variability is significant and must be considered. This variability occurs within and between rock types. The distance from the Denali fault has a negligible influence on fracture spacing and fracture length. Mean fracture aperture is constant with little variability within the first 4 km from the fault. The fracture aperture farther than 4 km from the fault is greater with greater standard deviation.

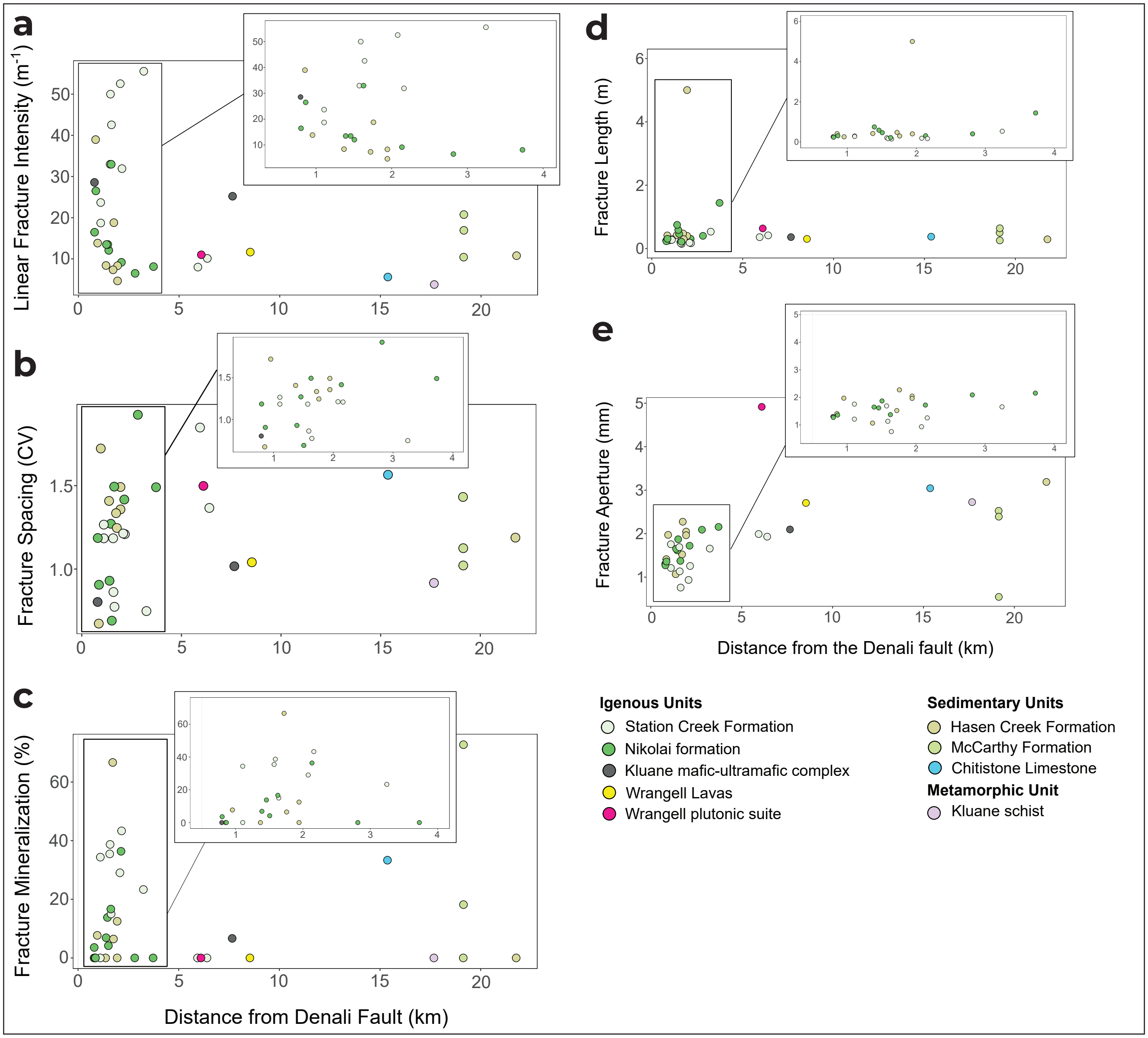

Figure 8. *Representation of the influence of lithology and distance from the Denali fault on geometric fracture attributes:* ***(a)*** *Linear fracture intensity,* ***(b)*** *fracture spacing,* ***(c)*** *fracture mineralization,* ***(d)*** *fracture length, and* ***(e)*** *fracture aperture. Large plots show all of the data collected, whereas the inset plots focus on the first 4 km from the Denali fault where the concentration of data points is greatest. This reduces the number of rock types represented, but the three dominant rock types in the region Nikolai formation, Station Creek Formation and Hasen Creek Formation, are all represented within 4 km of the fault. landscape*

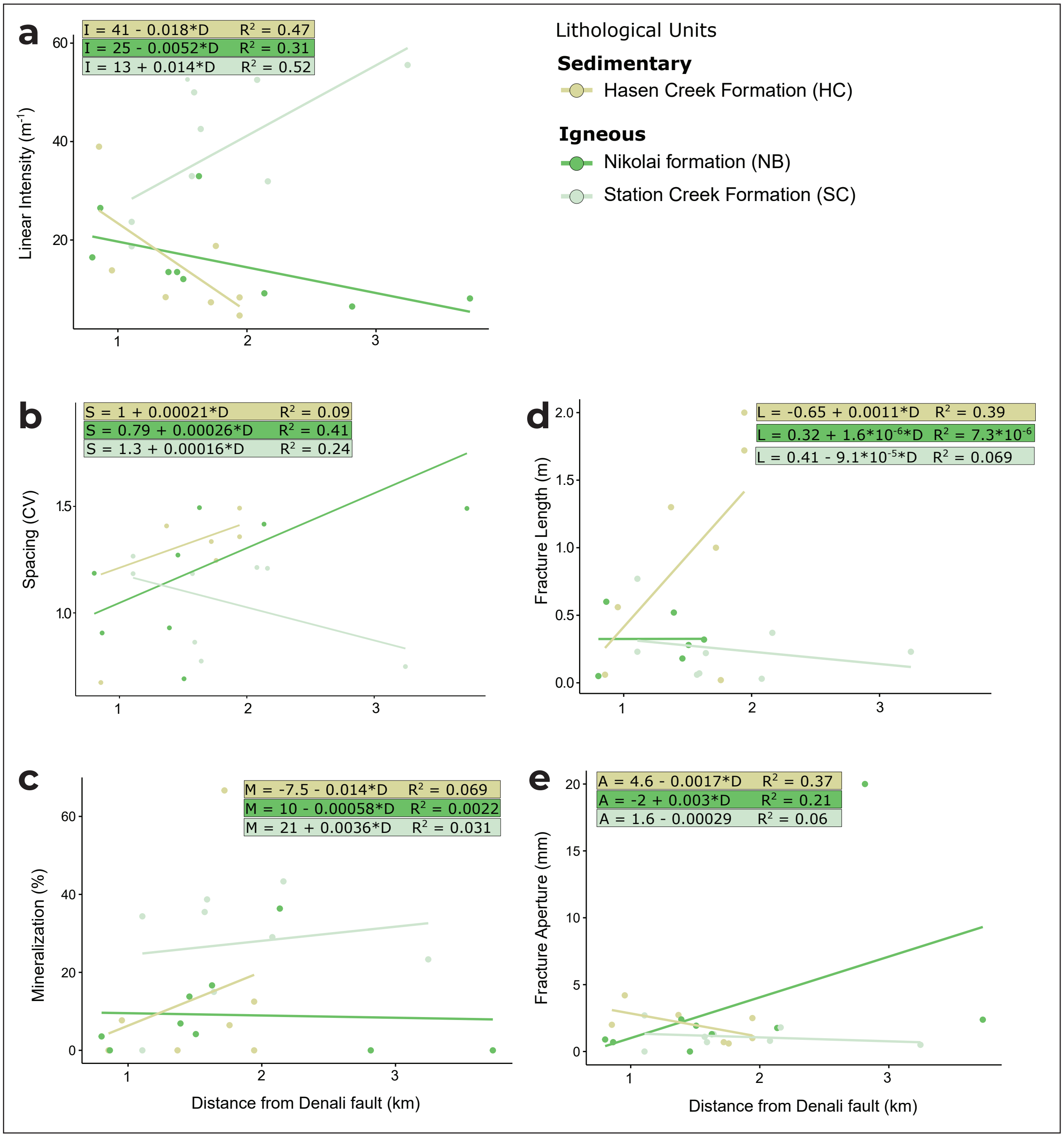

Figure 9. *Test for linearity of each geometric fracture attribute per lithology within the first 4 km of the Denali fault. The geometric fracture attributes evaluated are:* ***(a)*** *linear fracture intensity,* ***(b)*** *fracture spacing (CV),* ***(c)*** *mineralization,* ***(d)*** *fracture length, and e) fracture aperture.*

Table 3. *Assumptions required to perform an ANCOVA test. All assumptions must be true with no outliers to be able to control for the covariate (distance). A statement is considered to be TRUE if it falls within a 90% confidence interval.*

Assumptions	Linear Intensity (m^{-1})	Spacing (CV)	Mineralization (%)	Length (m)	Aperture (mm)
Homogeneity of regression slopes	FALSE	TRUE	TRUE	TRUE	TRUE
Normality of residuals	TRUE	TRUE	FALSE	FALSE	TRUE
Homogeneity of variances	TRUE	TRUE	TRUE	TRUE	TRUE
Outliers	No outliers	No outliers	One outlier M = 66.7% at 1721 m (HC)	One outlier: L = 5.003 at 1943 m (HC)	No outliers

Table 4. *Pairwise t-test to compare geometric fracture attributes for units for which there were two or more scanlines over the complete study area:* ***(a)*** *linear fracture intensity,* ***(b)*** *coefficient of variation of fracture spacing,* ***(c)*** *fracture length, and* ***(d)*** *fracture aperture. Units are abbreviated to: HC (Hasen Creek Formation), KMUM (Kluane mafic-ultramafic complex), McC (McCarthy Formation), NB (Nikolai formation), SC (Station Creek Formation).*

(a) Linear fracture intensity

(t-value)	HC	KMUM	McC	NB
KMUM	1.0	---	---	---
McC	1.0	1.0	---	---
NB	1.0	1.0	1.0	---
SC	0.04	1.0	0.55	0.06

(b) Fracture spacing (CV)

(t-value)	HC	KMUM	McC	NB
KMUM	1.0	---	---	---
McC	1.0	1.0	---	---
NB	1.0	1.0	1.0	---
SC	1.0	1.0	1.0	1.0

(c) Fracture length

(t-value)	HC	KMUM	McC	NB
KMUM	1.0	---	---	---
McC	0.96	1.0	---	---
NB	0.37	1.0	1.0	---
SC	0.12	1.0	1.0	1.0

(d) Fracture aperture

(t-value)	HC	KMUM	McC	NB
KMUM	1.0	---	---	---
McC	1.0	1.0	---	---
NB	1.0	1.0	1.0	---
SC	0.66	1.0	1.0	1.0

Table 5. *Linear fracture intensity summarized by distance. Distance is grouped into two ranges at 1 km intervals close to the fault (0–2 km), 3 ranges of 3 km intervals mid-distance from the fault (2–11 km), and one range greater than 11 km for scanlines recorded far from the fault. The count represents the number of scanlines which fall into the distance range. S.D.: standard variation*

Distance group (km)	Linear Fracture Intensity (m^{-1})		Coefficient of variance fracture spacing		Fracture Length (m)		Fracture Aperture (mm)		Count
	Mean	S.D.	Mean	S.D.	Mean	S.D.	Mean	S.D.	
[0, 1[	24.9	10.1	1.1	0.4	0.3	0.3	1.5	0.3	5
[1, 2[	20.5	14.1	1.2	0.3	0.6	0.6	1.6	0.4	14
[2, 4[	27.3	22.7	1.3	0.4	0.2	0.2	1.6	0.5	6
[4, 7[	9.7	1.5	1.6	0.2	0.4		2.9	1.7	3
[7, 10[	18.4	9.6	1.0	0.02	0.5	0.6	2.4	0.4	2
[10, 30[	11.4	6.5	1.2	0.2	0.4	0.3	2.4	1.0	6

Influence of subsidiary faults on fracture density and aperture

Linear fracture intensity and fracture aperture have been shown to have the greatest control on permeability. The Denali fault is the major regional fault, but there are also numerous smaller faults. These subsidiary faults likely contribute to the variability in geometric fracture attributes (Fig. 10). The linear fracture intensity is smallest in outcrops along Burwash Creek where the distance between the Denali fault and the first subsidiary fault is the greatest; these are followed by outcrops at Copper Joe Creek. The variation in fracture aperture does not seem to be related to the subsidiary faults.

Discussion

Fracture orientation

Fault networks typically consist of two to three fracture families, whereas joint networks can consist of one to an indistinguishable number of fracture families (Berkowitz et *al.*, 2000). On outcrops in the Duke River area some minor faults were noted, but fracture networks consisted mainly of joints and veins.

The dip of the Denali fault has not been defined but this strike-slip fault is assumed to be near-vertical. The fractures in the Duke River area are steeply dipping which is consistent with the geological environment in which they were formed. Steep fractures in steeply dipping fault zones can increase vertical permeability which is favourable to convective heat transport that can potentially increase near-surface temperature gradients (Timar-Geng et *al.*, 2009).

Average fracture attributes

The geometric fracture attributes, density, spacing (CV), length and aperture of open fractures control present-day permeability. The mean linear fracture intensity of open fracture in the Duke River area is significantly higher (11.3 frac m^{-1}) compared to other naturally fractured geothermal reservoirs. For example, the crystalline reservoir rocks in the northern Upper Rhine Graben (2.17 frac m^{-1}; Bossennec et *al.*, 2022), Saint Pierre Bois Quarry (0.79 frac m^{-1}; Dezayes et *al.*, 2021), or in the Central Upper Rhine Graben (~0.76 frac m^{-1}; Glaas et *al.*, 2021) all have lower linear fracture intensity. The fracture density distribution is described based on fracture spacing (Gillespie et *al.*, 1999; Odling et *al.*, 1999). In the Duke River area, the fracture spacing is heterogeneous and poorly clustered.

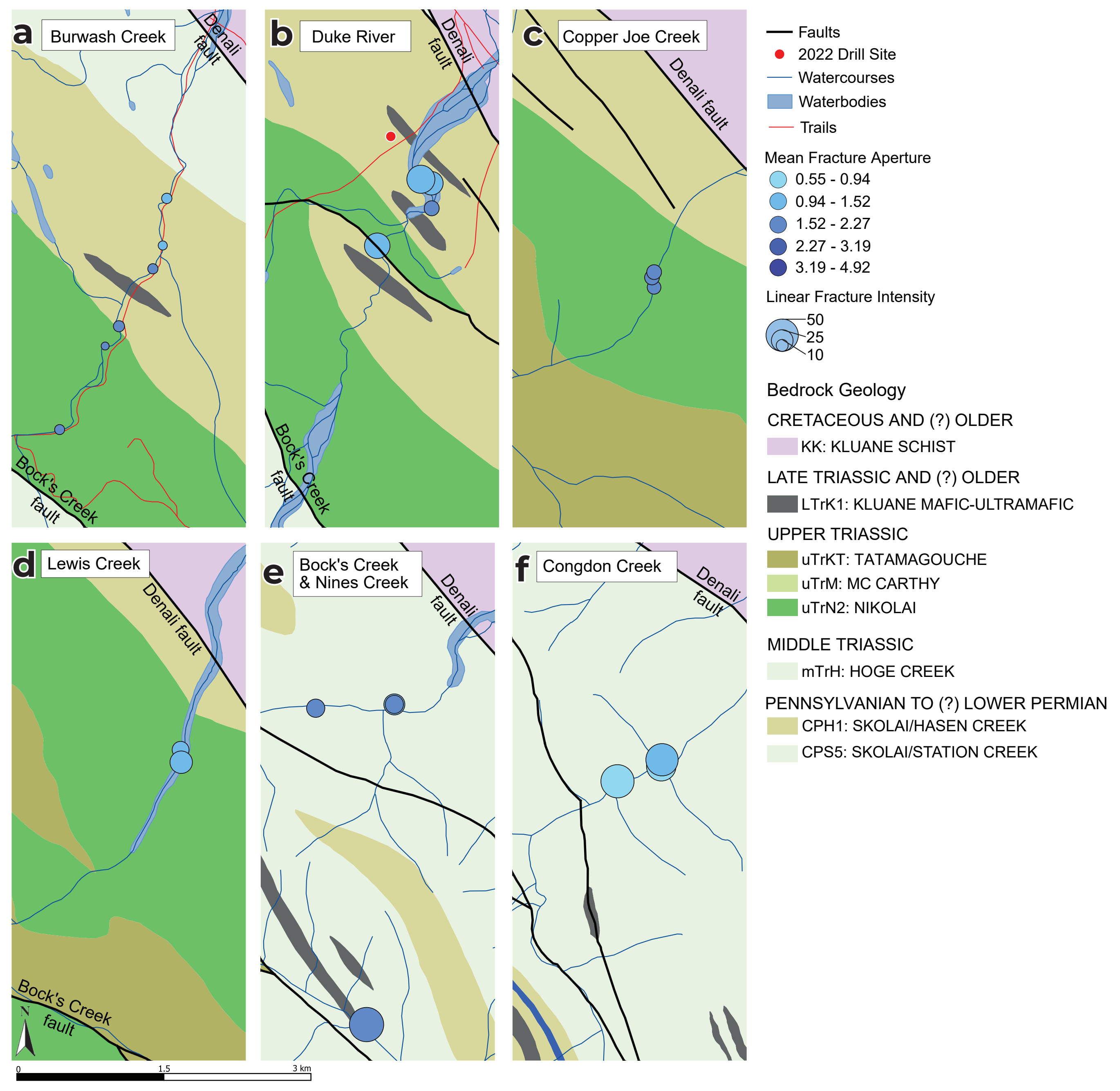

Figure 10. *Linear fracture intensity per scanline collected on foot at outcrops located along creeks. These indicate the proximity of each outcrop to faults in addition to the Denali fault. These include the Bock's Creek and unnamed faults.*

The distribution of fracture lengths is central to developing stochastic discrete fracture networks and evaluating secondary permeability (*e.g.*, Bour and Davey, 1997; Bonnet et *al.*, 2001; Darcel et *al.*, 2003). The distribution of fracture lengths can inform whether connectivity is controlled by small fractures, large fractures, or equally by both small and large fractures (Bour and Davy, 1997).

Fracture length is related to fracture aperture wherein longer fractures typically have greater aperture. The association between fracture length and aperture is integrated into discrete fracture models (Bossennec et *al.*, 2022). However, the aperture of shear-dependent fractures has also been shown to depend on the maximum horizontal stress direction such that fractures oriented parallel to the maximum stress direction exhibit apertures two to three times greater than fractures oriented perpendicular to the maximum stress direction (Reinecker et *al.*, 2021). As a result, fractures oriented parallel to the maximum stress direction act as preferential flow pathways (Reinecker et *al.*, 2021).

Regional scale focal mechanism data indicate a NE-SW dominant compressive stress direction in southwestern Yukon (Ristau et *al.*, 2007). Based on the focal mechanism data available and a localized stress inversion around the eastern Denali fault near Duke River, the maximum compressive stress direction (N50°E) is nearly perpendicular to the eastern Denali fault (T. Finley, personal communication). This orientation is consistent with the results of Choi et *al.* (2021) in northwestern British Columbia ~200 km to the southeast. Therefore, open fractures oriented around N50°E would be expected to have a greater fracture aperture than open fracture oriented around N140°E. Based on the scanline data, there is no correlation between fracture aperture and orientation, but surface weathering likely camouflage the true fracture aperture.

The effect of weathering on surface outcrops causes fracture aperture measured on outcrops to consistently overestimate subsurface aperture, even if corrected for pressure (Peacock et *al.*, 2022). Comparably, drilling mechanically erodes the surface of fracture rims on the well wall but fracture apertures are preserved in the drill core (Glaas et *al.*, 2021). Therefore, further aperture analysis on drill core is required to confirm fracture aperture and detect any preferential strike for wider aperture fractures.

Potential for permeability based on described fracture data

The geometric fracture attributes described will be fitted into a small-scale discrete fracture model to determine the permeability (*e.g.*, Bossennec et *al.*, 2022). However, modelling large-scale fracture networks requires a lot of computational power. In a regional groundwater flow model, the permeability may be described by an equivalent porous media. This data set may be well suited to be represented as an equivalent porous media due to the high fracture density and homogeneous fracture distribution in all orientations (Zareidarmiyan et *al.*, 2021).

Before developing a discrete fracture model, a first-order estimation of permeability can be deduced based on fractured areas with similar conditions. For example, pemeability was determined to range between 1×10^{-17} and 1.1×10^{-16} m^2 in the Upper Rhine Graben where significantly lower fracture density was reported (Bossennec et *al.*, 2022). The permeability of the Upper Rhine Graben is slightly lower than the typical permeability of moderately fractured low-porosity rocks (10^{-15} m^2; Forster and Smith, 1989). Therefore, we can expect the permeability of the Duke River area to be at least on the order of 10^{-15} m^2. The steeply dipping fractures can create an anisotropy such that the near-vertical permeability exceeds the horizontal permeability (Lazear, 2009). A combination of steep fractures and high permeability is known to facilitate forced convection in mountainous regions (Forster and Smith, 1989; Timar-Geng et *al.*, 2009).

Influence of lithology and distance on geometric fracture attributes

Herein, fracture data were analyzed as a whole, by lithology, and by distance from the fault. This was an important distinction as previous research in the Central Upper Rhine Graben has shown that linear fracture intensity varied by lithology (Glaas et *al.*, 2021). In the Central Upper Rhine Graben, linear fracture intensity was lower in the sedimentary unit (sandstone) than in the igneous unit (granite). This comparison is more complex in the Duke River area as we need to consider the influence of distance from the Denali fault. The only parameter that met the assumptions to be controlled for distance over the first four kilometres from the Denali fault, where data were abundant, was the fracture aperture. The Hasen Creek and Nikolai formations could be grouped as they are significantly different from the Station Creek Formation; however this variation is not significant over the whole study area, when not controlled for the influence of distance from the Denali fault.

There are only significant variations in the linear fracture intensity when considering the whole study area without controlling for distance. However, this is not aligned with Glaas et *al.* (2021) observations as the significant difference are between two volcanic units (Station Creek and Nikolai formations). Rather than simplifying the regional geology to rock types, our results show that there is only significant difference between the Station Creek Formation and other rock types. Therefore, when considering linear fracture intensity in the conceptual model, rock types can be grouped into Station Creek Formation (Group 1) and a combination of all other major units (Group 2; including the Hasen Creek, Nikolai and McCarthy formations, and the Kluane mafic-ultramafic complex).

Insufficient to no data were collected on three sedimentary units in the cross sections of interest: Hoge Creek succession, Tatamagouche succession and Quaternary deposits. The Hoge succession overlies the Hasen Creek Formation (Fig. 3) and is included in Group 2 to consider linear fracture intensity. The Tatamagouche succession and Quaternary deposits are surficial units. The Tatamagouche succession coverage is sparse and is expected to have little influence on deep groundwater circulation. The permeability of Quaternary deposits is controlled by primary porosity.

There was not a significant difference in the coefficient of variance for fracture spacing and fracture length between rock types. Therefore, only the influence of distance will be considered for these attributes. Fracture aperture increased non-linearly with increasing distance from the Denali fault (Table 5). The fracture apertures will be considered in two groups: within 4 km from the Denali fault and farther than 4 km from the Denali fault.

Influence of subsidiary faults on linear fracture density and aperture

Herein, we assumed that the dominant stress field was related to the Denali fault. However, other faults have been mapped in the Duke River area and there is regional compressional deformation in the St. Elias region that contributes to the continuous exhumation of the St. Elias mountain ranges southwest of the Duke River area. This regional compression likely contributes to the variation in measured fracture networks. The statistical significance of proximity of fractures to subsidiary faults was not evaluated. However, there is a general trend of high linear fracture intensity when subsidiary faults are closer together (e.g., Fig. 10b,f), compared to when faults are farther apart (e.g., Fig. 10a,c).

Conclusions

Overall, linear fracture intensity in the Duke River area is high and open fractures are equally oriented in all directions. The linear fracture intensity, and other geometric fracture attributes (fracture spacing, length and aperture) influence large-scale permeability. Based on the fracture analysis completed in this work, rock types with similar attributes can be grouped into two main hydrostratigraphic units of a conceptual groundwater flow model. Group 1 only includes the Station Creek Formation, and Group 2 includes all other rock types. The fracture spacing and fracture length attributes are independent of the distance from the Denali fault. There is a weak non-linear correlation between distance from the Denali and both fracture intensity and fracture aperture wherein fracture density is greatest within the first 4 km of the fault, but fracture aperture is greatest farther than 4 km from the Denali fault. This relationship is weak, and fractures may also be associated to other faults and the exhumation of the Saint Elias Mountains, which contributes to the above-average fracture intensity of the area.

These conclusions were drawn based on scanline data distributed over the study area at 0.8 km to 22 km from the Denali fault. This data set lacks fracture measurements within the first 750 m from the Denali fault due to extensive Quaternary sediment coverage and farther than 5 km due to outcrop accessibility constraints. The data gap next to the Denali fault could be filled by analysis of drill core from exploration boreholes. The core would also improve fracture aperture data as current fracture aperture measurements were recorded on weathered outcrops.

Ultimately, the orientation and geometric fracture attributes described herein will be used to develop a discrete fracture network and evaluate large scale permeability. Thereafter, future research will integrate these results into a hydrothermal model to evaluate the deep geothermal potential in the Duke River area.

References

Allmendinger, R.W., 2022. Stereonet 11.4.5. Software, https://www.rickallmendinger.net/stereonet.

Andrews B.J., Roberts J.J., Shipton Z.K., Bigi S., Tartarello M.C. and Johnson G., 2019. How do we see fractures? Quantifying subjective bias in fracture data collection. Solid Earth, vol. 10, p. 487–516, https://doi.org/10.5194/se-10-487-2019.

Bender, A.M. and Haeussler, P.J., 2017. Eastern Denali Fault Surface Trace Map, Eastern Alaska and Yukon, Canada. U.S. Geological Survey, Open-File Report 2017-1049, 10 p., https://doi.org/10.3133/ofr20171049.

Beranek, L.P. and Mortensen, J.K., 2011. The timing and provenance record of the late Permian Klondike Orogeny in northwestern Canada and arc-continent collision along Western North America. Tectonics, vol. 30, https://doi.org/10.1029/2010tc002849.

Berkowitz, B., Bour, O., Davy, P. and Odling, N., 2000. Scaling of fracture connectivity in geological formations. Geophysical Research Letters, vol. 27, p. 2061–2064, https://doi.org/10.1029/1999GL011241.

Blais-Stevens, A., Clague, J.J., Brahney, J., Lipovsky, P., Haeussler, P.J. and Menounos, B., 2020. Evidence for Large Holocene Earthquakes along the Denali Fault in Southwest Yukon, Canada. Environmental & Engineering Geoscience, vol. 26, p. 149–166, https://doi.org/10.2113/EEG-2263.

Bonnet, E., Bour, O., Odling, N.E., Davy, P., Main, I., Cowie, P. and Berkowitz, B., 2001. Scaling of Fracture Systems in Geological Media. Reviews of Geophysics, vol. 39, p. 347–383, https://doi.org/10.1029/1999RG000074.

Bossennec, C., Seib, L., Frey, M., van der Vaart, J. and Sass, I., 2022. Structural Architecture Permeability Patterns of Crystalline Reservoir Rocks in the Northern Upper Rhine Graben: Insights from Surface Analogues of the Odenwald. Energies, vol. 15, https://doi.org/10.3390/en15041310.

Bour, O. and Davey, P., 1997. Connectivity of random fault networks following a power law fault length distribution. Water Resources Research, vol. 33, p. 1567–1583, https://doi.org/10.1029/96WR00433.

Camanni, G., Vinci, F., Tavani, S., Ferrandino, V., Mazzoli, S., Corradetti, A., Parente, M. and Iannace, A., 2021. Fracture density variations within a reservoir-scale normal fault zone: A case study from shallow-water carbonates of southern Italy. Journal of Structural Geology, vol. 151, https://doi.org/10.1016/j.jsg.2021.104432.

Chabani, A., Mehl, C., Cojan, I., Alais, R. and Bruel, D., 2020. Semi-automated component identification of a complex fracture network using a mixture of von Mises distributions: Application to the Ardeche margin (South-East France). Computers & Geoscience, vol. 137, https://doi.org/10.1016/j.cageo.2020.104435.

Chakraborty, S. and Wong, S.W., 2021. BAMBI: an R Package for Fitting Bivariate Angular Mixture Models. Journal of Statistical Software, vol. 99, https://doi.org/10.18637/jss.v099.i11.

Choi, M., Eaton, D.W. and Enkelmann, E., 2021. Is the Eastern Denali fault still active? Geology, vol. 49, 5 p., https://doi.org/10.1130/G48461.1.

Colpron, M., Crowley, J.L., Gehrels, G.E., Long, D.G.F., Murphy, D.C., Beranek, L.P. and Bickerton, L., 2015. Birth of the northern Cordilleran orogen, as recorded by detrital zircons in Jurassic synorogenic strata and regional exhumation in Yukon. Lithosphere, vol. 7, p. 541–562, https://doi.org/10.1130/L451.1.

Colpron, M., Israel, S. and Friend, M., 2016. Yukon plutonic suites. Yukon Geological Survey, Open File 2016-37, scale 1:750 000.

Colpron, M., Nelson, J. L. and Murphy, D. C., 2007. Northern Cordillera terranes and their interactions through time. GSA Today, vol. 17, p. 4–10, https://doi.org/10.1130/GSAT01704-5A.1.

Colpron, M., Sack, P.J., Crowley, J.L., Beranek, L.P. and Allan, M.M., 2022. Late Triassic to Jurassic magmatic and tectonic evolution of the Intermontane terranes in Yukon, northern Canadian Cordillera: Transition from arc to syn-collisional magmatism and post-collisional lithospheric delamination. Tectonics, vol. 41, https://doi.org/10.1029/2021TC007060.

Darcel, C., Bour, O. and Davy, P., 2003. Stereological analysis of fractal fracture networks. Journal of Geophysical Research: Solid Earth, vol. 108, https://doi.org/10.1029/2002JB002091.

Dezayes, C., Lerouge, C., Innocent, C. and Lach, P., 2021. Structural control on fluid circulation in a graben system: Constraints from the Saint Pierre Bois quarry (Vosges, France). Journal of Structural Geology, vol. 146, https://doi.org/10.1016/j.jsg.2021.104323.

Elliott, J.L., Larsen, C. F., Freymueller, J.T. and Motyka, R. J., 2010. Tectonic block motion and glacial isostatic adjustment in southeast Alaska and adjacent Canada constrained by GPS measurements. Journal of Geophysical Research: Solid Earth, vol. 115, https://doi.org/10.1029/2009JB007139.

Faulds, J.E. and Hinz, N.H., 2015. Favorable Tectonic and Structural Settings of Geothermal Systems in the Great Basin Region, Western USA: Proxies for Discovering Blind Geothermal Systems. Proceedings World Geothermal Congress 2015, Melbourne, Australia, April 2015.

Finley, T., Salomon, G., Stephen, R., Nissen, E., Cassidy, J. and Menounos, B., 2022. Preliminary results and structural interpretations from drone lidar surveys over the Eastern Denali fault, Yukon. Yukon Exploration and Geology 2021, K.E. MacFarlane (ed.), Yukon Geological Survey, p. 83–105.

Formenti, S., Peace, A., Eyles, C., Lee, R. and Waldron, J., 2022. Fractures in the Niagara Escarpment in Ontario, Canada: distribution, connectivity, and geohazard implications. Geological Magazine, https://doi.org/10.1017/S0016756822000462.

Forster, C. and Smith, L., 1989. The Influence of Groundwater Flow on Thermal Regime in Mountainous Terrain: A Model Study. Journal of Geophysical Research: Solid Earth, vol. 94, p. 9439–9451, https://doi.org/10.1029/JB094iB07p09439.

Fossen, H., 2010. Structural geology: First Edition. Cambridge University press.

George, S.W.M., Nelson, J.L., Alberts, D., Greig, C.J. and Gehrels, G.E., 2021. Triassic-Jurassic Accretionary History and Tectonic Origin of Stikinia from U-Pb Geochronology and Lu-Hf isotope Analysis, British Columbia. Tectonics, vol. 40, https://doi.org/10.1029/2020tc006505.

Gillespie, P.A., Johnston J.D., Loriga, M.A., McCaffrey, K.L.W., Walsh, L.L. and Watterson, L., 1999. Influence of layering on vein systematics in line samples. *In:* Fractures, Fluid Flow and Mineralization, K. McCaffrey, L. Lonergan and J.J. Wilkinson (eds.), Geological Society, London, Special Publication No. 155, p. 35–56, https://doi.org/10.1144/GSL.SP.1999.155.01.05.

Glaas, C., Vidal, J. and Genter, A., 2021. Structural characterization of naturally fractured geothermal reservoirs in the central Upper Rhine Graben. Journal of Structural Geology, vol. 148, https://doi.org/10.1016/j.jsg.2021.104370.

Haeussler, P.J., Matmon, A., Schwartz, D.P. and Seitz, G.G., 2017. Neotectonics of interior Alaska and the late Quaternary slip rate along the Denali fault system. Geosphere, vol. 13, p. 1445–1463, https://doi.org/10.1130/GES01447.1.

Haneberg, W.C., 2004. Special Plots for Geoscience Data. *In:* Computational Geosciences with Mathematica. Springer, Berlin, Heidelberg, p. 25–55, https://doi.org/10.1007/978-3-642-1854-0_2.

Israel, S., Tizzard, A. and Major, J., 2006. Bedrock Geology of the Duke River area, parts of NTS 115G/2, 3, 4, 6 and 7, southwestern Yukon. *In:* Yukon Exploration and Geology 2005, D.S. Emond, G.D. Bradshaw, L.L. Lewis and L.H. Weston (eds.), Yukon Geological Survey, p. 139–154.

Lazear, G.D., 2008. Fractures, convection and underpressure: hydrogeology on the southern margin of the Piceance basin, west-central Colorado, USA. Hydrogeology Journal, vol. 17, p. 641–664, https://doi.org/10.1007/s10040-008-0381-3.

Leonard, L.J., Mazzotti, S. and Hyndman, R.D., 2008. Deformation rates estimated from earthquakes in the northern Cordillera of Canada and eastern Alaska. Journal of Geophysical Research: Solid Earth, vol. 113, https://doi.org/10.1029/2007JB005456.

Lowey, G.W., 1998. A new estimate of the amount of displacement on the Denali fault system based on the occurrence of carbonate megaboulders in the Dezadeash Formation (Jura-Cretaceous), Yukon, and the Nutzotin Mountains sequence (Jura-Cretaceous), Alaska. Bulletin of Canadian Petroleum Geology, vol. 46, p. 379–386, https://doi.org/10.35767/gscpgbull.46.3.379.

Marechal, A., Ritz, J.-F., Ferry, M., Mazzotti, S., Blard, P.-H., Braucher, R. and Saint-Carlier, D., 2018. Active tectonics around the Yakutat indentor: New geomorphological constraints on the eastern Denali, Totschunda and Duke River Faults. Earth and Planetary Science Letters, vol. 482, p. 71–80, https://doi.org/10.1016/j.epsl.2017.10.051.

McDermott, R.G., Ault, A.K., Caine, J.S. and Thomson, S. N., 2019. Thermotectonic History of the Kluane Ranges and Evolution of the Eastern Denali Fault Zone in Southwestern Yukon, Canada. Tectonics, vol. 38, p. 2983–3010, https://doi.org/10.1029/2019TC005545.

Mezger, J.E., Creaser, R.A., Erdmer, P. and Johnston, S.T., 2001a. A Cretaceous back-arc basin in the Coast belt of the northern Canadian Cordillera: evidence from geochemical and neodymium isotope characteristics of the Kluane metamorphic assemblage, southwest Yukon. Canadian Journal of Earth Sciences, vol. 38, p. 91–103, https://doi.org/10.1139/e00-076.

Mezger, J.E., Chacko, T. and Erdmer, P., 2001b. Metamorphism at a late Mesozoic accretionary margin: a study from the Coast belt of the North American Cordillera. Journal of metamorphic Geology, vol. 19, p. 121–137, https://doi.org/10.1046/j.0263-4929.2000.00300.x.

Morgan, P., Harder, V., Swanberg, C.A. and Daggett, P.H., 1981. Groundwater convection model for Rio Grande rift geothermal resources. *In:* Geothermal Direct Heat Program: Glenwood Springs Technical Conference Proceedings, Volume 1. Papers Presented State Coupled Geothermal Resource Assessment Program, p. 228–231, https://www.geothermal-library.org/index.php?mode=pubs&action=view&record=1013845.

Nelson, J. and Colpron, A., 2007. Tectonics and Metallogeny of the British Columbia, Yukon, and Alaskan Cordillera, 1.8 Ga to the Present. *In:* Mineral Deposits of Canada: A Synthesis of Major Deposit-Types, District Metallogeny, the Evolution of Geological Provinces, and Exploration Methods, W.D. Goodfellow (ed.), Geological Association of Canada, Special Publication No. 5, p. 755–791.

Odling, N.E., Gillespie, P., Bourgine, B., Castaing, C., Chiles, J.P., Christensen, N.P., Fillion, E., Genter, A., Olsen, C., Thrane, L., Trice, R., Aarseth, E., Walsh, J.J. and Watterson, J., 1999. Variations in fracture system geometry and their implications for fluid flow in fractured hydrocarbon reservoirs. Petroleum Geoscience, vol. 5, p. 373–384, https://doi.org/10.1144/petgeo.5.4.373.

Peacock, D.C.P., Sanderson, D.J. and Leiss, B., 2022. Use of Analogue Exposures of Fractured Rock for Enhanced Geothermal Systems. Geosciences, vol. 12, https://doi.org/10.3390/geosciences12090318.

Reinecker, J., Gutmanis, J., Foxford, A., Cotton, L., Dalby, C. and Law, R., 2021. Geothermal exploration and reservoir modelling of the United Downs deep geothermal project, Cornwall (UK). Geothermics, vol. 97, https://doi.org/10.1016/j.geothermics.2021.102226.

Ristau, J., Rogers, G.C. and Cassidy, J.F., 2007. Stress in western Canada from regional moment tensor analysis. Canadian Journal of Earth Sciences, vol. 44, p. 127–148, https://doi.org/10.1139/e06-057.

Saar, M., 2010. Review: Geothermal heat as a tracer of large-scale groundwater flow and means to determine permeability fields. Hydrogeology Journal, vol. 19, p. 31–52, https://doi.org/10.1007/s10040-010-0657-2.

Sanderson, D.J. and Peacock, D.C.P., 2019. Line sampling of fracture swarms and corridors. Journal of Structural Geology, vol. 122, p. 27–37, https://doi.org/10.1016/j.jsg.2019.02.006.

Singhal, B.B.S. and Gupta, R.P., 2010. Applied Hydrogeology of Fractured Rocks: Second Edition. Springer, https://doi.org/10.1007/978-90-481-8799-7.

Stanley, B., 2012. Structural geology and geochronology of the Kluane schist, southwestern Yukon Territory. Unpublished MSc thesis, University of Waterloo, Ontario, Canada, 113 p.

Štulc, P., 1998. Combined effect of topography and hydrogeology on subsurface temperature — implications for aquifer permeability and heat flow. A study from the Bohemian Cretaceous basin. Tectonophysics, vol. 284, p. 161–174, https://doi.org/10.1016/S0040-1951(97)00171-6.

Tang, H.M., Huang, L., Bobet, A., EzEldin, M.A.M., Wang, L.Q., Wu, Y.P. and Hu, X.L., 2016. Identification and mitigation of error in the Terzaghi Bias Correction for inhomogeneous material discontinuities. Strength of Materials, vol. 48, p. 825–833, https://doi.org/10.1007/s11223-017-9829-9.

Timar-Geng, Z., Henk, A. and Wetzel, A., 2009. Convective heat transfer in a steeply dipping fault zone and its impact on the interpretation of fission-track data – a modelling study. *In:* Thermochronological Methods: From Palaeotemperature Constraints to Landscape Evolution Models, Geological Society of London, Special Publications 324, p. 87–98. https://doi.org/10.1144/SP324.7.

Townend, J. Sutherland, R., Toy, V.G., Doan, M.L., *et al.*, 2017. Petrophysical, geochemical, and hydrological evidence for extensive fracture-mediated fluid and heat transport in the Alpine Fault's hanging-wall damage zone. Geochemistry, Geophysics, Geosystems, vol. 18, p. 4709–4732, https://doi.org/10.1002/2017GC007202.

Tschirhart, V., Colpron, M., Craven, J., Ghalati, F.H., Enkin, R.J. and Grasby, S.E. 2022. Geothermal Exploration in the Burwash Landing Region, Canada, Using Three-Dimensional Inversion of Passive Electromagnetic Data. Remote Sensing, vol. 14, https://doi.org/10.3390/rs14235963.

Vaughn, A., Collins, N., Krus, M. and Rourke, P., 2014. Recent Development of an Earth Science App – FieldMove Clino. EGU General Assembly 2014, Vienna, Austria, April 27–May 2, 2014.

Waldien, T.S., Roeske, S.M. and Benowitz, J.A., 2021. Tectonic underplating and dismemberment of the Maclaren-Kluane schist records Late Cretaceous terrane accretion polarity and ~480 km of post-52 Ma dextral displacement on the Denali fault. Tectonics, vol. 40, https://doi.org/10.1029/2020TC006677.

Watkins, H., Bond, C.E., Healy, D. and Butler, W.H., 2015. Appraisal of fracture sampling methods and a new workflow to characterise heterogeneous fracture networks at outcrop. Journal of Structural Geology, vol. 72, p. 67–82, https://doi.org./10.1016/j.jsg.2015.02.001.

Witter, J.B., 2020. Early-stage exploration for geothermal energy resources along the Denali fault near Duke River, Yukon. Yukon Geological Survey, Open File 2020-3, 62 p.

Yukon Geological Survey, 2020. A digital atlas of terranes for the northern Cordillera. Yukon Geological Survey, https://data.geology.gov.yk.ca/Compilation/2, [accessed November 20, 2022].

Yukon Geological Survey, 2022. Yukon Digital Bedrock Geology. Yukon Geological Survey, http://data.geology.gov.yk.ca/Compilation/3, [accessed October 22, 2022].

Zareidarmiyan, A. Parisio, F., Maknenko, R.Y., Salarirad, H. and Vilarrasa, V., 2021. How equivalent are equivalent porous media? Geophysical Research Letters, vol. 48, https://doi.org/10.1029/2020GL089163.

Zeeb, C., Gomez-Rivas, E., Bons, P.D. and Blum, P., 2013. Evaluation of sampling methods for fracture network characterization using outcrops. American Association of Petroleum Geologists Bulletin, vol. 97, p. 1545–1566, https://doi.org/10.1306/02131312042.

Appendix A

Nomenclature

s – number of scanlines

f – number of fracture measurements

S – spacing

a – fracture strike

a' – scanline strike

P – fracture position

L – scanline length

I – linear fracture intensity

N – number of fractures

H – number of fracture families

CV – coefficient of variation

MvM – Mixture von Mises

vM – von Mises

θ – strike (radians)

κ - concentration parameter

f – function

ω – weight

$NLlik$ – Negative Log-likelihood

Subscripts

i – initial/first measurement

f – final/last measurement

Appendix A continued.

The approach used to determine fracture families using a Mixture von Mises distribution (MvM) is based on Chabani et al. (2020). A Mixture of von Mises (MvM) distribution is the weighted sum of several von Mises (vM) distributions, where a von Mises distribution is described by:

$$\mathrm{f}(\theta|\mu,\kappa) = \frac{1}{2\pi I_0(\kappa)}\mathrm{e}^{\kappa\cos(\theta-\mu)} \qquad \text{(A1)}$$

where θ is the simplified strike in radians ($0 \leq \theta \leq \pi$; Eq. 2), μ is the circular mean ($0 \leq \mu \leq \pi$) and κ is the concentration parameter ($\kappa \geq 0$). The parameter $1/\kappa$ is analogous to the standard deviation (σ^2) in a normal distribution.

Here, all fracture strikes have been simplified to range between 0° and 180°, therefore when $a_\mathrm{i} > 180°$:

$$a = a_\mathrm{i} - 180 \qquad \text{(A2)}$$

where a_i is the initial azimuth and a is the simplified azimuth. All strikes must be converted to radians such that:

$$\theta = \frac{a2\pi}{180} \qquad \text{(A3)}$$

Within the von Mises distribution, $I_0(\kappa)$ is the modified Bessel function (Mardia and Jupp, 2000), given by:

$$I_0(\kappa) = \frac{1}{2\pi}\int_0^{2\pi}\mathrm{e}^{\kappa\cos\theta}\,d\theta \qquad \text{(A4)}$$

In multimodal data sets, the Mixture of Von Mises distribution considers H components such that each component is described by:

$$f_\mathrm{h}(\theta) = \frac{1}{2\pi I_0(\kappa_\mathrm{h})}\mathrm{e}^{\kappa_\mathrm{h}\cos(\theta-\mu_\mathrm{h})} \qquad \text{(A5)}$$

As the weighted sum of serval von Mises (vM) distributions, the Mixture of Von Mises distribution (MvM) is given by:

$$MvM_\mathrm{H}(\theta) = \sum_{\mathrm{h}=1}^{\mathrm{H}}\omega_\mathrm{h} f_\mathrm{h}(\theta) \qquad \text{(A6)}$$

where H is the number of components and ω_h is the weight of the h_th component.

The negative log-likelihood (NLlik) for each MvM with different number of components in each fracture category is determined by:

$$NLlik(\theta) = -\sum_{i=1}^{n}\log\left[\sum_{h=1}^{H}\omega_\mathrm{h} f_\mathrm{h}(\theta_\mathrm{i})\right] \qquad \text{(A7)}$$

Appendix B

Table B1. *Average values of the geometric attributes measured during, or calculated based on, the scanline surveys by lithology. CV: coefficient of variation.*

Lithology	Linear Intensity (m^{-1})		Spacing (CV)		Length (m)		Aperture (mm)	
(Open)	Median	S.D.	Mean	S.D.	Mean	S.D.	Mean	S.D.
Granodiorite Pluton	11.0	---	1.5	---	0.6	0.5	4.9	5.8
Kluane mafic-ultramafic	26.9	2.4	0.9	0.2	0.3	0.3	1.7	1.3
Nikolai formation	13.5	8.8	1.3	0.4	0.4	0.6	2.2	5.2
Station Creek Formation	32.4	17.4	1.2	0.3	0.2	0.2	1.5	1.9
Wrangell Lavas	11.6	---	1.0	---	0.3	0.2	2.7	3.0
Chitistone Limestone	5.6	---	1.6	---	0.4	0.3	3.0	1.9
Hasen Creek Formation	9.6	11.0	1.3	0.3	0.6	0.6	1.8	2.1
McCarthy Formation	16.9	5.2	1.2	0.2	0.5	0.4	2.0	1.5
Kluane schist	3.8	---	0.9	---	0.7	0.5	2.7	0.5

Table B2. *Average values of the geometric attributes measured during, or calculated based on, the scanline surveys by rock type: igneous and sedimentary. There are insufficient data to summarize metamorphic units. CV: coefficient of variation.*

Lithology	Linear Intensity (m^{-1})		Spacing (CV)		Length (m)		Aperture (mm)	
(Open)	Median	S.D.	Mean	S.D.	Mean	S.D.	Mean	S.D.
Igneous	18.7	15.2	1.2	0.3	0.4	0.2	2.6	1.4
Sedimentary	10.6	9.5	1.3	0.3	0.5	0.1	2.3	0.6

Improvements in the regional earthquake focal mechanism catalogue for southwestern Yukon

Jeremy M. Gosselin*, Katherine Biegel, Mahdi Hamidbeygi and Jan Dettmer
Department of Geoscience, University of Calgary

Gosselin, J.M, Biegel, K, Hamidbeygi, M. and Dettmer, J., 2023. Improvements in the regional earthquake focal mechanism catalogue for southwestern Yukon. *In:* Yukon Exploration and Geology 2022, K.E. MacFarlane (ed.), Yukon Geological Survey, p. 63–76 plus digital appendices.

Abstract

Earthquake source characteristics provide a valuable constraint on fault behaviour, crustal stress, and regional plate tectonics. In southwestern Yukon, a region of complex active tectonics, studies of earthquake sources have historically been limited by sparse seismic network coverage. In this work, we leverage recent improvements in station coverage to estimate focal mechanisms for small and moderate-magnitude ($M \geq 2.0$) earthquakes from P-wave first-motion polarity data. We invert these data using a probabilistic method that rigorously quantifies mechanism uncertainties. We present preliminary solutions for 363 events, which improve the spatial coverage of the focal mechanism catalogue for this region. We observe contrasting P-axis orientations for events on either side of the Fairweather fault. For events within southwestern Yukon, the distribution of faulting mechanism types and P-axis orientations are relatively consistent. Our focal mechanism solutions support the existence of an unmapped fault south of the Duke River fault. Finally, our results provide a valuable input for subsequent detailed analysis of crustal stress throughout the region.

---

* jeremy.gosselin@ucalgary.ca

Introduction

Tectonic setting

Southwestern Yukon is a region of complex active tectonics, where strike-slip motion along the Queen Charlotte-Fairweather fault system transitions to oblique convergence of the Pacific plate (and Yakutat block/microplate) with the North American plate (Leonard *et al.*, 2007). This convergence is partitioned between the Aleutian trench subduction system and a series of right-lateral crustal strike-slip fault systems (Fig. 1), with oblique convergence of the Pacific plate (relative to North America) occurring at a rate of approximately 57 mm/yr (Kreemer et *al.*, 2014). In southeastern Alaska and Yukon, plate motion is accommodated by deformation along the Denali fault and associated nearby fault systems, including thrusting and uplift of the St. Elias Mountains.

The arcuate Denali fault system extends over 2000 km from British Columbia, through Yukon and central Alaska, and ultimately to the Bering Sea (Fig. 1 inset). The Denali fault represents a geological boundary between the accreted Insular and Intermontane terranes of the North American Cordillera (Nelson et *al.*, 2013), and has experienced total right-lateral displacement of approximately 400 to 480 km (Lowey, 1998; Waldien et *al.*, 2021). Topography, geodetic constraints, and Quaternary fault mapping suggest that the Central Denali fault (also called the McKinley segment; through central Alaska) is more tectonically active compared to the Eastern Denali fault that extends through Yukon (*e.g.*, Haeussler et *al.*, 2008; Bemis et *al.*, 2015; Marechal et *al.*, 2015, 2018). The Eastern Denali fault includes the Shakwak segment that intersects the Totschunda fault, as well as the southernmost Dalton segment that extends southward to the Chatham Strait (Grantz, 1966). Slip rates along the Denali fault are estimated to decrease eastward from approximately 12 mm/yr along the central section, to 5–8.4 mm/yr along the Shakwak segment, and 1–2.5 mm/yr along the Dalton segment (*e.g.*, Matmon et *al.*, 2006; Leonard et *al.*, 2007, 2008; Kalbas et *al.*, 2008; Elliott et *al.*, 2010).

The 2002 M 7.9 Denali earthquake ruptured portions of the Central Denali fault before propagating southeastward along the Totschunda fault, instead of continuing along the Eastern Denali fault (Eberhart-Phillips et *al.*, 2003). Paleoseismic investigations along the Eastern Denali fault suggest multiple large (M >6) earthquakes have occurred over the last several thousand years (Blais-Stevens et *al.*, 2020). Furthermore, records of the largest dextral motion along the Denali fault are from the eastern segments (Lowey, 1998; Haeussler et *al.*, 2008). This suggests that the Eastern Denali fault played an important role in terrane assembly through geologic history and may have experienced local deformation. Yet, the Eastern Denali fault is currently seismically quiescent, and recent studies have proposed that it serves as a regional stress boundary while active deformation occurs farther westward (*e.g.*, Choi et *al.*, 2021). This is further supported by the hypothesis of an unmapped ‘connector fault’ that links the Fairweather and Totschunda faults and transfers strain between them (Richter and Matson, 1971; Lahr and Plafker, 1980; Doser, 2014). This structural feature is required to explain spatial variations in the direction and deformation rate observed from GPS measurements (*e.g.*, Elliott and Freymueller, 2020). Lastly, geodynamic modelling (Jadamec et *al.*, 2013) suggests the Denali fault system is a major geological boundary spanning from the surface through the entire lithosphere, and is required to explain deformation in south-central Alaska (the Wrangell block).

Seismicity

Understanding modern seismicity provides a valuable constraint on fault behaviour, crustal stress and regional plate tectonics. Yet, studies on seismicity in southwestern Yukon have historically been limited by the sparse seismic network coverage throughout the region (Fig. 1). This is a consequence of the inaccessibility of the terrain, which is largely at high elevation and covered by ice. In 2010, network coverage in southwestern Yukon improved from effectively no broadband stations to more than 10, which decreased the minimum magnitude of catalogue completeness (in certain regions) from ~3.0 to ~1.0 (Meighan et *al.*, 2013). Since 2016, station coverage throughout the region has further improved with the deployment of large campaign experiments such as the Earthscope Transportable Array deployment in

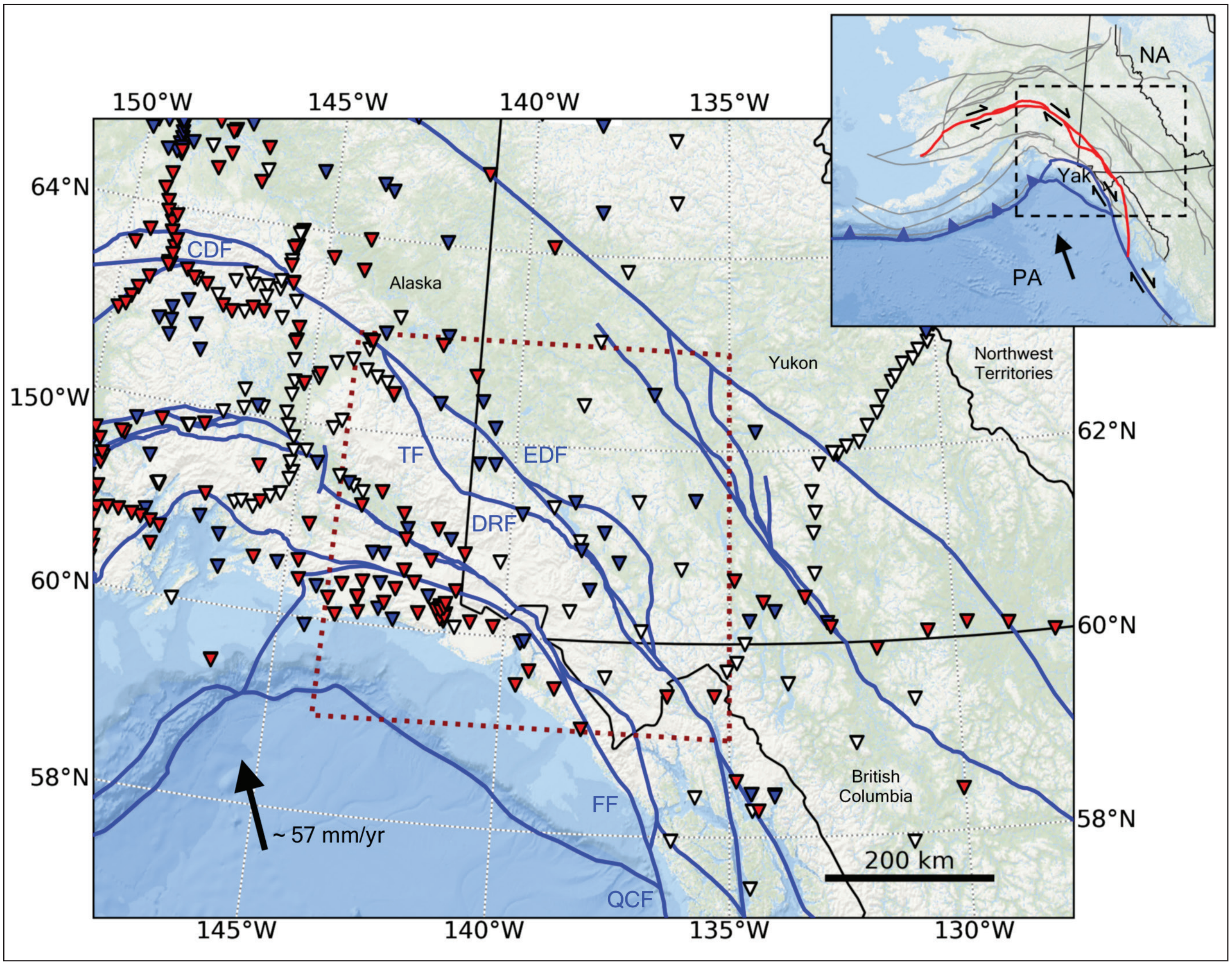

Figure 1. *Regional tectonic setting and seismic station coverage. Permanent and temporary broadband seismic stations shown are coloured according to deployment date: prior to 2010 (red); between 2010 and 2016 (blue); and after 2016 (white). Note the relatively sparse broadband seismic station coverage in Yukon. Major faults are shown as blue lines (after Yukon Geological Survey, 2020). Faults discussed in the text are labelled: Central Denali fault (CDF); Eastern Denali fault (EDF); Totschunda fault (TF); Duke River fault (DRF); Fairweather fault (FF); Queen Charlotte fault (QCF). The red dashed box defines the study area shown in Figure 3. The inset map provides large-scale tectonic context of the interaction between the Pacific plate (PA), North American plate (NA), and Yakutat microplate (Yak). Plate boundaries are shown in blue. The Denali fault and associated faults discussed in the text are shown in red. Other major faults are shown in grey. Black arrow in both maps illustrates the plate vector and velocity of PA relative to NA (Kreemer et al., 2014).*

Alaska and western Yukon (Busby and Aderhold, 2020), and the Earthscope Mackenzie Mountains Transect (Baker et *al.*, 2020). These further decreased the minimum magnitude of earthquake detection by 0.25–0.5 units in southwestern Yukon (Ruppert and West, 2020). These seismic station network improvements have also improved systematic earthquake location (horizontal) errors by up to tens of kilometres (Meighan et *al.*, 2013).

Previous investigations on seismicity in this region have focused on local scales (*e.g.*, Power, 1988), considered relatively large events recorded by distant stations (*e.g.*, Horner, 1983; Doser, 2000, 2004; Doser and Rodriguez, 2011), or investigated nearby aftershock sequences (*e.g.*, Doser, 2012). Seismological constraints on crustal stress necessitates analysis of earthquake source characteristics, including focal mechanisms and moment tensors. Such quantified stress estimates are sparse in southwestern Yukon (Heidbach et *al.*, 2018). Most studies on earthquake source characteristics in the region predate seismic station network improvements, and so generally only consider few of the largest events (*e.g.*, Risteau et *al.*, 2007; Kao et *al.*, 2012; Doser, 2014). The global centroid moment tensor catalogue (Ekström et *al.*, 2012) includes more than 30 events in southwestern Yukon (and surrounding regions) since 1980. The earthquake focal mechanism catalogue of the International Seismological Centre (ISC; Lentas et *al.*, 2019) currently provides the most complete source characteristics catalogue, with over 123 events in the region since 2000. In general, seismicity throughout the region is dominated by reverse and dextral strike-slip faulting. In particular, seismicity is concentrated near the Duke River fault which exhibits mostly reverse faulting (*e.g.*, Doser, 2014). The Central Denali fault and the northern extent of the Totschunda fault also exhibit abundant seismicity.

Improvements in seismic station network coverage over the last decade have significantly improved earthquake catalogues in southwestern Yukon. Yet, detailed seismological constraints on the crustal stress field throughout the region necessitate additional earthquake source mechanism estimates, with greater spatial coverage. In this report, we use P-wave first-motion polarities to probabilistically invert for focal mechanisms of small and moderate-magnitude earthquakes in southwestern Yukon and surrounding regions. We present an updated earthquake focal mechanism catalogue with 363 new events, and significantly improve spatial coverage. This work is part of a larger, multi-year study of natural hazards and geothermal resource potential in Yukon. The estimation of shallow Curie point depths (*e.g.*, Li et *al.*, 2017), the mapping of radiogenic rocks (*e.g.*, Friend and Colpron, 2017; Colpron, 2019), and the presence of warm water springs (*e.g.*, Langevin et *al.*, 2020) suggest locations in Yukon may represent ideal targets for geothermal resources development. Results from this study will enable more detailed examination of the current behaviour of the Eastern Denali fault, and surrounding fault systems. This can be used to help assess natural hazards of the region as well as to estimate rock permeability near (and within) these systems, which is valuable for targeted geothermal exploration.

Data and methods

For this study, we use earthquakes reported in the United States Geological Survey (USGS) catalogue as our study region spans part of southeastern Alaska. Specifically, we consider all events between 2016 and 2022 within our study region (dashed red box shown in Fig. 1) with M ≥3.0 and depth ≤30 km for focal mechanism estimation. Given the limited seismicity along the Eastern Denali fault, we extend our search criteria for candidate earthquakes to include all events within 50 km of the surface trace of the Eastern Denali fault between 2010 and 2022 with M≥2.0. For selected events, vertical-channel waveform data were retrieved for all seismic stations within 450 km epicentral distance. After applying a 1Hz high-pass filter, first-motion polarities (*i.e.*, dilatational or compressional) were manually selected for stations with clear P-wave arrival onsets. Azimuth and takeoff angles were calculated using ray propagation through the standard velocity model used by the USGS for southeastern Alaska (Fogleman et *al.*, 1993). Finally, polarities were inverted to estimate earthquake focal mechanisms within a Bayesian (probabilistic) framework using recent improvements (Hamidbeygi, 2022) to the Bayesian Earthquake Analysis Tools (BEAT) software (Vasyura-Bathke et *al.*, 2020.

Understanding and quantifying the uncertainties in estimated earthquake focal mechanisms allows for more reliable interpretations of fault behaviour and, ultimately, regional tectonics. Bayesian inversion offers a means of rigorous model parameter uncertainty quantification, and its use in seismic source studies is established (see Vasyura-Bathke et *al.*, 2020). Within a Bayesian inversion framework, model parameters and data are treated as random variables. The model parameters (strike, dip and rake of the focal mechanism) are constrained by data (P-wave polarities) as well as prior information. This can be informative (thereby providing additional constraint) or uninformative (allowing the solution to be predominantly constrained by data information). Specifically, Bayesian inversion updates the prior knowledge of the model parameters using data to determine the posterior probability density (PPD) of the model parameters, which represents the solution to the inverse problem (Jaynes, 2003).

These are related through Bayes' theorem, which is given by:

$$P(\boldsymbol{m}|\boldsymbol{d}) = \frac{P(\boldsymbol{m})P(\boldsymbol{d}|\boldsymbol{m})}{P(\boldsymbol{d})} \tag{1}$$

where $\boldsymbol{m}$ and $\boldsymbol{d}$ are vectors of model parameters and data, respectively. $P(\boldsymbol{m})$ is the prior probability density of the model parameters, independent of the data. In this study, priors are uniform distributions bounded by the physical limits of strike, dip and rake (*i.e.*, uninformative). $P(\boldsymbol{m}|\boldsymbol{d})$ is the conditional probability of the model parameters given the data, which is the PPD. Conversely, is the conditional probability of the data given the model parameters. In practice, once the data are measured/observed they represent a fixed realization of a random variable. In which case, this conditional probability represents the likelihood $L(\boldsymbol{m})$ that a set of model parameters can reproduce the observed data. $P(\boldsymbol{d})$ provides a normalization independent of the model parameters and is not required to be known for the purpose of this study (MacKay, 2003).

Assuming the data residuals (differences between observed and predicted data) to be a representation of data errors, a likelihood function can be formulated by assuming their statistical distribution (given the model). The likelihood function implemented in BEAT for the inversion of P-wave polarity data assigns higher probability to arrivals that have a greater theoretical amplitude, depending on their location on the focal sphere (Brillinger et *al.*, 1980). This is chosen as P-wave polarity data that are located near mechanism planes theoretically have smaller amplitudes and are likely to be less reliable due to potential modelling errors in azimuths and takeoff angles (due to inaccurate velocity models, event hypocentres, etc.). Furthermore, it stands to reason that higher amplitude P-wave arrivals provide more reliable (higher signal-to-noise ratio; SNR) waveforms for first-motion polarity assignment.

Specifically, this likelihood is the product of probabilities (for independent polarity data) given by:

$$L(\boldsymbol{m}) = \prod_{i=1}^{N} \pi_i^{\frac{(1+d_i)}{2}} (1-\pi_i)^{\frac{(1-d_i)}{2}} \tag{2}$$

where d_i is the polarity datum at station i, and π_i is given by:

$$\pi_i = \gamma + (1-2\gamma)\phi\left(\frac{A_i(\boldsymbol{m})}{\sigma}\right). \tag{3}$$

Here, $\phi(\cdot)$ is the cumulative distribution function of the normal distribution, which provides an estimate of polarity probability given a theoretical amplitude $A_i(\boldsymbol{m})$ and modelling error standard deviation σ (where $\sigma > 0$). Lastly, defines the probability that the polarity has been assigned incorrectly $(0 \geq \gamma \geq 0.5)$, and can be considered small for high SNR data. In this work, we treat as a hyper-parameter that is estimated as part of the inversion. We define a uniform prior on σ, bounded between 0 and 0.2. This provides a flexible representation of data errors, which is solved for as part of the inversion. We assume a conservative probability of incorrect polarity assignment of 0.2 (value for γ) that enables additional flexibility in the error model.

In general, it is challenging (and sometimes impossible) to determine an analytical solution for the PPD (Equation 1). Instead, numerical methods are used to draw samples from the PPD. The ensemble of samples can then be used as an approximation of the PPD to estimate its properties. The inversion method implemented in BEAT, and used in this study, estimates the PPD via a sequential Monte Carlo sampler (Del Moral et *al.*, 2006). The samples are independent and based on a sequence of intermediate distributions (*i.e.*, stages) that transition between the prior and posterior, controlled by a scaling parameter. Depending on the choice of prior, this implementation allows for wide (unrestricted) initial exploration of the parameter space, which then becomes more constrained by the data (via the likelihood function) as the inversion progresses towards the posterior. All inversions in this work are run with 2000 sampling chains with 300 steps each. The number of sequential stages is adapted according the polarity data set for each inversion (typically <5);

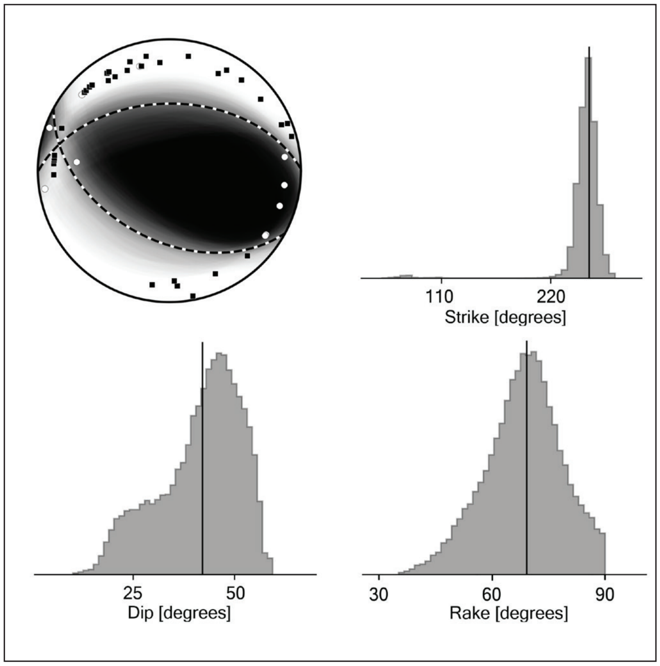

Figure 2. *An example of Bayesian focal mechanism inversion from polarity data. Inversion results are shown for an M3.6 event that occurred on February 28, 2017. The 'fuzzy beachball' is shown for an ensemble of 200 focal mechanisms drawn from the posterior probability density (top left). White circle and black squares represent positive and negative polarity data, respectively, located at the modelled azimuth and take-off angles. The marginal posterior distributions are also shown for the strike, dip and rake of one of the mechanism planes. Vertical lines in the marginal distribution plots identify the location of the maximum probability model. The geographic location of this earthquake is shown in Figure 3.*

see Del Moral et *al.* (2006) and Vasyura-Bathke et *al.* (2020) for details. BEAT is a highly flexible program that can consider many additional parameters (*e.g.*, corrections to hypocentre locations), more complex source types, as well as other seismic and geodetic data types (*e.g.*, waveforms). Future research directions include comprehensive use of BEAT capabilities for data from southwestern Yukon, as well as improvements to BEAT for polarity data inversion.

Figure 2 shows an example of the results of Bayesian focal mechanism inversion of P-wave polarity data for an M 3.6 earthquake that occurred on February 28, 2017. A focal mechanism solution is typically represented graphically by a 'beachball' diagram that is a stereonet projection of the lower half of the focal sphere. The advantage of Bayesian inversion is rigorous uncertainty quantification. In this case, uncertainty in the focal mechanism solution is visually represented by a 'fuzzy beachball' diagram, which is estimated from samples drawn from the PPD (in this case 200 samples). If the diagram is a sharp image, it implies the PPD is more localized in the model parameter space (*i.e.*, smaller uncertainty). Figure 2 also shows the marginal posterior distributions for the individual focal mechanism parameters (strike, dip and rake of one of the mechanism planes), which reveal the uncertainty in these parameters. The geographic location of the earthquake used in this example is shown in Figure 3.

Results and discussion

We performed Bayesian focal mechanism inversions for events with a minimum of 10 polarity observations. In total, we present focal mechanism inversion results for 363 events in southwestern Yukon and the surrounding region. Figure 3 summarizes our updated focal mechanism catalogue by showing the P-axis (pressure) trends for the maximum probability focal mechanism model from each inversion, coloured according to event faulting type (as defined by Kaverina et *al.*, 1996, and Álvarez-Gómez, 2019). It is well known that P-wave first-motion polarity data provide no information to constrain which of the two nodal planes in each focal mechanism is the actual fault plane. Furthermore, the P-axis of a focal mechanism is a geometrical property related to an individual earthquake, whereas the vector of principle crustal stress applies to a volume of rock, and can activate faults with a variety of geometries (McKenzie, 1969). Specifically, the principle stress vector lies within the pressure quadrant of an individual focal mechanism (McKenzie, 1969). Despite these limitations, examination of P-axis trends provides insight into the behaviour of regional seismicity and individual fault structures, as well as a first-order understanding of crustal stress.

Along the Eastern Denali fault (and Duke River fault), we observe relatively consistent southwest-trending P-axis orientations, with a slight rotation to a more south-southwest (or even south) orientation for events located farther toward the northwest, particularly along the western segment of the Duke River fault. Events to the southwest of the Fairweather fault system

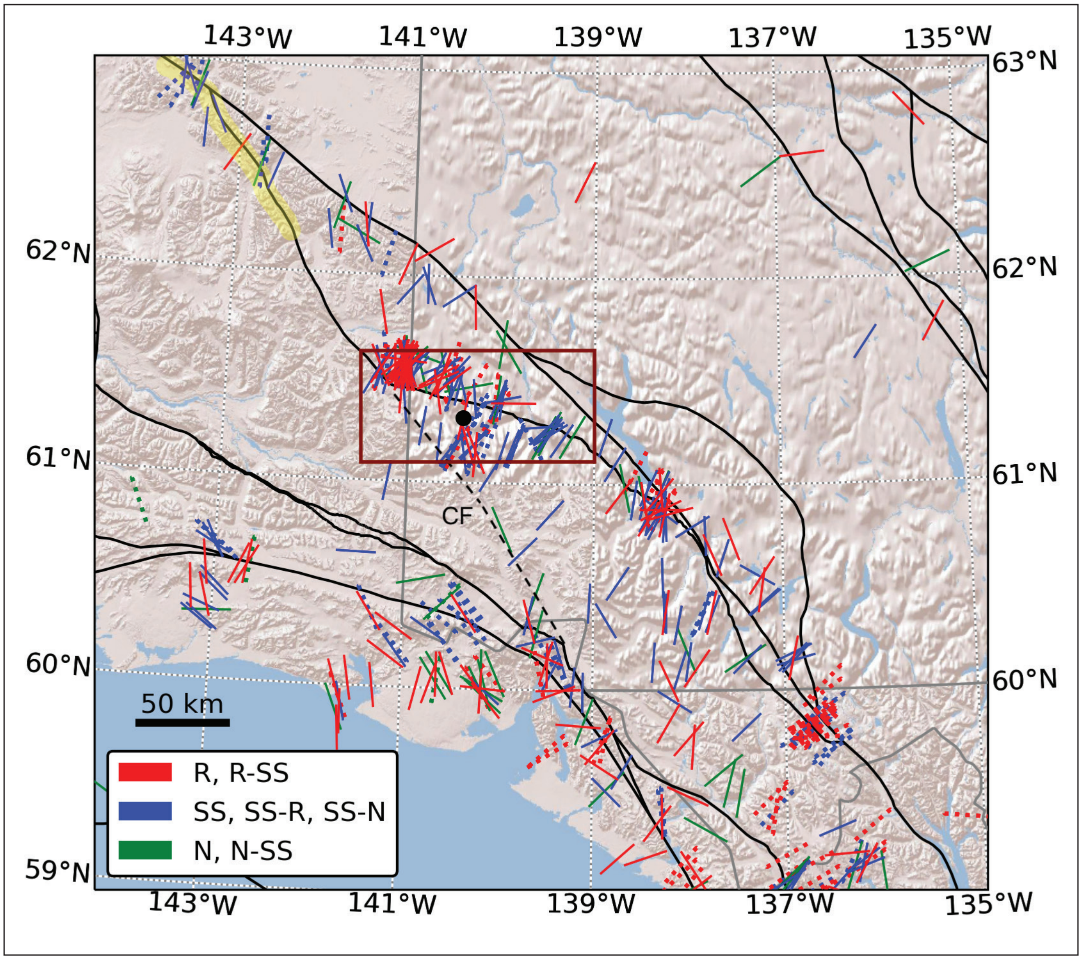

Figure 3. *Updated earthquake focal mechanism catalogue for the SW Yukon. P-axis trends are shown for all focal mechanism estimates, coloured according to faulting mechanism classification (abbreviations for mechanism types as in Fig. 5). Dashed P-axis trends are from the ISC catalogue (between 2000 and 2022; Lentas et al., 2019). The location of the February 28, 2017 event (Fig. 2) is shown by the black circle. The boundary of the map shown in Figure 6 is delineated by the dark red box. The surface traces of major faults are shown as black lines (after Yukon Geological Survey, 2020). The dashed black line illustrates the postulated Connector fault (CF). The approximate rupture of the 2002 Denali earthquake is highlighted in yellow (after Eberhart-Phillips et al., 2003).*

exhibit P-axis orientations that are predominantly south-trending or rotated to southeasterly trends (Fig. 4), potentially indicating distinct stress orientations on either side of this fault system.

The ternary plot (Kaverina et *al.*, 1996; Álvarez-Gómez, 2019) shown in Figure 5 indicates that our results consist mostly of a mixture of reverse and strike-slip faulting mechanisms. We also observe this general combination of faulting mechanisms spatially (Fig. 3), but note few, localized normal-faulting events. Furthermore, we note that the majority of the focal mechanism solutions are reported for events clustered near the Duke River fault, as well as an apparent (geologically) unmapped fault south of the Duke River fault. This focus region is highlighted in Figure 6. Specifically, we note that the Duke River fault exhibits predominantly reverse mechanisms with P-axes trending south-southwest, while the unmapped fault trace appears to be west-southwestward oriented and it exhibits predominantly strike-slip faulting with P-axes trending to the southwest. This is likely a continuation of a fault mapped at lower elevations to the northwest (e.g., Dodds and Campbell, 1992) that exhibit seismicity beneath the St. Elias icefields.

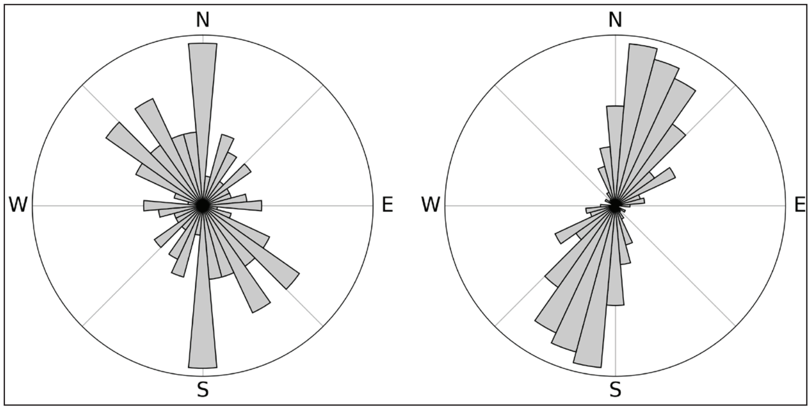

Figure 4. Regional P-axis trends from focal mechanisms estimated for events located southwest of the Fairweather fault system (left) and northeast of the Fairweather fault system (right).

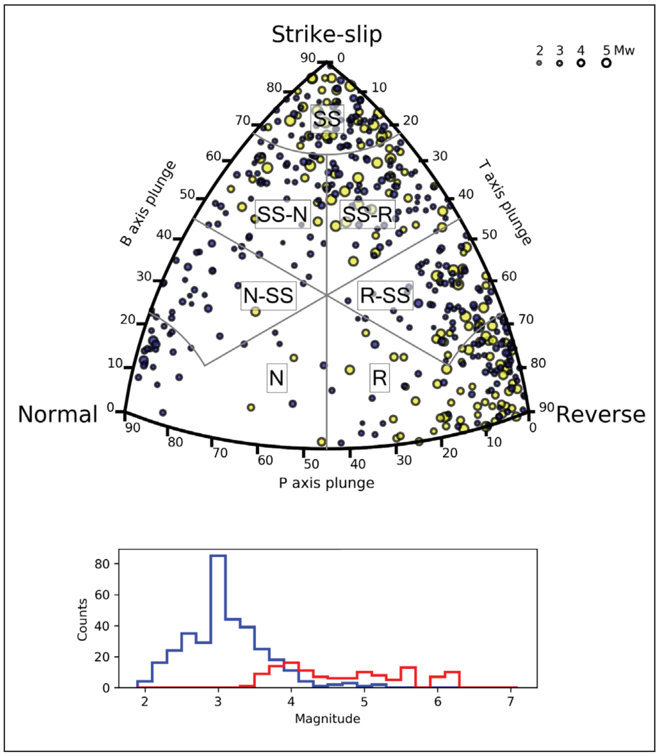

Figure 5. Focal mechanism distributions for southwestern Yukon. Earthquake faulting mechanism types are shown on the ternary diagram (top), with corresponding mechanism classification boundaries (Kaverina et al., 1996; Álvarez-Gómez, 2019). Dark blue and yellow circles represent focal mechanisms from this study and the ISC catalogue (between 2000 and 2022; Lentas et al., 2019), respectively. P and T axes refer to pressure and tension axes, respectively. The B axis is the intersection of the focal mechanism nodal planes, and is normal to the P and T axes. The distribution of earthquake magnitudes considered for focal mechanism estimation is shown (bottom) for the ISC catalogue (red) and this study (blue).

Of note, Meighan et *al.* (2013) and Doser (2014) identified a band of seismicity south of the Duke River fault, which is likely the same unmapped feature discussed above. Seismicity also suggests the westernmost Duke River fault may be connected to this unmapped feature via a south-oriented fault; potentially the 'connector fault' that connects farther south with the Fairweather fault system. Limited focal mechanism estimates (Figs. 3 and 6) suggest consistent strike-slip faulting on this feature. Meighan et *al.* (2013) and Doser (2014) also identified a westward-oriented band of seismicity between the Totschunda fault and Eastern Denali fault, above 62° northern latitude (Fig. 3). Our results suggest a mixture of mostly strike-slip and reverse faulting here. Interestingly, this feature intersects the Totschunda fault near the rupture terminus of the 2002 Denali earthquake (Doser, 2014), suggesting a possible avenue for strain transfer that circumvents the southern Totschunda fault (Fig. 3).

Focal mechanism estimates from the ISC catalogue between 2000 and 2022, for our study region, are also shown in Figures 3, 5 and 6 (Lentas et *al.*, 2019). We note that this catalogue only consists of the largest events in the region over the last 2 decades. By comparison, the results presented in this work include focal mechanisms for smaller events over a shorter time period (of significantly improved seismic station spatial coverage), that has allowed us to improve the total focal mechanism catalogue for southwestern Yukon by approximately a factor of 4 (Fig. 5). We also note an improvement in focal mechanism spatial coverage throughout the region (Fig. 3). Lastly, the localized consistency between the results presented here and the ISC catalogue (Figs. 3 and 6) lend confidence in our analysis.

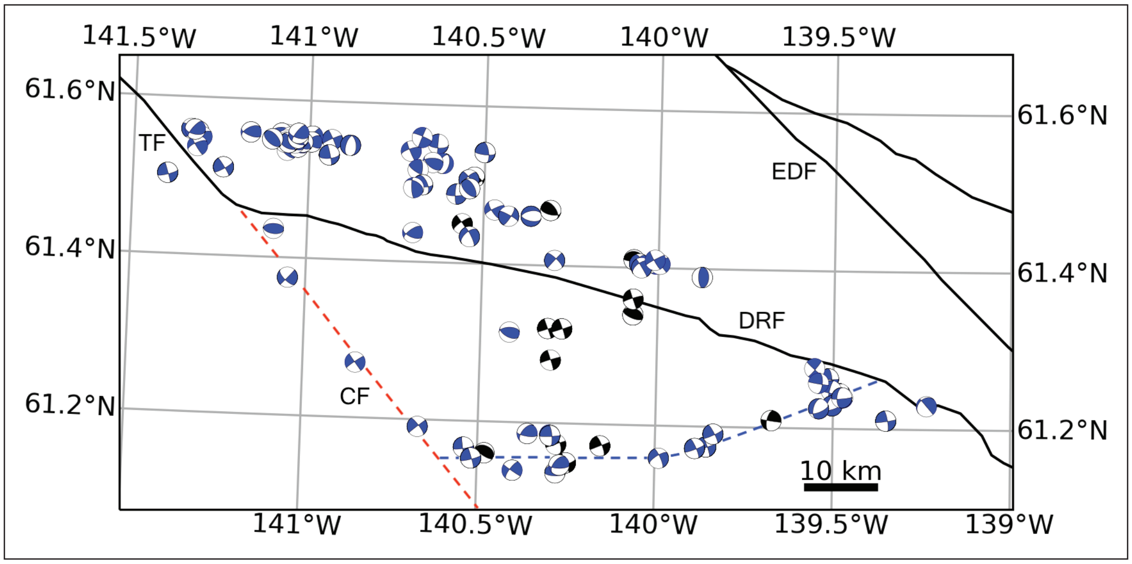

Figure 6. *Earthquake focal mechanism solutions near the Duke River fault (DRF). Solutions from this study and the ISC catalogue (between 2000 and 2022; Lentas et al., 2019) are shown as blue and black beachball diagrams, respectively. The boundary of this map is shown in Figure 3. The surface traces of major faults are shown as black lines (after Yukon Geological Survey, 2020), including: the Totschunda fault (TF), the DRF, and the Eastern Denali fault (EDF). The red dashed line illustrates the postulated Connector fault (CF), and the blue dashed line illustrated the unmapped fault discussed in the text.*

A future research objective includes further refinement of the regional focal mechanism catalogue for southwestern Yukon. Specifically, we intend to use a relocated event catalogue (Biegel et *al.*, 2023) to update event hypocentres and more-accurately model azimuths and take-off angles. It has recently been demonstrated that centroid moment tensors for small earthquakes (~M 1.0) can be estimated via joint inversion of multiple seismic data types including P-wave first-motion polarities, amplitude spectra, and low-frequency waveforms (Hamidbeygi, 2022). We intend to augment our catalogue of earthquake source characteristics by analyzing smaller events in regions within southwestern Yukon where few events occur that are large enough for reliable focal mechanism estimation from polarity data alone. Furthermore, we have recently deployed seismic stations at several focus areas throughout southern Yukon with the aim of improving seismicity catalogues, including estimating event source characteristics, in order to help in the assessment of natural hazards and geothermal resource potential at these locations. Finally, we intend to use our estimated focal mechanism catalogue, with associated uncertainty, as input for the inversion of regional crustal stress (e.g., Arnold and Townend, 2007; Herrera et *al.*, 2021). Stress analysis from individual geographical clusters of earthquakes will allow us to quantify how stress varies spatially through this complex tectonic environment.

Conclusions

Southwestern Yukon is a region of complex active tectonics, with historically sparse seismic station coverage. We leverage recent improvements in station coverage over the last decade to estimate focal mechanisms for smaller earthquakes than those that are routinely considered throughout the region. We employ a Bayesian (probabilistic) inversion method to estimate focal mechanism parameters, and rigorously quantify uncertainty, for 363 events. Examination of the spatial variability of faulting types and orientations reveals consistent mechanism throughout the region, with the majority of events exhibiting reverse and strike-slip faulting. We observe a contrast in P-axis orientation for events northeast vs. southwest of the Fairweather fault system, potentially suggesting different stress regimes. Furthermore, we observe a rotation in P-axis orientations along strike of the Eastern Denali and Duke River fault systems. Our results provide additional constraints on the faulting behaviour of features previously identified from regional seismicity.

Our results are also consistent with previous studies of earthquake source characteristics in the region, and provide an improvement in overall constraint and spatial coverage that will enable more-detailed analysis of regional active tectonics. The results presented here represent a preliminary update to the regional focal mechanism catalogue. Future work will aim to further refine and augment this catalogue.

Acknowledgements

This work is supported by the Natural Science and Engineering Research Council (Canada) through a Postdoctoral Fellowship to Jeremy M. Gosselin and a Discovery Grant to Jan Dettmer, and by the Yukon Geological Survey through funding from Natural Resources Canada's Emerging Renewal Power Program and the Yukon government's *Our Clean Future* initiative. We thank Kluane First Nation for their support of this research. All seismic data used in this work are freely available for download through the international Federation of Digital Seismograph Networks (FDSN) Web Services of the facilities of the Incorporated Research Institutions for Seismology (IRIS; https://service.iris.edu/). Data were downloaded and processed using ObsPy (Beyreuther *et al.*, 2010), and polarities were manually assigned using Pyrocko/Snuffler (Heimann *et al.*, 2017). We thank Carlos Herrera for useful early discussions on focal mechanism inversion, and Maurice Colpron for helpful comments that improved this manuscript. We thank Clément Estève for a constructive critical review of this work. Tabulated focal mechanism solutions are available (Appendix 1) for download alongside this manuscript.

References

Álvarez-Gómez, J.A., 2019. FMC—Earthquake focal mechanisms data management, cluster and classification. SoftwareX, vol. 9, p. 299–307, https://doi.org/10.1016/j.softx.2019.03.008.

Arnold, R. and Townend, J., 2007. A Bayesian approach to estimating tectonic stress from seismological data. Geophysical Journal International, vol. 170, no. 3, p. 1336–1356, https://doi.org/10.1111/j.1365-246X.2007.03485.x.

Baker, M.G., Heath, D.C., Schutt, D.L., Aster, R.C., Cubley, J.F. and Freymueller, J.T., 2020. The Mackenzie Mountains EarthScope Project: Studying active deformation in the northern North American Cordillera from margin to craton. Seismological Research Letters, vol. 91, no. 1, p. 521–532, https://doi.org/10.1785/0220190139.

Beyreuther, M., Barsch, R., Krischer, L., Megies, T., Behr, Y. and Wassermann, J., 2010. ObsPy: A Python toolbox for seismology. Seismological Research Letters, vol. 81, p. 530–533, https://doi.org/10.1785/gssrl.81.3.530.

Biegel, K., Gosselin, J. and Dettmer, J., 2023. Preliminary double-difference relocation catalogue of southwestern Yukon centred along the Denali fault zone. *In:* Yukon Exploration and Geology 2022, K.E. MacFarlane (ed.), Yukon Geological Survey.

Bemis, S.P., Weldon, R.J. and Carver, G.A., 2015. Slip partitioning along a continuously curved fault: Quaternary geologic controls on Denali fault system slip partitioning, growth of the Alaska Range, and the tectonics of south-central Alaska. Lithosphere, vol. 7, p. 235–246, https://doi.org/10.1130/L352.1.

Blais-Stevens, A., Clague, J.J., Brahney, J., Lipovsky, P., Haeussler, P.J. and Menounos, B., 2020. Evidence for large Holocene earthquakes along the Denali fault in southwest Yukon, Canada. Environmental and Engineering Geoscience, vol. 26, p. 149–166, https://doi.org/10.2113/EEG-2263.

Brillinger, D.R., Udias, A. and Bolt, B.A., 1980. A probability model for regional focal mechanism solutions. Bulletin of the Seismological Society of America, vol. 70, p. 149–170, https://doi.org/10.1785/BSSA0700010149.

Busby, R.W. and Aderhold, K., 2020. The Alaska transportable array: As built. Seismological Research Letters, vol. 91, p. 3017–3027, https://doi.org/10.1785/0220200154.

Choi, M., Eaton, D.W. and Enkelmann, E., 2021. Is the Eastern Denali fault still active? Geology, vol. 49, p. 662–666, https://doi.org/10.1130/G48461.1.

Colpron, M., 2019. Potential radiogenic heat production from granitoid plutons in Yukon. Yukon Geological Survey, Open File 2019-16.

Del Moral, P., Doucet, A. and Jasra, A., 2006. Sequential monte carlo samplers. Journal of the Royal Statistical Society: Series B (Statistical Methodology), vol. 68, p. 411–436.

Dodds, C.J. and Campbell, R.B., 1992. Geology of SW Kluane Lake Map Area (115G and F (E 1/2)) southwestern Yukon (1:250 000 scale). Geological Survey of Canada, Open File 2188.

Doser, D.I., 2004. Seismicity of the Denali–Totschunda fault zone in central Alaska (1912–1988) and its relation to the 2002 Denali fault earthquake sequence. Bulletin of the Seismological Society of America, vol. 104, p. S132–S144, https://doi.org/10.1785/0120040611.

Doser, D.I., 2012. Revisiting the 1979 St. Elias, Alaska, aftershock sequence and its regional significance. Bulletin of the Seismological Society of America, vol. 102, p. 2392–2404, https://doi.org/10.1785/0120120007.

Doser, D.I., 2014. Seismicity of southwestern Yukon, Canada, and its relation to slip transfer between the Fairweather and Denali fault systems. Tectonophysics, vol. 611, p. 121–129, https://doi.org/10.1016/j.tecto.2013.11.018.

Doser, D.I. and Lomas, R., 2000. The transition from strike-slip to oblique subduction in south- eastern Alaska from seismological studies. Tectonophysics, vol. 316, p. 45–65, https://doi.org/10.1016/S0040-1951(99)00254-1.

Doser, D.I. and Rodriguez, H., 2011. A seismotectonic study of the southeastern Alaska region. Tectonophysics, vol. 497, p. 105–113, https://doi.org/10.1016/j.tecto.2010.10.019.

Eberhart-Phillips, D., Haeussler, P.J., Freymueller, J.T., Frankel, A.D., Rubin, C.M., Craw, P., ... and Wallace, W.K., 2003. The 2002 Denali fault earthquake, Alaska: A large magnitude, slip-partitioned event. Science, vol. 300, p. 1113–1118, https://doi.org/10.1126/science.1082703.

Ekström, G., Nettles, M. and Dziewoński, A.M., 2012. The global CMT project 2004–2010: Centroid-moment tensors for 13,017 earthquakes. Physics of the Earth and Planetary Interiors, vol. 200, p. 1–9, https://doi.org/10.1016/j.pepi.2012.04.002.

Elliott, J.L., Larsen, C.F., Freymueller, J.T. and Motyka, R.J., 2010. Tectonic block motion and glacial isostatic adjustment in southeast Alaska and adjacent Canada constrained by GPS measurements. Journal of Geophysical Research: Solid Earth, vol. 115, B09407, https://doi.org/10.1029/2009JB007139.

Elliott, J. and Freymueller, J.T., 2020. A block model of present-day kinematics of Alaska and western Canada. Journal of Geophysical Research: Solid Earth, vol. 125, e2019JB018378, https://doi.org/10.1029/2019JB018378.

Fogleman, K.A., Lahr, J.C., Stephens, C.D. and Page, R.A., 1993. Earthquake locations determined by the southern Alaska seismograph network for October 1971 through May 1989. US Geological Survey Open-File Report 93-309, 54 p.

Friend, M. and Colpron, M., 2017. Potential radiogenic heat production from Cretaceous and younger granitoid plutons in southern Yukon (1:1 000 000 scale). Yukon Geological Survey, Open File 2017-60, 1 map and data.

Grantz, A., 1966. Strike-slip faults in Alaska. US Geological Survey Open-File Report 66-53, 82 p.

Haeussler, P.J., 2008. An overview of the neotectonics of interior Alaska: Far-field deformation from the Yakutat microplate collision. *In*: Active Tectonics and Seismic Potential of Alaska, J.T. Freymueller, P.J. Haeussler, R.L. Wesson, and G. Ekström (eds), American Geophysical Union, Geophysical Monograph, vol 179, p. 83–108, https://doi.org/10.1029/179GM05.

Hamidbeygi, M., 2022. Nonlinear Bayesian estimation of centroid moment tensors using multiple seismic data sets in the Kiskatinaw seismic monitoring and mitigation area. Unpublished MSc thesis, University of Calgary, Alberta, Canada.

Heidbach, O., Rajabi, M., Cui, X., Fuchs, K., Müller, B., Reinecker, J., ... and Zoback, M., 2018. The World Stress Map database release 2016: Crustal stress pattern across scales. Tectonophysics, vol. 744, p. 484–498, https://doi.org/10.1016/j.tecto.2018.07.007.

Heimann, S., Kriegerowski, M., Isken, M., Cesca, S., Daout, S., Grigoli, F., Juretzek, C., Megies, T., Nooshiri, N., Steinberg, A., Sudhaus, H., Vasyura-Bathke, H., Willey, T. and Dahm, T., 2017. Pyrocko - An open-source seismology toolbox and library. GFZ Data Services. https://doi.org/10.5880/GFZ.2.1.2017.001.

Herrera, C., Cassidy, J.F., Dosso, S.E., Dettmer, J., Bloch, W., Sippl, C. and Salazar, P., 2021. The crustal stress field inferred from focal mechanisms in northern Chile. Geophysical Research Letters, vol. 48, e2021GL092889, https://doi.org/10.1029/2021GL092889.

Horner, R.B., 1983. Seismicity in the St. Elias, region of northwestern Canada and southeastern Alaska. Bulletin of the Seismological Society of America, vol. 73, p. 1117–1137, https://doi.org/10.1785/BSSA0730041117.

Jadamec, M.A., Billen, M.I. and Roeske, S.M., 2013. Three-dimensional numerical models of flat slab subduction and the Denali fault driving deformation in south-central Alaska. Earth and Planetary Science Letters, vol. 376, p. 29–42, https://doi.org/10.1016/j.epsl.2013.06.009.

Jaynes, E.T., 2003. Probability theory: The logic of science. Cambridge university press.

Kalbas, J.L., Freed, A.M., and Ridgway, K.D., 2008. Contemporary fault mechanics in southern Alaska. *In:* Active Tectonics and Seismic Potential of Alaska, J.T. Freymueller, P.J. Haeussler, R.L. Wesson, and G. Ekström (eds), American Geophysical Union, Geophysical Monograph Series 179, p. 321–336.

Kaverina, A.N., Lander, A.V. and Prozorov, A.G., 1996. Global creepex distribution and its relation to earthquake-source geometry and tectonic origin. Geophysical Journal International, vol. 125, p. 249–265, https://doi.org/10.1111/j.1365-246X.1996.tb06549.x.

Kao, H., Shan, S.J., Bent, A., Woodgold, C., Rogers, G., Cassidy, J.F. and Ristau, J., 2012. Regional centroid-moment-tensor analysis for earthquakes in Canada and adjacent regions: An update. Seismological Research Letters, vol. 83, p. 505–515, https://doi.org/10.1785/gssrl.83.3.505.

Kreemer, C., Blewitt, G. and Klein, E.C., 2014. A geodetic plate motion and Global Strain Rate Model. Geochemistry, Geophysics, Geosystems, vol. 15, p. 3849–3889, https://doi.org/10.1002/2014GC005407.

Lahr, J.C. and Plafker, G., 1980. Holocene Pacific-North America plate interaction in southern Alaska: implications for the Yakataga seismic gap. Geology, vol. 8, p. 483–486, https://doi.org/10.1130/0091-7613(1980)8<483:HPAPII>2.0.CO;2.

Langevin, H., Raymond, J. and Fraser, T., 2020. Assessment of thermo-hydraulic properties of rock samples near Takhini Hot Springs, Yukon. *In:* Yukon Exploration and Geology 2019, K.E. MacFarlane (ed.), Yukon Geological Survey, p. 57–73.

Lentas, K., Di Giacomo, D., Harris, J. and Storchak, D.A., 2019. The ISC Bulletin as a comprehensive source of earthquake source mechanisms. Earth System Science Data, vol. 11, p. 565–578, https://doi.org/10.5194/essd-11-565-2019.

Leonard, L.J., Hyndman, R.D., Mazzotti, S., Nykolaishen, L., Schmidt, M. and Hippchen, S., 2007. Current deformation in the northern Canadian Cordillera inferred from GPS measurements. Journal of Geophysical Research: Solid Earth, vol. 112, B11401, https://doi.org/10.1029/2007JB005061.

Leonard, L.J., Mazzotti, S. and Hyndman, R.D., 2008. Deformation rates estimated from earthquakes in the northern Cordillera of Canada and eastern Alaska. Journal of Geophysical Research: Solid Earth, vol. 113, B08406, https://doi.org/10.1029/2007JB005456.

Li, C.F., Lu, Y. and Wang, J., 2017. A global reference model of Curie-point depths based on EMAG2. Scientific reports, vol. 7, p. 1–9, https://doi.org/10.1038/srep45129.

Lowey, G.W., 1998. A new estimate of the amount of displacement on the Denali fault system based on the occurrence of carbonate megaboulders in the Dezadeash Formation (Jura-Cretaceous), Yukon, and the Nutzotin Mountains sequence (Jura-Cretaceous), Alaska. Bulletin of Canadian Petroleum Geology, vol. 46, p. 379–386, https://doi.org/10.35767/gscpgbull.46.3.379.

MacKay, D.J., 2003. Information theory, inference and learning algorithms. Cambridge university press.

Matmon, A., Schwartz, D P., Haeussler, P.J., Finkel, R., Lienkaemper, J.J., Stenner, H.D. and Dawson, T.E., 2006. Denali fault slip rates and Holocene–late Pleistocene kinematics of central Alaska. Geology, vol. 34, p. 645–648, https://doi.org/10.1130/G22361.1.

Marechal, A., Mazzotti, S., Elliott, J.L., Freymueller, J.T. and Schmidt, M., 2015. Indentor-corner tectonics in the Yakutat-St. Elias collision constrained by GPS. Journal of Geophysical Research: Solid Earth, vol. 120, p. 3897–3908, https://doi.org/10.1002/2014JB011842.

Marechal, A., Ritz, J.F., Ferry, M., Mazzotti, S., Blard, P.H., Braucher, R. and Saint-Carlier, D., 2018. Active tectonics around the Yakutat indentor: New geomorphological constraints on the eastern Denali, Totschunda and Duke River Faults. Earth and Planetary Science Letters, vol. 482, p. 71–80, https://doi.org/10.1016/j.epsl.2017.10.051.

McKenzie, D.P., 1969. The relation between fault plane solutions for earthquakes and the directions of the principal stresses. Bulletin of the Seismological Society of America, vol. 59, p. 591–601, https://doi.org/10.1785/BSSA0590020591.

Meighan, L.N., Cassidy, J.F., Mazzotti, S. and Pavlis, G.L., 2013. Microseismicity and tectonics of southwest Yukon Territory, Canada, using a local dense seismic array. Bulletin of the Seismological Society of America, vol. 103, p. 3341–3346, https://doi.org/10.1785/0120130068.

Nelson, J., Colpron, M. and Israel, S., 2013. The cordillera of British Columbia, Yukon, and Alaska: tectonics and metallogeny. *In:* Tectonics, Metallogeny, and Discovery: The North American Cordillera and Similar Accretionary Settings. Colpron, M., Bissig, T., Rusk, B.G., and Thompson, J.F.H., Society of Economic Geologists Special Publication, vol. 17, p. 53–109.

Power, M., 1988. Microearthquake seismicity on the Duke River, Denali Fault system. In: Yukon Geology, vol. 2, Exploration and Geological Services Division, Yukon, Indian and Northern Affairs Canada, p. 61–68.

Richter, D.H. and Matson, N.A., 1971. Quaternary faulting in the eastern Alaska Range. Geological Society of America Bulletin, vol. 82, p. 1529–1540.

Ristau, J., Rogers, G.C. and Cassidy, J.F., 2007. Stress in western Canada from regional moment tensor analysis. Canadian Journal of Earth Sciences, vol. 44, p. 127–148, https://doi.org/10.1139/e06-057.

Ruppert, N.A. and West, M.E., 2020. The impact of USArray on earthquake monitoring in Alaska. Seismological Research Letters, vol. 91, p. 601–610, https://doi.org/10.1785/0220190227.

Vasyura-Bathke, H., Dettmer, J., Steinberg, A., Heimann, S., Isken, M.P., Zielke, O., ... and Jónsson, S., 2020. The Bayesian earthquake analysis tool. Seismological Research Letters, vol. 91, p. 1003–1018, https://doi.org/10.1785/0220190075.

Waldien, T.S., Roeske, S.M., and Benowitz, J.A., 2021. Tectonic underplating and dismemberment of the Maclaren-Kluane Schist records Late Cretaceous terrane accretion polarity and ~480 km of post-52 Ma dextral displacement on the Denali fault. Tectonics, vol. 40, e2020TC006677, https://doi.org/10.1029/2020TC006677.

Yukon Geological Survey, 2020. A digital atlas of terranes for the northern Cordillera. Yukon Geological Survey, http://data.geology.gov.yk.ca/Compilation/2, [accessed, November, 2022].

Appendix

The appendix is only available as a digital file (csv). It is included in a .zip file and accompanies this document; download from https://data.geology.gov.yk.ca.

Appendix 1 – Tabulated focal mechanism solutions

Geomorphic assessment of Tsā̈lnjik Chú (Nordenskiold River) near Carmacks, Klondike region, Yukon

Carolyn Hatton*
Harquail School of Earth Sciences, Laurentian University

Alessandro Ielpi
Department of Earth, Environmental and Geographic Sciences, University of British Columbia
Vale Living with Lakes Centre, Laurentian University

Derek C. Cronmiller and Moya Painter
Yukon Geological Survey

Hatton, C., Ielpi, A., Cronmiller, D.C. and Painter, M., 2023. Geomorphic assessment of Tsā̈lnjik Chú (Nordenskiold River) near Carmacks, Klondike region, Yukon. *In:* Yukon Exploration and Geology 2022, K.E. MacFarlane (ed.), Yukon Geological Survey, p. 77–91.

Abstract

River course migration is controlled by discharge, sediment supply, and bank vegetation, and its study informs watershed responses to environmental stressors like climate change and permafrost thaw. We present a preliminary characterization of Tsā̈lnjik Chú (Nordenskiold River) near Carmacks (Klondike region, Yukon), based on geomorphic observations, time-series photogrammetry and hydrological analysis. We report channel-migration data in relation to flooding patterns, including the records of a recent ~10-year recurrence flood that took place in the spring of 2022. Boreholes drilled in the river's floodplain have encountered discontinuous permafrost at depths of >0.7 m, and preliminary morphodynamic analyses show similar relationships between channel size, curvature and migration rate to rivers outside the permafrost zone. Results provide a coarse characterization of hazards related to bank erosion and channel overspill at Carmacks, and will inform future work that integrates aspects of fluvial morphodynamics and biogeochemistry in relation to flooding elsewhere in Yukon.

---

* chatton@laurentian.ca

Introduction

Meandering rivers are ubiquitous fluvial landforms in the intermountain lowland plains of western and northern Canada (Nanson, 1980; Nanson and Hickin, 1983), and are characterized by a low-gradient (~0.01%) mainstem with anabranching side-channels. These rivers are characterized by planform whereby horseshoe-shaped bends (meanders) with opposite sense of curvature are found in sequence. Each meander is sided by an inner and an outer bank, which are characterized, in turn, by predominantly depositional and erosional processes (Jackson, 1976) constitute the bulk of surficial point-bar sediment in very sharply curved bends and in gently curved bends, and can be preserved preferentially by common types of bend migration. Preservation of the depositional facies of each meander bend depends upon the type of deformation (migration). In actively migrating meanders, erosional processes related to the inertia of the channel flow erode soil, vegetation and underlying sediment from outer banks. Eroded materials are variably redistributed over variable length-scales along inner banks, which grow over time into sediment accumulations with curved planform known as point bars. Concurrent depositional and erosional processes along the banks result in an outwards, lateral migration of the river channel; notably, outer bank erosion is matched by inner bank deposition over decadal to centennial timescales, such that the channel maintains constant width (Mason and Mohrig, 2019). Continued migration of meanders can lead to two bends intersecting each other and isolating a channel section in between (neck cutoff); alternatively, the growth of meanders is at times interrupted by cross-bar channels carved during exceptional floods (chute cutoff; Lewis and Lewin, 1983; Constantine and Dunne, 2008).

Processes of fluvial deposition and erosion, including those that lead to meander migration, take place at rates that are nonlinearly controlled by a multitude of factors, some of which are intrinsic (e.g., the curvature of a channel bend) and other extrinsic (e.g., water discharge and sediment supply; Donovan *et al.*, 2021). Discharge and sediment availability are, in turn, dependent on the hydro-climatic, geological and geomorphological context of a region. As such, river morphodynamics are affected, over certain spatial and temporal scales, by environmental changes in such things as precipitation, temperature or land-use (Horton *et al.*, 2017). The western Canadian Arctic is one such region where ecosystems are impacted by climate change (*e.g.*, increasing temperature and precipitation). Compared to localities in Canada's southern provinces, the mean temperature increase over the past several decades has nearly doubled in some arctic areas (Gillet *et al.*, 2019), and northern regions such as Yukon are currently experiencing among the sharpest warming trends on Earth. Trends in temperature and precipitation affect flood magnitude and frequency and, by extension, impact infrastructures and communities located along riverbanks that may depend on waterways for seasonal transportation or traditional food harvesting.

This report deals with Tsā̱lnjik Chú, also known as the Nordenskiold River, upstream of its confluence into the Yukon River, near the hamlet of Carmacks, in the Klondike region of Yukon (Fig. 1). This section of river includes a reach with a well-developed meandering planform characterized by an ~15–20 m-wide channel. The river and its floodplain are found in the traditional and ancestral lands of the Little Salmon Carmacks First Nation. Here, we present the preliminary results of a geomorphic assessment of landscape change related to meander migration, including long-term analyses and a characterization of patterns of erosion and deposition related to a recent flood (June 2022) that resulted in widespread floodplain inundation upstream of Carmacks (Figs. 2 and 3). This study is part of a broader research effort aimed at investigating the morphodynamics and biogeochemistry of meandering rivers in the permafrost zone, and may serve as a template for the assessment of landscape change elsewhere in northern fluvial systems.

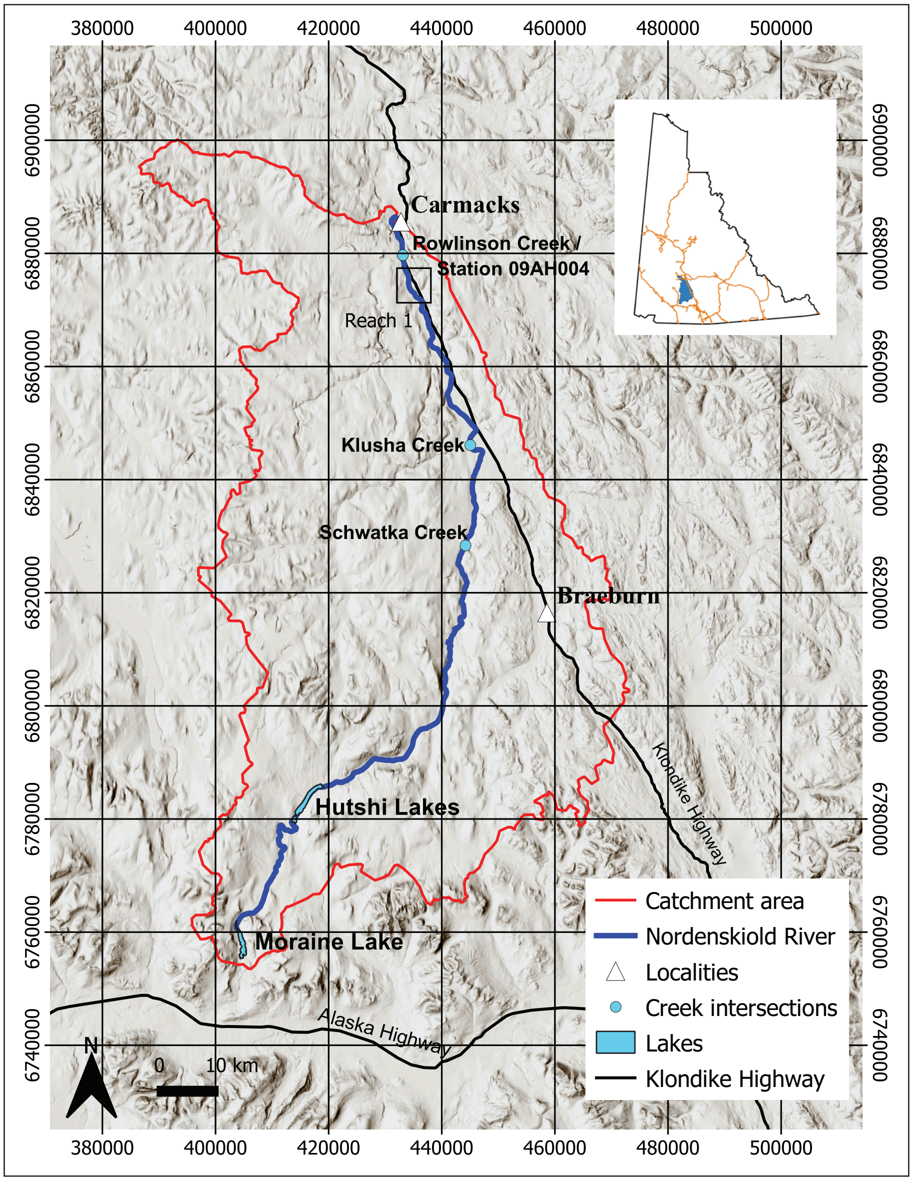

Figure 1. *Geographic sketch representing the Nordenskiold River's watershed (reported in blue in the inset; also includes Yukon highways, in orange, for geographic reference). Grid coordinates refer to metres in the WGS 84 UTM 8N projection. Reaches 2 and 3 are omitted for clarity.*

Regional setting

The Nordenskiold River flows through the Lewes plateau, in the northern Coast Mountain range of the Northern Cordillera (Mathews, 1986). The river originates from Moraine Lake at an elevation of 910 m (60.946° N, 136.760° W) and flows northward to eventually join the Yukon River at Carmacks at an elevation of 519 m (62.102° N, 136.301° W). The Nordenskiold River is approximately 185 km in length, draining a basin of ~6620 km^2. The river is characterized by a predominantly meandering planform with minor straight reaches, and runs northward through Hutshi Lakes (61.178° N, 136.566° W), joining Schwatka Creek (61.582° N, 136.053° W), Klusha Creek (61.735° N, 136.030° W) and Rowlinson Creek (62.044° N, 136.279° W). The average gradient of the river is 2.11‰, although it locally steepens downstream of the confluence with Rowlinson Creek, where it reaches an average gradient of 4.64‰. In this final, steeper reach, the river flows by a gap between glaciofluvial terraces on its hydrographic right-hand side that has previously been identified as a site of possible avulsion (*i.e.*, sudden channel relocation towards a steeper, shorter corridor) by Cronmiller et al. (2020). Such potential avulsion would pose significant flooding hazard to the community of Carmacks.

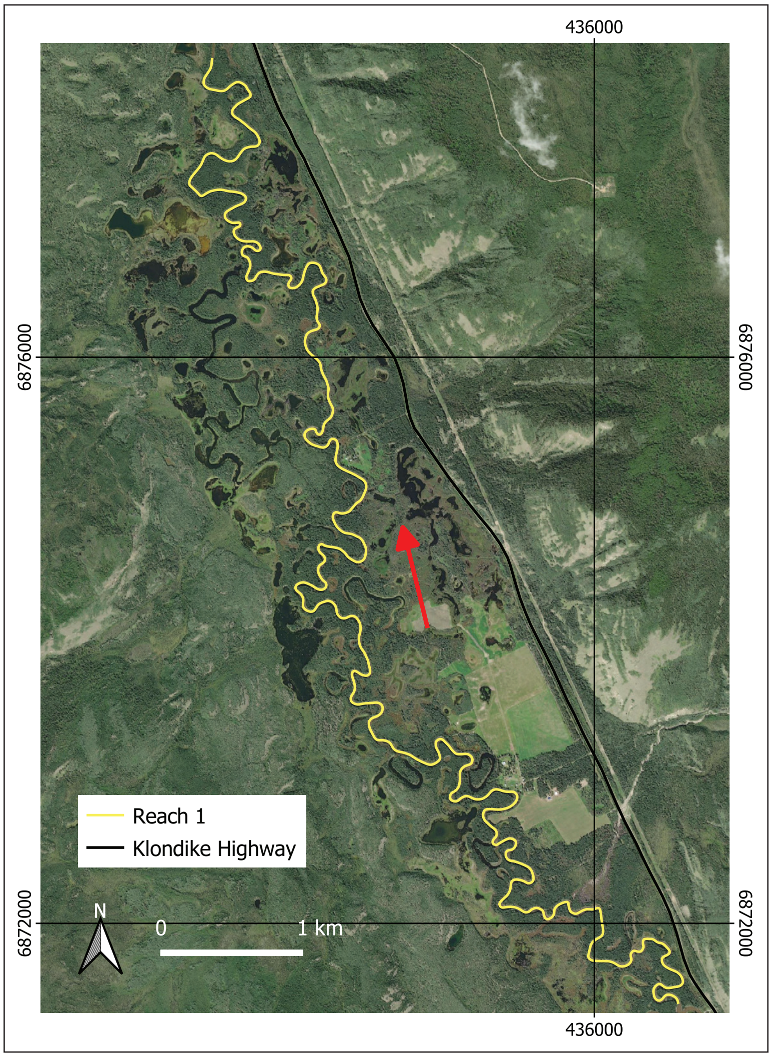

Figure 2. *Satellite view of the Nordenskiold River's reach 1. Grid coordinates refer to metres in the WGS 84 UTM 8N projection. Arrow indicates direction of flow.*

The river watershed is underlain by the Yukon-Tanana terrane, which includes metamorphosed and deformed siliciclastic and volcanic rocks of Late Proterozoic to Devonian age (Nelson and Colpron, 2007). The area has undergone a number of glaciations, which sculpted the hills around Carmacks, and led to the deposition of a mantle of till over uplands in the area (Cronmiller et *al.*, 2020). Large glaciofluvial outwash plains were formed at the terminus of ice sheets and were subsequently eroded by incising drainage networks as the ice withdrew, leaving behind a variable topography consisting of terraces with small kettle depressions and large, chaotic, hummocky ice stagnation complexes. The latter record stationary ice that filled a large portion of the Nordenskiold and Yukon rivers' floodplains at the end of the McConnell Glaciation (Marine Isotope Stage 2; Cronmiller et al., 2020). During glacial recession, strong katabatic winds coming off the ice sheets mobilized fine sediment in large volumes and deposited veneers of loess and less commonly dune ridges over much of the landscape. Presently, fluvial processes and anthropogenic activities such as mining and road building modify the landscape. A few areas around Carmacks are also undergoing localized landslides due to the occurrence of fluvial undercutting, locally mediated by permafrost-thaw processes (Cronmiller et *al.*, 2020). The study area is in the extensive discontinuous permafrost zone (Heginbottom et *al.*, 1995; Bonnaventure and Lewkowicz, 2012). Permafrost is most common on north-facing slopes and in valley bottoms, particularly in areas where thick organic materials preserve cold ground temperatures.

The Nordenskiold River has been included in the Tsâwnjik Chu Habitat Protection Area (Government of Yukon, 2010). Most of the wetlands surrounding the river have shallow open water, encircled by sedge zones and vast beds of submergent vegetation. Some of the wetlands have more complex sedge-grass communities, flooded willow stands, spike rush beds and horsetail scouring rush beds. The treed areas surrounding the wetland are composed mainly of aspen and white spruce, with some pockets of black spruce (Government of Yukon, 2010). The wetlands of the Nordenskiold River offer a habitat for breeding ducks, swans and geese as they rest during the fall migration. The channel provides spawning habitat for salmon, and 11 species of fish have been recorded in the watershed: chinook and chum salmon, lake trout, Arctic grayling, round and lake whitefish, longnose sucker, burbot, northern pike, Arctic lamprey, and slimy sculpin (Government of Yukon, 2010).

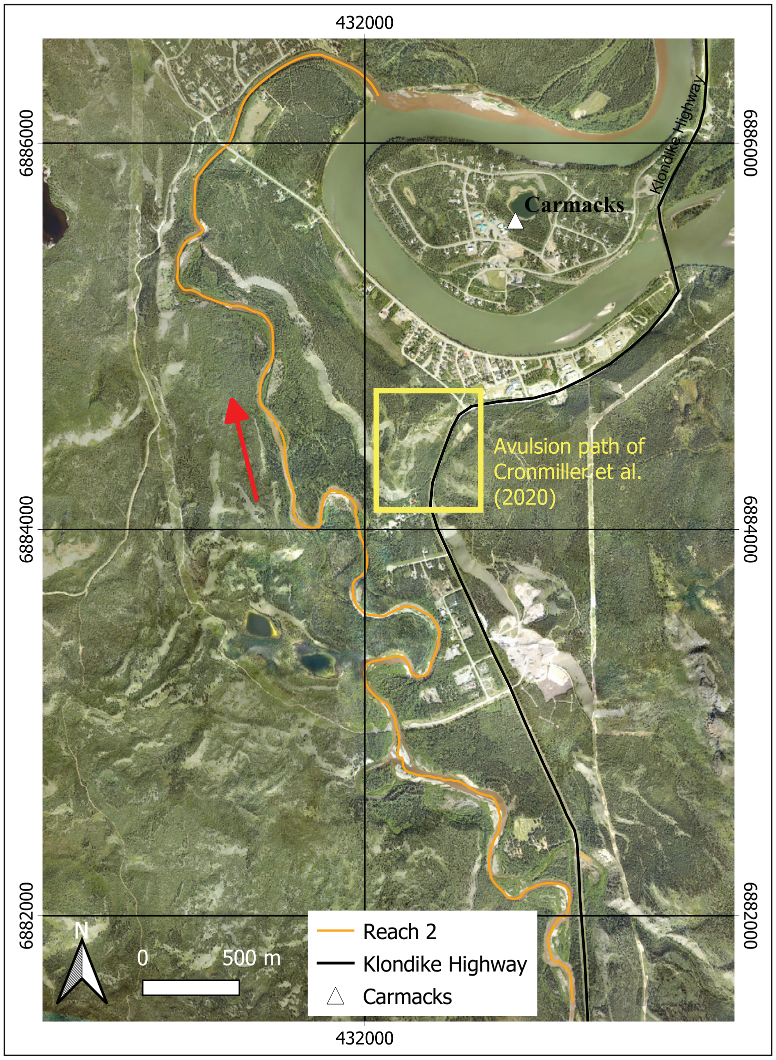

Figure 3. Satellite view of the Nordenskiold River's reach 2. Grid coordinates refer to metres in the WGS 84 UTM 8N projection.

Environment and Climate Change Canada operate a weather station in Carmacks (Station 1509; https://climate.weather.gc.ca/). The climate in this area is characterized by long, comfortable summers and frigid, snowy winters. Between the years of 1961 and 1990, daily mean temperatures ranged from -28.6°C (January) to 14.8°C (July), and average precipitation ranged from 6.8 mm per month (April) to 55.1 mm per month (July). A gauging station operated by Water Survey of Canada (Station 09AH004; https://wateroffice.ec.gc.ca/) is found immediately downstream of the Rowlinson Creek confluence (62.051° N, 136.280° W), and has been recording data since 1983. Minimum discharge levels (~3 $m^3 s^{-1}$) occur in the colder months (December–February), with an all-time estimated low of 1.19 m^3/s in January 1999. Maximum discharge levels occur during snowmelt, with a historical daily average maximum of 244 $m^3 s^{-1}$ in May 1983 (Fig. 4). A more detailed hydrological characterization is presented below.

Materials and methods

This study is based on the collection of photogrammetric and observational data of fluvial forms and processes from freely distributed satellite imagery and aerial photos, proprietary orthomosaics and digital surface models, and both planform and oblique imagery collected with unmanned aerial vehicles (UAVs). Freely distributed satellite imagery was accessed from the archives of Google™ Earth and ESRI™ World Imagery, with spatial resolution of 1.2 metres. Air photo 19, from flight A17344 (dated 1961) was retrieved from the Government of Yukon public archives. Drone North produced a proprietary orthomosaic and digital surface model for a subset of the study area with spatial resolutions of, respectively, 3.3 and 6.6 cm (Drone North, 2022). The collected drone imagery is characterized by variable spatial resolution based on flight attitude and altitude, notably with a set of planform images collected just upstream of Carmacks with centre-image ground resolution of ~10 cm.

Morphometric observations on meander geometry were first collected in order to provide a baseline data set to allow a comparison between the Nordenskiold River and meandering rivers elsewhere within and outside the permafrost zone. We consider individual meander bends with a sinuosity index (defined as the ratio between along-channel length and linear distance) higher than 1.2. The imagery was also employed to manually digitize polylines representing the

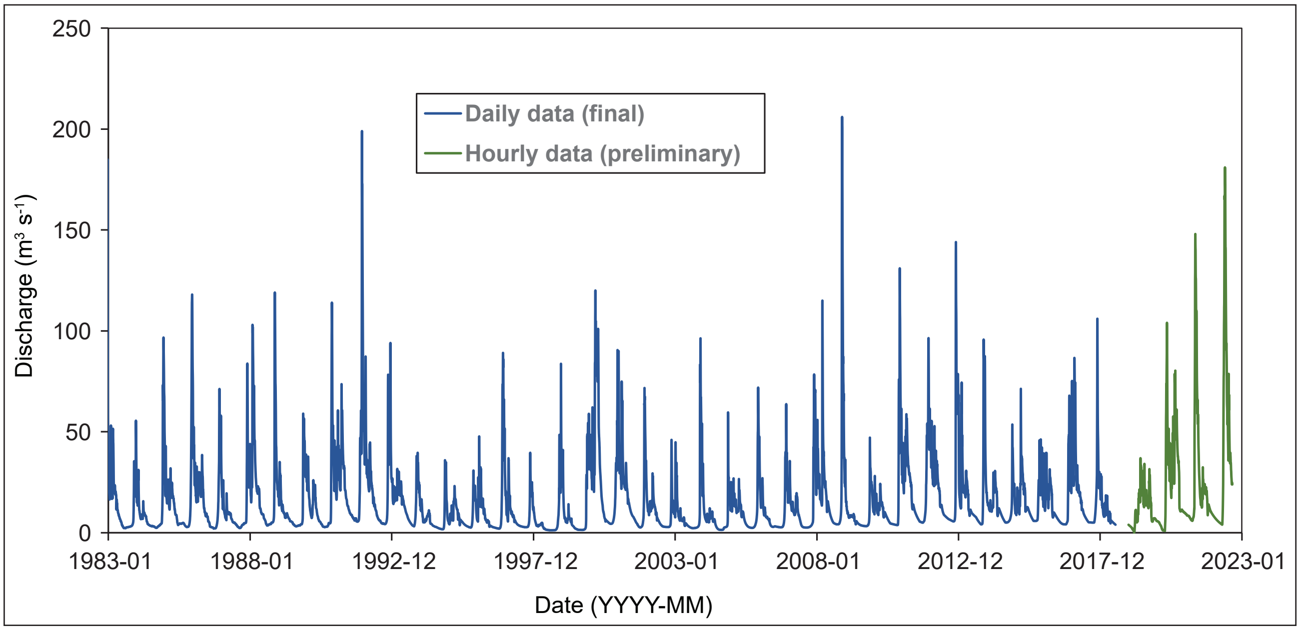

Figure 4. *Hydrograph of daily discharge data at Station 09AH004.*

position of the hydrographic left and right-hand banks of the main channel of the Nordenskiold River at different dates over three selected reaches that together capture the river's geomorphic variability. The comparison of digitized products at different times allowed for the characterization of landscape change associated with fluvial processes such as bank erosion, bar deposition and channel overspilling.

Reach 1 is defined from 61.971° N, 136.209° W to 62.029° N, 136.274° W, covering an along-channel distance of ~16 km. This reach is located about 2 km along-channel upstream of the confluence between the Nordenskiold River and Rowlinson Creek, and displays a classic high-sinuosity meandering channel planform. This reach shows evidence of widespread degrading (thermokarst) permafrost throughout its length. Bank lines along this reach were digitized from imagery dated September 24, 2008 and August 5, 2017. Two boreholes were drilled about 14 km upstream of reach 1 (61.857° N, 136.110° W). The boreholes are located about 50 m apart, and sample both an inner and outer bank along two consecutive meanders.

Reach 1 and 2 are separated by a ~3.5 km-long channel segment with straight planform, where the river is narrowly confined within a valley sided by glaciofluvial terraces. Reach 2 is defined from 62.060° N, 136.280° W to 62.102° N, 136.301° W, over an along-channel distance of ~8 km. This reach of the Nordenskiold River is immediately upstream of the Yukon River and displays a wandering to meandering channel planform. Bank lines along this reach were digitized from imagery dated 1961 (day and month unspecified and, based on lack of snow on the ground and low flow, arbitrarily set to August 1) and August 5, 2017. Reach 3 is developed along a subset of reach 2, from 62.073° N, 136.298° W to 62.082° N, 136.303° W, over an along-channel distance of ~2 km. This reach represents a sensitive area near active roadworks and town infrastructures and dwellings. Bank lines along this reach were digitized from imagery dated August 5, 2017 and October 11, 2022, which predate and postpone the June 2022 flood, respectively.

All bank lines and derived data products were digitized and processed in the QGIS environment as shapefiles. Specifically, pairs of hydrographic left and right-hand bank lines were used to construct channel centrelines through a process of skeletonization, using an open-access toolbox developed in the *R* programming language and chained within QGIS (http://mlt.github.io/QGIS-Processing-tools/tags/dtw.html). Skeletonization returns a centreline where each node is spaced from others at a defined interval (in this study, we employed a 10 m spacing that captures the changing curvature of the meandering channel). Centrelines representative of different dates were then compared, using the same toolbox, through dynamic time warping – an algorithm that compares polylines from different dates and stretches or compresses them to produce migration pathways at discrete spatial intervals (Giorgino, 2009). In other words, dynamic time warping generates lines representing migration pathways along the river course at discrete spatial intervals (here corresponding to the node spacing along the centrelines). Dynamic time warping was also employed to obtain channel-width data by comparing the hydrographic left and right-hand bank lines representative of a given date. Only channel bends that underwent planform change through actual lateral migration were included in this analysis, whereas channel sections that underwent cutoff, braiding, or relocation were manually removed. This analytical approach allows us to plot data such as channel width, curvature, and migration rate, as a function of along-channel distance. Finally, photogrammetric data were corroborated by observational data collected in the field during two visits, one in June and one in October 2022 (at high and low flow conditions). All field and photogrammetric observations were also compared against discharge data.

Preliminary results and discussion

Hydrology

Discharge data from the Nordenskiold River spanning from 1983 to 2018 were analyzed. Over this 35-year interval, the highest discharge typically occurred in relation to late spring/early summer freshet, *i.e.*, in the window between mid-May to late June, with a lowest maximum peak of 38.1 $m^3 s^{-1}$ in 1995, a maximum peak of 244 $m^3 s^{-1}$ in 1983, and a mean from all annual peaks of 102 $m^3 s^{-1}$. We constructed a record of discharge data plotted as a function of exceedance recurrence interval (Fig. 5), fitted with a Log-Pearson III regression. Peak annual discharges in the range of 50 to 125 $m^3 s^{-1}$ have return periodicities of 1 to 5 years, which can be used as a first order estimate for the range of bankfull discharge (*i.e.*, the typical formative discharge of a river, above which water overspill onto the adjoining floodplain takes place; Wolman and Miller, 1960). The plot in Figure 5 also shows the occurrence of three events with discharge >200 $m^3 s^{-1}$, which, considering the data set at hand, correspond to exceptional floods with return interval of 15 to at least 40 years. Peak-annual-discharge data show a log-normal distribution with respect to exceedance recurrence intervals, as observed in rivers elsewhere across a range of biogeomorphic regimes (Ielpi et *al.*, 2020; Kuras et *al.*, 2021).

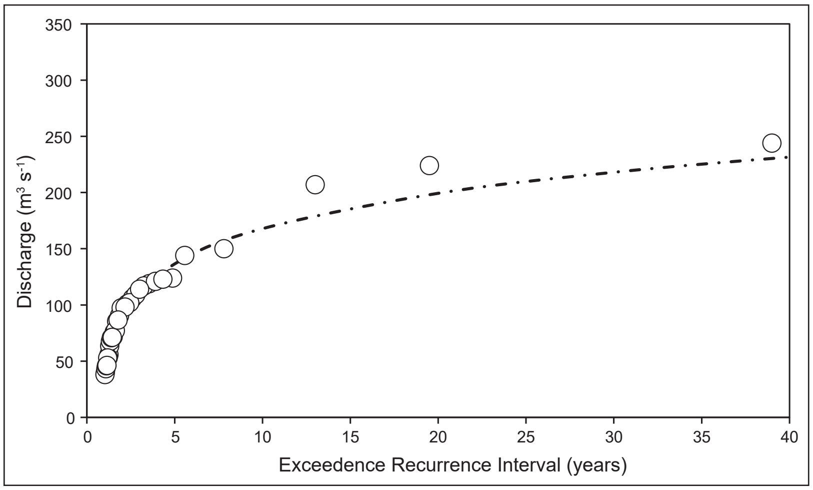

Figure 5. *Peak annual discharge from Station 09AH004 plotted as a function of exceedance recurrence interval. A Log-Pearson III fit is reported for reference.*

In the late spring and early summer of 2022, the Nordenskiold River experienced higher flood levels than average. Preliminary data (that is, not yet been subject to full quality assessment and control by the Water Survey of Canada) show that discharge began increasing on April 24, starting at 4 m^3 s^{-1} and eventually reaching a peak of 186 m^3 s^{-1} on May 28 (Fig. 6). Discharge levels then steadily decreased, with the exception of two secondary peaks on July 1 and 15 related to significant precipitation impacting the watershed. Discharge plateaued back to low-flow stages on August 6. According to the data compiled in Figure 5, the spring 2022 flood categorizes as a discharge event with a return interval of about 10 years. This flood lead to widespread overspill onto the river's floodplain (Fig. 7). Overspilling affected mostly thermokarst lowland areas located within 2 km of the active channel, especially along reach 1. Notwithstanding higher-than-usual water levels, no significant overspill took place along reach 2, likely due to the channel being more confined along its final, steeper section upstream of the Yukon River confluence. This observation suggests that, at least considering floods with ~10 years of recurrence interval, no impending risk of channel avulsion occurs at the gap between glaciofluvial terraces near Carmacks (cf., Cronmiller *et al.*, 2020).

Morphodynamics

Permafrost was intersected in the two boreholes upstream of reach 1 at depths of about 0.7 m. Frost probing in the area likewise found a highly variable active layer thickness ranging from 0.7 to >1.3 m. No evidence of permafrost was observed along reaches 2 and 3, though it may be present in portions of the floodplain distal to the active channel and topographically shielded from insolation. Fifty-four meanders were measured along reach 1 (Fig. 8), yielding a median ±1σ range in channel length of 287^{+238}_{-122} m (where σ defines the deviation between of the 16th and 84th percentiles in a distribution from the median). Meander diameter data (*i.e.*, the along-valley distance between consecutive bend inflection points) along reach 1 yielded a median ±1σ range of 111^{+80}_{-51} m. Accordingly, the sinuosity index data for reach 1 yielded a median ±1σ range of $2.44^{+1.15}_{-0.68}$. Twelve meanders were measured along the shorter reach 2 (Fig. 8). These meanders produce a median ±1σ channel length of 616^{+237}_{-112} m, a median ±1σ diameter of 319^{+115}_{-112} m, and a median of ±1σ sinuosity index of $2.06\pm^{+1.08}_{-0.64}$. These preliminary results show that the Nordenskiold River has similar scalar relationships as rivers elsewhere both within and outside the permafrost zone (Williams, 1986; Ielpi *et al.*, 2021; Whitney, 2022). More detailed analyses will investigate possible departures between the morphodynamics of the Nordenskiold and other rivers in diverse bioclimatic regions.

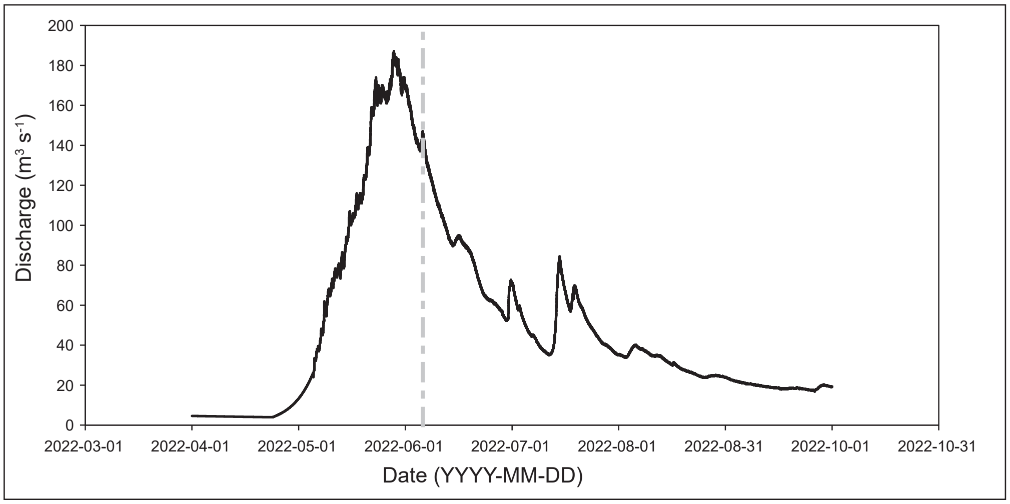

Figure 6. *Hydrograph of preliminary instantaneous discharge data at Station 09AH004, detailing the May–June 2022 flood. The dashed grey line indicates the day of the field visit and photograph in Figure 7.*

Figure 7. *Oblique aerial photograph depicting the Nordenskiold River (foreground) and adjoining inundated floodplain near the upstream-most part of reach 1. Photograph taken in early June 2022; arrow depicts flow direction in mainstem channel. The thermokarst ponds, as depicted here as flooded lowlands siding the main channel, are ubiquitous in Reach 1.*

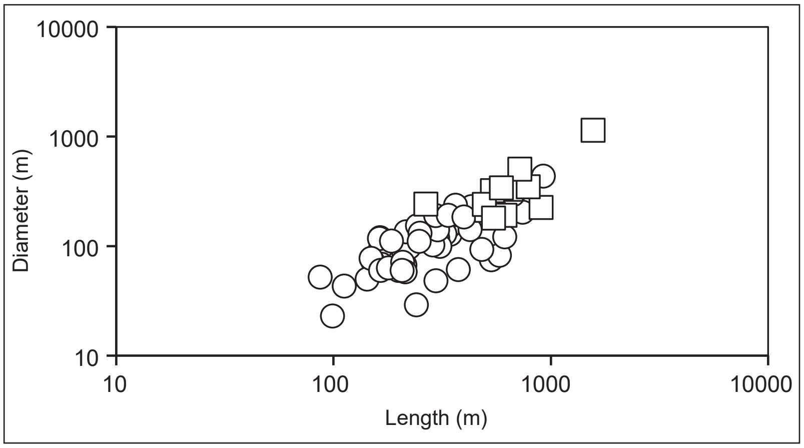

Figure 8. *Log-log plot of morphometric data on meander-size distribution for the Nordenskiold River along reaches 1 and 2. Length and diameter indicate, respectively, along-channel and along-valley distances between bend-inflection points.*

Data on migration rate, channel width and bend curvature obtained through dynamic time warping are reported in Figures 9 through 14. Along reach 1, absolute curvature has a median ±1σ range of $1.1^{+1.4}_{-0.8} \times 10^{-2}\,\mathrm{m}^{-1}$ (Fig. 9), channel width a median ±1σ range of $23.6^{+4.3}_{-3.2}$ m (Fig. 10), and migration rate averaged from 2008 to 2017 a median ±1σ range of $0.45^{+0.16}_{-0.21}\ \mathrm{m\,yr}^{-1}$ (Fig. 11). Along this reach, both bend curvature, channel width and migration rate show decreasing trends downstream (Figs. 9–11). Whereas the decrease in bend curvature is minimal, channel width ranges from about 15 to 45 m in the upstream-most 3 km and from about 15 to 25 m in the downstream-most 2 km (*i.e.*, a relative decrease of about ⅓; Fig. 10). Migration rates also show a decrease of comparable magnitude, ranging from local maxima of $1.4\ \mathrm{m\,yr}^{1}$ in the upstream-most tract to $0.7\ \mathrm{m\,yr}^{1}$ in the downstream-most tract (Fig. 11).

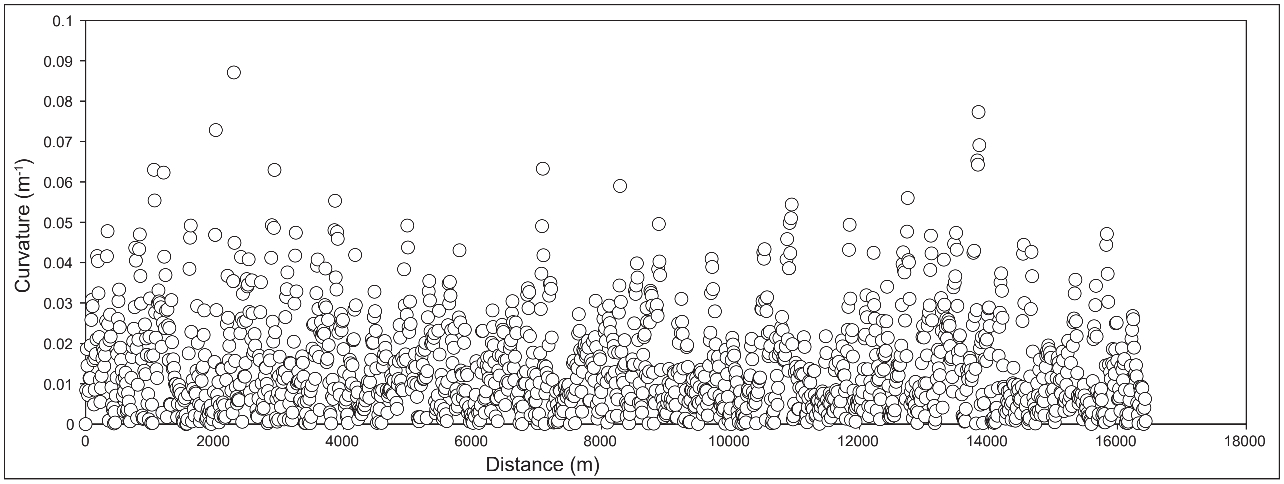

Figure 9. *Bend curvature along reach 1 plotted as a function of downstream distance.*

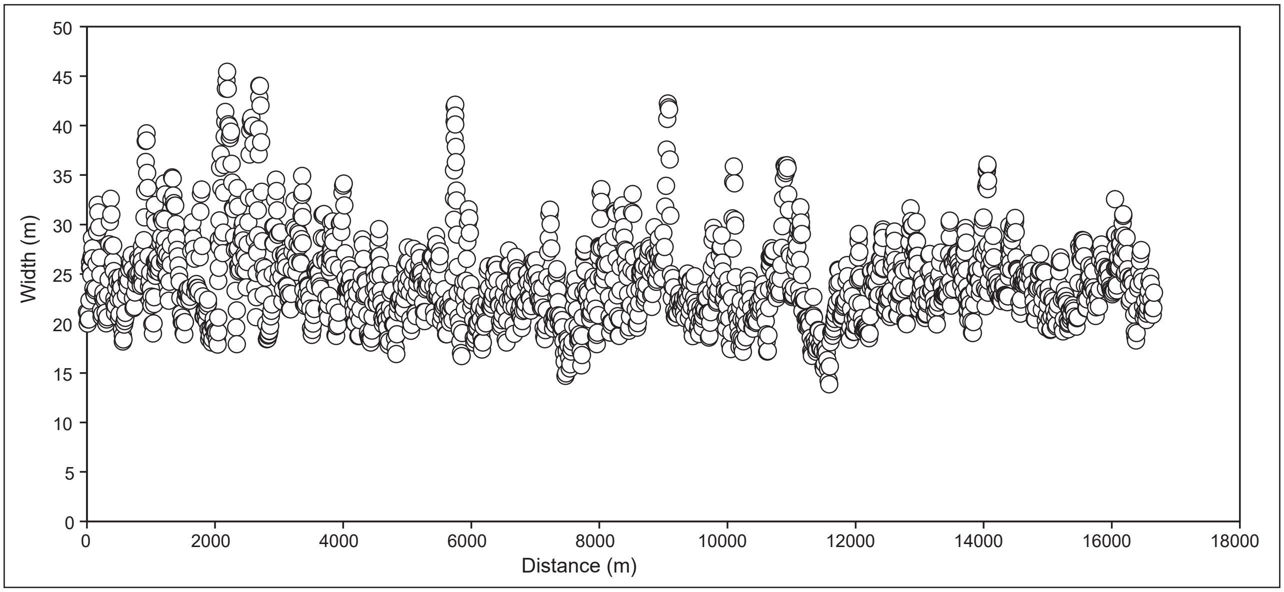

Figure 10. *Channel width along reach 1 plotted as a function of downstream distance.*

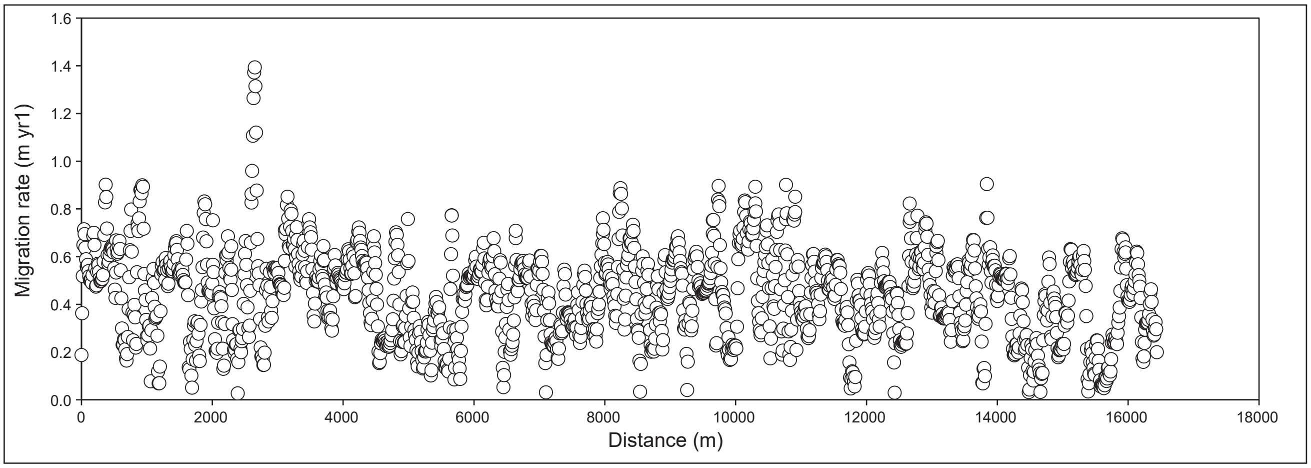

Figure 11. *Migration rate along reach 1 plotted as a function of downstream distance.*

Along reach 2, absolute curvature has a median ±1σ range of $7.0^{+1.2}_{-0.05} \times 10^{-2}\,\mathrm{m}^{-1}$ (Fig. 12), channel width a median ±1σ range of $35.7^{+25.5}_{-10.7}$ m (Fig. 13), and migration rate averaged from 1961 to 2017 a median ±1σ range of $0.22^{+0.59}_{-0.16}\,\mathrm{m\,yr}^{-1}$ (Fig. 14). These parameters likewise display slightly decreasing trends downstream, although with sharper relative variations than in reach 1 (Figs. 12–14). The morphodynamic data presented through dynamic time warping show that, overall, the Nordenskiold River is characterized by similar curvature and migration rate in relation to channel width to other rivers found in different bioclimatic regions (Constantine *et al.*, 2014; Sylvester *et al.*, 2019; Ielpi and Lapôtre, 2020, 2022). The above suggests that the presence of discontinuous permafrost in the river's alluvial plain does not noticeably affect parameters like bank strength, such that the river's morphodynamic characteristics are similar to those of other watercourses outside the permafrost zone. That being said, the marked downstream decrease in channel width and migration observed along reach 1 may be related to changes in stream power related to, hydrologic loss of the channel towards the floodplain's aquifer.

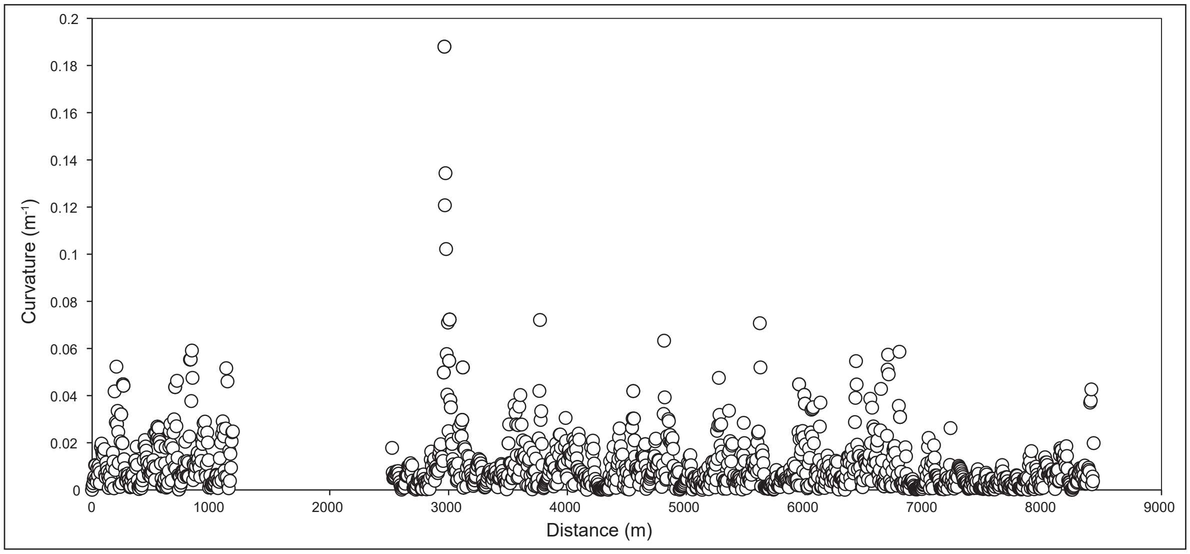

Figure 12. *Bend curvature along reach 2 plotted as a function of downstream distance. Omitted values are along a reach that underwent chute cutoff and that were not considered in the dynamic time warping.*

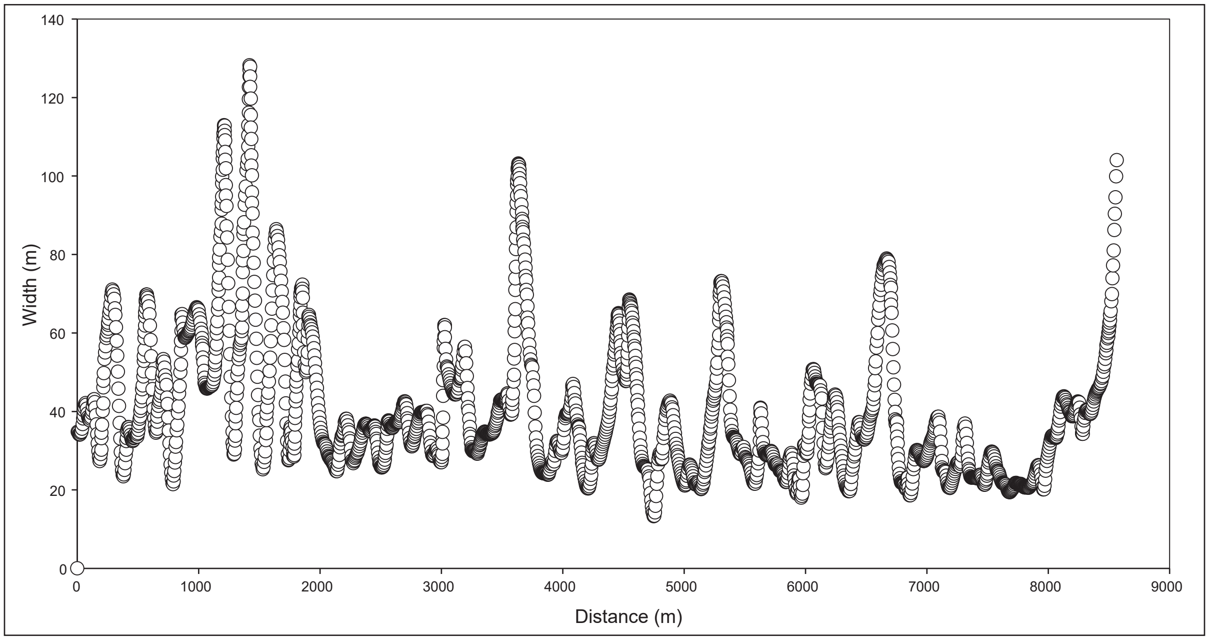

Figure 13. *Channel width along reach 2 plotted as a function of downstream distance.*

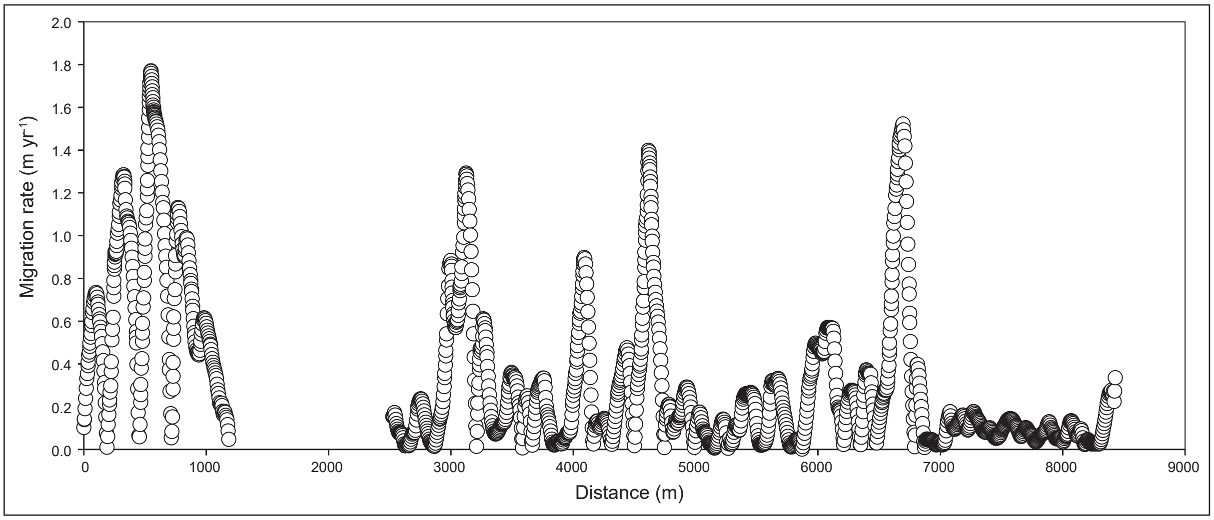

Figure 14. *Migration rate along reach 2 plotted as a function of downstream distance. Omitted values are along a reach that underwent chute cutoff and were not considered in the dynamic time warping.*

Results above inform potential hazards related to fluvial processes near Carmacks — hazard being broadly defined as risk in relation to a phenomenon that can potentially lead to harm or damage to lives and existing properties and infrastructures. Reach 1 has little potential hazard related to channel migration since bank erosion is not likely to impact infrastructures (with the notable exception of locations where the channel's outer bank impinges directly on the Klondike Highway, e.g., at 61.970° N, 136.205° W). The hazard is however greater along reach 2 (and its subset, reach 3) in response to floods with above-decadal recurrence interval based on migration rates and pathways, but also on the occurrence of infrastructures and dwellings (Fig. 15). That being said the potential for a significant avulsion of the Nordenskiold River at Carmacks (as discussed by Cronmiller et *al.*, 2020) is deemed low, considering the patterns of migration of the channel and its confined nature immediately upstream of the Yukon River confluence.

Conclusions

This report presented the preliminary results of a geomorphic survey focused on Tsā̈lnjik Chú (Nordenskiold River) near Carmacks, in the southern Klondike region of Yukon. Geomorphic assessments were aimed at acquiring baseline data on the morphometry and migration rate of the river in relation to hydrographic stages, including planform change in the aftermath of a ~10-year recurrence flood that took place in the spring of 2022. This report is part of a larger project focused on understanding the morphodynamics and biogeochemistry of meandering rivers in the permafrost zone. We employed hydrological analysis, photogrammetric measurements, borehole drilling, and algorithms such as dynamic time warping to investigate river-landscape change. Preliminary results indicate that the river plain is underlain by discontinuous permafrost, with thaw-front depths as shallow as ~0.7 m, and that the river is characterized by similar relationships between channel size, curvature and migration

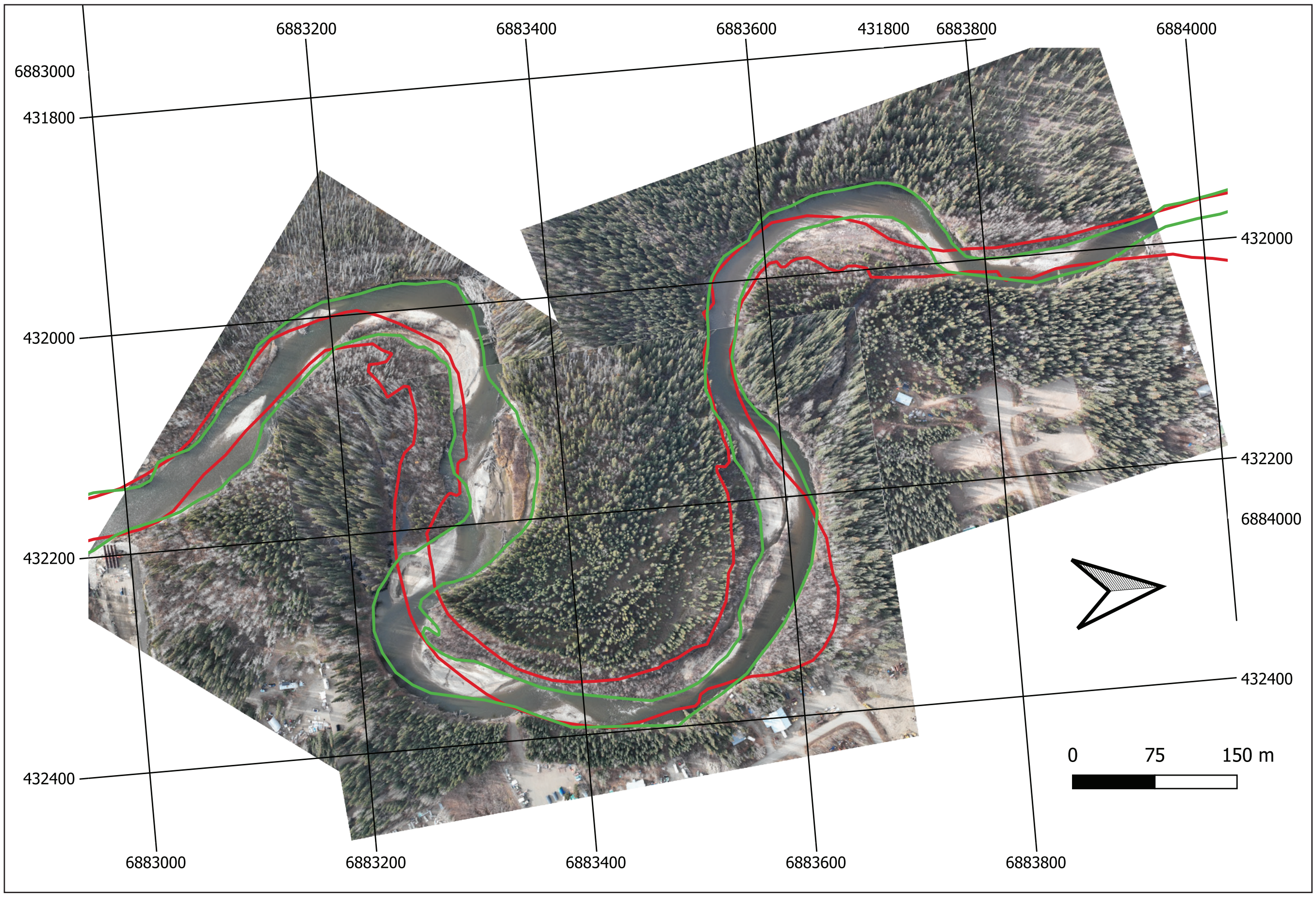

Figure 15. *Collage of georeferenced planview UAV imagery from October 2022 of reach 3 (flow to the right), with channel banks from 1961 and 2017 reported, respectively, in red and green. Note locally ongoing erosion along hydrographic right banks (bottom of the image), in the vicinity of infrastructures and dwellings. Grid coordinates refer to metres in the WGS 84 UTM 8N projection.*

rate to other rivers located outsized the permafrost zones. Channel migration and flooding related to ~10+ year-recurrence floods have little predicted impact on upstream meandering reaches of the river located several kilometres away from Carmacks, whereas channel migration and overspill in the terminal reach immediately upstream of the confluence with the Yukon River has the potential to affect infrastructures and dwellings. That being said, an analysis of the river profile suggests that avulsion events in the lowermost river course (e.g., along Carmacks) are unlikely. These results will inform future work: (i) an investigation of patterns of organic-carbon budgeting in the river's floodplain thanks to recently acquired soil samples; and (ii) a fuller characterization of ground-temperature profiles in relation to ice content and, more broadly, permafrost distribution along the two boreholes drilled in the river's floodplain.

Acknowledgements

Stefan Gronsdahl is acknowledged for reviewing the manuscript, and for helping with the Log-Pearson III fit of flood recurrence intervals. This work is part of the BSc Honours thesis of the lead author. CH and AI acknowledge financial support from the Yukon Geological Survey, Polar Knowledge Canada's Northern Scientific Training Program, and the Natural Sciences and Engineering Research Council of Canada's Discovery Grant Program.

References

Bonnaventure, P.P. and Lewkowicz, A.G., 2012. Permafrost probability modeling above and below treeline, Yukon, Canada. Cold Regions Science and Technology, vol. 79-80, p. 92–106, https://doi.org/10.1016/j.coldregions.2012.03.004.

Constantine, J.A. and Dunne, T., 2008. Meander cutoff and the controls on the production of oxbow lakes. Geology, vol. 36, p. 23–26, doi:10.1130/G24130A.1.

Constantine, J.A., Dunne, T., Ahmed, J., Legleiter, C. and Lazarus, E.D., 2014. Sediment supply as a driver of river meandering and floodplain evolution in the Amazon Basin. Nature Geoscience, vol. 7, p. 899–903, doi:10.1038/ngeo2282.

Cronmiller, D.C., McParland, D.J., Goguen, K.M. and Mckillop, R.J., 2020. Carmacks surficial geology and community hazard susceptibility mapping. Yukon Geological Survey, Miscellaneous Report 20, 16 p.

Donovan, M., Belmont, P. and Sylvester, Z., 2021. Evaluating the relationship between meander-bend curvature, sediment supply, and migration rates. Journal of Geophysical Research: Earth Surface, vol. 126, doi:10.1029/2020JF006058.

Drone North, 2022. Nordenskiold river project uav photogrammetry survey – October 2022, 15 p.

Gillet, N., Flato, G., Zhang, X., Derksen, C., Bonsal, B., Greenan, B., Bush, E., Shepherd, M., Peters, D. and Gilbert, D., 2019. Canada's Changing Climate Report. Government of Canada, 444 p., http://www.changingclimate.ca/CCCR2019.

Giorgino, T., 2009. Computing and Visualizing Dynamic Time Warping Alignments in R: The dtw Package. Journal of Statistical Software, vol. 31, p. 1–24, doi:10.18637/jss.v031.i07.

Government of Yukon, 2010. Tsâwnjik Chu Nordenskiold Habitat Protection Area Management Plan. Prepared by the Nordenskiold Steering Committee and Yukon Department of Environment, 28 p.

Heginbottom, J.A., Dubreuil, M.A. and Harker, P.A., 1995. Canada, Permafrost. *In:* National Atlas of Canada, Natural Resources Canada, Geomatics Canada, MCR Series no. 4177 (5th Edition), 1 sheet.

Horton, A.J., Constantine, J.A., Hales, T.C., Goossens, B., Bruford, M.W. and Lazarus, E.D., 2017. Modification of river meandering by tropical deforestation. Geology, vol. 45, p. 511–514, doi:10.1130/G38740.1.

Ielpi, A. and Lapôtre, M.G.A., 2020. A tenfold slowdown in river meander migration driven by plant life. Nature Geoscience, vol. 13, p. 82–86, doi:10.1038/s41561-019-0491-7.

Ielpi, A. and Lapôtre, M.G.A., 2022. Linking sediment flux to river migration in arid landscapes through mass balance. Journal of Sedimentary Research, vol. 92, p. 695–703, https://doi.org/10.2110/jsr.2022.118.

Ielpi, A., Lapôtre, M.G.A., Finotello, A. and Ghinassi, M., 2021. Planform-asymmetry and backwater effects on river-cutoff kinematics and clustering. Earth Surface Processes and Landforms, vol. 46, p. 357–370, doi:10.1002/esp.5029.

Ielpi, A., Lapôtre, M.G.A., Finotello, A., Ghinassi, M. and D'Alpaos, A., 2020. Channel mobility drives a diverse stratigraphic architecture in the dryland Mojave River (California, USA). Earth Surface Processes and Landforms, vol. 45, p. 1717–1731, doi:10.1002/esp.4841.

Jackson, R.G., 1976. Depositional Model of Point Bars in the Lower Wabash River. SEPM Journal of Sedimentary Research, vol. 46, doi:10.1306/212f6ff5-2b24-11d7-8648000102c1865d.

Kuras, P., Trubilowicz, J. and McLean, R., 2021. British Columbia Extreme Flood Project, Regional Flood Frequency Analysis – Technical development report and manual to complete a regional flood frequency analysis. Bulletin 2020-1-RFFA, doi: 10.13140/RG.2.2.29177.80480.

Lewis, G.W. and Lewin, J., 1983. Alluvial cutoffs in Wales and the Borderlands. *In:* Modern and ancient fluvial systems, J.D. Collinson and J. Lewin (eds), Wiley Online Library, p. 145–154, https://doi.org/10.1002/9781444303773.ch11.

Mason, J. and Mohrig, D., 2019. Differential bank migration and the maintenance of channel width in meandering river bends. Geology, vol. 47 p. 1136–1140, doi:10.1130/G46651.1/4836975/g46651.pdf.

Matthews, W.H., 1986. Physiographic map of the Canadian Cordillera. Geological Survey of Canada, Series Map 1701A, 1 sheet, doi:10.4095/122821.

Nanson, G.C., 1980. Point bar and floodplain formation of the meandering Beatton River, northeastern British Columbia, Canada. Sedimentology, vol. 27, p. 3–29, doi:10.1111/j.1365-3091.1980.tb01155.x.

Nanson, G.C. and Hickin, E.J., 1983. Channel Migration and Incision on the Beatton River. Journal of Hydraulic Engineering, vol. 109, p. 327–337, doi:10.1061/(asce)0733-9429(1983)109:3(327).

Nelson, J. and Colpron, M., 2007. Tectonics and metallogeny of the British Columbia, Yukon and Alaskan Cordillera, 1.8 Ga to the present. *In*: Mineral Deposits of Canada: A Synthesis of Major Deposit-Types, District Metallogeny, the Evolution of Geological Provinces, and Exploration Methods, W.D. Goodfellow (ed.), Geological Association of Canada, Special Publication No. 5, p. 755–791.

Sylvester, Z., Durkin, P. and Covault, J.A., 2019. High curvatures drive river meandering. Geology, vol. 47, p. 263–266, doi:10.1130/G45608.1.

Whitney, J., 2022. Geomorphic and carbon dynamics in a continuous permafrost floodplain: Blackstone River, Yukon, Canada. MSc thesis, Laurentian University, 100 p.

Williams, G.P., 1986. River meanders and channel size. Journal of Hydrology, vol. 88, p. 147–164.

Wolman, M.G. and Miller, J.P., 1960. Magnitude and Frequency of Forces in Geomorphic Processes. The Journal of Geology, vol. 68, p. 54–74, doi:10.1086/626637.

A preliminary geological interpretation of the Mount Grant–Evelyn Creek area, southern Yukon (parts of 105C/11, 12, 13, 14)

David Moynihan*
Yukon Geological Survey

Moynihan, D., 2023. A preliminary geological interpretation of the Mount Grant–Evelyn Creek area, southern Yukon (parts of 105C/11, 12, 13, 14). *In:* Yukon Exploration and Geology 2022, K.E. MacFarlane (ed.), Yukon Geological Survey, p. 93–107.

Abstract

The Evelyn Creek–Mount Grant area includes a large region of igneous and meta-igneous rocks; here termed the Mount Grant batholith. The batholith comprises mostly deformed Mississippian metatonalite of the Simpson Range suite and variably, but mostly non-deformed Cretaceous granitic rocks of the Cassiar suite. The metatonalite has a sheet-like geometry and is in contact with contrasting metasedimentary successions. Overlying the metatonalite is the Slate Mountain succession, which includes quartzite, psammite, phyllite and limestone. The metatonalite overlies rocks of the Evelyn Creek succession (new), which has a tripartite stratigraphy; its lower part is dominated by chert and siliceous argillite, the middle unit comprises chlorite-muscovite schist and quartzite, while the upper unit is a prominent interval of pale coloured marble/calc-silicate. The contact between the Evelyn Creek succession and the overlying Mississippian metatonalite is interpreted to be structural rather than intrusive. Rocks of the Cassiar suite include large volumes of non-deformed granite and quartz monzonite and lesser amounts of foliated equivalents. Low pressure metamorphism is recorded by andalusite and/or sillimanite bearing schists that are restricted to the eastern part of the area. This metamorphism and deformation did not affect the remainder of the area, where latest penetrative structures are crosscut by Early Jurassic rocks of the Lokken suite.

* David.Moynihan@yukon.ca

Introduction

This report describes the geology of part of the Big Salmon Range in southern Yukon, based on 1:50 000 scale mapping carried out during the summer of 2022 (Fig. 1). The area described (Fig. 2) is approximately enclosed by the South Canol road, the access road to the Red Mountain deposit, and the Teslin River valley. It includes parts of the NTS 1:50 000 map sheets 105C/11—14 and is along strike to the south of the area described in Moynihan and Crowley (2022).

The Big Salmon Range is mostly underlain by rocks of the Yukon-Tanana terrane (Fig. 1). The Teslin fault crosses the southwestern edge of the map area and separates Yukon-Tanana terrane from rocks of the Whitehorse trough (Figs. 1 and 2). Previous mapping of the area was carried out by Mulligan (1963) and Stevens (1993). Mulligan (1963) documented the presence of hornblende-bearing gneiss, as well as assorted schistose and gneissic rocks, which he collectively referred to as the Big Salmon complex. Stevens *et al.* (1996) established that hornblende-bearing gneissic rocks are Mississippian orthogneisses that are characteristic of the Simpson Range plutonic suite (Mortensen, 1992; Murphy *et al.*, 2006); they also recognized two main metasedimentary units, one dominated by graphitic phyllite, and another dominated by more quartzose rocks. Stevens *et al.* (1996) assigned rocks east of the Teslin fault to the Nisutlin allochthonous assemblage, a now obsolete term that comprises part of Yukon-Tanana terrane (Colpron *et al.*, 2006). The previous authors also recognized the presence of Cretaceous plutonic rocks in the area.

The new mapping (Fig. 2) shows that metaplutonic rocks of the Simpson Range suite are more widespread than previously recognized (Mulligan, 1963; Stevens, 1993). The central part of the area is dominated by the Mount Grant batholith, which includes deformed Mississippian rocks of the Simpson Range suite, as well as mostly post-tectonic Cretaceous granitic rocks (Fig. 2). The metasedimentary rocks of the area are assigned to two successions, which differ from the subdivisions of Stevens (1993). The Slate Mountain succession (Moynihan and Crowley, 2022) is interpreted to overlie a large sheet of metatonalite, while the Evelyn Creek succession (this report) underlies the metatonalite (Figs. 2 and 3). The contact between the Evelyn Creek succession and the overlying metatonalite is interpreted to be a folded thrust fault.

Rock units

Evelyn Creek succession

A succession of siliceous metasedimentary rocks overlain by schist and marble is exposed below Mississippian metatonalite in the vicinity of Evelyn Creek. The same rocks are exposed to the southwest, on the west side of a NW–SE striking fault that extends from the Teslin fault to the north end of the Murphy Creek pluton. The succession comprises three divisions.

The lower division is dominated by metachert and siliceous argillite (Fig. 4a-d). Metachert ranges from black to white-pale grey to pale brown, is typically strongly banded, and commonly breaks along partings that are spaced at intervals ranging from several millimetres to several centimetres. Partings and thin layers of medium grey siliceous argillite alternate with metachert layers. This compositional layering is commonly repeated across tight to isoclinal folds and in highly deformed areas, layering forms prominent parallel ribs on outcrop surfaces. More massive varieties of metachert include brown layers up to 1 m-thick, and paler metachert with prominent colour striping. These outcrops have smooth weathering surfaces and layering is mostly defined by subtle colour variations. These cherts are mostly pale coloured, with thin lamellae of grey, black, green or pink. These grade into intervals of medium grey to black, carbonaceous, siliceous argillite and chert.

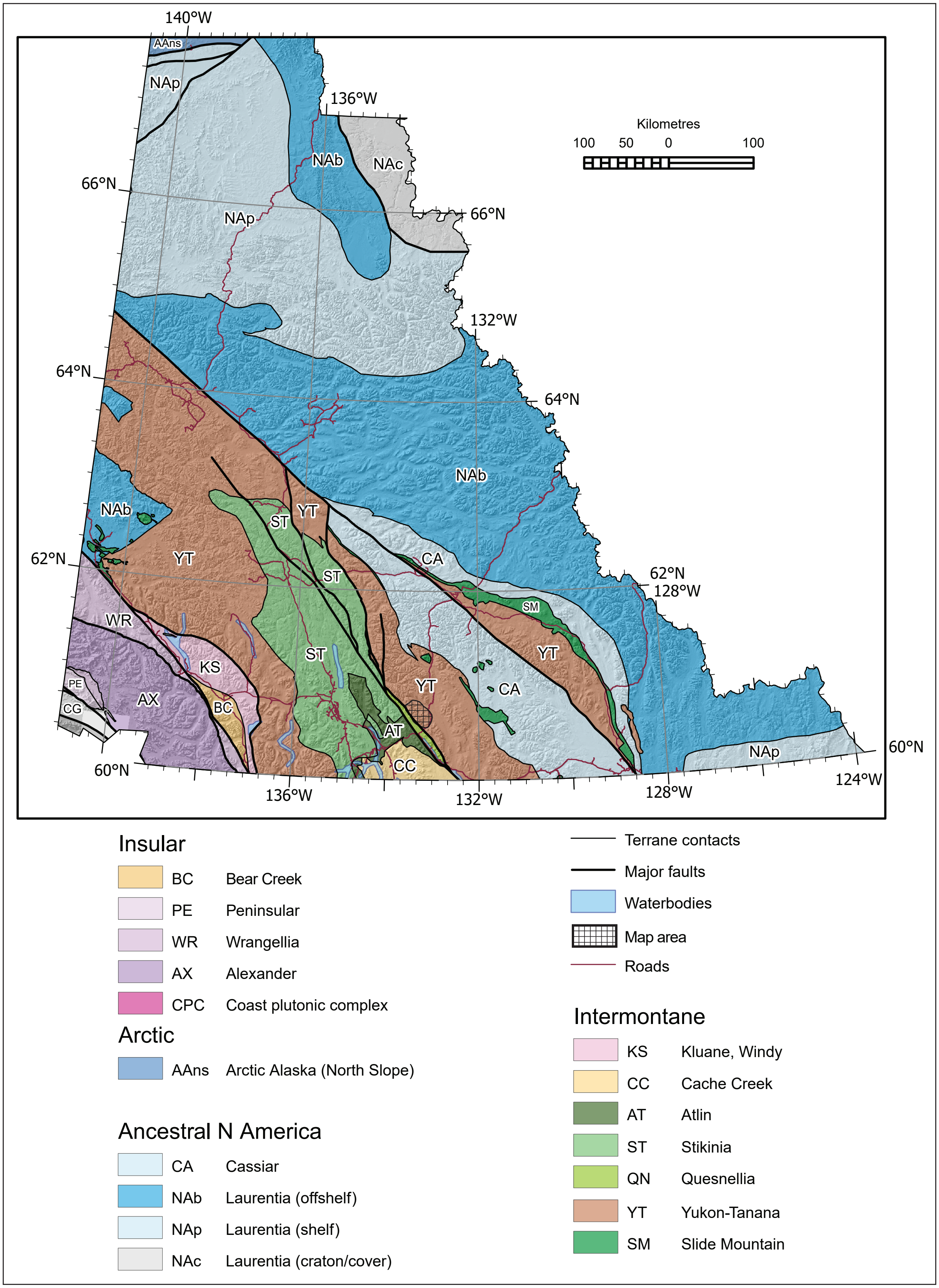

Figure 1. *Terrane map of southern Yukon (Yukon Geological Survey, 2022), showing the location of the study area (outlined).*

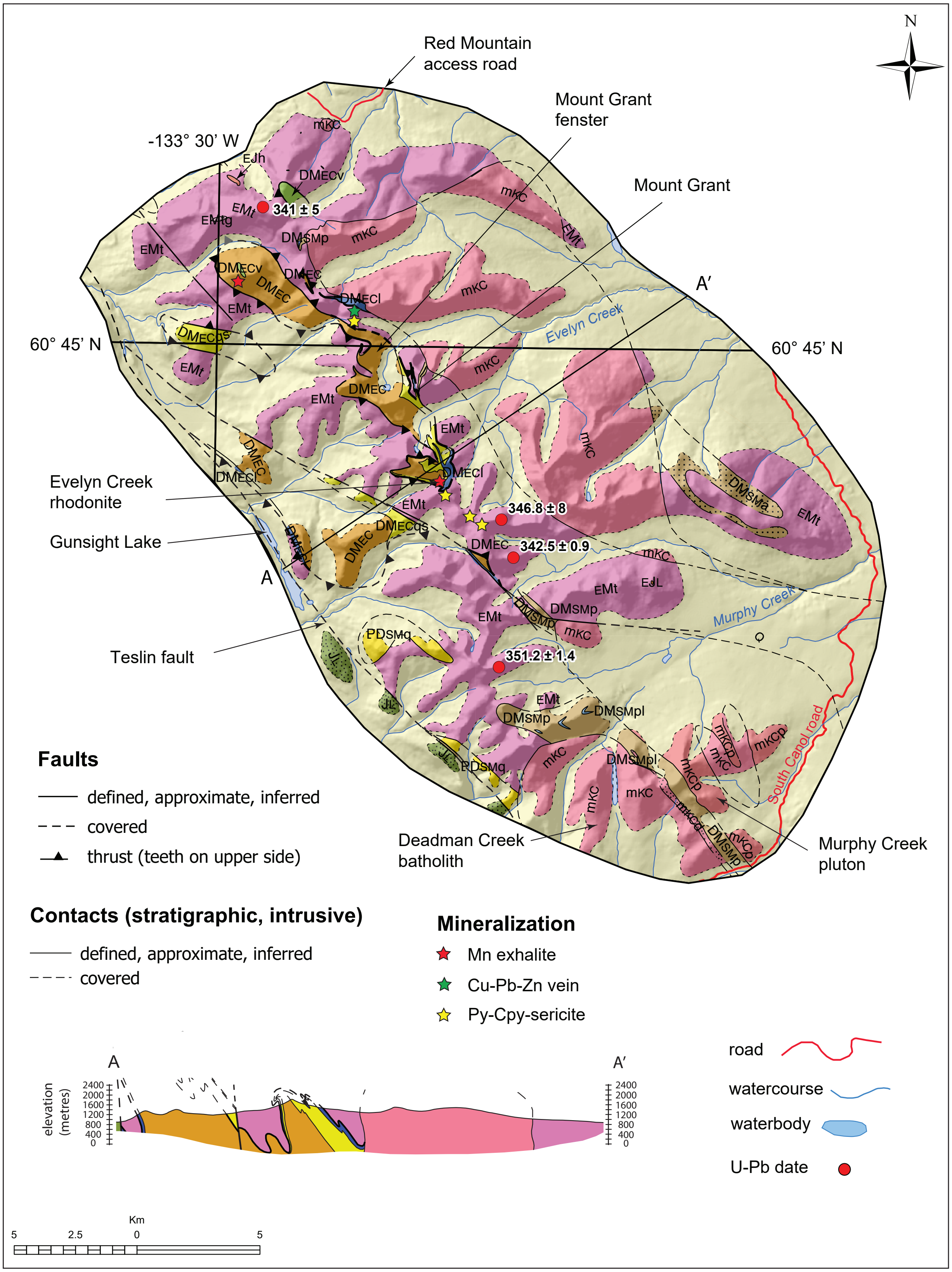

Figure 2. *Simplified geological map and cross-section (A-A') of the study area. Features and areas discussed in the text are labelled. U-Pb dates are from Stevens et al. (1996). Map legend on next page.*

LEGEND

CRETACEOUS

mKCp	Cassiar suite: porphyritic to megacrystic biotite granite
mKC	Cassiar suite: muscovite-biotite granodiorite; mostly equigranular
mKCd	Cassiar suite: deformed Bt-bearing quartz monzonite to granite; penetratively foliated and recrystallized.

TRIASSIC-JURASSIC

EJh	Lokken suite: hornblendite, hornblende-biotite pegmatite, monzodiorite

MISSISSIPPIAN

EMg	Simpson Range suite: metagranodiorite with abundant white mica, epidote; pink and green colour
EMtg	Simpson Range suite: garnet-amphibole-chlorite-muscovite schist; interpreted as recrystallized metatonalite

Quaternary

Q	Unconsolidated glacial, glaciofluvial and glaciolacustrine sediments; fluvial silt, sand and gravel deposits; volcanic ash; partly covered by soil and organic deposits

Jurassic

JL	Laberge Group: green siltstone, sandstone and conglomerate; commonly rhythmically layered with graded bedding

Devonian-Mississippian?

Evelyn Creek succession

DMECl	Evelyn Creek succession, upper: pale grey and white marble; calc-silicate
DMECv	Evelyn Creek succession: greenschist and metabasaltic breccia; amphibole-rich schist; jade-green metachert
DMECqs	Evelyn Creek succession, middle: chlorite-muscovite schist, quartzite
DMEC	Evelyn Creek succession, lower: grey, white and pale brown metachert; metachert with local pink or green partings; steel grey siliceous argillite; rare quartz grit in upper part

Slate Mountain succession

DMSMpl	Slate Mountain succession: medium to dark grey, sooty limestone and marble; interlayered with siliceous schist, commonly sulphide-rich; locally fossiliferous
DMSMp	Slate Mountain succession: grey, rusty weathering phyllite and graphitic siliceous schist; minor sooty limestone/marble lenses
PDSMq	Slate Mountain succession: micaceous quartzite, lesser pure white quartzite; semi-pelitic schist and metapsammite
DMSMa	Slate Mountain succession: amphibolite facies, coarse grained pelitic and semi-pelitic schist; commonly sillimanite-rich; quartzite; contains abundant small lenses of pegmatite and aplite, many of which have been penetratively deformed

Figure 2 *continued.*

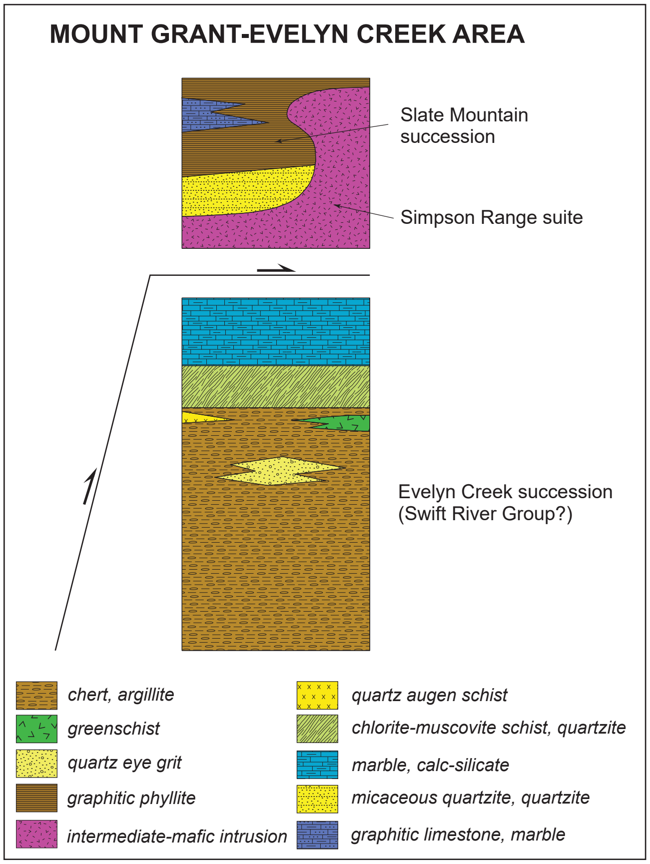

Figure 3. *Schematic summary of stratigraphic and tectonic relationships in the Mount Grant area. An upper structural level, comprising the Simpson Range suite and Slate Mountain succession is interpreted to have been thrust over the Evelyn Creek succession. Not to scale.*

The lower interval also includes extensive intervals of sooty grey siliceous argillite. While ostensibly similar to some fine-grained clastic rocks of the Slate Mountain succession, these rocks are more siliceous, and have little phyllitic sheen or penetrative cleavage, owing to the relative paucity of micaceous minerals. The grey siliceous argillite hosts resistant layers of white quartzite, which is also probably recrystallized metachert.

At one locality, a thick layer of quartz granule grit was identified within an interval of siliceous argillite and quartzite (Fig. 4e). In another locality, a single 30 cm-thick layer of greenschist is interlayered with metachert (Fig. 4f). A pale green quartz-eye schist was identified at a single location. This rock is highly strained and it contains millimetre-scale quartz and feldspar augen in a pale green sericite-rich matrix; it is interpreted as a volcanic rock or high-level subvolcanic intrusion. Each of these unusual rock types occur near the upper boundary of the lower division. A single garnet and amphibole-bearing layer was recognized in the lower part of the Evelyn Creek succession; elsewhere chlorite is widespread and higher-grade minerals were not recognized. The anomalous garnet-bearing horizon may result from an unusual bulk composition (e.g., a Mn-rich layer) rather than higher metamorphic grade.

The lower siliceous interval is overlain by grey or green chlorite-muscovite schist and quartzite (Fig. 5).

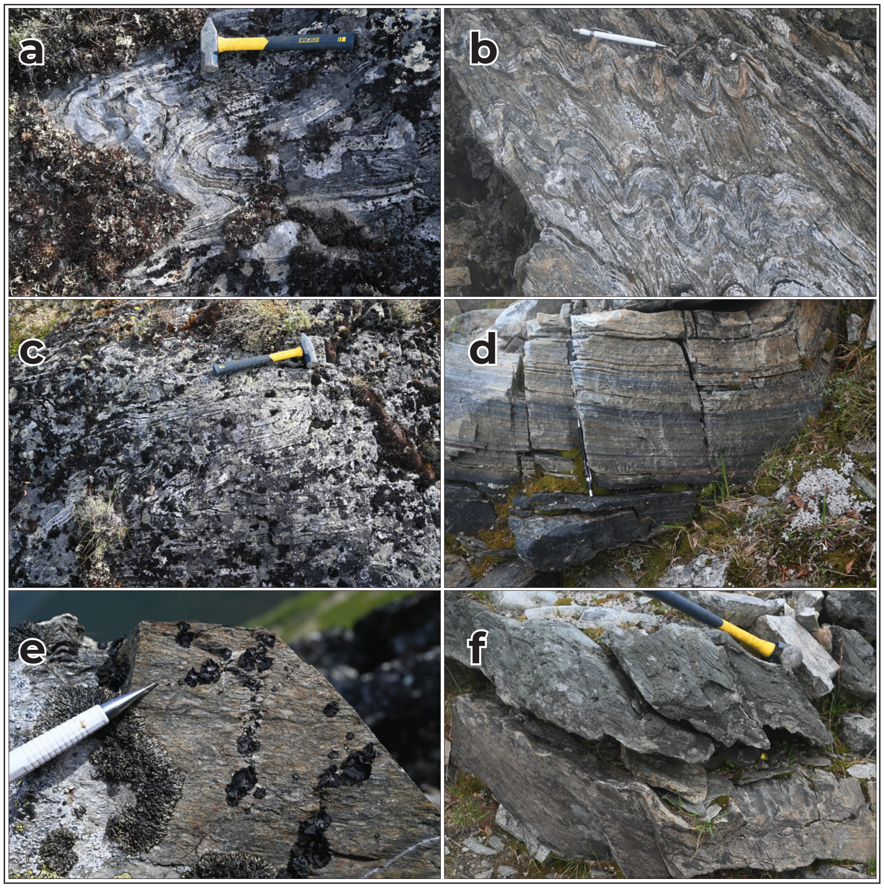

Figure 4. *Evelyn Creek succession, lower division.* ***(a)*** *Tight to isoclinally folded, white to pale grey metachert interlayered with grey weathering siliceous argillite. Hammer for scale.* ***(b)*** *Pale grey chert alternating with pale cream-brown weathering argillite layers. Pencil for scale.* ***(c)*** *Tight to isoclinally folded white to pale grey metachert. Hammer for scale.* ***(d)*** *Black metachert (lower part of outcrop) grades into pale metachert. The pale metachert includes numerous thin black layers. Pencil for scale.* ***(e)*** *Rare, thin (~30 cm thick) layer of metabasaltic greenschist within the metachert succession. Hammer for scale.* ***(f)****Grit layer containing quartz augen several mm in diameter. Pencil for scale.*

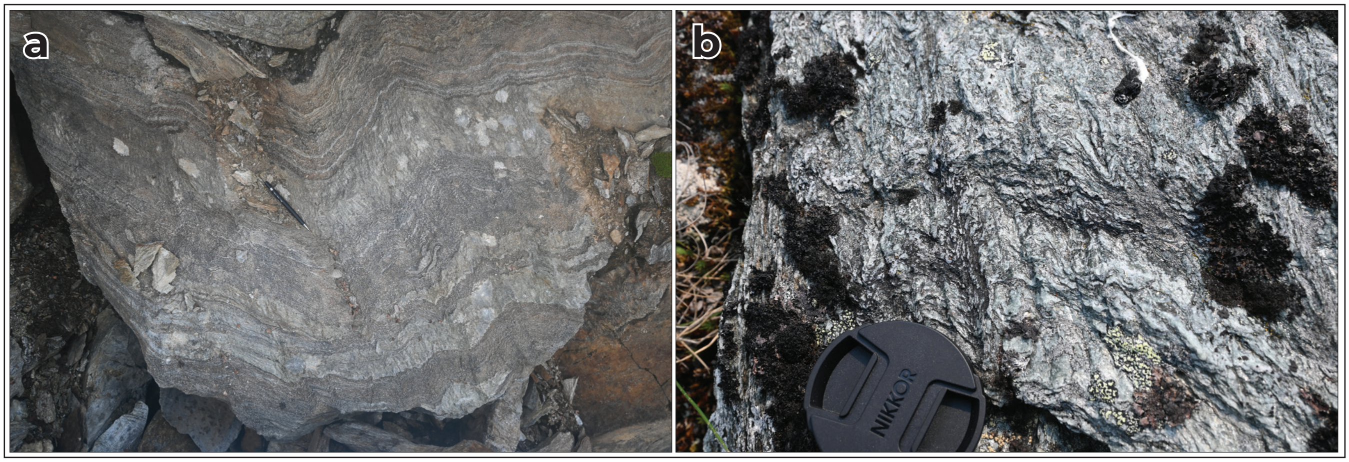

Figure 5. *Evelyn Creek succession, middle division.* ***(a)*** *Chlorite and muscovite-rich schist interlayered with layers of quartzite and quartz-rich schist. Pencil for scale.* ***(b)*** *Crenulated chlorite-muscovite schist, composed of streaky quartz-rich layers separated by chlorite and muscovite-rich folia. 46 mm lens cap for scale.*

Figure 6. *Evelyn Creek succession, upper division. Marble forms prominent, vegetation-poor exposures in the central part of the area. This example is from south of the Evelyn Creek rhodonite occurrence. Tents for scale. The elevation difference between the tents and the peak is approximately 120 m.*

The schist has variable mica content and ranges from near pure quartzite to highly crenulated/folded micaceous schist (Fig. 5 a,b). The quartzite is platy and pale grey to white, while the chlorite schist weathers pale brown to yellow and is grey green on fresh surfaces (Fig. 5b). This unit is relatively resistant, but does not form the massive slabby outcrops exhibited by many rocks of the Simpson Range suite. The contact between metachert and the overlying schist is sharp (over <1 m) but was not directly observed.

The upper division of the Evelyn Creek succession is a thick (tens of metres thick) band of marble and calc-silicate. The marble is white or grey on fresh surfaces and weathers pale grey to buff; and locally, near the contact with the underlying schist the marble weathers yellow to pale brown. The marble unit includes varying proportions of siliceous folia and selvages, and zones of calc-silicate. The bright colour and vegetation-free character of the marble make it easily identifiable from a distance (Fig. 6). The marble is thoroughly recrystallized and no fossil remnants were identified. Some interlayering of marble and chlorite schist was noted at the contact between these units, but it is unclear whether this results from sedimentary alternation or (more likely) structural repetition.

The marble is in sharp contact with overlying metatonalite (Fig. 7). This is generally a single surface, but centimetre-scale repetition of the contact was observed at one locality. The contact is invariably parallel to the foliation in marble and metatonalite, and no metatonalite was identified in the underlying rocks. This contact is interpreted as a fault due to the sharp, geographically extensive nature of the surface, the absence of metatonalite below the surface, and the contrasting nature of the rock units above and below the metatonalite. Where marble is absent, metatonalite is in direct contact with lower parts of the Evelyn Creek succession along the same fault.

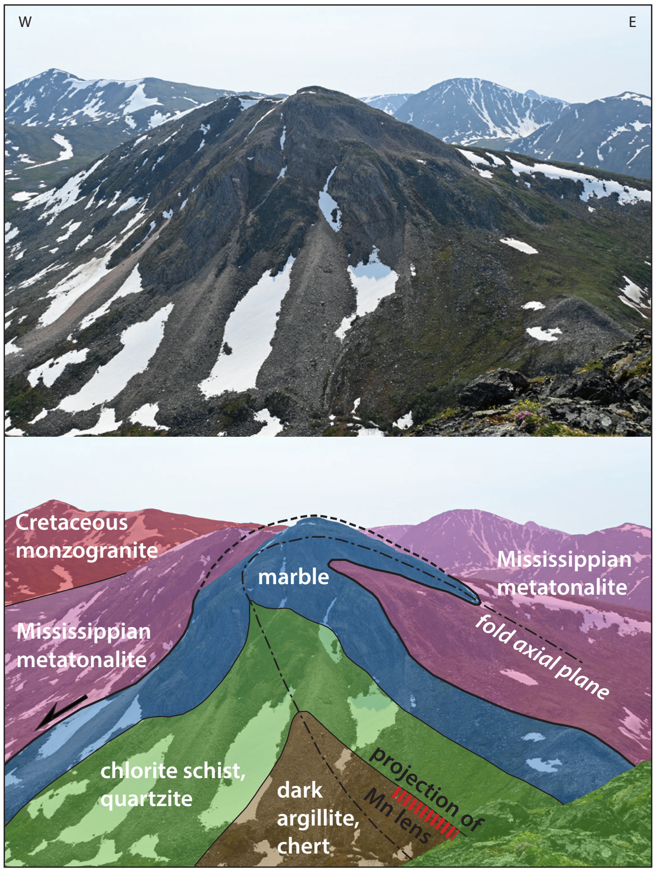

Figure 7. *View towards the south of the hillslopes, south of the Evelyn Creek rhodonite occurrence. The Mn lens is hosted by metachert in the core of a refolded fold, above which lies chlorite schist, quartzite and a thick marble. The marble is in contact with metatonalite of the Simpson Range suite. This contact is interpreted to be a folded thrust fault. The height of the slope facing the viewer (to the peak underlain by marble) is approximately 220 m.*

There are two small regions of anomalous rock types in the northern part of the area that have been recorded as a separate map unit (DMECv). Carbonate-altered mafic volcanic breccia and amphibole schist is in contact with metatonalite of the Simpson Range suite. The breccia is mostly composed of clasts of greenschist but includes some serpentinite clasts, while the amphibole schist is a banded, pale green unit with abundant crystals of metamorphic amphibole and biotite. To the southwest, there is another small region of foliated greenschist that is interlayered with jade green metachert. These outcrops are adjacent to more typical rocks of the Evelyn Creek succession, but the contacts are not exposed. These two small belts may represent a volumetrically minor part of the Evelyn Creek succession; alternatively they may be a younger unit.

The lower part of the Evelyn Creek succession is similar to the Swift River Group of the Yukon–BC border region (Roots et *al*., 2006). The Swift River Group is overlain by a thick Mississippian limestone/marble unit, which could plausibly correlate with the upper division of the Evelyn Creek succession. Further age constraints are required to evaluate this possible correlation.

Mississippian metatonalite (Simpson Range plutonic suite)

Most of the central part of the Big Salmon Range in the study area is underlain by Mississippian metatonalite of the Simpson Range plutonic suite (Fig. 8). The rocks are plagioclase-rich schist and gneiss with variable amounts of mafic minerals, now mostly represented by chlorite (Fig. 8a, see Moynihan and Crowley, 2022 for further description and images). There is a broad range of composition from quartz diorite to granodiorite and many outcrops are compositionally variable, with a banded or streaky appearance. Distinctive varieties include leucotonalite, and metatonalite with abundant long bladed amphibole crystals or pseudomorphs (Fig. 8b). The latter is mostly developed near structural boundaries and is locally sulphide-rich. In most places, metatonalite is well foliated, strongly recrystallized, and the dominant foliation is commonly overprinted by younger fold structures.

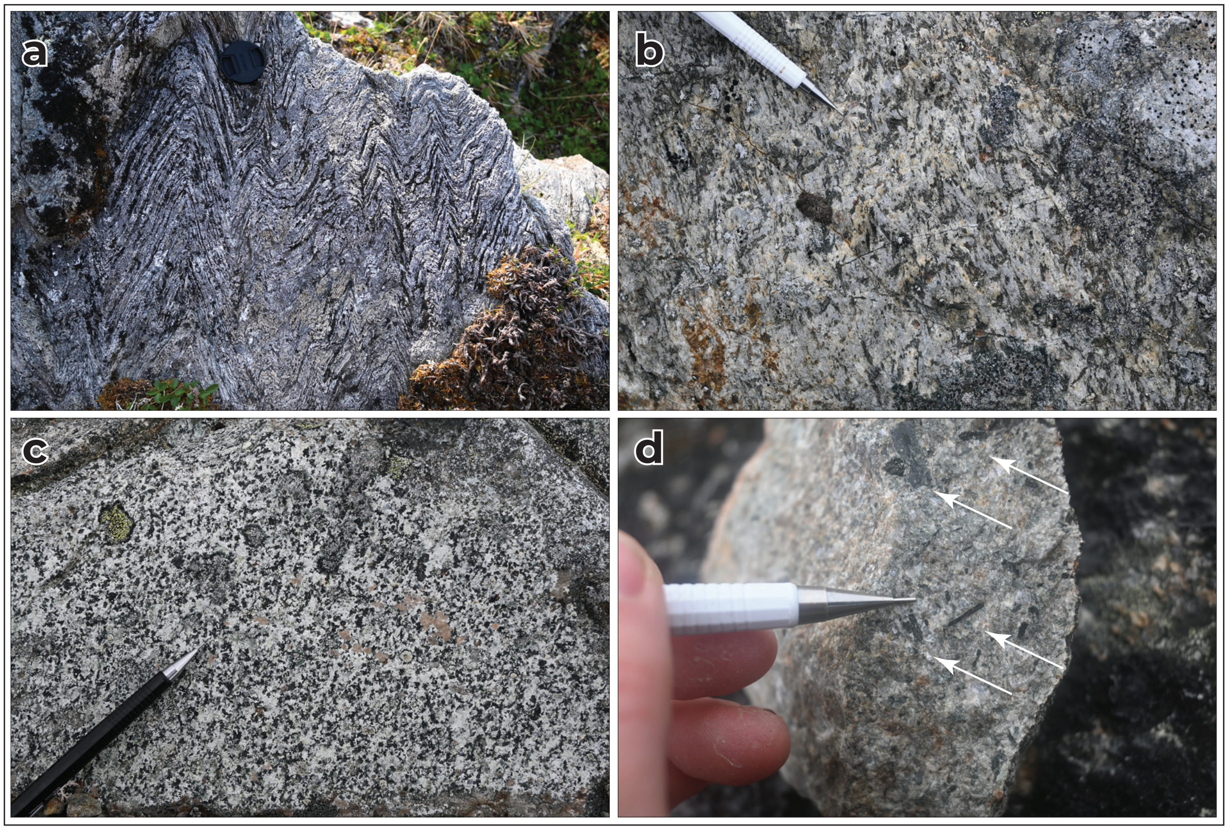

Figure 8. *Simpson Range suite.* ***(a)*** *Metatonalite is penetratively foliated and commonly folded in much of the area. 46 mm lens cap for scale.* ***(b)*** *Foliated, sulphide-rich metatonalite with abundant elongate amphibole crystals. Pencil for scale.* ***(c)*** *Hornblende metatonalite in the southern part of the area is locally non-foliated.* ***(d)*** *Primary twinned hornblende crystals are preserved in non-foliated metatonalite. Plane polarized light; field of view is 2.8 mm.*

In contrast, some of the tonalite in the southern part of the area (structurally high in the metatonalite sheet) lacks penetrative deformation, and primary (igneous) crystals are preserved (Fig. 8c,d). Garnet-chlorite-muscovite schist is developed in a small region within metatonalite in the northern part of the area (map unit EMtg). This schist has gradational boundaries with non-garnet-bearing metatonalite, which is interpreted as the protolith of the schist.

Slate Mountain succession

In the southern part of the area, on the eastern flank of the Big Salmon Range, metatonalite is overlain by graphitic phyllite and associated rocks, all of which exhibit a penetrative foliation. These are similar to rocks exposed farther north in the Big Salmon Range (Moynihan and Crowley, 2022). The main rock type is rusty weathering, dark grey graphitic phyllite (Fig. 9a). This is thinly interlayered with pale grey siliceous quartzite, and locally with sooty grey limestone or marble (Fig. 9b). Limestone layers range from centimetre-thick intervals within graphitic phyllite and siliceous schist, to limestone-dominated intervals several metres to tens of metres thick. Limestone is generally sooty grey to blue–grey and thinly laminated. Locally, it contains resistant nodules from 2 mm to 2 cm in diameter (Fig. 9c). Where affected by contact metamorphism adjacent to the Murphy Creek pluton, calcareous layers weather buff to yellow and comprise a mix of relatively pure marble and calc-silicate layers; the boundaries between these rock types are irregular and siliceous layers are commonly disarticulated.

On the west flank of the Big Salmon Range in the southern part of the area, metatonalite is in contact with interlayered phyllite, metasandstone and quartzite. The quartzite layers are typically tens of centimetres-thick, weather white, and are white and translucent on fresh surfaces. Poorly sorted detrital grains are visible and range from medium to very coarse sand-sized particles. Metasandstone is grey and fine-grained with indistinct layering. Phyllite is cream to brown weathering and fresh surfaces are grey to pale green. Primary thin laminations are locally discernible in the phyllite. In addition to quartzite and phyllite, the succession includes rare cream to brown weathering calcareous layers less than 30 cm thick.

While phyllite is generally penetratively foliated throughout, there is significant variation in the degree of strain recorded by these rocks. Quartzite lacks a penetrative foliation, whereas adjacent to the southwestern boundary of the Mount Grant batholith, it exhibits a foliation and stretching lineation. In some locations near the trace of the Teslin fault, foliated quartzite is brecciated and the foliation rotated between adjacent breccia clasts (Fig. 9d).

Several thin screens of Slate Mountain succession are included within metatonalite. A screen on Mount Grant includes garnet schist, garnet-bearing amphibole schist (calc-silicate) and marble. It is not clear whether these rocks record regional metamorphism, contact metamorphism from the nearby Cretaceous intrusion, or both.

In the easternmost part of the area, metatonalite is in contact with polydeformed amphibolite-facies, semi-pelitic to pelitic schist (Fig. 10). The schist is rusty brown weathering, coarse grained and comprises biotite, muscovite, quartz, plagioclase and andalusite ± sillimanite; the presence of the latter minerals indicates low pressure metamorphism. The schist is interlayered with quartzite layers centimetre to decimetre thick and locally marble or calc-silicate. The schist is locally migmatitic, with abundant, variably deformed granitic lenses and pods, including pegmatite and aplite (± muscovite, garnet) similar to that exposed in the region between the Deadman Creek batholith and Murphy Creek pluton (see below).

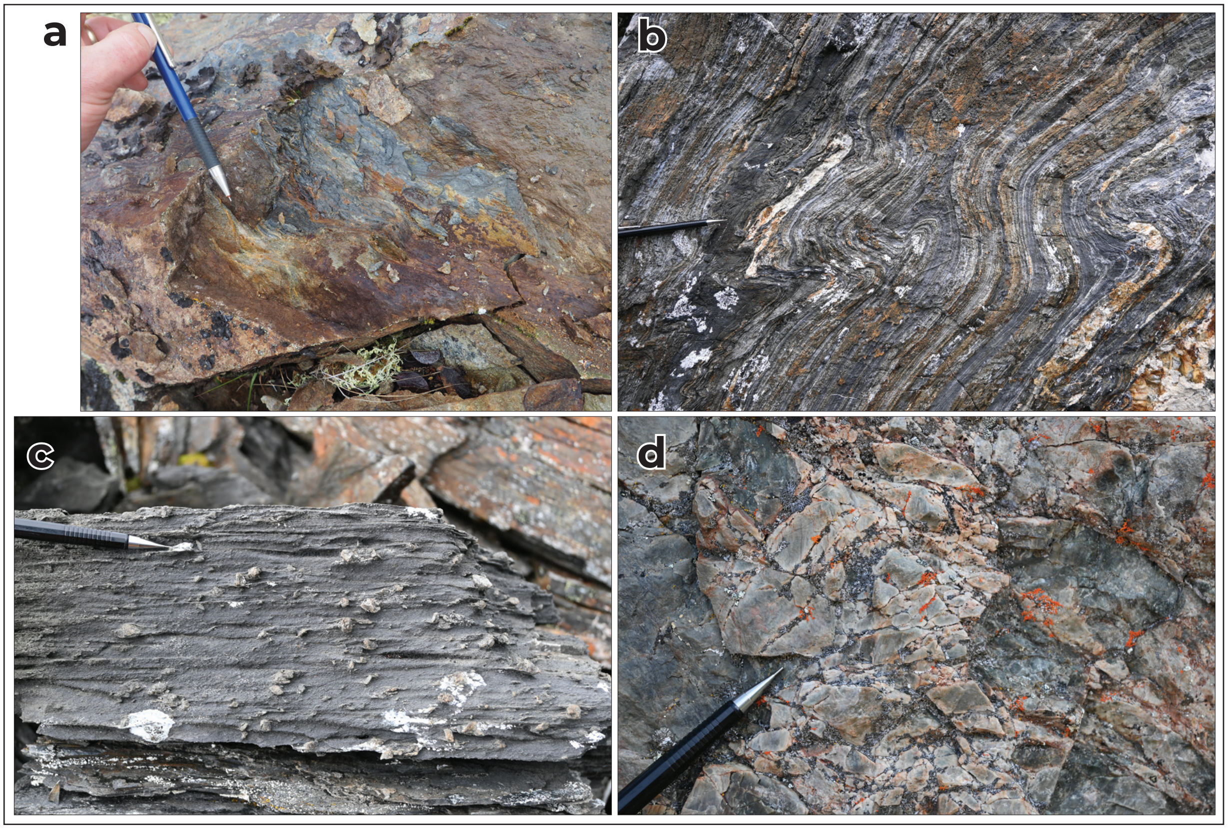

Figure 9. *Slate Mountain succession.* ***(a)*** *Rusty weathering graphitic phyllite. Pencil for scale.* ***(b)*** *Interlayered sooty limestone and sulphide-rich, siliceous schist. Pencil for scale.* ***(c)*** *Grey carbonaceous limestone with prominent nodules (fossil pseudomorphs?). Pencil for scale.* ***(d)*** *Quartzite of the Slate Mountain succession is brecciated near the trace of the Teslin fault. Pencil for scale.*

This belt of schist/gneiss is interpreted as part of the Slate Mountain succession that was metamorphosed at higher grade than other parts of the succession.

Cassiar suite intrusions and associated rocks

The eastern part of the Mount Grant batholith includes a large body of largely non-deformed biotite quartz monzonite, and similar intrusions occupy most of the southernmost part of the study area (Fig. 2). These plutons are assigned to the Cassiar plutonic suite based on their composition, their largely non-deformed nature, and their similarity/continuity with dated intrusions.

The pluton east of Mount Grant is composed of mostly equigranular, locally sparsely K-feldspar porphyritic, coarse-grained biotite quartz monzonite to granite (Fig. 11a,b). The western and northern contacts were observed, and each is sharp, with no deformation of the intrusive rock near these boundaries.

To the south, the Murphy Creek pluton is dominated by porphyritic biotite quartz monzonite or granite. K-feldspar phenocrysts are abundant (Fig. 11c,d) and glomerophyric clusters are locally developed (Fig. 10e). A second, volumetrically less significant phase within this pluton is pale grey, equigranular, finer grained biotite granite (Fig. 11f). The Murphy Creek pluton is not deformed, except for a narrow zone along its northern boundary. Here, there is a foliated zone approximately 5 m wide that includes scaly slip surfaces with subhorizontal slickenlines. An intrusive boundary on the western margin of the Murphy Creek pluton is indicated by the presence of an andalusite-bearing contact aureole in the narrow belt of country rocks separating it from the Deadman Creek batholith (Fig. 2).

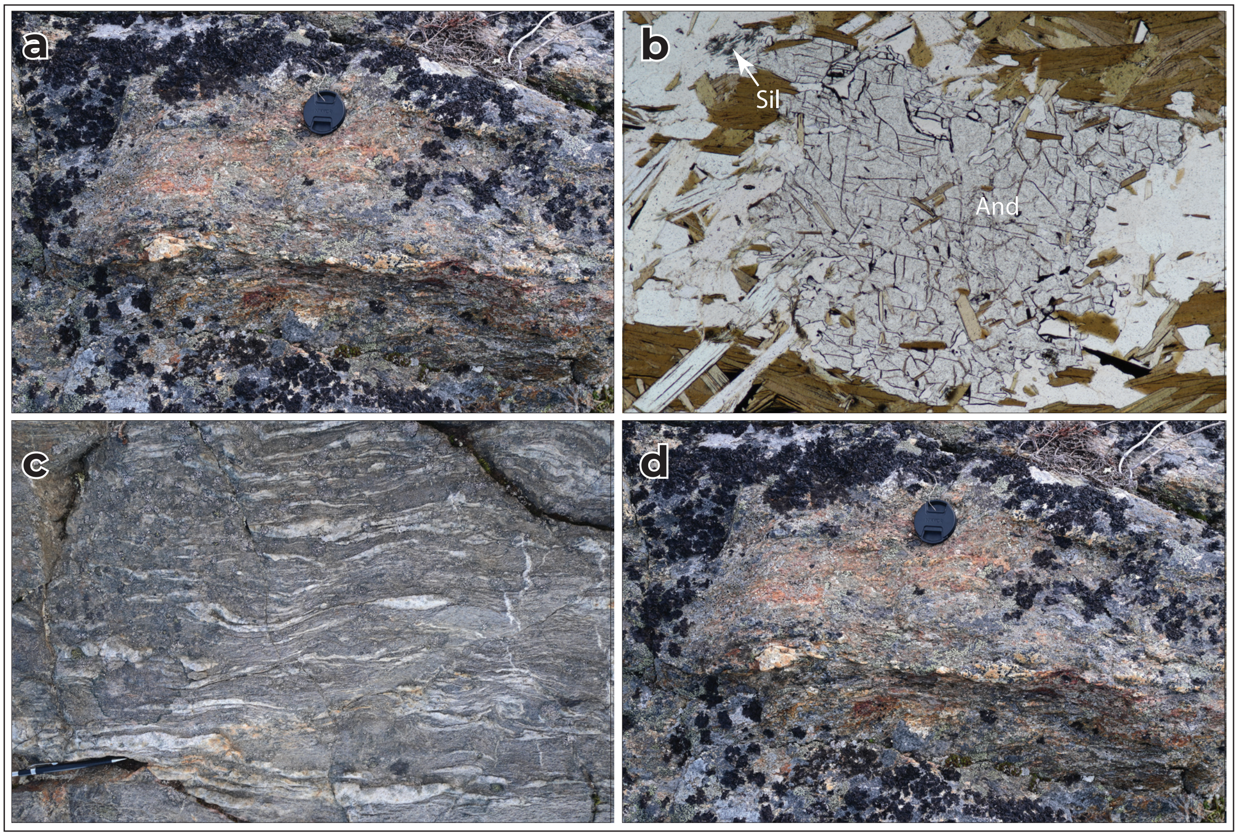

Figure 10. *Amphibolite-facies schist and gneiss in the eastern part of the study area.* ***(a)*** *Coarse, rusty-weathering metapelitic schist. 46 mm lens cap for scale.* ***(b)*** *Andalusite and sillimanite in pelitic schist indicates low pressure metamorphism. The field of view is ~2.8 mm; plane polarized light.* ***(c)*** *and* ***(d)*** *The amphibolite-facies schist contains abundant layers, lenses and pods of leucosome. These exhibit a range of relationships to the foliation, suggesting their generation and emplacement during deformation. Pencil for scale in* ***(c)*** *and* ***(d)****.*

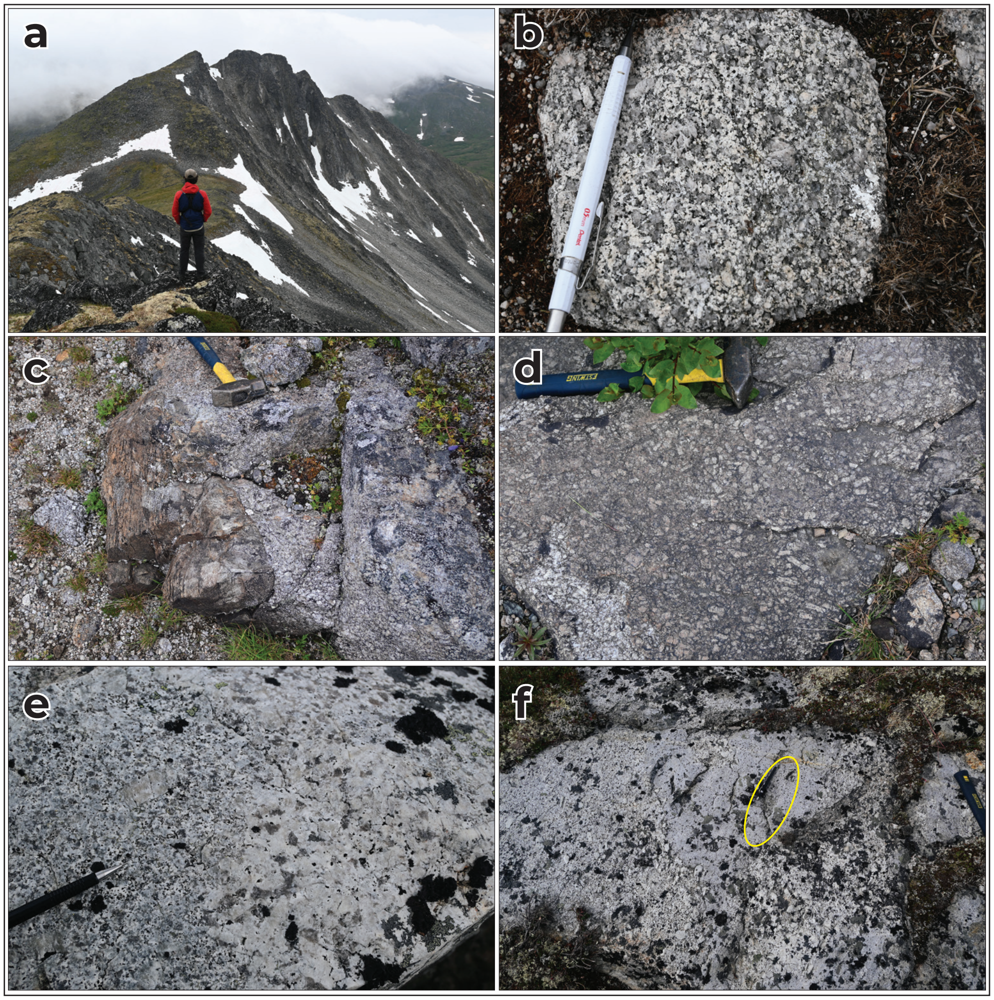

Figure 11. *Undeformed Cretaceous intrusions.* *(a) Steep talus slopes derived from granitic rocks in the northern part of the Mount Grant batholith (Cassiar suite phase). Man for scale.* *(b) Coarse-grained, mostly equigranular biotite quartz monzonite from the northern part of the Mount Grant batholith (Cassiar suite phase). Pencil for scale.* *(c) Sharp contact between country rock (metasandstone of the Slate Mountain succession) and porphyritic biotite quartz monzonite of the Murphy Creek pluton. Hammer for scale.* *(d) Close-up view of crowded porphyritic texture near the western margin of the Murphy Creek pluton. Hammer for scale.* *(e) Boundary between a glomerophyric cluster and sparsely porphyritic phase of the Murphy Creek pluton. Pencil for scale.* *(f) Boundary between relatively fine-grained, pale grey, equigranular biotite quartz monzonite and coarse, porphyritic phase of the Murphy Creek pluton. Pencil for scale.*

The northern end of the Deadman Creek batholith extends across the Canol Road into the southernmost part of the area (Fig. 2). Most of this is non-foliated, coarse-grained biotite quartz monzonite with intergrown perthitic, pink K-feldspar, white plagioclase and grey quartz. Locally hornblende is also present. The eastern boundary of the Deadman Creek batholith is marked by a zone of deformation approximately 200–300 m wide (Fig. 12a–c). There is an eastward increase in strain across this zone from unfoliated massive granitoid to slabby outcrops of recrystallized biotite-bearing orthogneiss with foliation that dips NE at moderate angles. The most deformed rocks exhibit stretching lineations that are approximately down the dip of the foliation (Fig. 12c).

The belt of country rock that separates the Murphy Creek pluton and Deadman Creek batholith (Fig. 2) is host to numerous small lenses (from <1 m to tens of metres long) of pegmatite and aplite (Fig. 12d–f). Pegmatite locally contains coarse muscovite and/or garnet (Fig. 12f). These lenses are variably foliated and recrystallized. The boundaries of these intrusions generally crosscut the foliation (Fig. 12e), indicating emplacement relatively late in the deformation history, after much of the strain recorded in the country rocks had accumulated.

Other intrusions

An intrusion of hornblendite and diorite forms cliffs above the Red Mountain access road, in the northernmost part of the area. This is similar to other intrusions of the Lokken suite farther north (Sack et al., 2020; Moynihan and Crowley, 2022). Small hornblende-diorite dikes that are assigned to this suite were also identified in other parts of the area,

Figure 12. *Deformed Cretaceous intrusions.* ***(a)*** *Moderately foliated hornblende-biotite granodiorite from the northern part of the Deadman Creek batholith. Pencil for scale.* ***(b)*** *Slabby outcrops formed by highly strain rocks along the eastern margin of the Deadman Creek batholith. Hammer for scale.* ***(c)*** *A down-dip mineral lineation is developed in the outcrops. 46 mm lens cap for scale.* *d) Foliation in deformed portion of the Deadman Creek batholith is cut by more weakly deformed aplite and pegmatite. 46 mm lens cap for scale.* ***(e)*** *Similar pegmatite and aplite intrusions crosscut the foliation in adjacent phyllite of the Slate Mountain succession. Variable recrystallization and foliation of these intrusions demonstrates reactivation of the dominant foliation during or after their emplacement. Hammer for scale.* ***(f)*** *Abundant garnet in pegmatite that intrudes the Slate Mountain succession adjacent to the eastern flank of the Deadman Creek batholith. Some of these intrusions also contain coarse-grained muscovite. Pencil for scale.*

in the Evelyn Creek succession and the Simpson Range suite. These intrusions are not penetratively deformed. Other minor, post-tectonic biotite-bearing dikes were also observed.

Laberge Group

Rocks of the Laberge Group are exposed west of the Teslin fault, where they form bluffs overlooking the Teslin River valley. They were only given a cursory examination during this study. The outcrops are dominated by mint green, cream to brown weathering siltstone and sandstone, with lesser conglomerate. Siltstone-sandstone exhibits fine laminations and rhythmic layering.

Mineralization

The Evelyn Creek stratiform rhodonite occurrence (also known as the Marlin; Yukon MINFILE 105C 017) is located near the crest of the Big Salmon Range (Figs. 2 and 13). The mineralized zone has been traced for approximately 350 m along strike; the main pod is 4–7 m wide with a strike length of ~25 m (Shearer, 1991). The ore rock, which is coated in black Mn oxide, includes raspberry red and pink gemstone composed of combinations of the minerals tephroite, rhodonite, rhodochrosite, bustamite and spessartine (Shearer, 1991). The host rock is metachert of the lower Evelyn Creek succession and the Mn lens is close to the top of this unit, near the contact with the overlying chlorite schist-quartzite unit. The pit where mining has taken place exposes a crosscutting dike of hornblende diorite, which is similar to other parts of the Lokken suite and therefore probably Early Jurassic. Rock similar to the host chert is widely distributed in the area; and another zone of black Mn oxide staining was recognized near the northern end of the Mount Grant fenster, approximately 11.5 km away (60.772943 N, -133.484435 W; Fig. 2). This suggests there is potential for further identification of stratiform Mn, and possibly VMS mineralization elsewhere in the lower Evelyn Creek succession.

Other mineralization reported in the area includes vein hosted Cu, base metal and Mo vein mineralization (Yukon MINFILE 105C 018, 105C016, 105C 030). Elsewhere, galena, sphalerite and malachite vein-hosted mineralization was observed along the margin of a post-tectonic dike (60.763450 N, -133.400756 W; Fig. 2). Metatonalite of the Simpson Range suite locally contains rusty weathering, approximately strike-parallel gossanous zones that range in thickness from metres to tens of metres (e.g., at 60.689538 N, -133.308202 W and 60.670557 N, -133.404287 W; Fig. 2). These zones include altered, sulphide-rich metatonalite that contains abundant pyrite, chalcopyrite and Cu-bearing replacement products, and more heavily altered sericite-rich rock.

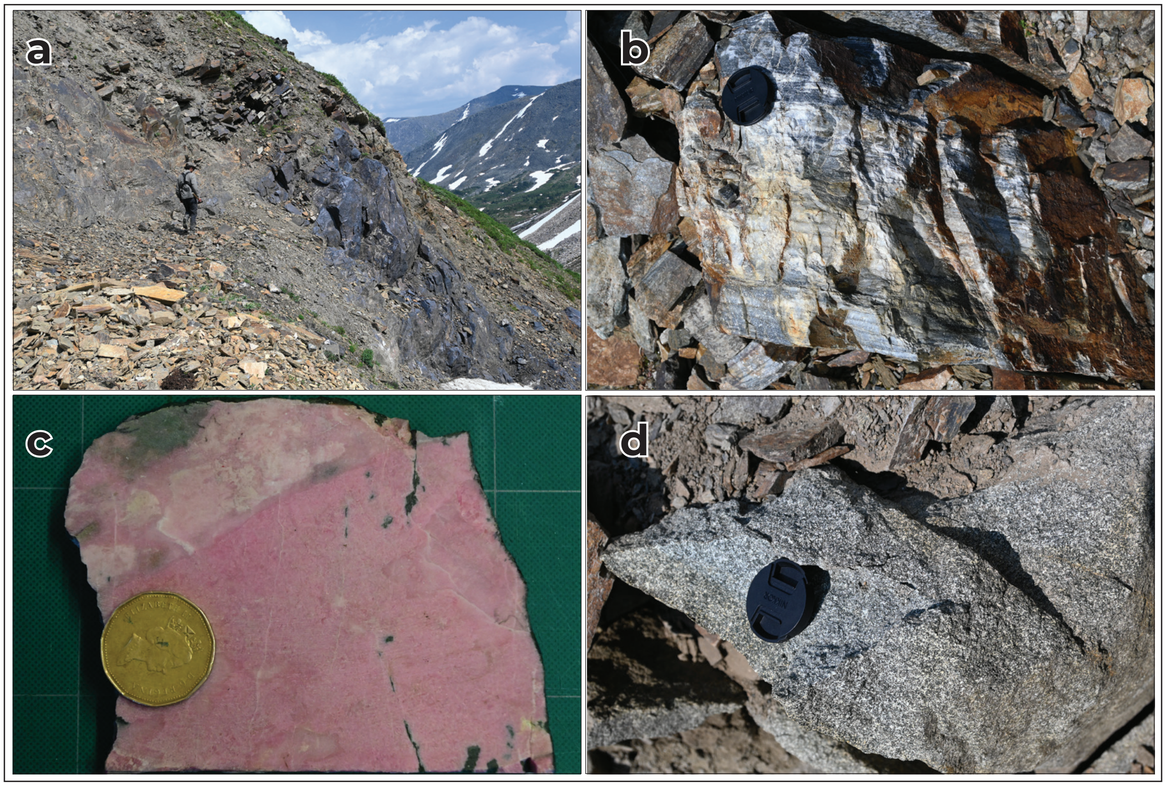

Figure 13. *Geology of the Evelyn Creek rhodonite occurrence.* ***(a)*** *Black weathering oxidized Mn-rich lens at the Marlin occurrence. Man for scale.* ***(b)*** *The Mn-enriched lens passes laterally into metachert. 46 mm lens cap for scale.* ***(c)*** *Pink rhodonite and associated minerals on freshly cut surface. Dollar coin for scale.* ***(d)*** *The pit where rhodonite has been extracted includes a dike of hornblende diorite. These dikes, which are scattered throughout the broader area, are interpreted to form part of the Early Jurassic Lokken suite. 46 mm lens cap for scale.*

Acknowledgements

Thanks to Matteo Ferri for his enthusiastic assistance in the field, to Maurice Colpron for reviewing an earlier version of the manuscript, and to Karen MacFarlane for technical editing and production.

References

Colpron, M., Nelson, J.L. and Murphy, D.C., 2006. A tectonostratigraphic framework for the pericratonic terranes of the northern Cordillera. In: Paleozoic Evolution and Metallogeny of Pericratonic Terranes at the Ancient Pacific Margin of North America, Canadian and Alaskan Cordillera, M. Colpron and J.L. Nelson (eds.), Geological Association of Canada, Special Paper 45, p. 1–23.

Mortensen, J.K., 1992. Pre-Mid-Mesozoic tectonic evolution of the Yukon-Tanana terrane, Yukon and Alaska. Tectonics, vol. 11, p. 836–853.

Moynihan, D. and Crowley, J.L., 2022. Preliminary observations on the geology of the southern Big Salmon Range, south-central Yukon (parts of NTS 105C/13,14, 105F/4 and 105E/1). *In:* Yukon Exploration and Geology 2021, K.E. MacFarlane (ed.), Yukon Geological Survey, p. 217–265.

Mulligan, R., 1963. Geology of Teslin map-area. Geological Survey of Canada, Memoir 326, 96 p.

Murphy, D.C., Mortensen, J.K., Piercey, S.J., Orchard, M.J. and Gehrels, G.E., 2006. Mid-Paleozoic to early Mesozoic tectonostratigraphic evolution of Yukon-Tanana and Slide Mountain terranes and affiliated overlap assemblages, Finlayson Lake massive sulphide district, southeastern Yukon. In: Paleozoic Evolution and Metallogeny of Pericratonic Terranes at the Ancient Pacific Margin of North America, Canadian and Alaskan Cordillera, M. Colpron and J.L. Nelson (eds.), Geological Association of Canada, Special Paper 45, p. 75–105.

Roots, C.F., Nelson, J.L., Simard, R.-L. and Harms, T.A., 2006. Continental fragments, mid-Paleozoic arcs and overlapping late Paleozoic arc and Triassic sedimentary strata in the Yukon-Tanana terrane of northern British Columbia and southern Yukon. *In:* Paleozoic Evolution and Metallogeny of Pericratonic Terranes at the Ancient Pacific Margin of North America, Canadian and Alaskan Cordillera, M. Colpron and J.L. Nelson (eds.), Geological Association of Canada, Special Paper 45, p. 153–177.

Sack, P.J, Colpron, M., Crowley, J., Ryan, J., Allan, M.M., Beranek, L.P. and Joyce, N.L., 2020. Atlas of Late Triassic to Jurassic plutons in the Intermontane terranes of Yukon. Yukon Geological Survey, Open File 2020-1, 365 p.

Shearer, 1991. Geological, trenching and mining report on the Evelyn Creek rhodonite property (Eve claims), South Canol road area, Whitehorse mining district, Yukon Territory. Yukon Department of Energy, Mines and Resources, Assessment Report 092977.

Stevens, R.A., 1993. Geology of the Teslin suture zone in parts of Laberge (105E/1), Quiet Lake (105F/4) and Teslin (105C/11,13,14) map areas, Yukon territory. Geological Survey of Canada, Open File 2768.

Stevens, R.A., Erdmer, P., Creaser, R.A. and Grant, S.L., 1996. Mississippian assembly of the Nisutlin assemblage: evidence from primary contact relationships and Mississippian magmatism in the Teslin tectonic zone, part of the Yukon-Tanana terrane of south-central Yukon. Canadian Journal of Earth Sciences, vol. 33, p. 103–116.

Yukon Geological Survey, 2020. Yukon MINFILE - A database of mineral occurrences. Yukon Geological Survey, http://data.geology.gov.yk.ca, [accessed December 2022]

Yukon Geological Survey, 2022. A digital atlas of terranes for the northern Cordillera. Yukon Geological Survey, http://data.geology.gov.yk.ca/Compilation/2, [accessed December 2022].

Mapping the rate of change of select glaciers using satellite and ground-based observations, Yukon and northwestern British Columbia

Moya Painter*, Derek C. Cronmiller and Jeffrey D. Bond
Yukon Geological Survey

Painter, M., Cronmiller, D.C. and Bond, J.D., 2023. Mapping the rate of change of select glaciers using satellite and ground-based observations, Yukon and northwestern British Columbia. *In:* Yukon Exploration Geology 2022, K.E. MacFarlane (ed.), Yukon Geological Survey, p. 109–126.

Abstract

Glacier mass loss is accelerating throughout Yukon. This mass loss is confirmed by multiple studies and methods. New remotely-sensed and field-measured terminus retreat rates for select glaciers representative of the glaciated watersheds throughout Yukon are presented and compared to previous studies. Photographic data and measurements from field monitoring stations occupied from 2004 to 2022 confirm rapid mass-loss and provide relatable images for communicating the striking rate of glacier retreat. The rapid rate of glacier mass loss in Yukon will have variable impacts on downstream hydrology including discharge, temperature, chemistry, sedimentation and turbidity that are, with some exceptions, poorly quantified at present.

* Moya.Painter@yukon.ca

Introduction

Glaciers are perennial bodies of ice that move under their own mass through internal deformation, deformation of their beds, and sliding. Glaciers grow when the input of snow and ice from precipitation exceeds the output of melt, evaporation, or calving at the terminus (Benn and Evans, 2014) and shrink when the reverse is true. Glaciers are dynamic systems and sensitive to changes in the earth's climate, primarily precipitation and air temperatures. In the north, air temperatures are warming at more than double the rate of the global average, driven by anthropogenic contributions of greenhouse gases into the atmosphere (Meredith et *al*., 2019). Global glacier mass loss has accelerated in tandem with atmospheric warming (Hugonnet et *al*., 2021). Glaciers have an important influence on various aspects of hydrological and ecological systems, including, but not limited to, fish habitat, water temperatures, flow regulation and hydropower generation. This study outlines the current state of glaciers in Yukon and northwestern BC, and how they have changed since the late 1980s. Eleven glaciers were selected from the upper Yukon River basin, six from the St. Elias Mountains, four from the Mackenzie Mountains, and three from the Coast Mountain Plateau (Fig. 1). This paper gives an overview of the history of Yukon's glaciations and recent glaciological studies, summarizes the findings from selected glaciers, and provides a foundation for future monitoring.

Glacial history

Glacial extent in Yukon has fluctuated considerably throughout the Quaternary, from massive ice sheets covering much of the territory, to large-scale recession during interglacial warm periods relegating ice to high alpine locations. The Pleistocene glaciations of Yukon were comprehensively mapped in 1999 (Duk-Rodkin). Duk-Rodkin (1999) identified three main glacial extents of the Cordilleran Ice Sheet (CIS), which was the main ice sheet in Yukon. These three main limits were: the pre-Reid, a composite of ten or more separate glaciations from the latest Pliocene to marine-oxygen isotope stage (MIS) 8 or 10 (Barendregt et *al*., 2010); Reid (MIS 6); and McConnell (MIS 2) glaciations (Fig. 1). Even during the least extensive of the three, the CIS covered a large portion of Yukon and British Columbia (Duk-Rodkin, 1999; Menounos et *al*., 2009). The CIS comprised several lobes flowing out from source regions in the St. Elias Mountains in southwestern Yukon, Ogilvie Mountains in the north, Selwyn Mountains in northeastern Yukon, Cassiar and Coast Mountains in northern British Columbia, and the Pelly Mountains in central Yukon. The McConnell Glaciation was the most recent and least extensive of the three glaciations, reached its maximum approximately 16 500 years ago, and disappeared by the beginning of the Holocene, approximately 11 700 years ago (Menounos et *al*. 2009).

Some of the larger present-day glaciers, such as those in the St. Elias and Coast Mountains, are remnants of the Pleistocene ice sheets, while many of the smaller glaciers would have disappeared completely and regenerated later in the Holocene (Calkin, 1988). The Neoglacial period, which includes the Little Ice Age (LIA), was a period of glacial advance following a warm interval of the early-mid Holocene (Menounos et *al*., 2009). Glacial advances in many areas of Yukon, northern BC and Alaska occurred around 3000 years ago, followed by some minor recession beginning about 2000 years ago (Calkin, 1988; Menounos et *al*., 2009). Some minor advance was seen about 1200 years ago, around the time when Mt. Churchill erupted, depositing White River ash in many areas of Yukon (Calkin, 1988). This was followed by reduced activity until the major advances of the LIA, between 434 and 84 years ago (Calkin, 1988). It is important to note that there is some spatial variation between episodes of glacial advance and recession throughout the Holocene, mainly controlled by climate and rates of precipitation in different areas of Yukon (Jackson et *al*., 1991). While LIA advances were relatively limited in extent, in some cases the effects of these advances extended much farther than the glacier termini through impoundment of drainages and subsequent catastrophic drainage (Clague and Rampton, 1982).

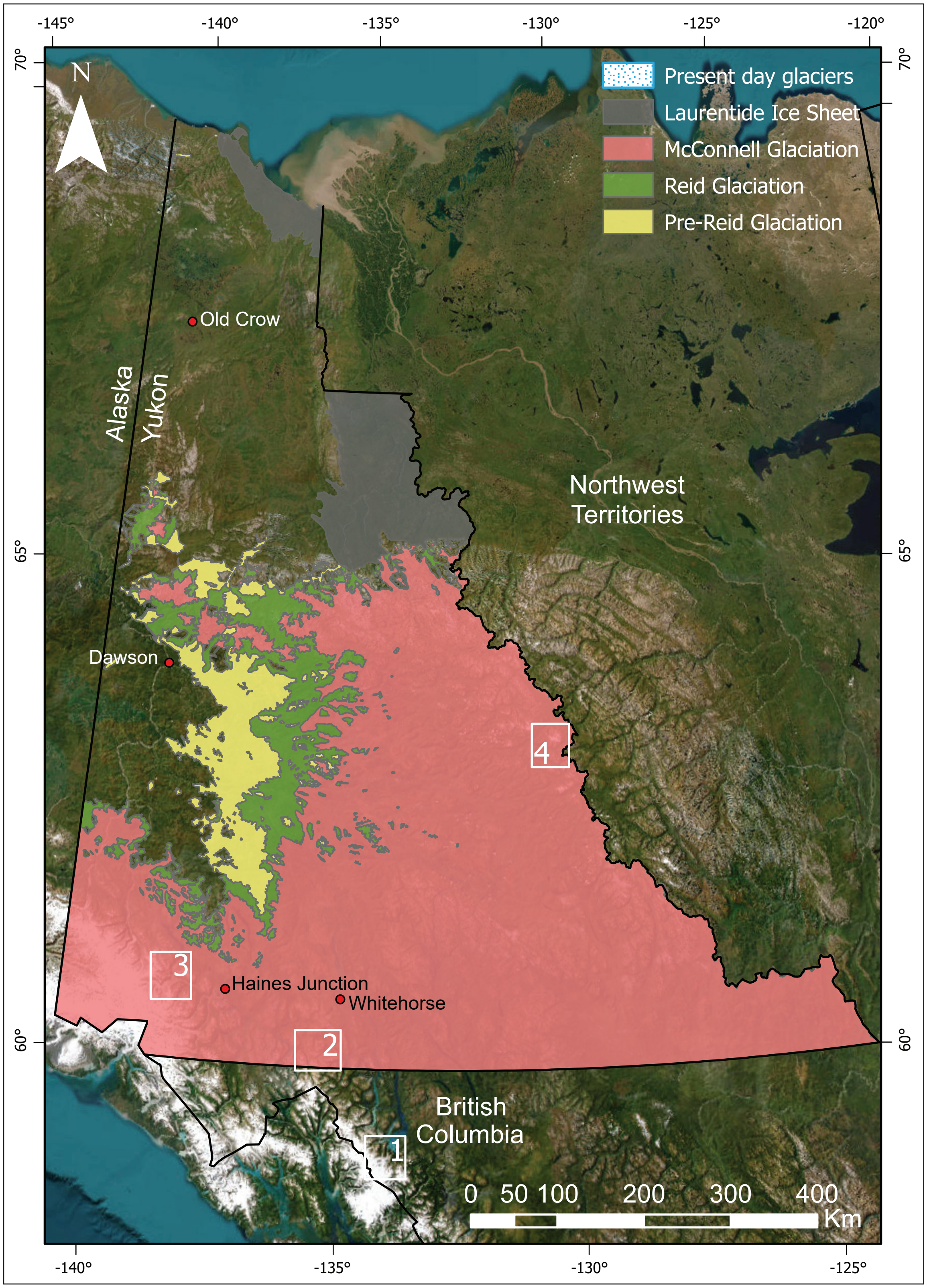

Figure 1. *Overview of glacial limits of Yukon and locations of selected study sites discussed in text:* ***(1)*** *Llewellyn Glacier, see Figure 2;* ***(2)*** *Wheaton and Radelet glaciers, see Figure 3;* ***(3)*** *Kaskawulsh Glacier, see Figure 8;* ***(4)*** *Keele Peak glaciers, see Figure 9. Glacial limits are modified from Duk-Rodkin (1999) based on updated mapping (Bond and Lipovsky, 2010; Cronmiller et al.,2018; Kennedy and Ellis, 2020; Lipovsky and Bond, 2022).*

Over the last two decades, glacier area and mass loss have accelerated in most areas of the world (Hugonnet et *al.*, 2021). Western Canada and the USA, which have a combined glacierized area of 14 524 km^2, had a mass loss of 7.6 ± 1.7 gigatonnes per year between 2000 and 2019 and a mean thinning rate of 0.62 ± 0.11 m per year (Hugonnet et *al.*, 2021). Clarke et *al.* (2015) estimate that glacier ice volume in western Canada will be diminished by 70 ± 10% by the end of the century, based on 2005 glacier volumes. The main driver of this accelerated mass loss is rising global temperatures, while some of the regional variation can be explained by changes in precipitation (Hugonnet et *al.*, 2021).

Methodology

Terminus and volume change

We used satellite imagery to track glacier terminus change at 5-year increments between 1986 and 2021. Landsat 4, 5, 7 and 8, and Sentinel 2A imagery was sourced from the United States Geological Survey (USGS) Earth Explorer. The imagery was visualized in ArcGIS Pro and shapefiles were created for each of the glaciers selected for monitoring. Representative glaciers from each of the different glaciated regions of Yukon were selected for analysis. The glaciers selected range greatly in size — from the Kaskawulsh Glacier, which had an area of 1122.26 km^2 in 2021, to Wheaton Glacier, which had an area of only 0.71 km^2 in 2021.

Glacier extents were delineated for each 5-year increment — 1986, 1991, 1996, 2001, 2006, 2011, 2016 and 2021. Delineations were completed in ArcGIS Pro using satellite imagery, and hillshade maps for areas where glacial limits were not visible on the satellite imagery. Little Ice Age (LIA) extents were delineated using Landsat, Sentinel and Maxar imagery. LIA extents were only digitized at the termini because up-glacier lateral LIA limits are difficult to delineate due to degradation from slope movement on valley walls. Once all glacial extent features were digitized, the average retreat was measured at several points along the terminus in ArcGIS Pro to calculate change from LIA–2021, 1986–2021, and for each of the three decades between 1991 and 2021; the areal rate of retreat per year was also calculated. LIA dates for smaller glaciers were estimated from nearby known larger glacier LIA dates (*e.g.*, Llewellyn, Donjek and Kaskawulsh).

Glacier surface elevation change maps were made using data from Hugonnet et *al.* (2021). The digital elevation models (DEMs) used to create these elevation maps were generated from the Advanced Spaceborne Thermal Emission and Reflection Radiometer (ASTER) stereo imagery, as well as ArcticDEM (Hugonnet et *al.*, 2021). These elevation changes represent volume gain/loss throughout the glacier at a resolution of 100 m (Hugonnet et *al.*, 2021).

Field surveys

Helicopter and ground-based field surveys were conducted at Wheaton and Radelet glaciers on June 15, 2004, and September 19, 2022. An overview flight of the region was also completed to collect notes and photographs of other minor glaciers and ice patches in the Wheaton, Takhini and Bennet Lake watersheds. During ground surveys, photos of the glaciers were taken at cairns built in 2004 at the 1995 and 2004 terminus locations. The 1995 terminus locations were determined from air photographs (flight line A28240). New cairns were constructed at the 2022 termini locations. Drone surveys of both glaciers captured oblique photos for visual comparison as well as a systematic grid of nadir photos for use in future photogrammetric volume change analyses.

The current state of glaciers

Upper Yukon River headwaters region

Llewellyn Glacier area

Llewellyn Glacier terminates at the southern end of Atlin Lake in British Columbia, and is a major source of water draining into the headwaters of the Yukon River. Llewellyn is the largest of the glaciers that drain into the upper Yukon River, and contains at least half of the total ice volume in the upper Yukon River basin (Northern Climate Exchange, 2014), with a total area of about 464.75 km^2 in 2021. By that same year, the glacier terminus had retreated an average of 2.58 km from its LIA maximum, which occurred some time in the seventeenth century (Clague et *al.*, 2010; Fig. 2).

Over the last three decades, the glacier retreat has accelerated. Llewellyn Glacier retreated 0.39 km between 1991 and 2001, 0.41 km between 2001 and 2011, and 0.66 km between 2011 and 2021 (Fig. 2).

Other glaciers in the headwaters of the Yukon River include Willison Glacier, which is located approximately 10 km northwest of Llewellyn Glacier, and Fantail Glacier, which is approximately 65 km northwest of Llewellyn Glacier. Both glaciers drain into Tagish Lake, are similar in size, but smaller than Llewellyn Glacier. Since the LIA, the terminus of Willison Glacier has retreated 4.13 km, while Fantail Glacier retreated 4.03 km. Similar to Llewellyn Glacier, the amount of retreat at Fantail Glacier increased each decade from 1991–2021. Between 2011 and 2021 the glacier retreated 0.93 km, while between 2001 and 2011 it retreated 0.54 km, and between 1991 and 2001 it retreated 0.23 km. This pattern is not the same at Willison Glacier, which retreated very similar distances over all three time periods: 0.24 km between both 1991 and 2001, and 2011 and 2021; and 0.21 km between 2001 and 2011.

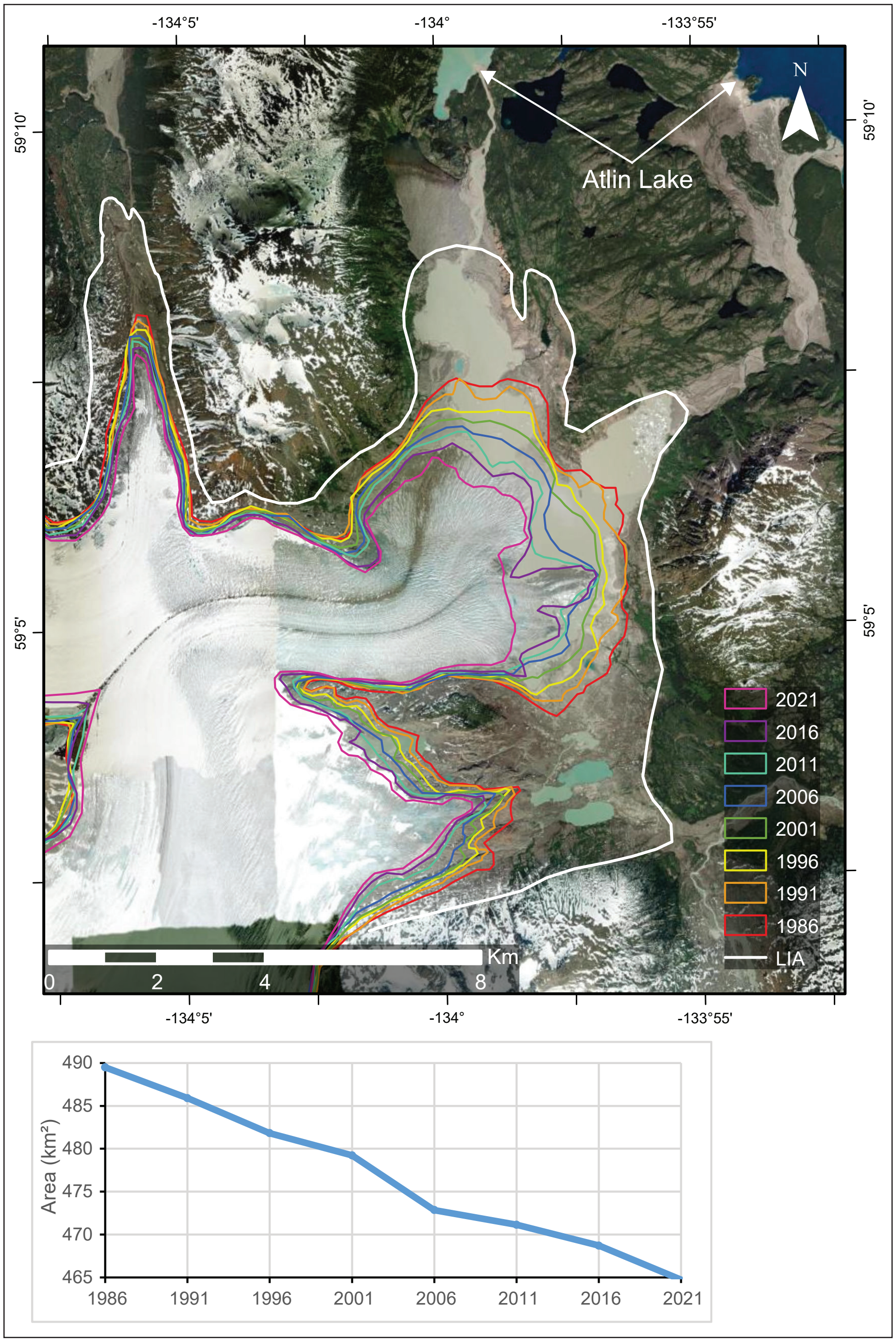

Figure 2. *Change in the areal extent of the Llewellyn Glacier, LIA to 2021. Graph depicts change in total glacier area. Satellite imagery from 2018.*

Wheaton River Basin

Meltwater from the Wheaton River glaciers also feed the upper Yukon River system. Two of the glaciers we studied in this area are the Wheaton Glacier and Radelet Glacier (Fig. 3). These two glaciers are a good representation of many of the glaciers in the area – small alpine glaciers that have retreated significantly and now cover an area of less than 1 km^2. The retreat of these glaciers, however, does not seem to follow the same pattern, despite being in very close proximity to each other. Wheaton Glacier, which is the larger of the two, has retreated 1.96 km since the LIA. Between 1991 and 2011, the Wheaton retreated 0.12 km, but only retreated 0.09 km between 2001 and 2011, and the greatest amount of retreat (0.28 km) occurred in the most recent decade. Previous work by Church and Clague (2009) found that in 2009, 92% of the mass loss since the LIA had occurred since 1948, again suggesting an acceleration in recent decades. They found that the main cause of mass loss was the increase in air temperatures, and if this warming trend continues the glacier will likely disappear within the century. At Radelet Glacier, the least amount of retreat (0.08 km) occurred during this most recent decade, while more retreat occurred during the previous two decades (0.14 km between 2001 and 2011, and 0.13 km between 1991 and 2001).

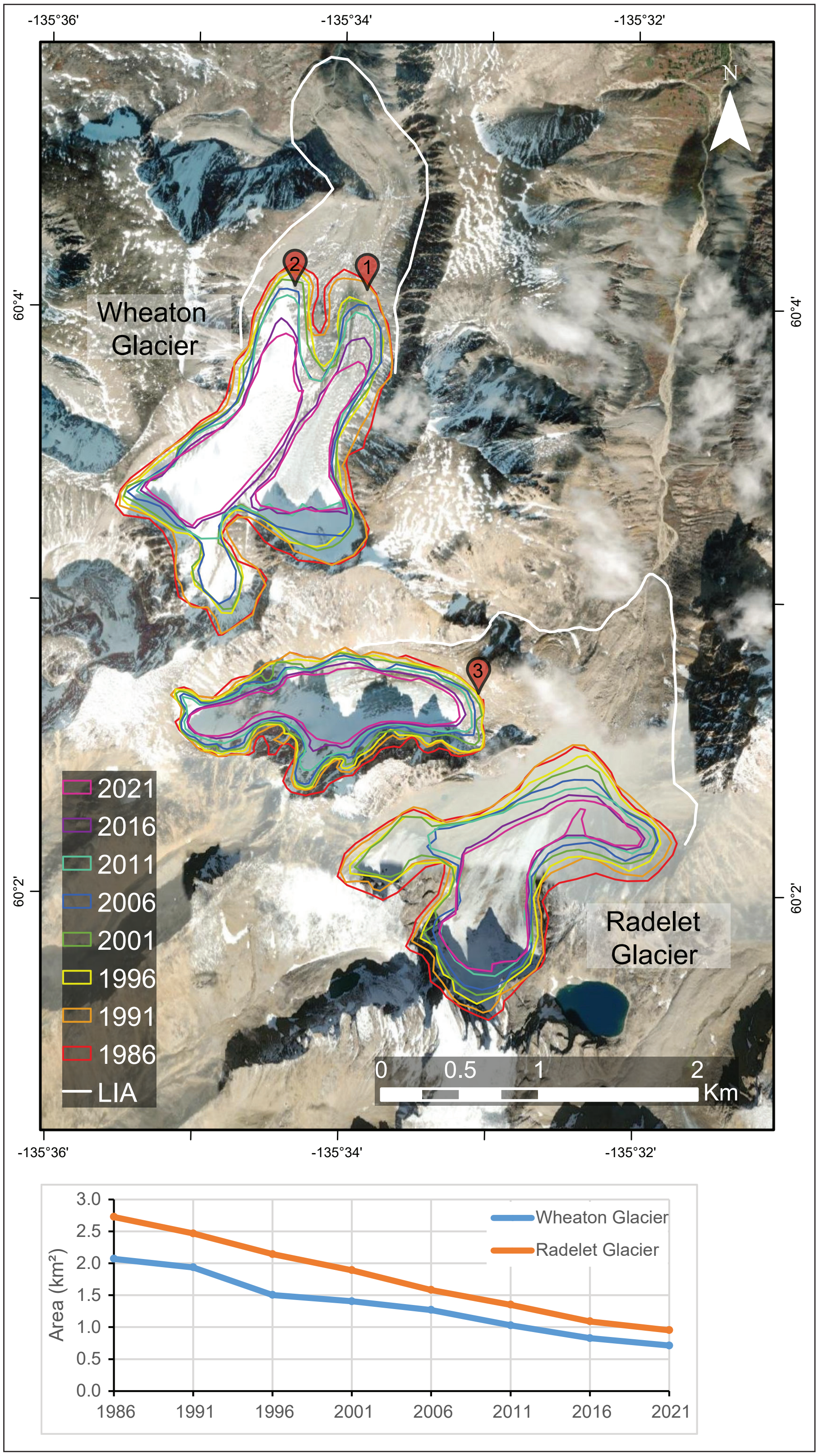

Figure 3. *Change in the areal extent of Wheaton and Radelet glaciers, LIA to 2021.* ***(1)*** *Location of photos taken in Figure 4;* ***(2)*** *location of photos taken in figure 5;* ***(3)*** *location of photos taken in figure 6. Satellite imagery from 2012.*

The Yukon Geological Survey established photo-monitoring stations at Radelet and Wheaton glaciers in 2004 that were reoccupied in 2022. Figures 4, 5 and 6 are photos taken from the same location to show the change in glacier extent over nearly 20 years. Figure 4 is the eastern lobe of the Wheaton Glacier, and Figure 5 is the western lobe of the Wheaton Glacier, which had retreated about 375 m and 310 m, respectively, between 2004 and 2021. Based on the area delineated from the satellite imagery, the Wheaton Glacier was 1.41 km^2 in 2001 and 0.71 km^2 in 2021, which is a loss of half the area of the glacier in 20 years. Figure 6 is the western side of Radelet Glacier, which covers a much smaller area than it did in 2004, and the ice thickness has visibly lowered across the entire glacier. The area of Radelet Glacier was 1.89 km^2 in 2001 and 0.95 km^2 in 2021, which is again a decrease of almost half the glacier area.

Figure 4. *East Wheaton Glacier in June 2004 (left) and September 2022 (right). Arrows point to the cairn erected in 2004 at the 1995 terminus location. The approximate 2004 extent is delineated on the 2022 photo (dashed line). Seasonal snow is present in the June 2004 photograph; however, it is not likely to significantly increase the apparent glacier extent.*

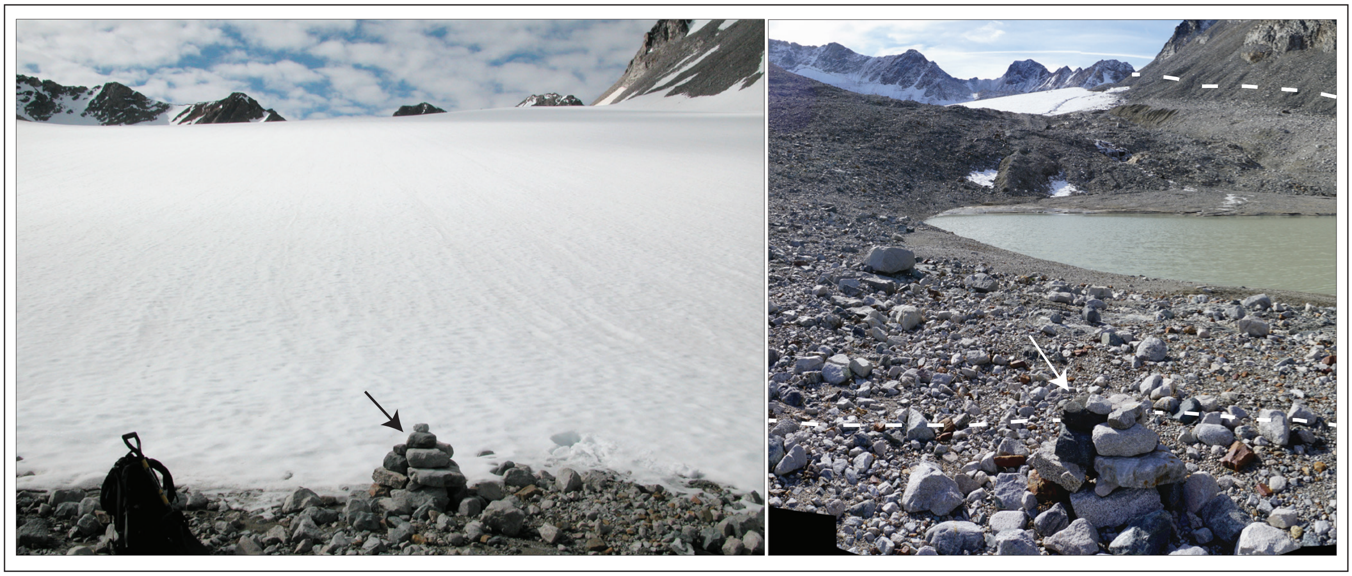

Figure 5. *West Wheaton Glacier in June 2004 (left) and September 2022 (right). The approximate 2004 extent is delineated on the 2022 photo (white line). Seasonal snow is present in the June 2004 photograph; however, it is not likely to significantly increase the apparent glacier extent. Note the Proglacial Lake present in 2022 was covered by ice in 2004.*

Figure 6. *West Radelet Glacier in June 2004 (top) and September 2022 (bottom) showing considerable retreat and thinning. Seasonal snow is present in the June 2004 photograph; however, it is not likely to significantly increase the apparent glacier extent.*

Many other small glaciers and perennial ice patches exist throughout the Wheaton River basin. During the September 2022 regional overview flight, névé was absent from nearly all of the observed glaciers or ice patches despite having 180% the typical snowpack in the Southern Lakes region (Government of Yukon, 2022) indicating a net mass loss in 2022. The lack of snowpack on these glaciers also suggests that the equilibrium line altitude has surpassed the highest point of the glacier.

St Elias Mountains region

The St. Elias Mountains are Canada's highest mountains, and contain the world's largest non-polar icefield (https://www.pc.gc.ca/en/pn-np/yt/kluane/nature/geomorph). The St. Elias Mountains are one of the few areas of the world that host a cluster of surge-type glaciers (Clarke et *al*., 1986), which are glaciers that undergo cyclical periods of rapid advance, followed by a long period of retreat. For this reason, surge-type glaciers can present differently in area change.

The only surge-type glacier that was a part of our study was the Donjek Glacier (Fig. 7), which is located in the St. Elias Mountains and drains into the Donjek River. Since 1986, the Donjek Glacier has surged three times: 1988–1990, 2000–2002 and 2012–2014 (Kochtitzky et *al*., 2019). During each of these surge events, the maximum terminus position has been farther back than the one previous, indicating a negative mass balance (Kochtitzky et *al*., 2019).

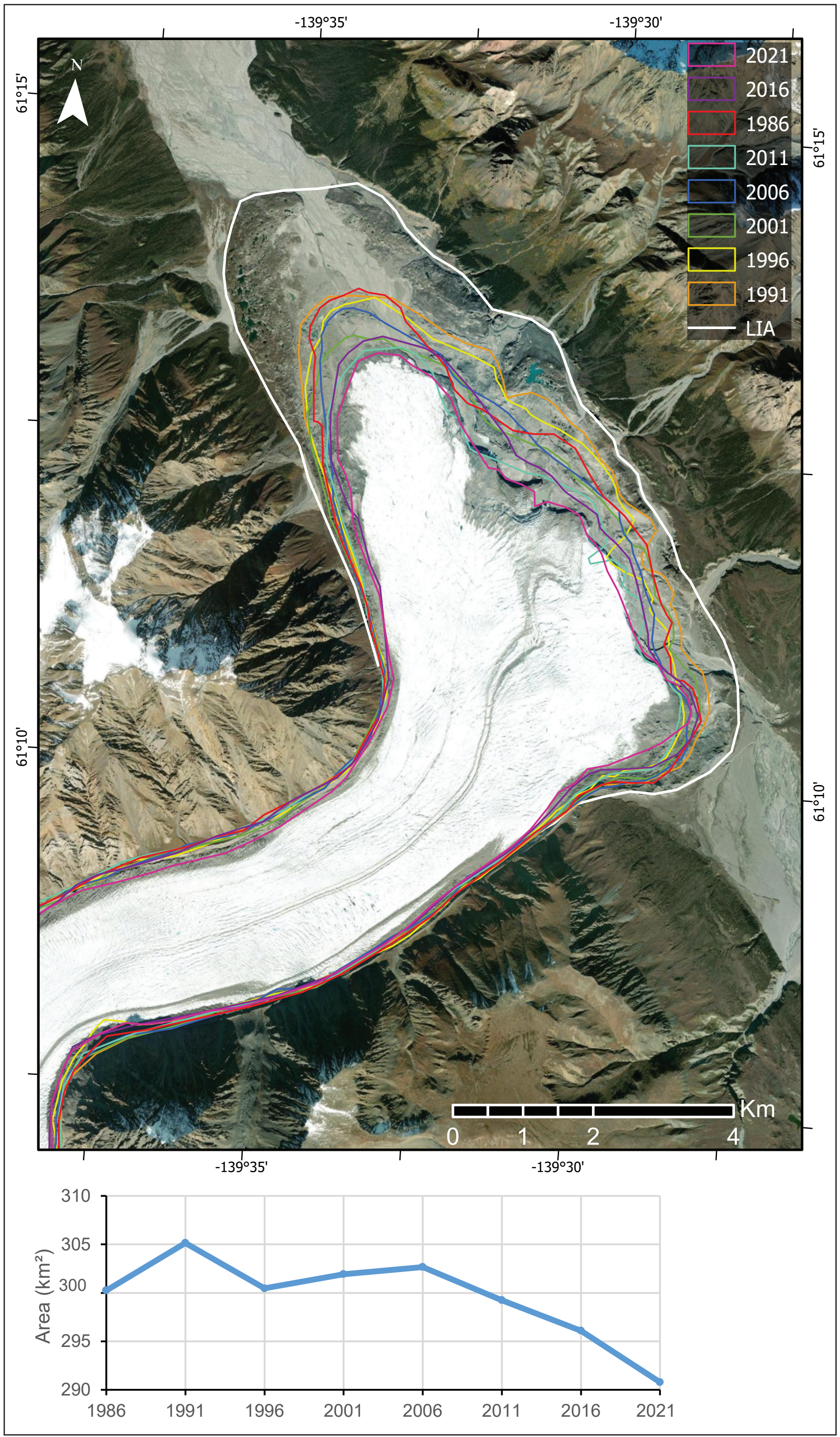

Figure 7. *Change in areal extent of the Donjek Glacier terminus, LIA to 2021. Graph depicts change in total glacier area. Satellite imagery from 2019.*

Another large valley glacier in the St Elias Mountains is the Kaskawulsh Glacier (Fig. 8), which is not a surge-type glacier. The Kaskawulsh has retreated 2.18 km since the LIA in the mid-1750s (Reyes et al., 2006). Between 1991 and 2001 the terminus retreated 0.2 km, whereas between 2011 and 2021, it retreated 0.33 km. The retreat of the Kaskawulsh Glacier has had significant recent impacts on the surrounding area. In 2016, the glacier retreated far enough that meltwater formerly draining northwards into Slims River (A’ ąy Chù’) and Kluane Lake (Łù’ àn Mân) was rerouted eastward into the Kaskawulsh and Alsek river system. Prior to 2016, meltwater from the Kaskawulsh Glacier was the main source of water for Kluane Lake, and lake levels have since dropped approximately 2 m (Shugar et al., 2017). A recent study suggests that as the Kaskawulsh Glacier adjusts to current mass imbalances it will see a terminus retreat of approximately 23 km over the next century and loss of 15% of its total volume under current climate conditions (Young et al., 2021).

Keele Peak area, Mackenzie Mountains

The Keele Peak area in the Mackenzie Mountains contains small alpine glaciers, four of which were included in our study. These glaciers ranged in size from 5.58 km^2 to 0.6 km^2 in 2021. Smaller alpine glaciers like these have different retreat patterns than large valley glaciers, which tend to retreat more at the terminus with much less change farther up-glacier. For example, the largest of the four glaciers studied, Mackenzie glacier 1 (Fig. 9), retreated only 0.33 km at the terminus between 1986 and 2021, which was the least of all the four glaciers. Its areal extent, however, dropped by 1.62 km^2 or 22.5%, during the same period which was the highest change in areal extent for the same four glaciers. One of the intermediate sized glaciers, Mackenzie glacier 2 (2.01 km^2 in area in 2021, Fig. 9), retreated 1.13 km during the same period. Mackenzie glacier 3 was the smallest glacier in 2021, at only 0.6 km^2, while Mackenzie glacier 4 had an area of 2.25 km^2. Both these glaciers retreated more than Mackenzie glacier 1, but less than Mackenzie glacier 2. Mackenzie glacier 3 retreated 0.54 km between 1986 and 2021, while Mackenzie glacier 4 retreated 0.99 km in that time.

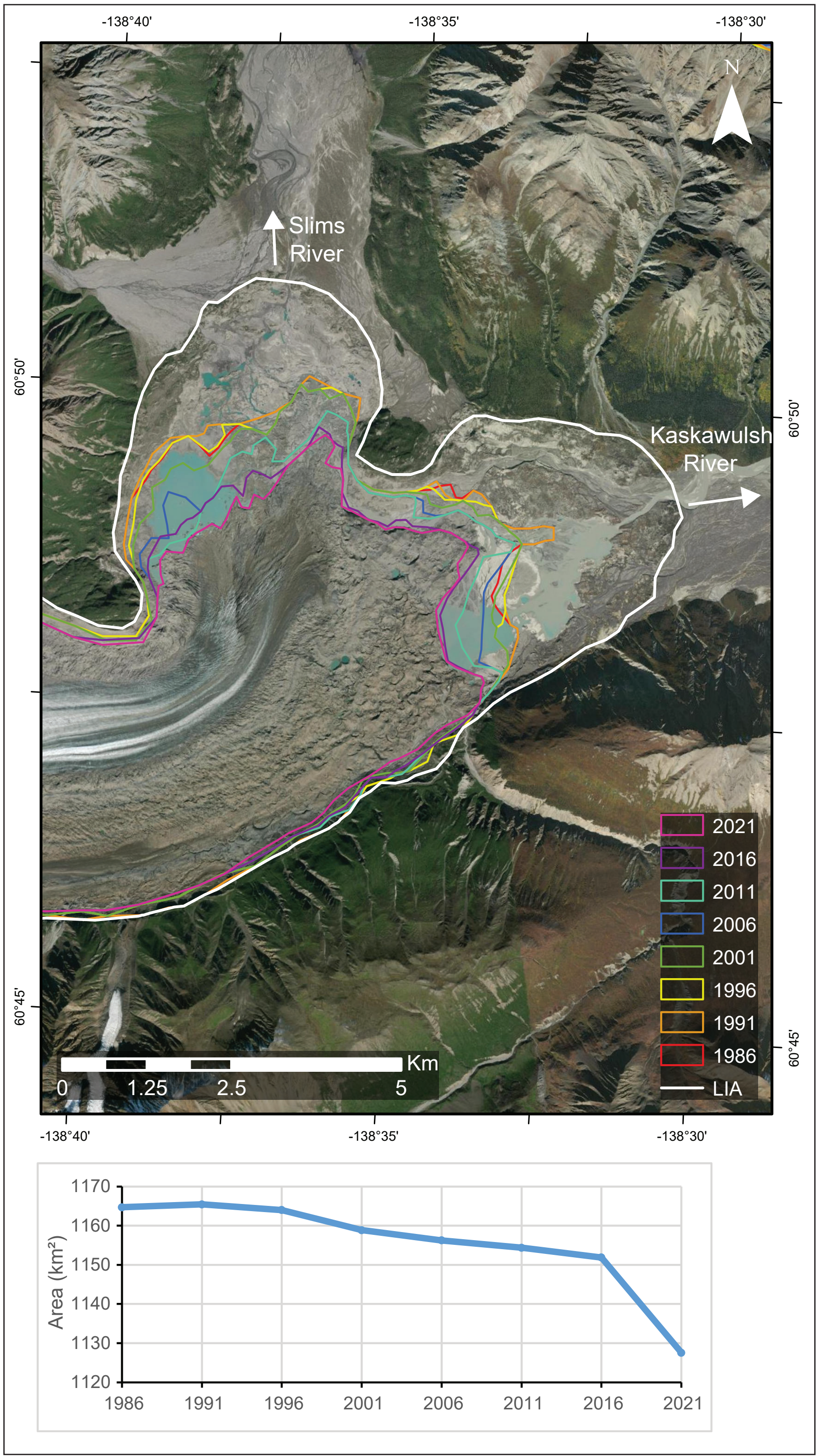

Figure 8. *Change in areal extent of the Kaskawulsh Glacier terminus, LIA to 2021. Graph depicts change in total glacier area. Satellite imagery from 2019.*

Glacier thickness changes

Glacier surface elevation data from Hugonnet *et al.* (2021) were used to determine approximate changes in glacier thickness between 2000 and 2019. Figure 10 shows part of the upper Yukon River watershed, including Llewellyn, Willison and Fantail glaciers. All glaciers in this region have experienced the most thinning at their fronts, with an average thinning rate of about 5 m/year over 20 years. Thinning rates at higher elevations are generally less than 3 m/year.

Figure 11 shows the glaciers that drain into the Donjek River. More elevation gain occurred on the glaciers in this region than for glaciers in the upper Yukon River watershed. This is because several glaciers in this region are surge-type.

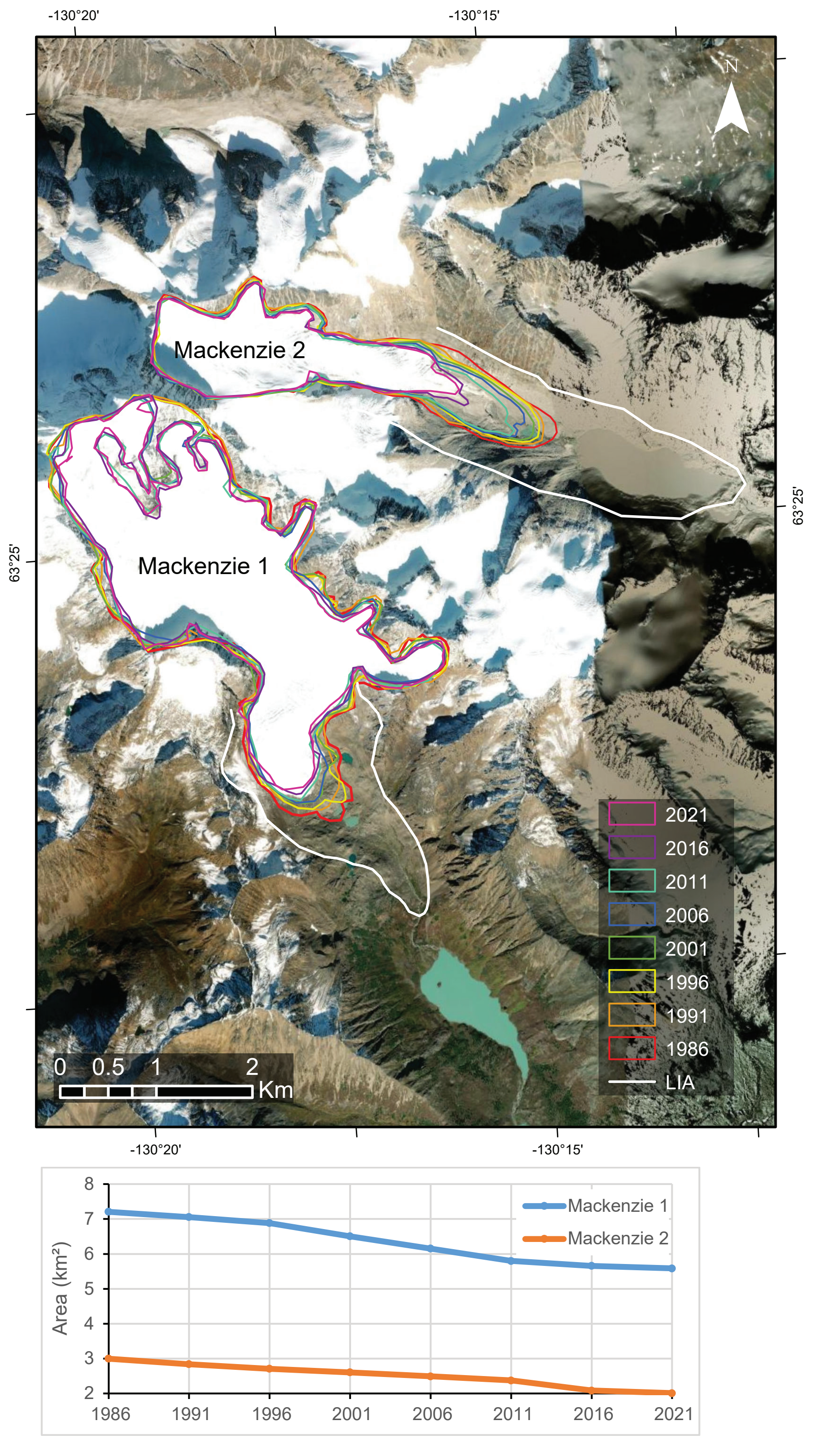

Figure 9. *Change in areal extent of Mackenzie glaciers 1 (south) and 2 (north), LIA to 2021. Satellite imagery from 2014.*

Before a glacier surges it will accumulate mass in one area, and then redistribute that mass downwards during the surge. For example, the Steele Glacier (Fig. 10) thinned significantly (up to 9 m/year) in the upper part of the glacier, but thickened up to 7 m/year in the middle of the glacier. A similar but less pronounced pattern also occurred at the Donjek Glacier. These surging glaciers still exhibit prominent thinning at their fronts, similar to the pattern for the upper Yukon River watershed glaciers. Smaller alpine glaciers, such as those in the Mackenzie Mountains, have thinned less than the larger glaciers of the upper Yukon and St. Elias Mountains. These smaller glaciers only thinned approximately 2 m/year between 2000 and 2020, even at their termini.

Previous work has been done by Yukon University and Yukon Energy Corporation (YEC) to assess changes to glaciers in the upper Yukon River watershed. YEC used data from NASA's Gravity Recovery and Climate Experiment (GRACE) to estimate glacier mass loss in northern British Columbia, southwestern Yukon and southeastern Alaska (Doumbia et al., 2020; Rousseau et al., 2020). This study found an average mass loss of about 40.82 Gt/year between 2002 and 2017 (Rousseau et al., 2020). Hugonnet et al. (2021) estimated a mass loss of about 66.7 ± 10.9 Gt/year for Alaska from 2000–2019; however, their study area covers the entirety of Alaska with a glacierized area of 86 725 km^2, while the YEC study area is much smaller, at only 55 000 km^2 glacierized area. Yukon University assessed the elevation change of glaciers between 1987 and 2000 using digital elevation models (Northern Climate Exchange, 2014).

Figure 10. *Glacier surface elevation change from 2000 to 2019 on the Canadian side of the Juneau Icefield, upper Yukon River headwaters. Data from Hugonnet et al., 2021.*

Their study found a surface lowering (thinning) of 80 to 100 m (*i.e.*, an average rate of 6.15 m/yr) at the termini of many of the larger glaciers in the upper Yukon River watershed. Hugonnet et *al.* (2021) data for the 2000-2005 period show a surface lowering of up to 6 m/year at the termini of some of the larger glaciers in the same area, including Fantail and Llewellyn glaciers. The thinning rates determined from both studies agree closely despite using contrasting methods.

Discussion/Impacts

Almost all the glaciers in our study have been retreating since 1986, the only exception being Donjek Glacier which has undergone three surge events since that time. The surge events at the Donjek Glacier have resulted in terminus advance over short periods, but the long-term mass balance trend is still negative (Kochtitzky et *al.*, 2019). Llewellyn Glacier and Fantail Glacier have both

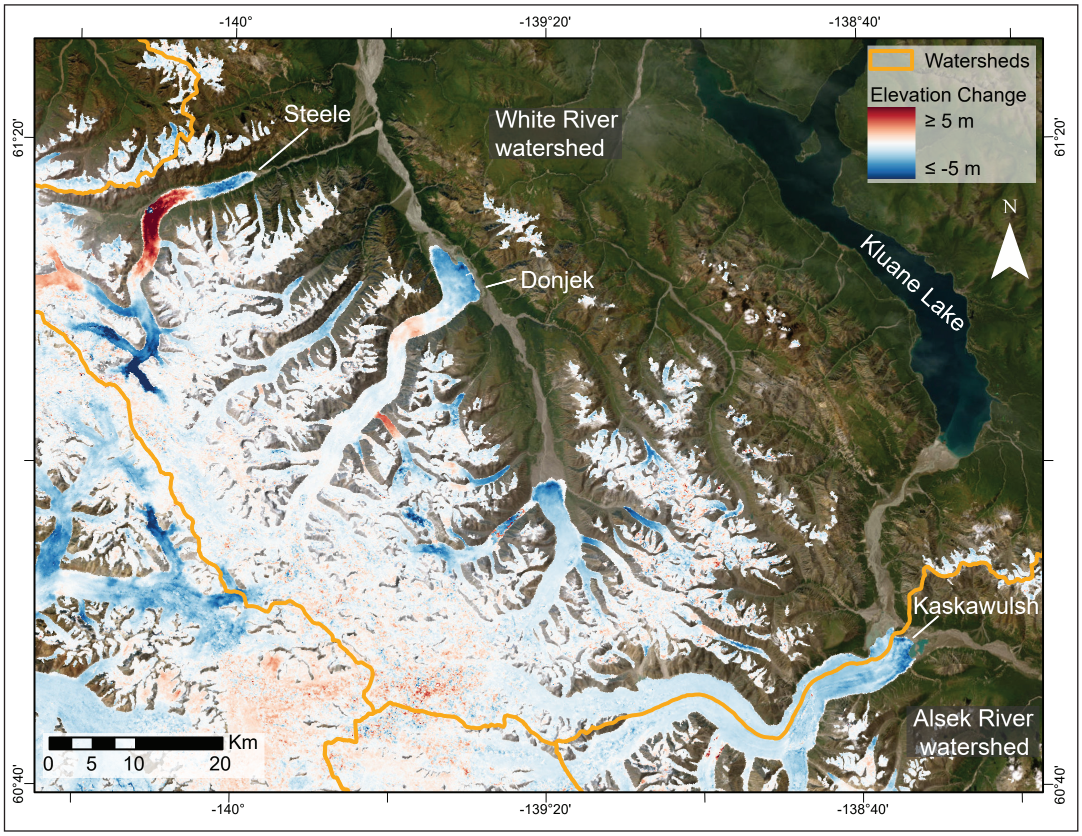

Figure 11. *Glacier surface elevation change from 2000 to 2019 in the White River watershed. Data from Hugonnet et al., 2021.*

experienced accelerated terminus retreat over the last three decades. Willison Glacier, which is located in the same region, has remained consistent in its retreat over this time. Donjek Glacier has slowed its terminus retreat in the three decades since 1991, but has also surged two times during that period, which advanced the terminus of the glacier. Kaskawulsh Glacier terminus retreat accelerated between 1991 and 2001, and 2001 and 2011, but the retreat in the most recent decade was very similar to that of 2001–2011. The glaciers on Keele Peak had contrasting retreat patterns, despite their close proximity and similar size. Mackenzie glacier 1 decelerated in terminus retreat over the last three decades, while Mackenzie glacier 2 accelerated. This same contrast was seen at the Wheaton Valley glaciers (Wheaton Glacier and Radelet Glacier). Wheaton Glacier has more than doubled its retreat from the first decade to the most recent one, while Radelet Glacier has slowed retreat. It is likely that some of the slow down in retreat at Radelet Glacier is due to the remaining ice being entirely within cirques, which provide increased shading from solar radiation and have higher altitude, which favours ice preservation due to topographic configuration (cf., DeBeer and Sharp 2009). As stated earlier, the Wheaton Valley glaciers aerial extent dropped by about 50% in the 20 years between 2001 and 2021; however, this amount of area change was not observed at the Keele Peak glaciers, which are small alpine glaciers similar to Wheaton and Radelet glaciers. Although there has not been universal acceleration of terminus retreat at all glaciers in our study (Table 1), there has been a significant acceleration in elevation loss over the last two decades. Average glacier elevation loss was calculated for four of the major watersheds in Yukon (Table 2), and all four had an increase of at least 300% from the 2000–2010 to the 2010–2020 period.

Table 1. *Decadal area and terminus change by glacier.*

	Area Change (km²)			Terminus Retreat (km)			
Glacier	**1991-2001**	**2001-2011**	**2011-2021**	**LIA-1991**	**1991-2001**	**2001-2011**	**2011-2021**
Kaskawulsh	-6.60	-4.49	-26.79	-1.30	-0.2	-0.35	-0.33
Donjek	-3.22	-2.68	-8.47	-0.69	-0.32	-0.24	-0.15
Wheaton	-0.53	-0.38	-0.32	-1.47	-0.12	-0.09	-0.28
Radelet	-0.58	-0.54	-0.40	-0.94	-0.13	-0.14	-0.08
Llewellyn	-6.67	-8.07	-6.41	-1.12	-0.39	-0.41	-0.66
Willison	-1.96	-1.44	-1.68	-3.44	-0.24	-0.21	-0.24
Fantail	-1.14	-2.19	-2.14	-2.33	-0.23	-0.54	-0.93
Mackenzie 1	-0.55	-0.71	-0.21	-0.54	-0.14	-0.13	-0.06
Mackenzie 2	-0.24	-0.23	-0.36	-2.01	-0.1	-0.31	-0.72

Table 2. *Average glacier elevation change (m/year) by watershed (data from Hugonnet et al. 2021).*

Watershed	2000–2010	2010–2020
White River	-0.09	-0.41
Alsek River	-0.37	-1.43
Tagish and Atlin Lake	-0.13	-1.43
Hess (Keele Peak)	-0.02	-0.72

Short-term negative glacier mass balance trends may cause short-term increases in summer water flows generated by increased glacial meltwater runoff resulting from warmer air temperatures. However, in the long term, continued negative mass balance will eventually result in glaciers becoming too small to produce increased amounts of meltwater (Barnett et *al.*, 2005). Stahl and Moore (2006) conducted a study on the effects of glacier cover on streamflow in British Columbia. They found mostly declining stream flows in glacier-fed streams, with exceptions in northwestern BC and the northern Rockies. This suggests that the larger glaciers in northern BC have not yet reached their maximum discharge levels, while glacier fed catchments in southern BC have already passed this threshold, and will likely continue to decline (Stahl and Moore, 2006). This coincides with Fleming and Clarke's (2003) study, which documented increasing annual flow volumes for glacier-fed rivers in southwestern Yukon due to increased meltwater production from larger glaciers similar to those in northwestern BC. "Peak water" is the term used for the maximum discharge reached as glacier meltwater volumes increase with continued glacier recession, followed by decreased meltwater discharge as the volume of water stored in the glacier depletes. Huss and Hock (2018) modelled glacier meltwater runoff changes up to the year 2100 in all large drainage basins outside of Greenland and Antarctica, including the Yukon River and Alsek River basins. Their study found that in the year 2017, peak water had already been reached in 45% of the basins, while runoff is expected to continue rising past 2050 in 22% of basins (Huss and Hock, 2018). Basins with large glaciers and glacierized area, such as the Yukon and Alsek watersheds, were modelled to reach peak water by the end of the 21st century, while basins with smaller glaciers could reach peak water within the next decade (Huss and Hock, 2018). The YEC project that peak water for the upper Yukon River watershed will occur around 2040 (Rousseau et *al.*, 2020).

Glacial fed streams and rivers also experience longer, larger and later spring high water, and have higher fall and winter base flows than rivers fed solely by snow (Fleming, 2005), allowing them to compensate for low precipitation or drought years. In 2020, Yukon was powered by 86% renewable energy primarily derived from three hydroelectric power stations in Whitehorse, Aishihik and Mayo (Yukon Energy, 2022). The Whitehorse hydro power station is in part supplied by runoff originating from glaciers in the upper Yukon River basin. Modelling completed by the YEC projects an increase in annual runoff until ~2040, followed by a steady decrease until 2070 (Rousseau et *al*., 2020). This is attributed to glacier mass loss in the region and the annual runoff at the end of 2070 is estimated to be similar to 1980 values (Rousseau et *al*., 2020).

Declining summer flows will also affect stream temperatures, turbidity and water chemistry. This may affect fish and downstream habitats (Milner et *al*., 2017; McKnight et *al*., 2021), as will large-scale changes to basin geometry or rerouting of stream and river systems caused by glacial retreat, as occurred at the Kaskawulsh Glacier in 2016 (Shugar et *al*., 2017). Natural hazards following glacier recession also include mass movements and ice avalanches from steep mountain glaciers (*e.g.*, Mt. Steele; Lipovsky et *al*., 2008), and the formation of more and larger proglacial lakes, which may be subject to outburst flooding (Milner et *al*., 2017; Painter, 2021; Shugar et *al*., 2020).

Future Work

Although glacier area change and terminus retreat rates are indicators of glacier health, mass and elevation changes provide a more comprehensive understanding of glacier change. Long-term high-resolution mass balance monitoring at select glaciers in Yukon, particularly in the upper Yukon River basin, would be beneficial to better understand glacier mass change and potential impacts. Remote sensing methods with select field validation are likely to be the most economically and environmentally sustainable approaches to this. In Yukon, one of the main concerns with glacier mass wasting is consequences for hydropower, which is currently the territory's main source of renewable energy. In order to have an improved understanding of the role that glaciers play on the territory's water resources, particularly in the upper Yukon River basin, monitoring of water flow, temperatures, chemistry and timing should be established.

Summary and Conclusions

On a global scale, there has been a significant trend of glacier recession in the recent decades, which is predicted to continue through the end of the century (Hock et *al*., 2019; Hugonnet et *al*., 2021). Yukon and northern BC have been no exception to this trend, as all glaciers in this study have been retreating since the late 1980s. Despite snowpack in the Wheaton basin greatly exceeding average depths during the winters of 2021 and 2022, net mass losses still occurred in the following melt seasons due to increasingly warm summers. Glacier runoff increases as glaciers continue to recede, but continued mass loss will inevitably result in diminished runoff and consequently diminished contribution to the upper Yukon River, which supplies the Whitehorse hydropower station. Glacier retreat and mass wasting will have an effect on stream and river characteristics, such as temperature and turbidity changes, which will in turn have an impact on fish populations (Milner et *al*., 2017; McKnight et *al*., 2021). Glacier retreat has also contributed to an increase in certain geohazards such as glacial lake outburst floods and mass movements (Milner et *al*., 2017; Shugar et *al*., 2020) which should be considered in regional land use planning.

Acknowledgements

The authors would like to thank Panya Lipovsky for her review of this paper, and Brian Horton for his comments. Dr. Mark Skidmore is thanked for his contributions to the initial Wheaton Glacier monitoring fieldwork in 2004.

References

Barendregt, R.W., Enkin, R.J., Duk-Rodkin, A. and Baker, J. 2010. Paleomagnetic evidence for multiple late Cenozoic glaciations in the Tintina Trench, west-central Yukon, Canada. Canadian Journal of Earth Science, vol. 47, p. 987–1002.

Barnett, T.P., Adam, J.C. and Lettenmaier, D.P., 2005. Potential impacts of a warming climate on water availability in snow-dominated regions. Nature, vol. 438, p. 303–309.

Benn, D.I. and Evans, D.J., 2014. Glaciers and glaciation; second edition. Routledge.

Bond, J. and Lipovsky, P., 2010. Pre-Reid surficial geology investigations in southwest McQuesten map area (115P). *In:* Yukon Exploration and Geology 2009, K.E. MacFarlane, L.H. Weston and L.R. Blackburn (eds.), Yukon Geological Survey, p. 103–117.

Calkin, P.E., 1988. Holocene glaciation of Alaska (and adjoining Yukon Territory, Canada). Quaternary science reviews, vol. 7, p. 159–184.

Church, A. and Clague, J.J., 2009. Recent deglacierization of the upper Wheaton River watershed, Yukon. *In:* Yukon Exploration and Geology 2008, L.H. Weston, L.R. Blackburn and L.L. Lewis (eds.), Yukon Geological Survey, p. 99–112.

Clague, J.J., Koch, J. and Geertsema, M., 2010. Expansion of outlet glaciers of the Juneau Icefield in northwest British Columbia during the past two millennia. The Holocene, vol. 20, p. 447–461.

Clague, J.J. and Rampton, V.N., 1982. Neoglacial Lake Alsek. Canadian Journal of Earth Sciences, vol. 19, p. 94–117.

Clarke, G.K., Jarosch, A.H., Anslow, F.S., Radić, V. and Menounos, B., 2015. Projected deglaciation of western Canada in the twenty-first century. Nature Geoscience, vol. 8, p. 372–377.

Clarke, G.K., Schmok, J.P., Ommanney, C.S.L. and Collins, S.G., 1986. Characteristics of surge-type glaciers. Journal of Geophysical Research: Solid Earth, vol. 91, p. 7165–7180.

Cronmiller, D., Ward, B. and Bond, J.D., 2018. Surficial geology of Gladstone Creek (NTS 115G/8 and part of 115G/7). Yukon Geological Survey, Open File 2018-20, scale 1:50 000.

DeBeeR, C.M. and Sharp, M.J., 2009. Topographic influences on recent changes of very small glaciers in the Monashee Mountains, British Columbia, Canada. Journal of Glaciology, vol. 55, p. 691–700.

Doumbia, C., Castellazzi, P., Rousseau, A.N. and Amaya, M., 2020. High Resolution Mapping of Ice Mass Loss in the Gulf of Alaska from Constrained Forward Modeling of GRACE Data. Frontiers in Earth Science, vol. 7, p. 360.

Duk-Rodkin, A., 1999. Glacial Limits Map of Yukon. Exploration and Geological Services Division, Indian and Northern Affairs Canada, Geoscience Map 1999-2.

Fleming, S.W., 2005. Comparative analysis of glacial and nival streamflow regimes with implications for lotic habitat quantity and fish species richness. River Research and Applications, vol. 21, p. 363–379.

Fleming, S.W. and Clarke, G.K., 2003. Glacial control of water resource and related environmental responses to climatic warming: empirical analysis using historical streamflow data from northwestern Canada. Canadian Water Resources Journal, vol. 28, p. 69–86.

Government of Yukon, 2022. Yukon Snow Survey Bulletin and Water Supply Forecast, May 1, 2022.

Hock, R., Rasul, G., Adler,C., Cáceres, B., Gruber, S., Hirabayashi, Y., Jackson, M., Kääb, A., Kang, S., Kutuzov, S., Milner, A.I., Molau, U., Morin, S., Orlove, B. and Steltzer, H., 2019. High Mountain Areas. *In:* IPCC Special Report on the Ocean and Cryosphere in a Changing Climate 2019, H.-O. Pörtner, D.C. Roberts, V. Masson-Delmotte, P. Zhai, M. Tignor, E. Poloczanska, K. Mintenbeck, A. Alegría, M. Nicolai, A. Okem, J. Petzold, B. Rama and N.M. Weyer (eds.), Cambridge University Press, p. 131–202.

Hugonnet, R., McNabb, R., Berthier, E., Menounos, B., Nuth, C., Girod, L., Farinotti, D., Huss, M., Dussaillant, I., Brun, F. and Kääb, A., 2021. Accelerated global glacier mass loss in the early twenty-first century. Nature, vol. 592, p. 726–731.

Huss, M. and Hock, R., 2018. Global-scale hydrological response to future glacier mass loss. Nature Climate Change, vol. 8, p. 135–140.

Jackson, L., Ward, B., Duk-Rodkin, A. and Hughes, O., 1991. The last Cordilleran ice sheet in southern Yukon Territory. Géographie physique et Quaternaire, vol. 45, p. 341–354.

Kennedy, K.E. and Ellis, S.E., 2020. Surficial geology of the northern Kluane Ranges (parts of NTS 115G/5, 6, 11, 12). Yukon Geological Survey, Open File 2020-5, 4 sheets, scale 1:50 000.

Kochtitzky, W., Jiskoot, H., Copland, L., Enderlin, E., McNabb, R., Kreutz, K. and Main, B., 2019. Terminus advance, kinematics and mass redistribution during eight surges of Donjek Glacier, St. Elias Range, Canada, 1935 to 2016. Journal of Glaciology, vol. 65, p. 565–579.

Lipovsky, P.S. and Bond, J.D., 2022. Surficial geology and Quaternary history of Stevenson Ridge and northern parts of Kluane Lake map areas, Yukon (115K and 115F). Yukon Geological Survey, Bulletin 18, 84 p. plus appendices.

Lipovsky, P.S., Evans, S.G., Clague, J.J., Hopkinson, C., Couture, R., Bobrowsky, P., Ekström, G., Demuth, M.N., Delaney, K.B., Roberts, N.J., Clarke, G. and Schaeffer, A., 2008. The July 2007 rock and ice avalanches at Mount Steele, St. Elias Mountains, Yukon, Canada. Recent Landslides, vol. 5, p. 445–455.

McKnight, E.A., Swanson, H., Brahney, J. and Hik, D.S., 2021. The physical and chemical limnology of Yukon's largest lake, Lhù'ààn Mân' (Kluane Lake), prior to the 2016 'A'ą̈y Chù' diversion. Arctic Science, vol. 7, p. 655–678.

Meredith, M., Sommerkorn, M., Cassotta, S., Derksen, C., Ekaykin, A., Hollowed, A., Kofinas, G., Mackintosh, A., Melbourne-Thomas, J., Muelbert, M.M.C., Ottersen, G., Pritchard, H. and Schuur, E.A.G., 2019. Polar Regions. *In:* IPCC Special Report on the Ocean and Cryosphere in a Changing Climate 2019, H.-O. Pörtner, D.C. Roberts, V. Masson-Delmotte, P. Zhai, M. Tignor, E. Poloczanska, K. Mintenbeck, A. Alegría, M. Nicolai, A. Okem, J. Petzold, B. Rama and N.M. Weyer (eds.). Cambridge University Press, p. 203–320.

Menounos, B., Osborn, G., Clague, J.J. and Luckman, B.H., 2009. Latest Pleistocene and Holocene glacier fluctuations in western Canada. Quaternary Science Reviews, vol. 28, p. 2049–2074.

Milner, A.M., Khamis, K., Battin, T.J., Brittain, J.E., Barrand, N.E., Füreder, L., Cauvy-Fraunié, S., Gíslason, G.M., Jacobsen, D., Hannah, D.M. and Hodson, A.J., 2017. Glacier shrinkage driving global changes in downstream systems. Proceedings of the National Academy of Sciences, vol. 114, p. 9770–9778.

Northern Climate ExChange, 2014. Projected Future Changes in Glaciers and their Contribution to Discharge of the Yukon River at Whitehorse. Northern Climate ExChange, Yukon Research Centre, Yukon College, 44 p.

Painter, M., 2021. Formation and drainage of glacier dammed Dań Zhùr (Donjek) Lake, Yukon. MSc thesis, University of Ottawa, Ontario, Canada, 75 p.

Reyes, A.V., Luckman, B.H., Smith, D.J., Clague, J.J. and Van Dorp, R.D., 2006. Tree-ring dates for the maximum Little Ice Age advance of Kaskawulsh Glacier, St. Elias Mountains, Canada. Arctic, p. 14–20.

Rousseau, A.N., Savary, S., Tremblay, S., Caillouet, L., Doumbia, C., Augas, J., Foulon, E. and Abbasnezhadi, K., 2020. A distributed hydrological modelling system to support hydroelectric production in northern environments under current and changing climate conditions. Centre Eau Terre Environment Report no. R1926, 246 p.

Shugar, D.H., Burr, A., Haritashya, U.K., Kargel, J.S., Watson, C.S., Kennedy, M.C., Bevington, A.R., Betts, R.A., Harrison, S. and Strattman, K., 2020. Rapid worldwide growth of glacial lakes since 1990. Nature Climate Change, vol. 10, p. 939–945.

Shugar, D.H., Clague, J.J., Best, J.L., Schoof, C., Willis, M.J., Copland, L. and Roe, G.H., 2017. River piracy and drainage basin reorganization led by climate-driven glacier retreat. Nature Geoscience, vol. 10, p. 370–375.

Stahl, K. and Moore, R.D., 2006. Influence of watershed glacier coverage on summer streamflow in British Columbia, Canada. Water Resources Research, vol. 42.

Young, E., Flowers, G., Berthier, E. and Latto, R., 2021. An imbalancing act: The delayed dynamic response of the Kaskawulsh Glacier to sustained mass loss. Journal of Glaciology, vol. 67, p. 313-330. https://www.pc.gc.ca/en/pn-np/yt/kluane/nature/geomorph.

Yukon Energy, 2022. Quick Facts. https://yukonenergy.ca/energy-in-yukon/electricity-101/quick-facts, [accessed December 2022}.

Yukon Geological Survey

Yukon Geological Survey staff are located in two buildings in Whitehorse: the Elijah Smith Building at 300 Main Street, room 102, and the H.S. Bostock Core Library at Mile 918 on the Alaska Highway.

Branch Director

H.S. Bostock Core Library

Relf, Carolyn – Director, (867) 667–8892 carolyn.relf@yukon.ca

Operations

H.S. Bostock Core Library

Minor, Julie – Manager, Finance & Operations, (867) 667–8508 julie.minor@yukon.ca

Outreach

H.S. Bostock Core Library

Weston, Leyla – Outreach Geologist, (867) 393–7187 leyla.weston@yukon.ca

Regional Geology

H.S. Bostock Core Library

Colpron, Maurice – Head, Regional Geology, (867) 667–8235 maurice.colpron@yukon.ca
Ambrose, Tyler – Project Geologist, (867) 667–5175 tyler.ambrose@yukon.ca
Cobbett, Rosie – Project Geologist, (867) 455–2802 rosie.cobbett@yukon.ca
Moynihan, David – Project Geologist, (867) 455–2805 david.moynihan@yukon.ca
Skipton, Diane – Project Geologist, (867) 667–5175 diane.skipton@yukon.ca
Sternbergh, Sarah – Project Geologist, (867) 332-2122 sarah.sternbergh@yukon.ca

Surficial Geology

Elijah Smith Building

Bond, Jeffrey – Head, Surficial Geology, (867) 667–8514 jeff.bond@yukon.ca
van Loon, Sydney – Placer Geologist, (867) 667–3408 sydney.vanloon@yukon.ca

H.S. Bostock Core Library

Cronmiller, Derek – Surficial Geologist, (867) 332–4961 derek.cronmiller@yukon.ca
Kennedy, Kristen – Surficial Geologist, (867) 393–7188 kristen.kennedy@yukon.ca
Lipovsky, Panya – Surficial Geologist, (867) 667–8520 panya.lipovsky@yukon.ca

Minerals Geology

Elijah Smith Building

Casselman, Scott – Head, Minerals Geology, (867) 667–8192 scott.casselman@yukon.ca
Bullen, Warwick – Mineral Assessment Geologist, (867) 667-3205 warwick.bullen@yukon.ca
Ellis, Sarah – Economic Geologist, (867) 332–9263 sarah.ellis@yukon.ca

H.S. Bostock Core Library

Emberley, Justin – Core Library Manager, (867) 393–6492 justin.emberley@yukon.ca
Sack, Patrick – Metallogenist, (867) 667–3203 patrick.sack@yukon.ca

Editorial & Technical Services

Elijah Smith Building

MacFarlane, Karen – Head, Technical Services, (867) 667–8519 karen.macfarlane@yukon.ca
Elliot, Brett – Geological Spatial Database Administrator, (867) 667–8481 brett.elliot@yukon.ca
Staffen, Bailey – GIS Technician/Web Manager, (867) 456–6801 bailey.staffen@yukon.ca

Yukon Geological Survey
Energy, Mines and Resources
Government of Yukon

Yukon Geological Survey

celebrating 30 years
of delivering
Yukon’s geological
information